July 2016

Geochemical Attributes of Hydraulically Active Fractures and Their Influence on Groundwater Quality

Amy L. Hudson
University of Massachusetts Amherst

GEOCHEMICAL ATTRIBUTES OF HYDRAULICALLY ACTIVE FRACTURES AND THEIR INFLUENCE ON GROUNDWATER QUALITY

A Dissertation Presented

By

AMY L. HUDSON

Submitted to the Graduate School of the
University of Massachusetts Amherst in partial fulfillment
of the requirements for the degree of

DOCTOR OF PHILOSOPHY

May 2016

Department of Geosciences

GEOCHEMICAL ATTRIBUTES OF HYDRAULICALLY ACTIVE FRACTURES AND THEIR INFLUENCE ON GROUNDWATER QUALITY

A Dissertation Presented

By

AMY L. HUDSON

Approved as to style and content by:

_____
David F. Boutt, Chair

_____
Michele L. Cooke, Member

_____
Steve Petsch, Member

_____
James F. Holden, Member

_____
Julie Brigham-Grette, Department Head
Department of Geosciences

DEDICATION

In loving memory of my father

ACKNOWLEDGEMENTS

To my husband Jayson Shane Hudson, thank you for all the love and support through the years that I have been a student; I couldn't have done this without you. To my mother Judith Ann Friant, thank you for the lifelong support of my academic career and believing that I could accomplish any goal I set for myself. To my father, Ronald James Friant, the scientific tree from which I fell, thank you for instilling and nurturing a scientific curiosity in me; I only wish you could have been here to see how closely I followed in your steps.

I am particularly grateful for the support, guidance, and direction provided to me by my advisor, Dr. David F. Boutt. I would also like to thank my other committee members, Dr. Michele L. Cooke, Dr. Steve Petsch, and Dr. James Holden for their support, insight, and encouragement through the dissertation process. The Geosciences Department graduate students and faculty have provided in valuable support through assistance with equipment and for the many insightful discussions during my time at UMass Amherst. I would also like to express my gratitude to the alumni of the Geosciences Department for their kind contributions to the department grants which provided funding for field equipment and sample preparation. Specific members of the department that I would like to thank are the UMass Amherst Hydrogeology Research Group (2011-2016) for always providing a supportive environment to exchange ideas and develop my research; Sean Regan for help in the rock room, assistance with sample preparation, and guidance through the optical methods; Greg de Wett for assistance with the Geokon MSCL scanning; Dr. J. Michael Rhodes and Pete Dawson for help with ITRAX XRF core scanner; and Dr. Michael J. Jercinovic for assistance with analyzing my thin sections with the microprobe.

I am appreciative of the Smith College Centre for Environment, Ecological Design & Sustainability (CEEDS) for meteorological data and allowing the installation of the groundwater wells MFS-1 and MFS-2 at the Ada & Archibald MacLeisch Field Station. To Reid Bertone-Johnson and Paul Wetzel with CEEDS and the MacLeish Field Station, thank you for allowing me access and support at the field site through my data collection. I would also like to thank Smith College, Dr. Marc Anderson, Dr. Robert Newton, and Dr. Amy Rhodes for allowing me access and use of the equipment of the aqueous geochemical laboratory, and for their assistance in running my analytical chemistry analysis.

It would be unkind of me not to express gratitude to my employer, Tetra Tech supporting my academic advancement through tuition reimbursement and a flexible work schedule. I am appreciative of the understanding and support the staff of the Littleton, Massachusetts; Golden, Colorado; and Louisville, Colorado offices have provided me. I am particularly grateful to Dr. Andrew Harley for the always interesting and intellectually challenging conversations and helping me think through the geologic and geochemical process. I would also like to thank Dr. Tiffany Thomas for being a great personal and professional friend through all of this and providing my quality assurance and quality control review of my data and geochemical modeling.

ABSTRACT

GEOCHEMICAL ATTRIBUTES OF HYDRAULICALLY ACTIVE FRACTURES AND THEIR INFLUENCE ON GROUNDWATER QUALITY

MAY 2016

AMY L. HUDSON, B.S. MARY WASHINGTON COLLEGE

M.S. COLORADO SCHOOL OF MINES

Ph.D. UNIVERSITY OF MASSACHUSETTS AMHERST

Directed by: Professor David F. Boutt

Groundwater is a widely utilized resource, and sustainability of the Earth's populations is becoming more and more dependent on access to clean, reliable groundwater sources for drinking water. Populations are becoming more dependent of fractured bedrock aquifers, particularly in arid regions, but the characteristics of hydraulically active fractures can be challenging to characterize. Limited research has focused on natural water-rock interactions to understand how the whole rock chemistry of the bedrock formation affects the groundwater quality. This study utilized discrete interval diffusion sampling of a fractured bedrock well completed in schist to investigate if a natural weathering signal can be used to identify hydraulically active fractures. The open borehole well MFS-1, is the focus of the study of the fractured crystalline bedrock aquifer and the groundwater quality data presented herein. The close proximity of Well MFS-1 to the recharge zone makes it an ideal location for testing the hypotheses of this study.

Through this study, the hydraulically active fractures of Well MFS-1 were identified as being present between 8.2 and 8.7 meters (26.9 and 28.5 feet) bgs, and the dominant mixing force of the water column of the well is driven by thermal convection in the upper portion of the well and upward gradients present above 24.3 meters (80 feet) bgs.

Additionally, the isotopic data collected from the well concludes that these forces are sufficient to fully mix the water in Well MFS-1 over the one month diffusion sampler deployment period. Carbonate dissolution and sulphide oxidation are the dominant weathering reactions and source of weathering products measured in the groundwater from Well MFS-1. Iron in groundwater is in the reduced form (ferrous) while flowing through the fractured system, and becomes oxygenated when it enters the well, resulting in a significant amount of iron hydroxide precipitate. The best signal of natural weathering and the systems response to changes in recharge is shown by the changes in silicon concentration in solution. The highest silicon concentrations measured in the groundwater samples were related to waters recharged during the highest precipitation period of the year. The greatest response to system perturbations were observed at the hydraulically active fractures, as shown in the changes in measured concentrations in this portion of Well MFS-1. Even though in-well mixing causes the concentrations of natural weathering products to be measureable throughout the water column, the signal and response to changes in system chemistry are greatest at the hydraulically active fractures.

The groundwater data provided sufficient information to determine the dominant weathering mineral groups (carbonates and sulphides), and inverse geochemical modeling was used to identify albite, pyrite, and goethite dissolution and precipitation of siderite as the minor weathering reactions contributing to the weathering products in groundwater. The more dominant mineral weathering reactions identified from the modeling are calcite, gibbsite, phlogopite dissolution and dolomite and muscovite precipitation. These reactions are the source of the sodium, sulphate, iron, calcium, and alkalinity being observed in the groundwater quality samples. The precipitation of siderite, or another iron carbonate

mineral, is the likely source of iron in the system. Simulation of oxygen transport was also complete for this study to investigate the presence of red staining on the surface of hydraulically active fractures and determine if it is likely the result of oxidation of ferric iron. The simulation of oxygen flow through a single fracture showed the transport of oxygen was limited to the first few meters of the fracture. This amount of oxygen transport would confine the weathering reactions requiring or limited by oxygen to locations within a few meters of the recharge of oxygenate water. This is consistent with the groundwater data collected from Well MFS-1 that showed that the water was under reducing conditions until it enters the borehole, but does not support the conclusion that red staining observed to be present in the rock matrix adjacent to hydraulically active fractures is an indication of the oxidation of iron.

Studying the rock core collected from the fractured bedrock well showed that the hydraulically active fractures are all associated with red staining on the fracture surface and in the matrix of the rock adjacent to the fracture, but the data does not support the conclusion that iron oxide is currently being precipitated. The spectrophotometry data did not show that the red staining is iron rich or oxides are present in the rock based on color and reflectance data. The elemental mapping of the rock samples from MFS-1 using XRF and electron microprobe further shows high iron concentrations throughout the rock, not just at the fracture surface. The fractures in the advective zone have lower potassium and aluminum concentrations toward the fracture surface, which does not support precipitation as the dominant reaction in this portion of the system, as would be expected if the red staining is iron oxide precipitate resulting from the current transport of water. Other observations about the rock, such as the presence and nature of garnet crystals show that

the current zone of advective flow in Well MFS-1 was previously active during a period of hydrothermal activity. More work is needed to fully understand the source of red staining and its relationship to hydraulic activity in fractured bedrock aquifers, but it has been shown in this study that the broad assumption that it represents iron oxide staining is not correct.

TABLE OF CONTENTS

Page

LIST OF TABLES

LIST OF FIGURES

Figure Page

CHAPTER 1

INTRODUCTION

Geochemical characteristics of the fracture surface, fracture coatings, and surrounding weathering rind, as well as the geochemical composition of water associated with fractured bedrock aquifers were investigated as tools for identification of hydraulically active fractures. This study is unique from previous investigations into fractured bedrock systems because it seeks to develop a relationship between fracture surface geochemical attributes of crystalline bedrock and a fractures' propensity to take part in advective transport.

1.1 Motivation and Purpose

Groundwater is a widely utilized resource, and sustainability of the Earth's populations is becoming more and more dependent on access to clean, reliable groundwater sources for drinking water. Fractured crystalline bedrock, characterized by low matrix permeability and flow primarily focused within the rock's secondary porosity, are being used more often as a primary source of potable water throughout the world. However, contamination of groundwater resources, hydraulic fracturing, and storage of various types of waste (e.g., deep injection, spent nuclear fuel storage, and mine waste facilities) threaten to reduce the number of aquifers that can be utilized for drinking water. Fractured bedrock systems present unique challenges for preventing contamination and remediation of aquifer contamination after it occurs, limiting the resources available to support water supply even further.

Having additional tools available to characterize the hydraulically active fractures will allow for a more detailed presentation of the aquifer behavior to the general public and

more effective decision making by stakeholders. Although bedrock aquifers typically exhibit low productivity, they are nonetheless important sources of potable water because they: 1) are the only sources of water in certain regions, 2) are easily accessible, 3) are very widespread, and 4) occur in many arid and semi-arid regions (Wright, 1992). Increasing the understanding of the stakeholders increases the likelihood of successful and sustainable development of our natural resources now and in the future.

1.2 Background

A significant body of research on saturated crystalline rocks has been amassed. The United States Geological Survey (USGS) Toxic Substances program studied fractured bedrock at the Mirror Lake site of the Hubbard Brook Experimental Forest, New Hampshire during a 20 year research program. Their research investigated the multi-scale properties and characterization techniques of groundwater flow and chemical transport in fractured rock, which has yielded tremendous insights into crystalline fractured rock environments (Shapiro et al., 2007). Local-scale investigations have been conducted over distances of tens of meters and focused on identification of fractures and fracture properties in outcrops (Barton, 1996), fractures in the subsurface using borehole and surface geophysics (Johnson and Dunstan, 1998; Paillet, 1985; Paillet and Kapucu, 1989), and hydraulic and transport properties of fractures by means of hydrologic testing (Hsieh, 1996; Hsieh and Shapiro, 1996; Tiedeman and Hsieh, 2001; Tsoflias et al., 2004; Halihan et al., 2005).

The hydrogeologic properties of fractured rocks are determined by the existence, aperture, and connectivity of discrete features (i.e., fractures and faults). The hydrogeologic state (degree of saturation, hydraulic gradient, etc.) of these rocks controls the occurrence, nature, and rate of fluid movement. Fracture permeability in crystalline rocks varies over

several orders of magnitude, exhibits considerable spatial variability over short distances, and shows a decrease with depth (Zhou et al., 2007). Hydrogeologists have long known that water wells in fractured bedrock typically have low yields (Meinzer, 1923). Davis and Turk (1964) found that the characteristics of hydraulically active crystalline rocks are primarily controlled by weathering and structure.

Fluid transport in fractured systems is controlled by fracture size, surface roughness, and matrix diffusion. Zhou et al. (2007) highlighted the range of matrix porosity, hydraulic conductivity, fracture aperture, matrix diffusion coefficient, and other fracture characteristics observed in the diverse range of studies summarized in their literature survey. Matrix diffusion controls chemical flow rate and concentrations through solute storage away from the primary flow path of the fracture (Grisak and Pickens, 1980), while rock type is commonly considered to be of secondary importance (Caine and Tomusiak, 2003; Surrette and Allen, 2008). Minerals that coat fractures can alter the porosity, reactive properties, and matrix diffusion coefficient (Grisak and Pickens, 1980). Wellman et al., (2009) examined the validity of simplifying the systems for simulation and changes with travel distance away from the source. Their work found that simplifications could be made, but reinforced that fractured rock aquifers are complex systems and the importance of being able to isolate the features that are active in order to minimize error in predicting fate and transport of chemical contaminants.

Weathering reactions within fractured bedrock aquifers are a function of the fluid residence time and flow within the fractures (Maher, 2010). Much of the work related to weathering reactions has been focused on developing weathering rates and understanding the mechanisms that control weathering rates (Berner, 1978; Malmstrom and Banwart,

1997; White, 2002), understanding the discrepancies between field based rates and laboratory based rates (Ganor et al., 2005; Malmstrom et al., 2000; Pacheco and Alencoao, 2006; Li et al., 2008; Steefel and Lichtner, 1998), or accurately simulating the various scales (single pore or fracture, short flow path, aquifer scale flow paths) of mineral weathering (Navarre-Sitchler et al., 2011; Steefel et al., 2005; Malmstrom et al., 2004).

The degree of weathering is often noted on borehole logs as the amount of red staining or surface coating present, and qualitative classification schemes are based on these indicators (Ehlen, 2002). However, the presence of red staining or fracture coatings may not be indicative of current weathering conditions or the presence of oxygen, but rather past alteration or weathering events. The most likely source of the red staining is iron rich minerals hosted in the pores of secondary minerals (Drake and Tullborg, 2006). Drake et al., (2008) furthered their understanding of the red staining and found that the source of the red staining was not current water flow and weathering reactions, but was due to historic hydrothermal alteration of iron already present in the rock, and in particular the alteration of plagioclase. Some work has investigated the possible connection between water quality and red staining or fracture coatings (Smith and Roychoudhury, 2013; Mathurin et al., 2014). These studies also found that the staining may not be an indication of the presence of oxygen, that there is little information available on the mobilization of iron and other metals relative to the whole rock composition, and that the fracture coatings limit the frayed edge sites and thus the exchange capacity of the rock with the groundwater. The Mathurin et al. study (2014) assumes that the high temperature alteration sourced coatings and low temperature fracture coatings are the same, but this was not confirmed. This assumption

would require that the weathering reactions and mechanisms would be similar whether sourced from low or high temperature solutions.

Work at the Susquehanna/Shale Hills Critical Zone Observatory (SSHO) has focused on understanding the development of regolith and how the regolith formation impacts fluid pathways and solute residence times. Part of this interdisciplinary team has focused on the water-rock interactions and weathering fronts that develop during regolith formation. Jin et al., (2010) investigated the mineral transformations in both the valley and ridge areas of the SSHO, focusing on constraining the weathering and erosion rates. Further studies highlighted the coupled geochemical and hydrologic processes that control weathering and erosion rates, as well as evidence for nested chemical weathering reaction fronts (Jin et al., 2011; Brantley et al., 2013). Although these studies allude to the changes in flow conditions that can develop as a result of chemical weathering, the scale of their focus did not address the pore or fracture characteristics that could be influencing the groundwater chemistry.

This study has furthered the understanding of red staining, how it relates to the whole rock composition and water quality, and what that can tell us about where the zone of advective flow is occurring. The specific questions answered/hypotheses tested as part of this study included:

- The fracture coating/red staining of a hydraulically active fracture is thinner than a hydraulically inactive fracture due to the disequilibrium between the fracture and the water moving past the fracture surface.

- Hydraulically active fractures host both dissolution and precipitation reactions due to departure from equilibrium, where inactive fractures will be subject to only precipitation.
- The red staining in the matrix adjacent to a hydraulically active fracture is the result of oxygen present in the water that is diffused into the rock matrix and oxidizes the iron present in the rock.
- The depth of the red staining and rate of diffusion of oxygen into the rock can be used to determine the minimum amount of time that the fracture has been actively transporting water.

1.3 Document Organization

This document has been organized into six parts, including three technical chapters. Chapter 1 has served to introduce the motivation for this study and background on the related research. The remainder of the document is organized to discuss the groundwater quality data in Chapter 2, the numeric modeling of oxygen transport along fractures and geochemical modeling of the water-rock interactions in Chapter 3, Chapter 4 presents the geochemical testing of bedrock core samples collected from the well that is the primary source of data for Chapter 2, Chapter 5 provides concluding remarks for the overall study, and references are provided after Chapter 5. Portions of Chapters 1 and 2 have been submitted to Groundwater, published by the National Groundwater Association, for consideration of publication.

CHAPTER 2

MEASUREMENT OF GROUNDWATER QUALITY FOR NATURAL WEATHERING PRODUCTS AND INDICATION OF ADVECTIVE FLOW IN A FRACTURED BEDROCK SYSTEM

Our dependence on fractured crystalline bedrock aquifers for potable sources of water is becoming ever greater, particularly in arid regions, making our need for accurate characterization of these systems and understanding how the rock affects water quality increasingly important. Strong preferential flow paths, very low porosity (0.001 to a few percent [Grisak and Pickens, 1980]), low storage, and high degrees of flow anisotropy are some of the properties of fractured bedrock aquifers that make them very different from classically studied aquifer materials (uncemented and cemented clastic sediments). As a result, classic aquifer characterization and analysis tools more appropriately applied to porous media (such as conceptual and numerical models), do not apply to fractured rock aquifers. In recent years, advances have been made to develop aquifer characterization techniques in two-dimensions (map view) based on structural and lithologic properties (e.g., Caine and Tomusiak, 2003; Surrette and Allen, 2008). These approaches led to a more realistic framework for conceptualizing fractured-rock flow systems, while allowing for more detailed regional hydrogeologic analyses. Studies at the Mirror Lake Research Site, Turkey Creek Basin, and Kamaishi Mine revealed that the average active fracture density is approximately 10^{-2} to 10^{-1} fractures per meter (Wellman et al., 2009). Boutt et al. (2010) also found that the small percentage of hydraulically active fractures (2.5% in their field study of Massachusetts) are generally isolated to the upper 100 meters and most are at even shallower depths. However, these studies do not reveal why only a small percentage (estimated to be no more than 5-10%) of the fractures are conductive, nor do they address how to identify hydraulically active fractures based on the physical and

chemical properties of the fracture surface, fracture coatings, and surrounding weathering rind or natural weathering signals in groundwater.

The geologic setting and associated hydrogeologic conditions present in the eastern United States are highly complex due to the numerous compressional and extensional tectonic events that have taken place (Seaton and Burbey, 2005). In the fractured bedrock systems of the Blue Ridge Province of the eastern United States, the fractured bedrock aquifer system underlies an upper saprolite aquifer and research has concluded that the flow in the fractured bedrock portion of the system is more significantly controlled by the tectonic history of the rock, than the weathering of bedrock as is the typical conceptual model (Seaton and Burbey, 2005). However, in areas further north along the eastern portion of the United States, the saprolitic unit has been removed through multiple glacial advances and retreats forming a connected aquifer system between the overlying till and the underlying fractured bedrock. The characteristics of hydraulically active crystalline rocks in the fractured bedrock of New England, are therefore expected to be primarily controlled by weathering and current structure. Several studies have identified the importance of residence time, rather than physical structure as a controlling mechanism of weathering reactions, and that the relative analyte concentrations released vary depending on the system (Davis and Turk, 1964; Malmstrom et al., 2004; Steefel et al., 2005; Maher, 2010; Navarre-Sitchler, 2011). It has been observed that continued flushing of minerals with fresh water can accelerate the dissolution reactions because the ions being released into solution are transported away from the mineral surface, maintaining a state of disequilibrium (Berner, 1978). Therefore, if sufficient residence time exists in an aquifer to develop weathering reactions due to the water-rock interactions, a correlation can be made between

weathering product concentrations measured in groundwater and the presence of advective flow within a fractured bedrock aquifer.

2.1 The Smith College Ada and Archibald MacLeish Field Station – Whately, Massachusetts

The Ada and Archibald MacLeish Field Station (MacLeish Field Station) in Whately, Massachusetts operated by Smith College was the primary site utilized for conducting this research (Figure 1). Specifically, the open borehole bedrock well MFS-1, installed in June 2012, was the focus of the study of the fractured crystalline bedrock aquifer and the groundwater quality data presented herein (Figure 2). Data is also presented for two additional groundwater wells installed at the MacLeish Field Station, the shallow monitoring well screened across the till/bedrock interface (MFS-2) and the deeper bedrock well being utilized as a water supply for the onsite classroom (MFS-tap) (Figure 2). Each well represents a different hydrogeologic condition at the MacLeish Field Station (i.e., thin till/shallow bedrock, unconsolidated sediment (thick and thin till), and thick till/deep bedrock), highlighting the complexity of this system. In addition to the data collected at the MacLeish Field Station, data collected by the USGS from 1995 to 2007 as part of the study of the New England Crystalline Rock Aquifers (NECRA) was also considered (Flanagan et al., 2011).

The MacLeish Field Station is a multi-use research facility currently supporting studies in hydrology, hydrogeology, geochemistry, ecology, natural art, as well as outdoor education. Figure 2 provides a detailed site layout, including the locations of the wells used in this study, as well as related and neighboring research project locations. The history and physical setting of the MacLeish Field Station have been well documented through

multiple graduate theses and dissertations. The following sections provide a general overview of the relevant site conditions applicable to this study.

2.1.1 Physiographic Setting

The MacLeish Field Station is located near the headwaters of the Westbrook Watershed and consists of two open fields, separated by a small unnamed tributary to Jimmy Nolan Brook and surrounded by dense forest. The surrounding forest is a mix of hardwood and softwood tree species. Near complete removal of the forested areas occurred during the colonial period resulting in a second or third generation forest. Historically, the site was operated as an apple orchard and currently a new orchard is being established in the western field, south of Wells MFS-1 and MFS-2 and the new site meteorological station (Figure 2). The vegetation along the riparian corridors of the unnamed tributary and Jimmy Nolan Brook are primarily softwood trees (white pine and eastern hemlock). Further upland and away from the surface water drainages, the forested areas support more hardwood tree species, such as northern red oak, white ash, sugar maple, and white birch.

2.1.2 Climate

The climate is characterized as northern temperate, which has four distinct seasons, with warm summers and cold winters. Precipitation occurs throughout the year, but can be highly variable location to location, with heavy snowfall and significant snowpack common during winter. Data has been collected at ten minute intervals from an onsite meteorological station located at the end of Poplar Hill Road since 2009. The station instruments are mounted at the top of 25.3 meter (83 feet) tall tower, and include measurement of relative humidity, temperature, barometric pressure, wind speed, wind direction, and solar radiation. Measurements collected from the tower ensure that the surrounding canopy does not influence the data. At ground level, a tipping bucket measures

precipitation. A new meteorological station was installed during 2014, in the orchard near the site wells, but only a limited amount of data is available from this station.

Weather Underground Station KMACONWA2 is located on Whately Road, less than one mile from the site and has been monitoring since February 2007 and is the longest and most complete record near the MacLeish Field Station. Figure 3 presents the data collected from Weather Underground Station KMACONWA2 for the period February 2007 to September 2015. In general, the lowest temperatures are measured in January and the highest in July. Average temperatures below freezing are common from early November to late March. As is typical of temperate climates, the humidity is relatively high, with average values above 50% much of the year. The lowest humidity periods are during the coldest months of the year. Wind speeds are typically low, with average values ranging from zero to two meters per second (m/s), with maximum gust speeds are below 15 m/s (33.5 miles per hour [mph]) except during large storm events, which can have gusts in excess of 45 m/s (100 mph).

2.1.3 Surficial Geology

The Westbrook Watershed is dominated by glacial sediments (glacial till and stratified drift) with numerous bedrock outcrops. During the last glacial period, the ice advanced in a south-southeastern direction and retreated in a south to north direction. The last glacial advance and retreat resulted in a layer of till being placed directly over the bedrock surface, with areas of thicker (and likely older) till in incised bedrock valleys and thinner layers deposited over higher bedrock surfaces. Figure 4 presents the surficial geology of the Williamsburg Quadrangle (Stone and DiGiacomo-Cohen, 2010). Table 1 provides a detailed description of the surficial geology interpretation of Segerstrom (1955) and Stone and DiGiacomo-Cohen (2010). The surficial geologic units of the MacLeish

Field Station are shallow bedrock on the western portion of the site and thick till deposits on the eastern portion.

The till thickness observed overlying crystalline bedrock during the drilling of Wells MFS-1 and MFS-2 and determined from geophysical surveys of the western field of the MacLeish Field Station is in the range of 1.5 meters (4.9 feet) near the western edge of the field and greater than 7.5 meters (24.6 feet) on the eastern side of the field, near the unnamed tributary to Jimmy Nolan Brook. The surficial geology map of the area (Figure 4) locates these wells in an area of shallow bedrock, which is consistent with conditions observed during drilling and the geophysical survey. Well MFS-tap is located near the western side of the eastern field at the MacLeish Field Station, in an area mapped as a thick till deposit. It is estimated that the location of the Well MFS-tap has greater than 100 feet of till overlying the bedrock surface, which is also consistent with the surficial geology map. A thin layer of soil is present in the open fields over the till deposits, which also thickens from west to east moving downhill across the site. Soils are well drained, and are classified as fine sandy loam with an average thickness of 75 centimeters (approximately 2.5 feet).

Stratified drift deposits are found at lower elevations in the Westbrook Watershed. These deposits are coarser than the till units with gravel, sand, and silt sized grains. The deposition of the stratified drift was associated with the erosion of the surrounding highlands during the period of Glacial Lake Hitchcock (Stone and DiGiacomo-Cohen, 2010). This unit is not present in the area of the wells being studied, but a thin area of glacial stratified deposits cuts across the southern portion of the MacLeish Field Station (orange yellow unit shown on Figure 4).

2.1.4 Bedrock Geology

The Waits River-Gile Mountain Province (Mc-wg), is a narrow North-South trending metamorphic geologic unit that runs parallel to the New Hampshire-Vermont state borders and along the western edge of the Connecticut River Valley in Massachusetts, as shown on Figure 5 (Flanagan et al., 2011). The rocks of the Waits River-Gile Mountain Province are metasedimentary deposits of Lower Devonian age, composed of metamorphosed clastic, calcareous, and semi-pelitic marine rocks (Flanagan et al., 2011). The rocks of this province were deposited under the Iapetus Ocean, which received contributions from the continental highlands, calcium carbonate from marine organisms, and detrital igneous clastics, which were subsequently metamorphosed during multiple tectonic collisions. Due to the variable nature of the deposition, the mineralogy and particle size distribution can be highly heterogeneous.

The Conway Formation (SOc) of the Waits River-Gile Mountain Province is the predominant bedrock geologic unit mapped as underlying the MacLeish Field Station (Figure 6), and specifically the undifferentiated Schist-Marble and Schist-Quartzite Members, (Socu) of this formation were observed to be present (Willard, 1956). Later mapping identified the Waits River-Gile Mountain Formations mapped further to the north and the Conway Formation mapped in Massachusetts as being the same geologic unit, and for consistency, regional maps do not differentiate the Conway Formation (Hatch et al., 1988). Hatch et al. (1988) describe the Waits River unit as a low-alumina, graphitic mica schist with localized sulphides. The marble is noted to weather brown and there are widespread quartz veins (Hatch et al., 1988). Berkley (1999) describes the bedrock geology at the MacLeish Site as being a quartz-mica schist, containing biotite marble, interbedded with even grained quartzite. Both the regional geologic unit and site specific geologic

descriptions are consistent with the geology observed to be present at the MacLeish Field Station during this study. Figure 6 presents the bedrock geologic map of Willard (1956), with an inset showing the detail of the geologic units underlying the MacLeish Field Station.

2.1.5 Hydrology

The glacial influence and the steep topographic setting have played key roles in the development of the current hydrologic system of the MacLeish Field Station. Areas of deposition of fine grained material have resulted in poorly drained wetland areas, while areas where the meltwater eroded through the deposited material, bedrock streams are present with numerous reaches of rapids and waterfalls. Wells MFS-1 and MFS-2 are positioned topographically and hydrologically above neighboring wetland areas and the small unnamed tributary to Jimmy Nolan Brook, and are not influenced by these features.

2.1.6 Hydrogeology

Groundwater is present in both the till and the fractured crystalline bedrock below the MacLeish Field Station. In the location of Wells MFS-1 and MFS-2, the groundwater level is relatively shallow, measuring between three and four meters below ground surface (bgs). Well MFS-2 is screened across the till/bedrock contact to observe if there is a connection or measureable gradients across this interface. The groundwater quality data from this well suggests that it did not intersect any hydraulically active fractures within the bedrock and is representative of till water.

A single electrical resistivity tomography (ERT) survey line was completed across the western field at the MacLeish Field Station, approximately 25 meters (82 feet) to the south of the site wells. A 25 electrode dipole-dipole array was installed with a ten meter (32.8 foot) spacing (Isaacson, in progress). Figure 7 shows the transect of the ERT survey

completed at the MacLeish Field Station. Figure 8 presents the modeled resistivity values of the ERT survey. The western side of the ERT transect is closest to the wells and provides further detail of the local hydrogeologic system. Area 4 shown on Figure 8, is interpreted to have a mean resistivity that corresponds to glacial deposits that are well drained and are partially saturated (Isaacson, in progress). Area 5 below this has the highest mean resistivity of the ERT survey, which is interpreted to represent crystalline bedrock with low saturation (Isaacson, in progress). The dark blue zone within this area are the highest measured resistivity values of the ERT survey, representing an area between the two wells that is less fractured than the surrounding bedrock. A bedrock outcrop is visible in the western field of the MacLeish Field Station in the area of this observation supporting the interpretation of the ERT survey values and the presence of a more competent area of bedrock. Figure 9 presents a closer view of the western portion of the ERT survey with the stratigraphy of the Wells MFS-1 and MFS-2 shown for further context.

The NECRA characterized the groundwater of the Waits River-Gile Mountain province as being young, with low concentrations of dissolved constituents (Flanagan et al., 2011). As with other lithologic groups in the NECRA, the hydraulic conductivities were observed to be low and well yields typically less than five gallons per minute (gpm) (Harte et al., 2008). Concentrations of iron and manganese were observed to be the lowest in the Waits River-Gile Mountain lithologic grouping when compared to the other eight lithologic groupings of the NECRA study (Flanagan et al., 2011). Locally, waters in this geologic formation have minimal neutralization capacity, although the pH is observed to increase along flow paths (Berkley, 1999). In general, calcium has been observed to increase with residence time in the groundwater of the NECRA (Flanagan et al., 2011). Based on the

observed relative concentration of common ions in MacLeish Field Station waters (magnesium < potassium < sodium < calcium), it was previously hypothesized that the cations measured in solution were the result of natural weathering reactions (Berkley, 1999).

2.2 Methods

A limited amount of research has focused on the groundwater quality resulting from natural water-rock interactions, and mineral mobilization from aquifer rocks, to understand how the whole rock chemistry of the bedrock formation affects the water quality (Smith and Roychoudhury, 2013). This study investigates the connections between water quality and mineralogy, if red staining is from the current water, and identifying zones of advective flow based on discrete interval water quality samples. Groundwater data from the open borehole well MFS-1, the other MacLeish Field Station wells, and the USGS data available for wells completed in the Waits River-Gile Mountain Province were utilized as the basis of the study. The methods applied involved field scale testing of boreholes and analytical testing of bulk and discrete interval water quality samples from the MacLeish Field Station wells.

2.2.1 Bedrock Well Installation

The open borehole well MFS-1 was installed in June 2012 using a CME-55 Hollow-Stem Auger (HSA) drilling rig. An 8¼-inch diameter HSA was used to drill through the till unit, to a point of refusal just below the till/bedrock contact (3.8 meters [12.5 feet] bgs). No samples were collected of the till during drilling but the cuttings were observed as they were evacuated from the hole. A steel casing was grouted into the open hole to a depth of 6.7 meters (22 feet) bgs. The bedrock was cored during drilling using an HQ-size bit to a total depth of 42.7 meters (140 feet) bgs. The cored hole was completed as an

open-borehole well below the steel casing. This allowed a detailed log of the mineralogy and structure present to be developed from the collected core and from downhole testing. The core log includes the percent recovery, the rock type and minerals present, indications of weathering or staining, and the orientation of fractures present (Figure 10). From the core log, zones of significant staining or weathering were noted for use in guiding the downhole geophysics and selecting depths for discrete interval groundwater sampling.

2.2.2 Till/Bedrock Contact Well Installation

Well MFS-2 was also installed in June 2012 using HSA and air-hammering drilling methods. The till unit was drilled using a HSA to a point of refusal at the bedrock contact. Samples of the undisturbed material were collected using 0.6 meter (two-foot) long split-spoon samplers, resulting in a single 0.6 meter (two-foot) sample for each 1.5 meter (five foot) interval drilled. After advancing each 1.5 meter (five foot) auger string, the split-spoon was driven ahead of drilling into the undisturbed material below the drill rods to collect the samples. The material recovered by the split-spoons was logged and composite samples from the full length of recovery were collected and placed in glass jars for further testing (not part of this study).

Below the till/bedrock contact (approximately 8.2 meters [27 feet] bgs), air-hammering was used to advance the hole of Well MFS-2 to a total depth of 15.2 meters (50 feet) bgs. No samples were collected of the bedrock and a core log was not developed for MFS-2. A 5.1 centimeter (two-inch) inner diameter polyvinylchloride (PVC) well was installed in the open hole, with a screened interval extending from approximately three meters (ten feet) above to 7.6 meters (25 feet) below the till-bedrock contact. The annular space of the well was completed with filter pack sand filled to approximately 0.6 meters (two feet) above the screened interval. A bentonite seal was placed above the filter pack

and the remainder of the well's annular space was filled with grout, completing the well with a steel outer casing at the surface. The purpose of this well is to study the till/bedrock interface and hydraulic connection between the aquifers.

2.2.3 Downhole Geophysics

Approximately two months after Well MFS-1 was installed, downhole geophysical testing was conducted to characterize the flow regime of the well. The two downhole geophysics tests that focused on identifying open fractures are the caliper, which measures changes in the borehole size as a three-pronged gauge is raised through the open borehole, and the Acoustic Televiewer (ATV), which images the borehole wall. The caliper measurements and ATV data show variations in the borehole wall and potential open fractures along the length of Well MFS-1; this in combination with the visible signs of weathering were used to identify specific sections of the borehole as hydraulically active and inactive.

Three additional downhole geophysical tests (temperature, resistivity, and heat pulse flow meter) were conducted that focus on the characteristics of the water in the borehole, to identify the zones of hydraulic activity and vertical gradients controlling in-well mixing of the water column. Temperature and resistivity measurements of the water column show abrupt changes at fractures that have inflow or outflow of water to/from the well. Heat Pulse Flow Meter (HPFM) measurements, collected under both ambient and pumped conditions, quantify flow rates of water entering and exiting the well and the direction of the vertical gradients, if present, within the water column of a well. Figure 11 presents the compiled results of the downhole geophysical data collection from Well MFS-1. The other site wells were not tested using downhole geophysics.

2.2.4 Water Quality Sampling

Due to the time and expense required to install, develop, and test groundwater wells, samples collected for the determination of a well's water quality often represent a single pumped, bulk sample that is representative of the average conditions across the entire open borehole or screened interval of the well (Pohlmann and Alduino, 1992). However, for wells open along long intervals of the aquifer and for fractured bedrock aquifers, a mixed sample from across a large portion of the water column or multiple active fracture zones could provide a very different water quality character than a discrete interval sample collected at an active fracture zone versus a more stagnant zone of the water column. Any natural signal that could be present at a specific depth within a fractured bedrock well and used to identify the specific zone would be masked by the rest of the water column using bulk sample collection methods (i.e. a mixed sample) typically applied to a porous media system. Therefore, this study focused on discrete interval groundwater sampling techniques.

Passive or discrete interval sampling techniques reduce the stress induced on the aquifer compared to traditional pumping and purging based groundwater sampling methods. Some examples of passive or targeted sampling techniques that are cost effective while providing high quality data are passive diffusion samplers, ZONFLO (Harte, 2013), hydrosleeve, inflatable packers, etc. ZONFLO (Harte, 2013) and packers are actively pumped sample collections methods. Passive diffusion samplers allow simultaneous collection of groundwater chemical data from specific depths vertically spaced along the water column without disturbing the ambient conditions of the system. Because this study is focused on the natural groundwater quality at specific locations along the water column and measuring natural weathering products under ambient conditions, pumping based

sample collection techniques were intentionally avoided and passive diffusion samplers were chosen.

Multiple types of passive diffusion samplers are available commercially; however, consideration must be given to the size of the elements being analyzed and their polarity. Volatile organic compounds (VOCs), which are typically the focus of contaminated site characterization and remediation, can be sampled with many of the passive diffusion samplers due to the small size of these molecules (generally less than ten angstroms) and the non-polar nature of these chemicals (ITRC, 2006); however, the analytes that are indicative of chemical weathering of rocks, such as sodium, potassium, magnesium, calcium, iron, and silicon (Malmstrom and Banwart, 1997; Pacheco and Alencoao, 2006), will not diffuse through the membranes of the diffusion bag samplers (ITRC, 2006), though most are less than ten angstroms in size (Appelo and Postma, 2005). Rigid Porous Polyethylene (RPP) samplers were selected for use in collecting water samples from Wells MFS-1 and MFS-2. The RPP samplers have pore sizes of 6 to 15 microns, allowing for testing across a broad range of soluble analytes, including polar molecules, and when completely filled with water the pores allow a water-water interface (ITRC, 2006).

In total five RPPs were deployed in Well MFS-1 to study two hydraulically active fracture zones and three hydraulically inactive fractures, as determined from the core log and downhole geophysics. Three RPPs were installed in Well MFS-2: in the till, at the till/bedrock contact, and below the base of the till. Figure 12 provides a conceptual model of the MacLeish Field Station and illustrates how the RPP samplers were deployed in Wells MFS-1 and MFS-2. Each sampler was filled with 100 milliliters (ml) of deionized water (DI water), and placed on the hanging assembly at the locations desired. A weight at the

bottom of the sampler string ensures the samplers sink to the desired depths. The assembled sampler string was lowered into the well, where they remained for approximately one month to allow equilibration with the water in the well and aquifer. The samplers were removed from the well each month to collect the water for analytical testing. The RPPs were refilled with DI water after the sample was collected and once all of the samplers on the string had been collected, the RPPs were redeployed in to the wells.

Samples were collected approximately monthly during the middle of the month, from July 2013 to July 2015, with the exception of February 2015 when the site could not be accessed due to the significant snowpack. In addition to the eight discrete interval samples collected from the RPPs, a sample was also collected from the onsite water supply well, MFS-tap. The sample from this well was collected using the tap on the outside of the classroom building. Because the construction details of this well are unknown, a specific volume of water or depth within the well could not be targeted for sampling. The tap was turned on for approximately five minutes to purge the well before a bulk sample of approximately 125 ml of water was collected. Water levels were also measured and a grab sample of water was collected for isotopic analysis from Well MFS-1 at the end of each month, by the UMass Amherst hydrogeologic research group, as part of the data collection for the USGS Northeast Climate Monitoring Network.

2.2.5 Aqueous Chemical Analyses

The groundwater samples collected each month from Wells MFS-1, MFS-2, and MFS-tap were taken to the Smith College aqueous geochemistry laboratory in Northampton, Massachusetts, the same day as the sample was collected for filtration, preservation, and measurement of total alkalinity. Approximately 100 ml of groundwater was collected from each RPP. The samples were filtered with a nominal 0.45 micron filter

using a ten ml syringe to draw the water through the filter. After filtering, 25 ml of sample was placed in a 30-ml acid washed bottle along with five drops of reagent grade nitric acid to preserve the sample for inductively coupled plasma atomic emission spectroscopy (ICP-AES) analysis. Approximately two ml of sample was placed in a glass vial, with no head space, for isotopic analysis and the remainder of the sample was returned to its original collection bottle, which had been flushed with DI water and wiped clean to ensure no reintroduction of precipitates, such as iron. The filtered and preserved samples were then placed in cold storage to maintain the samples at four degrees Celsius (ºC) until the analytical work could be performed.

The groundwater samples were analyzed using Protigy ICP-AES for cations and Dionex Ion Chromatography (IC) using either an AS18 or AS19 column for anions, to quantify the water quality of the aquifer and flowing out of the hydraulically active fractures. The focus of this analysis was on analytes that are indicative of chemical weathering of rocks (sodium, potassium, magnesium, calcium, iron, and silicon) that could be used as signatures of hydraulic activity (Malmstrom and Banwart, 1997; Pacheco and Alencoao, 2006). In addition to the most common products of rock weathering, the groundwater samples were also analyze for chloride, fluoride, nitrate, sulphate, aluminum, manganese, strontium, and zinc. Total alkalinity and pH were measured using an auto-titrater, employing the Gran Alkalinity Method.

The isotopic composition of hydrogen and oxygen of the water molecule (δ^2D-H_2O, δ^{18}O-H_2O) was measured by wavelength scanned cavity ring-down spectrometry on un-acidified samples by Picarro L-1102i WS-CRDS analyzer (Picarro, Sunnyvale, California). Samples were vaporized at 110ºC. International reference standards (International Atomic

Energy Agency [IAEA], Vienna, Austria) were used to calibrate the instrument to the Vienna Standard Mean Ocean Water (VSMOW)-Standard Light Antarctic Precipitation (SLAP) scale and working standards were used with each analytical run. Long-term averages of internal laboratory standard analytical results yield an instrumental precision of 0.51‰ for $\delta^{2}D\text{-}H_2O$ and 0.08‰ for $\delta^{18}O\text{-}H_2O$.

A five microliter (µl) Hamilton glass syringe draws one µl of sample to inject into a heated vaporizer port (110°C). For each injection, the absorption spectra for each isotope are determined 20 times and averaged. Between injections, the needle is rinsed with 1-Methyl-2-pyrrolidinone and the sample chamber is flushed with dry nitrogen. Each sample is injected six times and the results of the first three injections are discarded to eliminate as much memory effect as possible between samples. To further minimize memory effect, the lab has adopted a modified version of the technique of Penna et al. (2012), in which samples are run in groups in order of isotopic compositions and/or grouped by water source and location. Three standards that isotopically bracket the sample values are run alternately with the samples. Secondary lab reference waters (from Boulder, Colorado; Tallahassee, Florida; Amherst, Massachusetts) were calibrated with Greenland Ice Sheet Precipitation (GISP), SLAP, and VSMOW from the IAEA. Results are calculated based on a rolling calibration so that each sample is determined by the three standards run closest in time to that of the sample.

2.2.6 USGS NECRA Water Quality Database

Because the MacLeish Field Station and Well MFS-1 represent only one data point to relate groundwater quality measurements to the whole rock composition of the bedrock hosting an aquifer, additional data sources were needed. Starting in the late-1990's, the USGS developed a plan to characterize the NECRA, including the associated water quality

(Lapham, 1990). Under this study, the USGS compiled a much longer dataset relating rock type to water quality, across the NECRA. A USGS Scientific Investigations Report (SIR) published in 2011, provided a general overview of the relationship between the geologic setting and the observed water quality (Flanagan et al., 2011). The NECRA study and dataset was developed using the Plan for the Study of Hydrogeology of Bedrock of New England (Lapham, 1990) and the Framework for Evaluating Water Quality of the New England Crystalline Rock Aquifers (Harte et al., 2008). The aquifers investigated as part of these studies are characterized as systems dominated by secondary porosity, covered by a layer of glacial till or young unconsolidated material, which is consistent with the hydrogeologic conditions observed at the MacLeish Field Station.

The USGS studies identified three major lithologic categories with nine unique lithologic groups that describe the geology of the NECRA. One of the nine lithologic groups characterized in the USGS study is the calcareous metasedimentary rocks of the Waits River-Gile Mountain geologic province (M_c-wg) (Flanagan et al., 2011). Well MFS-1 is completed in this unit, and therefore can be correlated with the USGS dataset.

2.3 Results and Discussion

2.3.1 Relevant Geochemical Weathering Reactions

The geologic setting and mineralogy present has the greatest control over the anticipated weathering reactions that could be taking place in a fractured bedrock aquifer, and thus controlling the natural water quality of the aquifer. Studies have shown that flow rates that allow continuous flushing and inflow of clean water, such as flow along a hydraulically active fracture, can increase the weathering of minerals in solution due to the constant state of disequilibrium between the mineral surface and water in the fracture (Berner, 1978; Maher, 2010). This would suggest that the water quality measured at a

fracture that is participating in advective flow could be different than measurements taken near an inactive fracture in the same water column, depending on the vertical mixing taking place within the well. In addition, the groundwater chemistry can be used to determine the source of the weathering products and secondary minerals, such as the red staining on the fractures.

It is anticipated that hydrolysis, dissolution/leaching, and oxidation are the weathering reactions occurring in crystalline rock aquifers dominated by fracture flow. In nature, these reactions occur simultaneously (Krauskopf, 1967) Based on the core from MFS-1, the primary mineralogy of the Conway Formation at this location is typical of a schist and consists of biotite, muscovite, quartz, calcite, garnet, albite, anorthite, chalcopyrite, and pyrite. This mineralogy suggests that the geochemical weathering reactions can be considered in three main groups: dissolution of carbonate minerals, oxidation of sulphide minerals, and hydrolysis or dissolution of silicate minerals. Kinetically, the dissolution of carbonate minerals and oxidation of sulphide minerals will be faster than dissolution or hydrolysis of silicate minerals. However, in crystalline bedrock, silicate minerals can be more abundant than carbonate and sulphide minerals, and may offer a unique indicator of active weathering through the measurement of silicon in solution. The other typical products of rock weathering (sodium, potassium, magnesium, calcium, and iron) are common to most classes of minerals.

As noted by Hatch et al. (1988), the Waits River-Gile Mountain unit can have locally significant sulphides. Approximately 10% of the minerals identified in the core of MFS-1 are sulphide minerals, including pyrite and chalcopyrite, suggesting that oxidation reactions could be an important mechanism in the MacLeish Field Station groundwater

system. The oxidation of sulphide minerals readily occurs when these minerals are exposed to oxygen and water, which can cause acidic water with pH levels in the range of 2 to 4 to develop, through the formation of sulphuric acid and the release of the sulphide associated metals. Reaction 1 describes the oxidation of the iron sulphide mineral, pyrite (FeS_2), and the formation of sulphate, amorphous ferric hydroxide, and acidity (Bethke, 1996; Deutsch, 1997; Drever, 2002; Mills, 1995):

$$FeS_2 + {}^{15}/_4O_2 + {}^{7}/_2H_2O \leftrightarrow Fe(OH)_{3(s)} + 2SO_4^{2-} + 4H^+ \quad (1)$$

This represents the primary sulphide oxidation reaction that occurs above a pH of 5, where oxygen is the oxidant, as would be expected in shallow groundwater systems, such as that at the MacLeish Field Station.

Acidity formed by Reaction 1 is often neutralized by other minerals contained in the rock, thus preventing the development of acidic groundwater in most natural systems. For example, calcite or dolomite (Reactions 2 and 3) rapidly neutralize acidity and buffer the water to pH 6.5 to 8.0. Many other minerals (e.g. anorthite, [Reaction 4]) may also neutralize acidity, but these reactions are often kinetically slow and the pH will be buffered at lower levels (e.g. pH of 5.5 or less). (Bethke, 1996; Deutsch, 1997; Drever, 2002; Mills, 1995)

$$CaCO_3 + 2H^+ \leftrightarrow Ca_2^+ + CO_2 + H_2O, \text{ below a pH of 6} \quad (2)$$

$$CaCO_3 + H^+ \leftrightarrow Ca^{2+} + HCO_3^-, \text{ above a pH of 6} \quad (3)$$

$$CaAl_2Si_2O_8 + 2H^+ + H_2O \leftrightarrow Ca^{2+} + 2Al(OH)_3 + 2SiO_{2(aq)} + HCO_3^- \quad (4)$$

Considered in combination, the oxidation of sulphide minerals and the dissolution of carbonate minerals results in a near neutral pH and low TDS in most natural waters. These reactions are also expected to result in the release of calcium, iron, and magnesium

to solution. Fletcher's (1999) study of Avery Brook, located in the neighboring community of Conway, Massachusetts, found that the dissolution of anorthite to gibbsite (Reaction 4) was a representative weathering reaction of the surface water quality data.

Aluminosilicate minerals are an abundant mineral group present in the core collected from Well MFS-1. Weathering of aluminosilicates is dominated by hydrolysis and dissolution (Reaction 5) reactions.

$$4KAlSi_3O_8 + 4H^+ + 2H_2O \rightarrow 4K^+ + Al_4Si_4O_{10}(OH)_8 + 8SiO_2 \quad (5)$$

Secondary clay minerals, or the release of oxides, are the most common result of weathering of aluminosilicates. As these minerals continue to weather, sodium, potassium, calcium, magnesium, and iron are leached to maintain neutrality in the layers of the mineral or may be substituted within the mineral structure. These changes can prevent further entrance of water into the mineral structure, reducing their weathering rate.

2.3.1.1 Regional Water Quality of the Waits River-Gile Mountain Geologic Province

The USGS NECRA study provides descriptions of the average character of the Waits River-Gile Mountain (M_c-wg) lithologic group and its associated water quality. The rocks of this unit are metamorphosed marine deposits, deformed and altered during the Acadian orogeny. The Waits River-Gile Mountain Province (M_c-wg) is one of the primary lithologic groups discussed in the NECRA study. This lithologic group is noted as having the lowest iron and manganese groundwater concentrations in the NECRA, though these analytes are highly variable throughout the NECRA (Flanagan et al., 2011). The Waits River-Gile Mountain (M_c-wg) groundwater has lower arsenic concentrations than other metasedimentary units in the NECRA. The USGS study identified a similar calcareous metasedimentary unit, M_c-nm, which is part of the New Hampshire-Maine geologic province. The M_c-nm group experienced slightly different tectonostratigraphic setting, and

exhibits higher concentrations of sulphide minerals and iron-manganese fracture coatings than the M_c-wg unit.

2.3.1.2 Natural Signal of Weathering

The combination of weathering reactions described above and those associated with the mineralogy visually identified in the core of MFS-1, suggest that the concentrations of weathering products will be sufficiently high to be measured through typical analytical methods. To verify this, the geochemical modeling code PHREEQC version 3.3.3 (Parkhurst and Appelo, 2013), was used to calculate ranges of expected chemical concentrations of products associated with weathering the site mineralogy. Two approaches were used to simulate the weathering of minerals in solution and to develop the expected concentration ranges. The first approach assumes that the minerals being simulated are in equilibrium with water. A solution of pure water (pH = 7 at 12ºC temperature) and a water solution in equilibrium with atmospheric concentrations of carbon dioxide to develop carbonic acid in solution were allowed to equilibrate with the assigned mineralogy. The second method used a linear, step-wise reaction to determine the minimum and maximum quantities of weathering products in solution. Both methods considered all of the minerals being simulated reacting at the same time; interactions that could control or limit the amount of each element in solution were therefore considered. The minerals used in the geochemical modeling were albite, anorthite, calcite (representing the carbonate group of minerals), chalcopyrite, muscovite, phlogopite (representing the biotite group of minerals), pyrite, and quartz.

These simulations were not intended to be accurate representations of the system at the MacLeish Field Station, but to represent the general mineralogy present for development of an order of magnitude understanding of the expected concentrations and if

they can be measured through typical analytical techniques. Table 2 presents the results of the geochemical simulations, as well as the method detection limits associated with ICP-AES and IC analyses. In addition, the actual detection limits based on the analytical chemical standards used in the testing are provided. Calibration checks of these standards showed a greater than 0.9 R-value for linear trend line fits to the measured concentrations of the utilized chemical standards.

Comparing the simulated concentrations to the method detection limits and the actual detection limits used in this study, show that the concentrations of chemicals in solution resulting from natural weathering reactions are sufficiently high to be measured through typical laboratory methods. The linear step reaction approach simulated the lowest concentrations in solution, with most of the weathering products having concentrations in the range of 0.02 to 0.7 milligrams per liter (mg/l) (Table 2). The method detection limits for these elements (except iron, magnesium, silicon, and sulphur) are lower than the expected concentrations from the simulation. The equilibrium approach models showed slightly higher expected minimum values for iron, magnesium, silicon, and sulphur which are high enough to be measured using the standard analytical method detection limits.

2.3.2 Identifying Zones of Advective Transport

As with most studies of this type, a general understanding of the hydrogeologic character of Well MFS-1 was obtained from the logging of the core recovered during drilling (Figure 10). Using the basic assumption that the presence of red staining on the fracture surface is an indication of oxidation and therefore fluid transport (Drake et al., 2008), those fractures with noted staining were highlighted in the core log for further investigation. Particular attention was paid to depths associated with the core log comment

“iron staining on fracture”, such as is noted at 20.6 feet and 31.5 feet on the first page of Figure 10.

The initial downhole geophysical tests completed were caliper, temperature, and resistivity. Temperature and resistivity are measurements that represent the condition of the fluid within the borehole (Keys, 1990). These tests were completed first to ensure that mixing of the water had not occurred while moving the instruments along the water column. A single trip in to the well measured both temperature and resistivity of the water in the borehole, and the trip out measured the size of the borehole with the caliper. The temperature and resistivity were measure on the trip in (moving from the top of the borehole to the bottom at a rate of 1.5 meters [five feet] per minute) and the caliper on the trip out (moving from the bottom of the borehole to the top at a rate of 3.7 meters [12 feet] per minute).

The results of these tests were viewed in the field along with the core log to determine the depths for the HPFM tests. As can be seen on the first page of Figure 11, the temperature decreases rapidly, approximately 4ºC over the upper 4.5 meters (15 feet) of the water column. Convection can affect the temperature in the upper portion of a well, causing the measured values to be significantly different from the actual temperature that would be represented by the water being in contact with subsurface rock (Keys, 1990). Samuel (1968) found that convection could occur across the upper 11 to 210 centimeters (4.3 to 82.7 inches) of the water column of a 10 centimeter (four-inch) diameter well.

Based on the data from Well MFS-1, convection could be influencing temperatures measured in the upper portion of the water column. A minimum temperature of 6.6°C, was measured at a depth of 27.8 meters (91.2 feet) bgs. From 6.1 meters (20 feet) bgs to a depth

of 27.8 meters (91.2 feet) bgs, the temperature gradient decreases at a rate of 6.5ºC per 30.5 meters (100 feet), suggesting that a source of flow could be entering the well, causing the temperatures to be lowered. Below the measured minimum temperature in MFS-1, the temperature gradient increases at a rate of 0.37°C per 30.5 meters (100 feet), which is consistent with the thermal gradient observed when no flow is entering a well and the water is at thermal equilibrium with the surrounding rock (0.47 ºC to 0.6ºC increase per 30.5 meters [100 feet] of depth) (Keys, 1990). A small bump in the temperature occurs at a depth of 13 meters (42.5 feet) bgs (second page of Figure 11), but is not likely to be associated with a significant inflow of water. The results of the temperature measurements therefore show convection is controlling the temperature in the upper portion of the well and that there is limited inflow of water to the well below a depth of 27.8 meters (91.2 feet) bgs.

The resistivity measurements collected alongside of the temperature measurements only showed a significant change at a depth of approximately 8.7 meters (28.7 feet) bgs (first page of Figure 11). A decrease in resistivity is associated with an increase in the electrical conductivity (EC) of the water, which is a measure of the total dissolved solids (TDS) in solution. The significant decrease in resistivity at a depth of 8.7 meters (28.7 feet) bgs shows the inflow of higher TDS water to the well from a fracture at this depth. This depth is also associated with a core observation of red staining on the fracture surface (first page of Figure 10 and Figure 11 at 28.7 feet bgs) and caliper measurements showing a change in the borehole diameter.

The caliper measurements show several partially open fractures (changes in borehole diameter) between 8.2 meters and 8.7 meters (27 feet and 28.5 feet) bgs that could

be associated with the resistivity shift identified. Although the core log and downhole geophysical testing provide evidence of hydraulically active fractures, multiple fractures are present in the identified zone, so it is not possible to isolate which fracture is the source of the advective flow to the well. This highlights the challenges of using these techniques to characterize the flow in fractured crystalline rock aquifers.

The ATV image (Figure 11) confirmed the caliper measures, showing several fractures along the borehole wall. At approximately 8.5 meters (28 feet) bgs the core log noted near horizontal fractures and multiple fractures in zone, associated with iron staining on the fracture surfaces (page one of Figure 10). This provides another piece of evidence that the zone of open fractures between 8.2 meters and 8.7 meters (27 feet and 28.5 feet) bgs are actively participating in the hydrogeologic system. Additional fractures were observed using the ATV imaging at approximately 12.2 meters, 13.4 meters, 18.3 meters, 23.5 meters, 29.3 meters, 30.4 meters, and 36.6 meters (40 feet, 44 feet, 60 feet, 77 feet, 96 feet, 100 feet, and 120 feet) bgs (Figure 11).

HPFM measurements were taken at 13 depths along the length of Well MFS-1 starting at a depth of 6.1 meters (20 feet) bgs (just below the base of the steel casing) and ending at a depth of 42.1 meters (138 feet) bgs (just above the total depth of the borehole). Measurements under ambient conditions were collected on the instrument trip in to the borehole and pumped condition measurements were collected on the trip out. The results of both tests are shown on Figure 11. Under ambient conditions a slight downward gradient was identified during the test at 7.9 meters (26 feet) bgs and a slight upward gradient at the test depths of 18.2 meters and 21 meters (60 and 69 feet) bgs. The flow rates associated with these measurements are 0.01 gpm, which is at the detection limit for the instrument.

The HPFM results under ambient conditions indicate that there is limited vertical movement within the well under ambient conditions, but that some downward flow from upper portions of the water column and upward flow from lower zones could be occurring. No other zones of hydraulically active fractures were identified through the ambient HPFM measurements.

The pumped condition tests identified slight upward gradients at the eight highest testing depths (i.e., above 24.4 meters [80 feet] bgs). The tests performed at 6.7 meters and 7.9 meters (21.9 feet and 26 feet) bgs had the highest measured flows with an average rate over three tests of 0.19 gpm. An upward gradient with an associated flow rate of 0.07 gpm (average of two tests) was identified with the test completed at 9.1 meters (30 feet) bgs depth. A slight upward gradient was also measured at depths of 12.5 meters, 16.5 meters, 18.3 meters, 21.0 meters, and 24.1 meters (41 feet, 54 feet, 60 feet, 69 feet, and 79 feet) bgs. The results of the pumped conditions are shown on Figure 11.

When the core log, caliper, resistivity, ATV, and HPFM tests are considered together, the zone of fractures between 8.2 meters and 8.7 meters (27 feet and 28.5 feet) bgs are the primary inflow of water to Well MFS-1. The caliper testing and ATV showed several fractures in this zone of the borehole and the core log noted several fractures with iron staining, suggesting that water has been associated with these fractures. The depths of 12.5 meters, 18.3 meters, and 23.4 meters (41 feet, 60 feet, and 80 feet) bgs may also play a role in the flow of water in to or out of Well MFS-1. The HPFM measurements show a slight upward gradient was present at 18.3 meters (60 feet) bgs under both ambient and pumped conditions (Figure 11). The conceptual model for the flow regime of MFS-1 based on the core log and borehole geophysical data is that the fractures at 8.5 meters (28 feet)

bgs are the primary inflow to the well, but smaller advective zones are located between 12.5 and 18.3 meters (41 and 60 feet) bgs. Convection causes mixing in the upper portion of the well and upward gradients drive the mixing above 23.4 meters (80 feet) bgs. The depths of 8.5 meters, 12.5 meters, 18.3 meters, 23.4 meters, and 30.5 meters (28 feet, 41 feet, 60 feet, 80 feet, and 100 feet) bgs were therefore selected as the depths within Well MFS-1 to position the RPPs for collection of discrete interval water quality samples.

2.3.3 Natural Weathering and Groundwater Quality

The natural weathering product concentrations are measureable through typical laboratory methods based on the order of magnitude estimations for natural weathering of the minerals identified in the core of MFS-1 (Table 2). The physical setting of Well MFS-1, in a region that has been influenced by glacial advances and retreats but with thin till deposits, suggests that the groundwater quality will be representative of water interacting directly with the bedrock (Velbel, 1993). Table 3 presents the range of expected concentrations from the simulations compared to the average concentrations of samples collected from Well MFS-1. The average concentrations from all of the measurements collected from Well MFS-1, as well as the averages of the measurements from each of the discrete interval samples are provided on Table 3. The data is also presented graphically as a Piper Diagram (Figure 13). The minimum concentration from the linear reaction is used to represent the lower end of expected concentrations, while the simulation of the minerals in equilibrium with pure water represents the high end of the concentration range. The average of the concentrations from all depths in Well MFS-1 is within or slightly higher than the range of expected concentrations represented by the geochemical modeling. The exception to this is aluminum, with an average concentration of 0.008 mg/l, which is

significantly less than the expected minimum concentration of 0.19 mg/l from the linear reaction model.

Aluminosilicate minerals are present in significant quantities in the bedrock of the Waits River-Gile Mountain Province, which does not appear to be consistent with the low measured aluminum concentrations. However, aluminosilicates weather along reaction paths, resulting in successive changes in the mineralogy and solution as the reactions progress along a flow path (Steinmann et al., 1994). Helgeson et al. (1969) observed that in most natural aqueous systems, the activity of aluminum in solution is extremely low, and therefore most of the aluminum is conserved in the solid phase of the rock. Helgeson et al. (1969) further noted that no single reaction can be written to represent the compositional changes when there is more than one ion present and the expected changes are large, laying the foundation for later research of these processes through reaction paths.

Calcium, potassium, magnesium, and sulphate are toward the upper end of the expected range of concentrations resulting from natural weathering (equilibrium with pure water). Biotite is one of the most abundant minerals observed in the core from MFS-1. Potassium release from biotite can be fast and independent of flow and pH due to its position as the interlayer cation in the mineral structure (Malmstrom and Banwart, 1997; Klein and Hurlburt, 1993; Velbel, 1985), which could be the source of the high potassium concentrations measured in the groundwater at the MacLeish Field Station. Dissolution of carbonate minerals and oxidation of sulphide minerals are also fast reactions that are likely occurring in the groundwater at the MacLeish Field Station based on the mineralogy observed in the core from MFS-1. Normalizing the calcium and sodium concentrations to the total cations measured in solution and plotting them relative to each other, shows that

carbonate weathering is dominating the system (Figure 14). The sulphate concentrations were normalized to the total anions in solution and plotted against the normalized calcium values, which shows that weathering of sulphides are balancing the weathering of carbonates (Figure 15). Others have observed that water at the MacLeish Field Station are slightly acidic, but the pH increases along flow paths and calcium increases with residence time (Berkley, 1999), consistent with a system dominated by sulphide and carbonate weathering. The concentration of sulphate also increases with depth in the well and with distance from the hydraulically active zone of the well, suggesting that this may be indicative of reactions taking place in the well, rather than along the path of water transport.

2.3.3.1 Iron Measured in Groundwater and what it tells us about Red Staining on Fractures

Iron is one of the most sensitive elements to changes in oxidation-reduction (redox) conditions, so it can be an indicator of the availability of free oxygen in groundwater (Drever, 2002). Both ferrous (Fe^{2+}) and ferric (Fe^{3+}) are present in groundwater, but their relative proportions are a function of redox potential of the system (Deutsch, 1997) (Figure 16). The redox conditions of the groundwater are controlled by the introduction of oxygen with the recharge water, the distribution of organic matter, the circulation rate of the water, and the weathering reactions consuming the oxygen (Drever, 2002). In the vadose zone and porous media aquifers, iron oxidation can readily occur due to effective circulation of air and water (Zone A of Figure 16), and the levels of prolonged water table elevations may be identifiable through the top of the unoxidized zone (Krauskopf, 1967). Groundwater that contains free oxygen for reaction is considered to be related to a short residence time or a system limited in organic matter and/or chemical reactions depleting the oxygen content (Drever, 2002). If the system has a limited amount of organic matter and

weathering reactions are not consuming oxygen, high concentration can persist to depths of several hundred feet (Deutsch, 1997). If ferrous iron is present in the system, it will readily be oxidized to ferrihydrite ($Fe[OH]_3$), which is not soluble under typical groundwater pH values, resulting in dissolved iron groundwater concentrations less than 0.1 mg/l (Deutsch, 1997).

Organic matter and weathering of ferrous carbonates can quickly deplete the oxygen supplied by atmospheric air (Drever, 2002), and since no subsurface reactions produce oxygen, it will be reduced to low levels within a few meters (Krauskopf, 1967; Deutsch, 1997; Sidborn et al., 2010) (Zone B of Figure 16). Groundwater that has no free oxygen, and does not have significant amounts of sulphate reduction, is still considered to be of sufficient quality to be drinking water, but will have measured iron or manganese concentrations greater than 1 mg/l (Drever, 2002).

The iron concentrations measured in the discrete interval samplers was higher than the expected range of concentrations from the order of magnitude modeling completed. The modeling did not include an iron carbonate mineral, such as siderite, or an iron bearing member of the biotite group (pholgopite is the iron deficient biotite end member), leading to the underestimation of the iron concentration in solution from the modeling. Reduced minerals in the rock matrix, such as biotite and siderite, can be the main source of ferrous iron in groundwater, if there is limited organic matter in the system (Sidborn et al., 2010). The thin till unit at the recharge zone that is limited in organic matter should allow water with relatively high free oxygen to enter the fractured bedrock aquifer, but the dominant weathering reactions of the MacLeish groundwater system being carbonate dissolution and the quantities of biotite present are likely consuming the available oxygen shortly after

entering the saturated zone. The concentrations were greater than 0.1 mg/l through the testing period, and were measured at concentrations greater than 1 mg/l on multiple occasions, which is consistent with groundwater that has limited free oxygen, but is not reducing sulphate. This would suggest that the water from Well MFS-1 would plot at or near the boundary for Zones A and B on Figure 16. Iron oxidation and concentrations tend to parallel those of manganese (Krauskopf, 1967; Deustch, 1997), but the concentrations of manganese were measured to be less than 0.25 mg/l, suggesting some oxygen is available or that the system is more limited in manganese than iron. This could also be related to the presence of the well or the samplers, providing an air-water interface in which free oxygen can be introduced to the water column of the well. Manganese has a higher redox potential than iron and would be preferentially oxidized over the iron (Figure 16), until it has been mostly consumed, which could be leading to the lower manganese concentrations in solution compared to the iron.

Iron scaling of wells can be a significant problem (Mathurin et al., 2014), and is a common challenge for homeowners and public water suppliers with bedrock wells in New England and throughout the world (Bustos Medina et al., 2013). High iron groundwater that is also low in oxygen can result in iron stained fixtures, scaling in hot water heaters, and clogged pipes as the water is introduced to oxygen at the well or in the heating equipment. Dark red iron precipitate was noted to be present on the RPP samples and the pressure transducer deployed in the well, further suggesting that free oxygen in groundwater is limited, and the air being introduced to the water at the well, is causing the reduced iron in solution that is transported from the hydraulically active fracture to precipitate out of solution. Each of the RPP samplers placed in MFS-1 became stained with

iron precipitate, but the sampler closest to the air-water interface and the zone of thermal convection in the upper water column shows the most significant staining (Figure 17). The samplers placed in Well MFS-2 did not show the same staining, suggesting that this well is only in contact with a more oxygenate alluvial system aquifer (Figure 17).

Based on the amount of iron observed to precipitate in the well and the dissolved iron concentrations measured (greater than 0.1 mg/l and occasionally higher than 1 mg/l), it can be concluded that the iron in the bedrock aquifer and transported along the hydraulically active fractures is in the reduced form (ferrous iron). Once the water is exposed to oxygen, such as at a well or from oxygenated water in a passive sampler, the iron is oxidized to ferrihydrite ($Fe[OH]_3$), where it readily precipitates out of solution due to the near neutral pH of the water. If ferrous iron and not ferric iron is the dominant form being transported along the fracture and the red staining observed on the fracture surfaces is iron oxide, the data does not support the red staining is being sourced by the current flow of water. Another oxygenated water source or system perturbation is needed to provide the oxygen to promote formation of iron oxide and the precipitation of iron from solution along the transport pathway. The color of the iron precipitate suggests that it is a simple oxide (dark red), but the staining on the fractures has a more yellow or brown color, which is more typical of hydrates (Krauskopf, 1967). This is not an exact indicator of the form of iron being precipitated, but the color can be affected by impurities, shifting the color from the pure red color of a simple iron oxide (Krauskopf, 1967). Iron hydrates may form from the iron in the system, but the exact conditions for the formation of iron oxides (e.g., ferrihydrite [$Fe(OH)_3$], hematite or magnetite [Fe_2O_3]) versus iron hydrates (e.g., goethite [α-FeOOH], lepidocrocite [γ-FeOOH]) is not well understood (Krauskopf, 1967). Others

have concluded that red staining is not a good indicator of oxidation or current water flow (Drake et al., 2008, Mathurin et al., 2014) and the data from MFS-1 further supports this conclusion.

2.3.3.2 Water Chemistry Relative to the Hydraulically Active Fractures

At the outset of this study, it was anticipated that the five discrete interval samplers placed in Well MFS-1 and the three samplers placed in Well MFS-2 would show varied water quality along the water column, depending on the RPP's proximity to a hydraulically active or inactive zone of the well. The samplers placed in zones of hydraulically active fractures, were expected to have higher concentrations of elements indicative of rock weathering (sodium, potassium, magnesium, calcium, iron, and silicon) than the inactive zones of the well. However, the data collected over two years showed very little variability between the different sampling depths. Figures 18 through 22 present time series plots of the measured sodium, potassium, magnesium, calcium, iron, and silicon from the five RPP samplers placed in Well MFS-1 and Table 3 presents the average concentrations for these elements for the entire sample period. Included as Appendix A are Stiff diagrams of the 24 monthly groundwater chemistry compositions for each of the discrete intervals sampled in Well MFS-1. The concentrations of seven major ions (sodium, potassium, calcium, magnesium, chloride, carbonate/bicarbonate, and sulphate) are presented in units of milliequivalents per liter on the Stiff diagrams. The width of the diagrams is proportional to the ionic content and provides a means to compare and characterize water types (Hem, 1970). The most noticeable variations in the ionic content observed from the Stiff diagrams are the months in which the alkalinity (shown as the bicarbonate concentration on the Stiff diagrams) was highest at the samples collected from 8.5 meters (28 feet) bgs.

The measured concentrations of rock weathering products follow the same pattern of changes in response to system stresses regardless of depth and proximity to the hydraulically active fractures. As shown in Figures 18 through 22, most elements increased during the period of August 2013 to October 2013. This was determined to be related to an alkalinity addition associated with a neighboring project at the MacLeish Field Station and is not representative of natural weathering conditions. Two rows of approximately eight trees each were planted in the western field of the MacLeish Field Station, between Wells MFS-1 and MFS-2 (Figure 2) shortly after the wells were installed. These trees are part of a natural art research project, with the goal of promoting growth and establishment of the young trees in this location. Compost and a chelated-lime product were added as amendments for these trees in the spring of 2013 to promote their establishment. Anecdotal evidence suggests that approximately one cup of the liquid chelated-lime and compost was placed around each tree early in the growing season (personal communication with Dan Ladd, MacLeish Field Station Artist in Residence). The exact nature and date of this amendment addition were not known, but it is estimated to be between mid-April and mid-May of 2013, based on the start of the growing season in this region.

The signal of this alkalinity shift was most evident in the RPP placed at 8.5 meters (28 feet) bgs, though it was evident by the increase in total alkalinity concentrations observed in all five samplers. Figure 23 shows the total alkalinity measured in each of the RPPs over the two year period. Also shown on Figure 23 is the depth to water measured by the UMass Amherst hydrogeology research group and the precipitation measured at the MacLeish Field Station meteorological station. The results from the RPP sampler at 8.5 meters (28 feet) bgs show a greater than 100 mg/l increase in alkalinity in response to the

initial lime addition and continued pulses after large precipitation/recharge events. The increase in total alkalinity measured at the lower depths sampled in Well MFS-1 (and further from the hydraulically active fractures) showed significantly less response to the amendment addition, approximately 50 mg/l increase, and no response after the passing of the initial slug. Figure 23 highlights that the signal of the lime addition was most prevalent at 8.5 meters (28 feet) bgs supporting that the fractures at this depth are the hydraulically active fractures in the well.

The average and the range of concentrations for each rock weathering element is consistent for each of the discrete interval samples collected from Well MFS-1. This is shown on Figure 24, which presents box and whisker plots of the entire dataset from Well MFS-1 (combined dataset from all discrete interval samples collected) and the datasets from each of the discrete interval sample depths. The range of data for each element is represented by the length of the box and whisker, from the end of the positive whisker to the end of the negative whisker. The measured concentrations of most elements are not normally distributed and tend to be biased toward the lower concentrations. The samples collected from the 8.5 meter (28 foot) bgs depth have the largest range of results for most elements, though the range of concentrations measured for zinc from the depths of 12.5 and 18.3 meters (41 and 60 feet) bgs are larger than at 8.5 meters (28 feet) bgs. The larger range observed at the 8.5 meter (28 foot) depth could be indicative of inflow to the well and sensitivity to changes in recharge inputs.

Comparison of the dissolved silicon concentrations to the $\delta^{18}O\text{-}H_2O$ values at 8.5 meters (28 feet) and 30.5 meters (100 feet) bgs (Figure 24) show the same general pattern of increases and decreases over time, which also shows a sensitivity to changes in recharge.

The most positive $\delta^{18}O$-H_2O values are from precipitation occurring in the summer, the primary recharge period for New England. The highest silicon concentration occur at the same time as the highest $\delta^{18}O$-H_2O values, suggesting an increased period of weathering along this flow path due to the increased recharge. The measured changes in weathering products due to the changes in recharge is visible in the data collected at the hydraulically active fracture and at the inactive fractures, but the relative change in concentration between seasons in less near the inactive zone (Figure 25). Weathering rates are accelerated by flushing of water due to a state of disequilibrium (Berner, 1978) which is consistent with the observed concentration changes relative to the changes in seasonal recharge.

The average concentrations of all the measurements from Well MFS-1 and the average concentrations from each of the discrete intervals is the same, except for calcium and sulphate (Table 3). The calcium and sulphate are lowest at the depth associated with inflow to the well (8.5 meters [28 feet] bgs) and increase with depth and distance from the hydraulically active fracture. Calcium increases from an average of 9.7 mg/l at 8.5 meters (28 feet) bgs to 11.8 mg/l at 30.5 meters (100 feet) bgs, while sulphate increases from 6.3 mg/l to 7.7 mg/l across the same depths. Figure 15 shows that carbonate dissolution and sulphide oxidation are the dominant weathering reactions in this system. The water-rock interactions taking place away from the hydraulically active fracture are resulting in higher concentrations in solution due to the increased contact time with the bedrock and the higher oxygen content of the well's water column compared to the hydraulically active fracture. Because the dissolution and oxidation reactions of carbonates and sulphides, respectively, are fast and the water has free oxygen but is undersaturated with respect to calcium, magnesium, and sulphate, the longer contact time between the water and the bedrock in the

non-flowing portions of the well can increase the dissolved concentration compared to portions of the well with continuous inflow of fresh water, where the contact time between the rock and water is shorter.

The data show that the groundwater samples collected closest to the hydraulically active fractures have the greatest response to a chemical input to the system. The chemical input (alkalinity) was identifiable in the data from the other depths which are away from the well inflow. This indicates that in-well mixing may be occurring even though the results of the HPFM testing suggested minimal vertical movement under ambient conditions, particularly down through the water column. Other studies have identified this issue, but none have developed clear conclusions about the mechanism that could be causing the in-well mixing when other testing suggests limited or no flow along the water column (Vroblesky and Peterson, 2004; Sellwood et al., 2015, Harte et al., 2014). This could be a critical issue for contaminant remediation in fractured bedrock aquifers; samples collected away from the inflow to the well may not be representative of the conditions at that location vertically in the aquifer (Vroblesky and Peterson, 2004). Vroblesky and Peterson (2004) concluded that the in-well mixing and nearly uniform VOC concentrations being observed in the passive diffusion samples of their study were due to the influence of the neighboring Yukon River and changes in the hydraulic gradient associated with high and low water periods of the river. However, Well MFS-1 is not in close proximity to a surface water feature that could affect the well's hydraulics, suggesting that a different mechanism such as thermal convection, diffusion, response to pumping in a connected well, or in well movement below the detection limits of the HPFM is occurring.

For Well MFS-1 the pronounced response to the system perturbation (alkalinity addition) suggests that the recharge zone for Well MFS-1 is located in the central portion of the western field, near the cluster of trees planted between Wells MFS-1 and MFS-2. The ERT survey completed at the site shows a very thin area of till overlying a bedrock high that was less fractured in the same vicinity as the likely recharge zone (Isaacson, in progress). The intensity of the signal seen in the upper discrete interval sample of Well MFS-1 shows that the pathway between the area of recharge and the well is a preferential flow path with good connectivity and with limited mixing. The length of time between the lime addition and the signal being measured in Well MFS-1 is approximately six months, suggesting a transport time of six months along this preferential flow path.

2.3.4 Mean Residence Time and Isotopic Data

Time series analysis of deuterium and oxygen-18 of the water molecule are useful tracers to understand the relative proximity that groundwater has to the recharge zone and to estimate a mean residence time (MRT). The isotopic composition of the water molecule is related to the temperature of condensation of the precipitation event, when and where the water was infiltrated into the ground (Kendall and McDonnell, 1998). The isotopic composition is applied naturally over entire watersheds, and because deuterium and oxygen-18 are components of the water itself and are not additions to the water, they make highly reliable tracers if distinct sources can be identified. Deuterium and oxygen-18 are also not altered by water-rock interactions under low temperature conditions, making them excellent tracers of water sources (Kendall and McDonnell, 1998; Dewalle, et al., 1997; McQuire et al., 2002; Reddy et al., 2006). If recharge and infiltration of water to the groundwater system is fast, there will be little impact on the isotopic composition as the water moves downward at a uniform velocity (piston flow model) due to the limited impact

of evaporation, which can alter the isotopic composition from the precipitation values (Kendall and McDonnell, 1998).

The δD-H_2O and δ^{18}O-H_2O measurements from Well MFS-1 show a strong temporal variation over the period of sampling, with a 10‰ range of δD-H_2O and a 1.5‰ range for δ^{18}O-H_2O. This data supports the conclusion that MFS-1 is positioned in close proximity to the zone of recharge, where infiltration is fast, and minimal mixing is occurring as the water travels from the zone of recharge to Well MFS-1. Figure 26 presents the time series of δD-H_2O measurements and Figure 27 presents the time series of δ^{18}O-H_2O measurements from Well MFS-1. A significant variation in the measured isotopic concentration of groundwater over time as observed in Well MFS-1 is consistent with limited mixing and a MRT of less than five years (McGuire et al., 2002).

The seasonal pattern of δ^{18}O-H_2O values measured in precipitation can be represented by a sine function (Reddy et al., 2006):

$$\delta^{18}O = \text{mean}(\delta^{18}O) + A \sin[(2\pi\tau/b) + c] \quad (6)$$

where, mean (δ^{18}O) is the annual mean oxygen-18 value (‰), A is the seasonal amplitude of δ^{18}O-H_2O values (‰), b is the period of the seasonal cycle (365 days), t is time (days), and c is the phase lag (radians). Using a multi-year dataset such as that collected from Well MFS-1, that is composed of accurate, reproducible δ^{18}O-H_2O values for precipitation and groundwater, and that has sufficient travel time for attenuation of the precipitation amplitude of the δ^{18}O-H_2O, an amplitude-attenuation approach can be used to estimate the MRT of the groundwater sample (Reddy et al., 2006). A sine function was manually fit to the Well MFS-1 δ^{18}O-H_2O, which is presented on Figure 28.

The isotopic dataset representing precipitation at the MacLeish Field Station was not sufficient to develop the sine function of the dataset, so data from the IAEA Water Resources Program was used instead. The MacLeish Field Station is located at 42.455 latitude and -72.68 longitude; data from the IAEA stations with coordinates within 0.5 degrees latitude and longitude were used to develop an average $\delta^{18}O\text{-}H_2O$ sine function for local precipitation. The dataset developed from the IAEA database includes 38 stations for which the monthly data were averaged. The sine function that was manually fit to this data is provided on Figure 28. The amplitude attenuation method uses the precipitation data as a reference point for determining MRT of the other water being sampled (Reddy et al., 2006):

$$MRT = (1/b')[(A/A_p)^{-2} - 1]^{0.5} \quad (7)$$

where, A_p is the seasonal amplitude of precipitation $\delta^{18}O\text{-}H_2O$ (‰), A is the seasonal amplitude of the groundwater sample (‰), b' is a conversion factor (radians per day). Using the IAEA dataset to calculate A_p (3.87) and the data from the 8.5 meter (28 foot) depth data collected from Well MFS-1 to calculate A (0.90), it has been determined that the MRT time of the groundwater at Well MFS-1 is approximately 243 days or 0.66 years. This is consistent with the timing of the alkalinity increase observed in Well MFS-1.

Along a long flow path with multiple connected fractures contributing waters of different ages or a MRT greater than five years, the amplitude of the isotopic signal would be decreased, and the isotopic values would reach uniformity over time, showing the average isotopic concentration of the waters being mixed over multiple temperature periods (Kendall and McDonnell, 1998). This is the condition observed in the isotopic compositions of the other wells sampled at the MacLeish Field Station. The well completed

in the till (MFS-2) and the deeper water supply well at the site did not show variable δD-H_2O and $\delta^{18}O$-H_2O concentrations over the sampling period leading to a conclusion that they are hydrologically further from the recharge zone and represent a mixed water signal or water that has a MRT greater than five years (Figures 29 and 30). The δD-H_2O measurements varied by less than 5‰ and the $\delta^{18}O$-H_2O by less than 1‰, consistent with the having a more tortuous flow path with multiple waters mixing before entering the well, rather than a single recharge source. This also supports that there is a longer residence time between recharge and the water entering Wells MFS-2 and MFS-tap, than is being observed at Well MFS-1.

In addition to presenting the discrete interval data from Well MFS-1, the time series plot at the bottom of both Figures 26 and 27 present the data from the UMass Amherst hydrogeologic research group collected grab samples from this well. The thing to note from these figures is that the pattern and range of change for the discrete interval samples and the grab sample are the same, providing further evidence that the water in the well is being fully mixed within the water column over the period that the samples represent (approximately one month). The isotopic signal is not affected by dilution or water-rock interactions and is a better indication of the level of mixing within the well than the anion and cation chemistry data collected. The HPFM testing show minimal vertical gradients in the water column of Well MFS-1, but the isotopic data supports that even with these small gradients, complete mixing is occurring, resulting in the same range and pattern of concentrations for all five depths of the discrete interval samples, and the grab sample.

2.4 Study Limitations and Recommended Future Studies

The resolution (both spatial and temporal) of the methods used for determining the vertical gradient in the well and for sample collection appear to be the most significant limitations of this study. The HPFM testing method for determination of vertical gradients can generally measure flow between 0.01 and 1.5 gpm. The flows measured in Well MFS-1 were near the lower detection limits of the testing method at most depths and may not be providing an accurate assessment of the true in-well mixing that is occurring. The work of Harte et al. (2014) and Harte (2015) has proposed that Single Borehole Dilution Tests could be used to identify well flow rates as low as 0.0003 gpm, significantly lower than HPFM testing. Being able to measure vertical gradients at such low flow rates could show that there is more ambient mixing along the water column of Well MFS-1 than was observed from HPFM testing or may identify other zones of hydraulic activity not previously identified.

The other significant limitation of this study is the sample collection method. The RPP samplers are approximately 0.15 meters (0.5 feet) long, and if there are multiple hydraulically active fractures at a similar depth within the well, separate samples from each fracture could not be collected if they are spaced less than 0.15 meters (0.5 feet) apart. The zone of active fractures in Well MFS-1 is between 8.2 and 8.7 meters (26.9 feet and 28.5 feet), so the sampler was placed at 8.5 meters (28 feet) bgs to target the central portion of this zone. Although this sampler showed the greatest changes due to system perturbations, it is still not possible from this dataset alone to identify which of the fractures between 8.2 and 8.7 meters (26.9 and 28.5 feet) bgs is the one contributing most to advective flow in the well.

The passive diffusion testing method is ideal for this study in that it limits the stress on the system, allowing collection of samples under ambient conditions, which are needed to monitor for a natural weathering signal. However, because the samplers require at least two weeks to equilibrate with the system, the sample collected is representative of the water quality over that period of time, which may be sufficient for complete mixing of the well's water column. Using a method such as ZONFLO (Harte, 2013) could potentially address both of the sampling method limitations, though at a greater cost than diffusion sampling. The ZONFLO (Harte, 2013) method can collect a sample from a zone as small as 0.1 meters (0.25 feet), allowing for collection of samples from multiple fractures in a hydraulically active zone of a borehole. The method for sample collection is pumped, but under very low flow rates, allowing collection of a sample that is at near ambient conditions but is more representative of a single point in time than the diffusion samples collected from RPPs. Collecting discrete interval samples from multiple depths using the ZONFLOW (Harte, 2013) method may allow for isolation of the active and inactive zones of the well but could be impractical for a study like this due to the added time and cost to collect samples.

2.5 Conclusions

Fractured bedrock aquifers are prevalent in many parts of the world (Gustafson and Krasny, 1994). Contaminant pathways in fractured bedrock aquifers can be difficult to define and even more difficult to fully remediate. Being able to better identify the small number of active fractures that are participating in chemical fate and transport would allow for more targeted treatment of source zones and dissolved phase contaminants in geologically complex systems, as well as assuring protection of our water supplies. This study utilized discrete interval diffusion sampling of a fractured bedrock well completed in a schist to determine if a natural weathering signal could be used to identify hydraulically

active fractures and source of red staining on fracture surfaces. Based on the literature, it was expected that groundwater concentrations of rock weathering products at a fracture that is participating in advective flow would be higher concentrations than inactive zones of the well. The location of Well MFS-1 relative to the recharge zone makes it an ideal location for testing this hypothesis because it is located in a glacially altered environment with a thin till deposit, so the water chemistry will be indicative of water interactions with bedrock (Velbel, 1993). The conclusions of this study are:

1.) The hydraulically active fractures of Well MFS-1 are located between 8.2 and 8.7 meters (26.9 and 28.5 feet) bgs. This depth in the well was the only measured resistivity shift, consistent an inflow of water, which was also is associated with a change in borehole diameter and decreasing water temperatures. The dominant mixing in the water column of the well is driven by thermal convection in the upper portion of the well and upward gradients are present above 24.3 meters (80 feet) bgs, based on the fluid temperature measurements and HPFM testing results. The isotopic data collected from the well concludes that these forces are sufficient to fully mix the water in Well MFS-1 over a one month period.

2.) Carbonate dissolution and sulphide oxidation are the dominant weathering reactions and source of weathering products measured in the groundwater from Well MFS-1 based on the normalized calcium and sulphate groundwater data (Figures 14 and 15).

3.) Iron in the groundwater is in the reduced form while flowing through the fractured system, and does not become oxygenated until entering a well, where an air-water interface exists. The iron concentrations were greater than 0.1 mg/l through the testing period, and were measured at concentrations greater than 1 mg/l on multiple occasions,

which is consistent with groundwater that has limited free oxygen, but is not reducing sulphate. If ferrous iron and not ferric iron is the dominant form being transported along the fracture and the red staining observed on the fracture surfaces is iron oxide, the data does not support that the red staining is being sourced by the current flow of water. Another oxygenated water source or system perturbation is needed to provide the oxygen to promote formation of iron oxide and the precipitation of iron from solution along the transport pathway. The color of the iron precipitate in the well suggests that it is a simple oxide (dark red), but the staining on the fractures has a more yellow or brown color, which is more typical of hydrates (Krauskopf, 1967). This is not an exact indicator of the form of iron being precipitated, but the color can be affected by impurities suggesting that the forms of iron precipitate in the well and on the fracture surface are not the same form of iron, Therefore it is concluded that the current flow system is not the source of red staining on fracture surfaces or in the adjacent rock matrix.

4.) Seasonal changes in recharge affect the concentration of weathering products in solution. The highest silicon concentrations measured in the groundwater samples were related to waters recharged during the highest precipitation period of the year, providing a signal of seasonal responses to changes in the hydrogeologic system.

5.) The greatest responses to system perturbations are at the hydraulically active fractures, as shown in the changes in measured concentrations in this portion of Well MFS-1. Even though in-well mixing causes the concentrations of natural weathering products to be measureable throughout the water column, the signal and response to changes in system chemistry are greatest at the hydraulically active fractures.

6.) The evaluation of isotopic time series data shows that the location of Well MFS-1 is ideal for this type of study. It is in a thin till area and recharge to the aquifer is fast. Additionally, the isotopic data provides a seasonal signal from which a MRT of 0.7 years has been calculated.

Table 1: Detailed description of the surficial geology interpretation from Segerstrom (1955) and Stone and DiGiacomo-Cohen (2010)

Segerstrom (1955)			Stone and DiGiacomo-Cohen (2010)
Alluvium	Qal	Silt, sand, and gravel deposited by present streams.	Floodplain alluvium
Local thin deposits of gravel sand, and silt	Qsg	Unrelated to sequences; mostly deposits on floors of ice-block basins.	Glacial stratified deposits
Kame terrace deposits	Qkt	Deposits from glacial melt waters held above level of glacial Lake Hitchcock by temporary spillways	Glacial stratified deposits
Ground moraine	Qgm	Commonly thin till with many exposures of bedrock. Includes ground moraine from above glacial Lake Hitchcock and later covered by glacial Lake Hitchcock.	Glacial ice deposits
Thick ground moraine	Qgt	Thick till deposits with no exposure of bedrock. Includes thick till from above glacial Lake Hitchcock and later covered by glacial Lake Hitchcock.	Glacial ice deposits
Drumlins	Qgd	Thick till deposits in the form of elliptical hills with their long axes parallel to the direction of ice movement.	Glacial ice deposits

Table 2: Method detection limits, actual analytical detection limits, and expected ranges of concentrations of weathering products resulting from the reaction of albite, anorthite, calcite, chalcopyrite, muscovite, phologopite, pyrite, and quartz with water.

	Method Detection Limits	Actual Detection Limits	Equilibrium with Pure Water	Equilibrium with Pure Water and CO_2	Minimum Concentration from Linear Reaction	Maximum Concentration from Linear Reaction
Elements	**milligrams per liter (mg/l)**					
Al	0.03	0.001	5.02	15.1	0.19	189
Ca	0.0067	5	8.25	1.64	0.08	80
Cu	0.0036	NM	0.00	0.00	0.06	63
Fe	0.0041	0.001	0.79	9.75	0.00	0.11
K	0.087	0.5	0.00	0.00	0.08	78
Mg	0.02	0.001	0.16	75.3	0.07	73
Na	0.019	0.5	0.94	0.36	0.02	23
S	0.4	NM	0.90	11.2	0.13	128
Si	0.017	0.5	9.20	6.20	0.72	720
SO_4^{-2}	0.4	1	2.64	25.0	0.38	384

Table 3: Expected ranges of concentrations of weathering products resulting from the reaction of albite, anorthite, calcite, chalcopyrite, muscovite, phologopite, pyrite, and quartz with water compared with average measured concentrations of all samples collected from Well MFS-1 and average measured concentrations from each discrete interval sampled in Well MFS-1.

	Minimum Concentration from Linear Reaction	Equilibrium with Pure Water	Average of All Samples from MFS-1	Average of Samples from 8.5 meters (28 feet) bgs	Average of Samples from 12.5 meters (41 feet) bgs	Average of Samples from 18.3 meters (60 feet) bgs	Average of Samples from 23.4 meters (80 feet) bgs	Average of Samples from 30.5 meters (100 feet) bgs
Elements	**milligrams per liter (mg/l)**							
Al	0.19	5.02	0.008	0.006	0.009	0.008	0.008	0.007
Ca	0.08	8.25	10.8	9.7	10.6	10.7	11.0	11.8
Fe	0.00	0.79	0.60	0.78	0.67	0.65	0.52	0.62
K	0.08	0	1.4	1.4	1.4	1.3	1.3	1.4
Mg	0.07	0.16	1.1	1.0	1.1	1.0	1.1	1.1
Na	0.02	0.94	1.5	1.6	1.6	1.5	1.5	1.6
Si	0.72	9.2	4.5	4.3	4.5	4.5	4.5	4.5
SO_4^{-2}	0.38	2.64	7.1	6.3	7.1	7.1	7.3	7.7

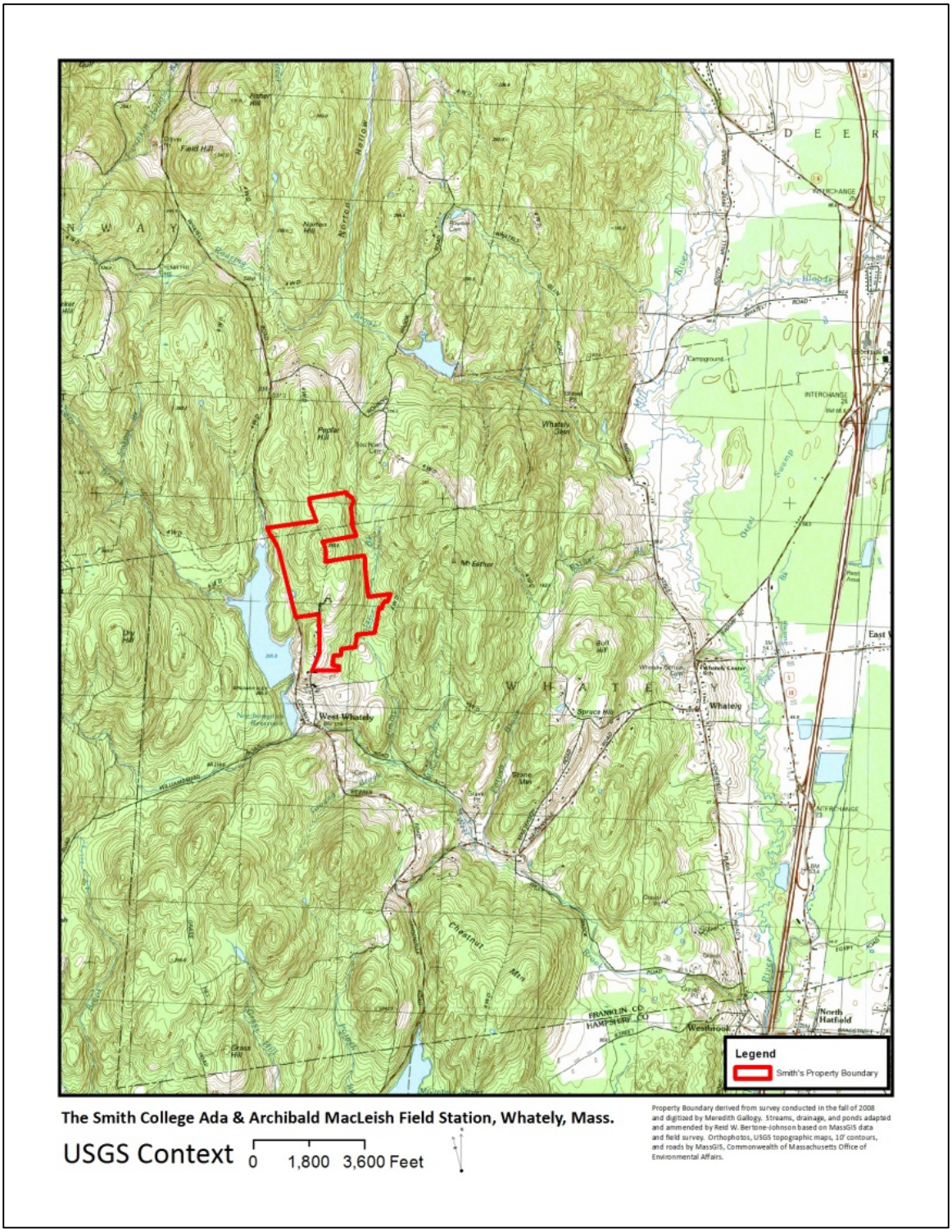

Figure 1: The Smith College Ada & Archibald MacLeish Field Station site location and topographic map. Map provided by the Center for the Environment, Ecological Design & Sustainability (CEEDS) at Smith College, Northampton, Massachusetts.

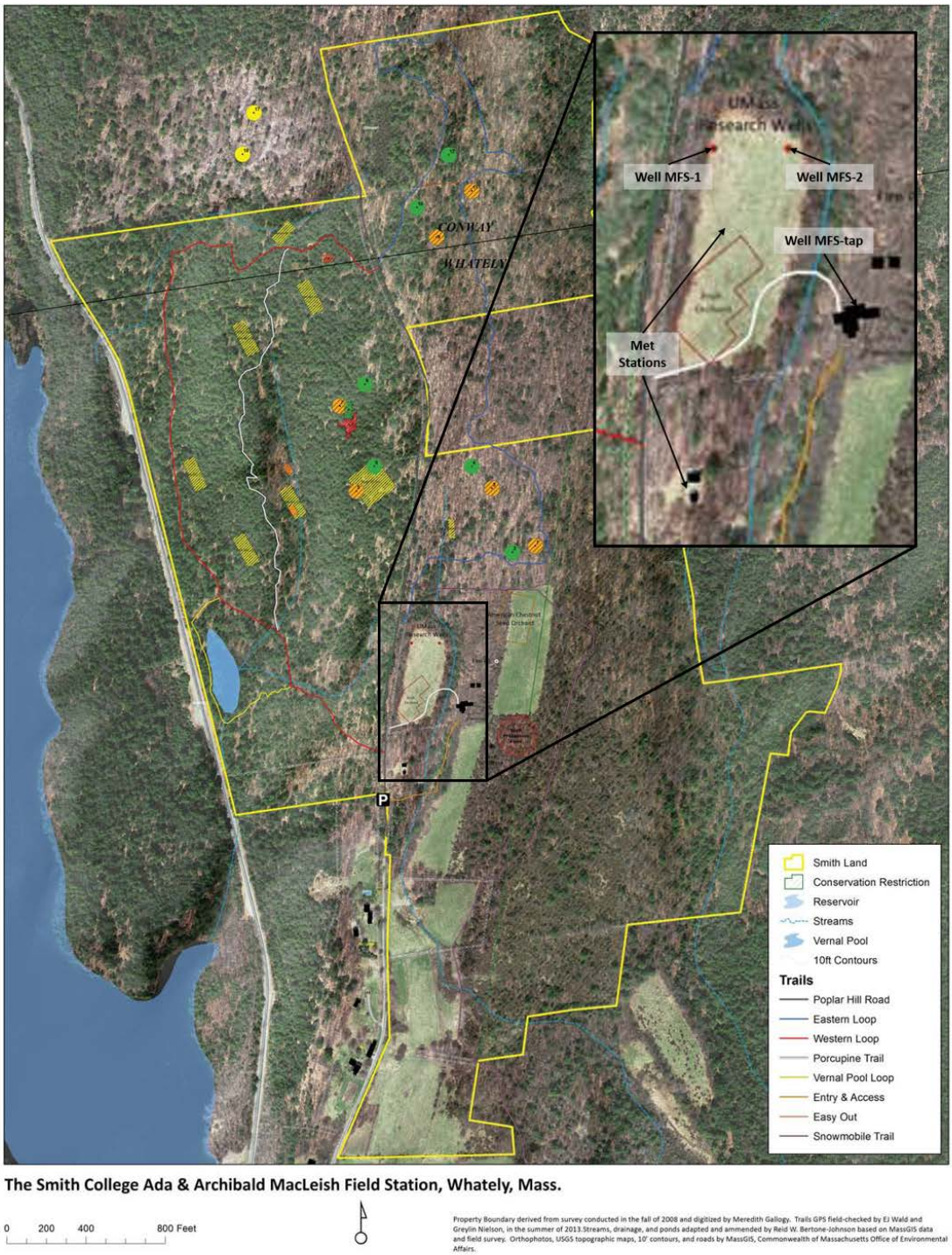

Figure 2: The MacLeish Field Station detailed site layout. Shown are the locations of open borehole bedrock well MFS-1, till-bedrock interface well MFS-2, deep water supply well MFS-tap, site meteorological stations, and other relevant neighboring research project sites. Map provided by the Center for the Environment, Ecological Design & Sustainability (CEEDS) at Smith College, Northampton, Massachusetts.

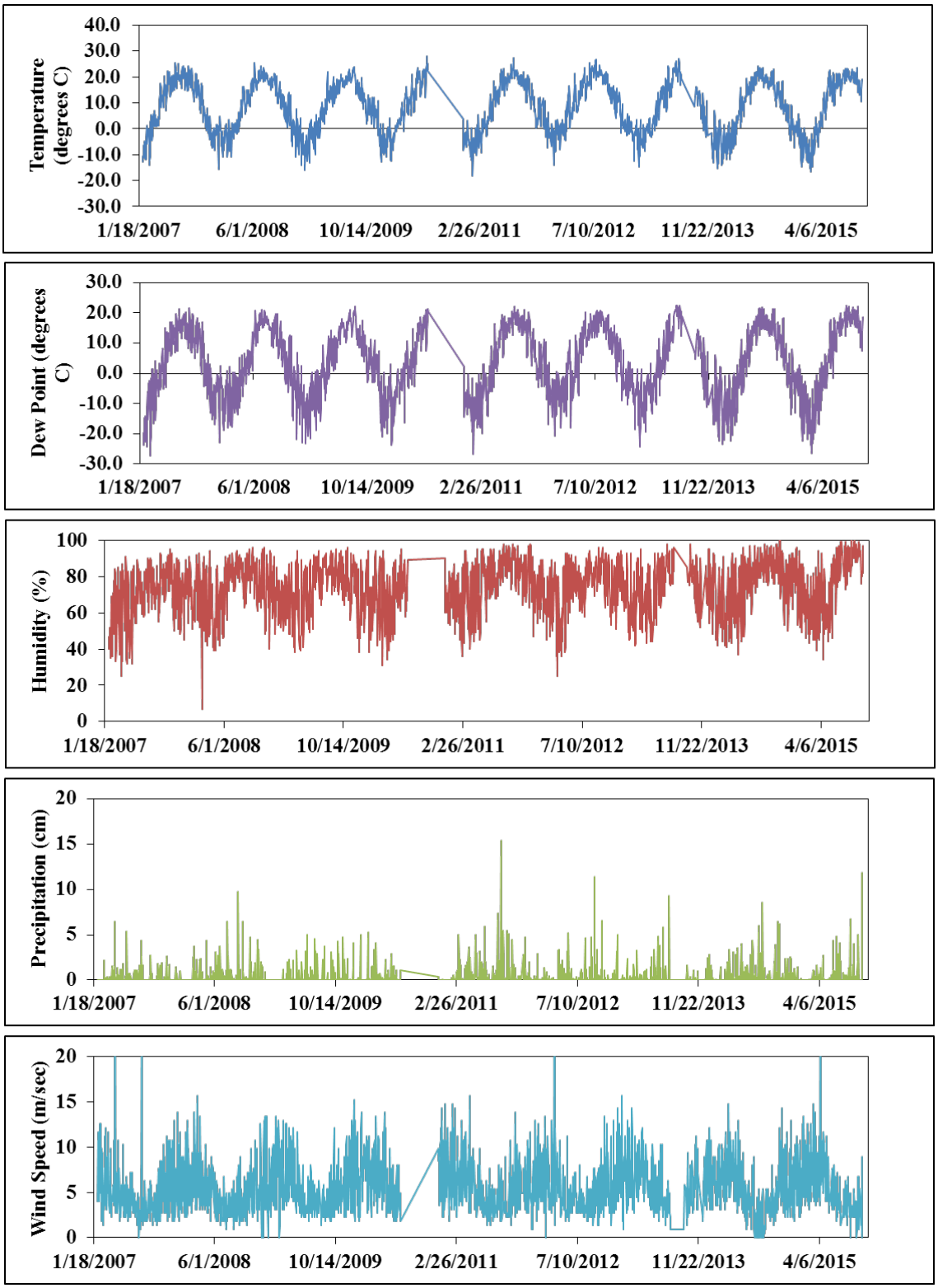

Figure 3: Meteorological data from Whately, Massachusetts, Weather Underground station Number KMACONWA2. Data included are daily average temperature, daily average dew point,daily average humidity, daily precipitation, and daily maximum wind speed. Note that no data is available for the period July 2010 to December 2010.

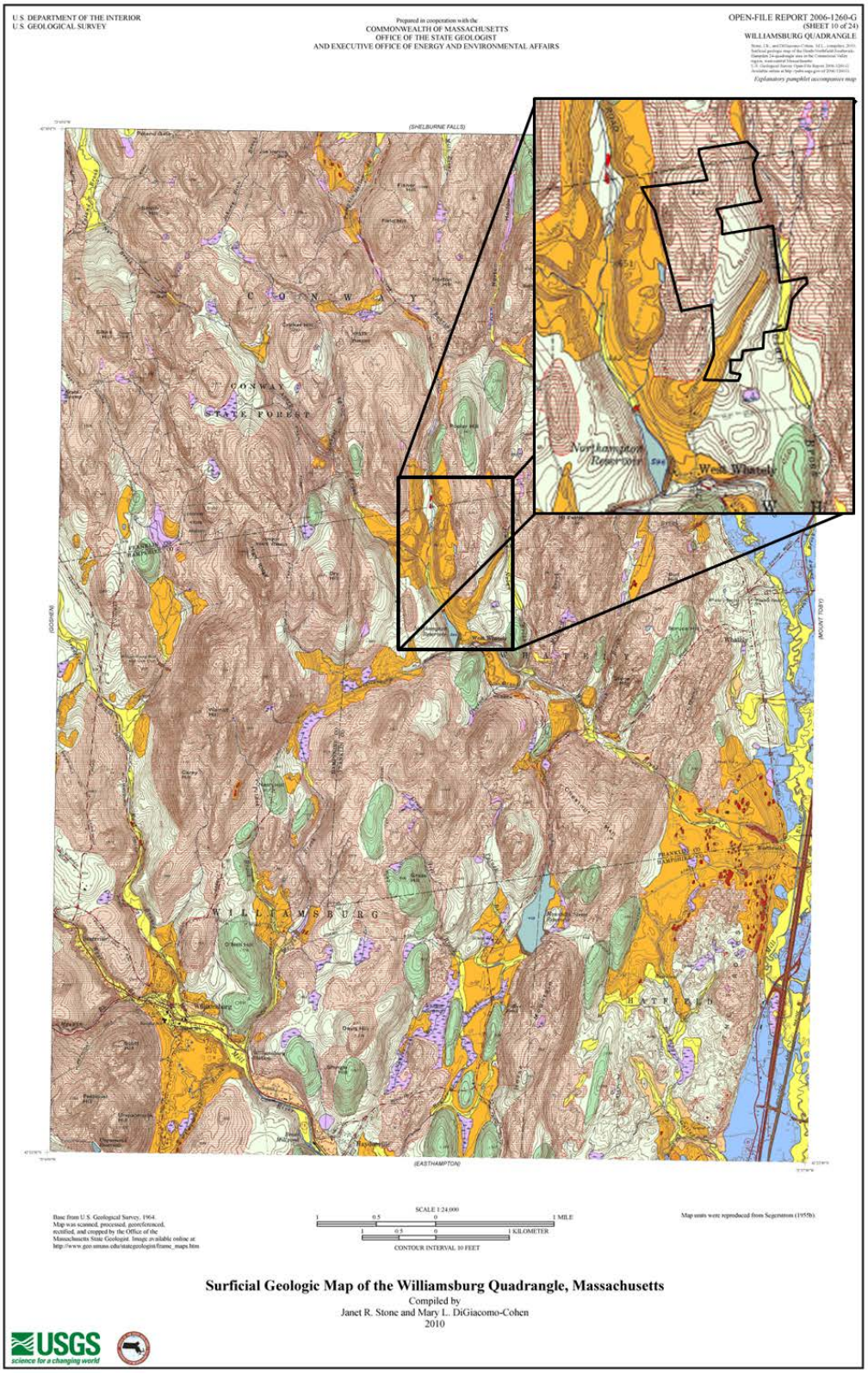

Figure 4: Surficial geology of the Williamsburg Quadrangle (Stone and DiGiacomo-Cohen, 2010) with inset showing the location of the MacLeish Field Station. A legend and description of the units mapped are described in Table 1.

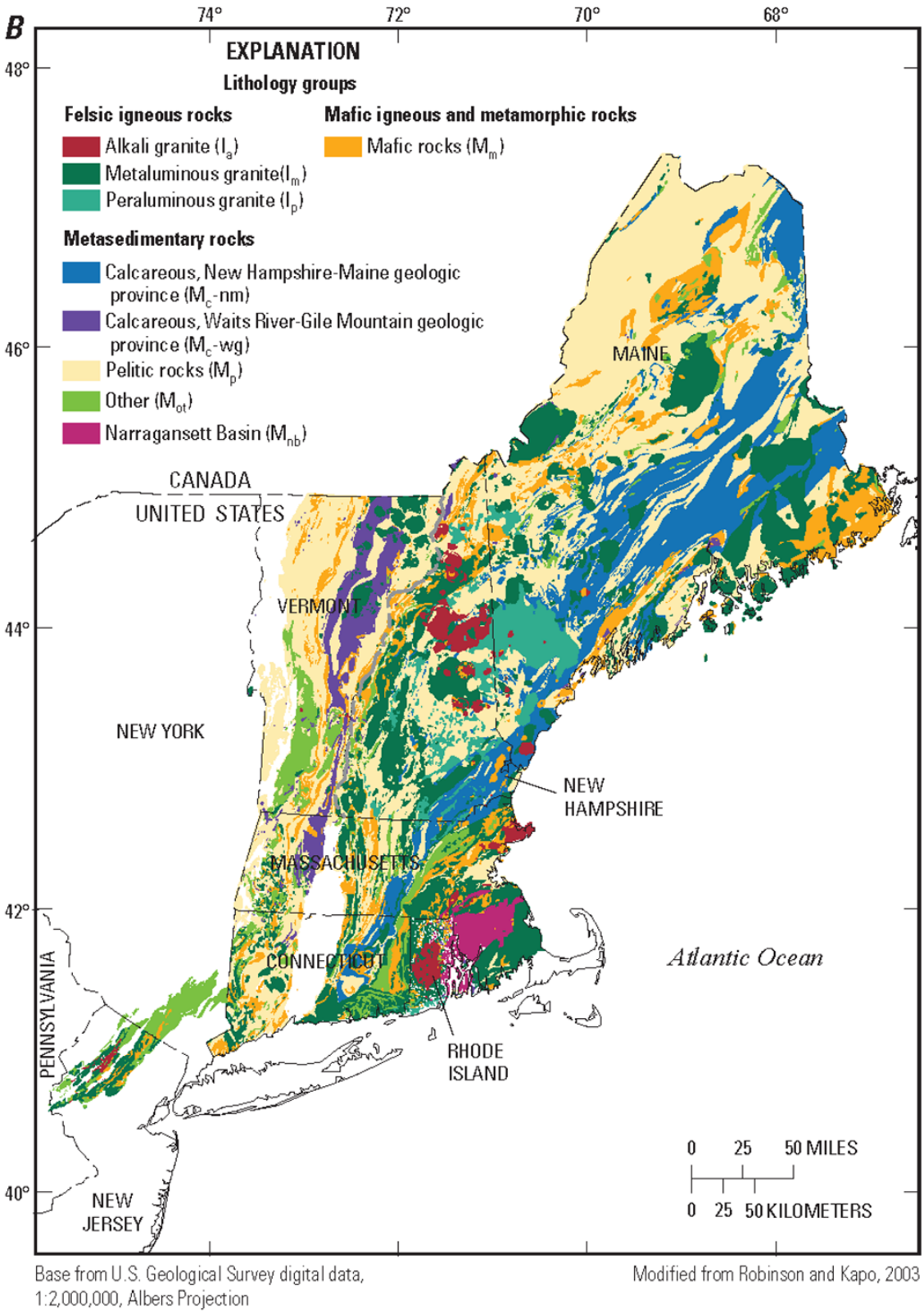

Figure 5: Regional bedrock geologic units of the New England Crystalline Rock Aquifer (NECRA) study area (Flanagan et al., 2011)

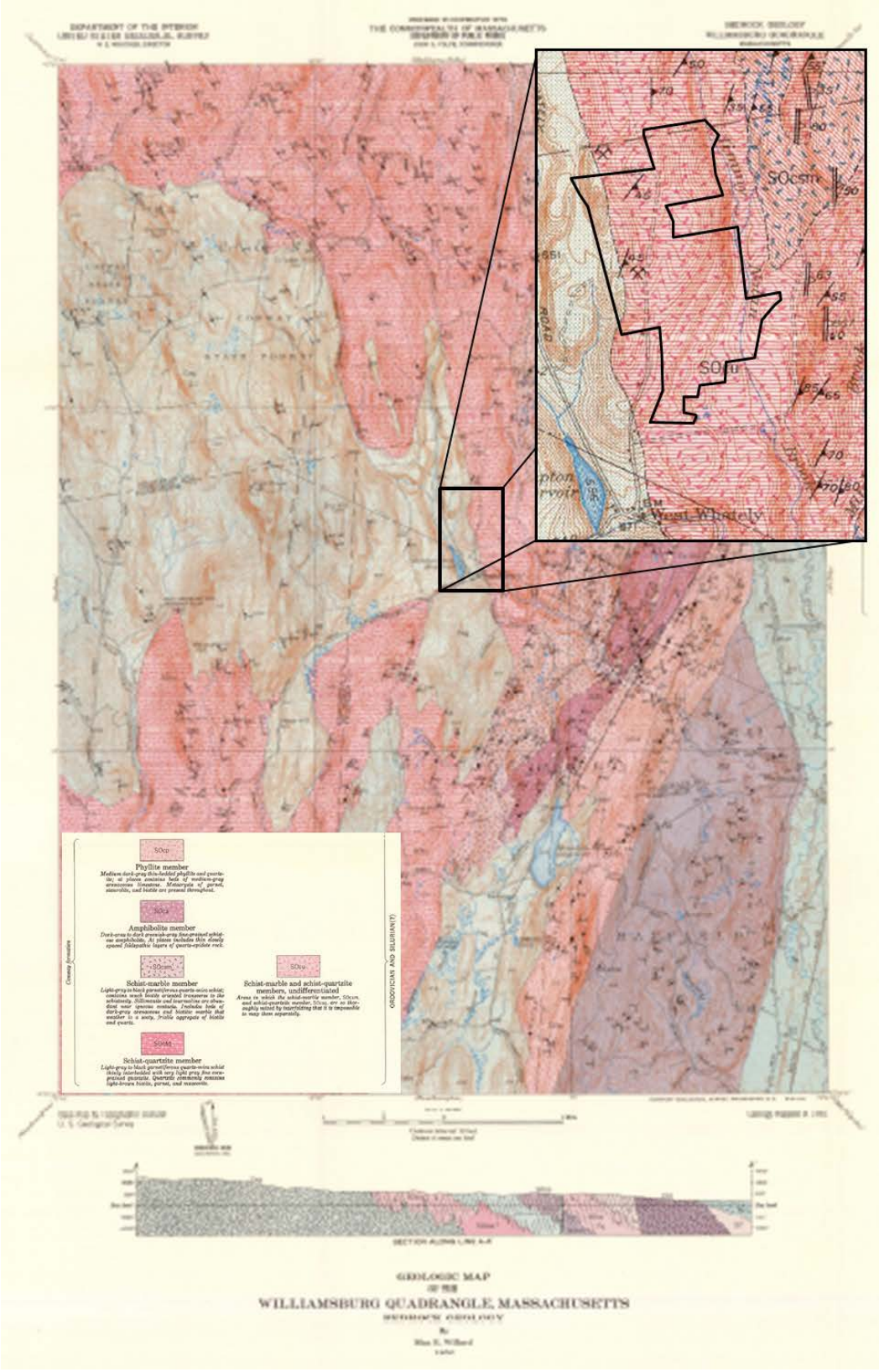

Figure 6: Bedrock geology of the Williamsburg Quadrangle (Willard, 1956) with inset showing the location of the MacLeish Field Station.

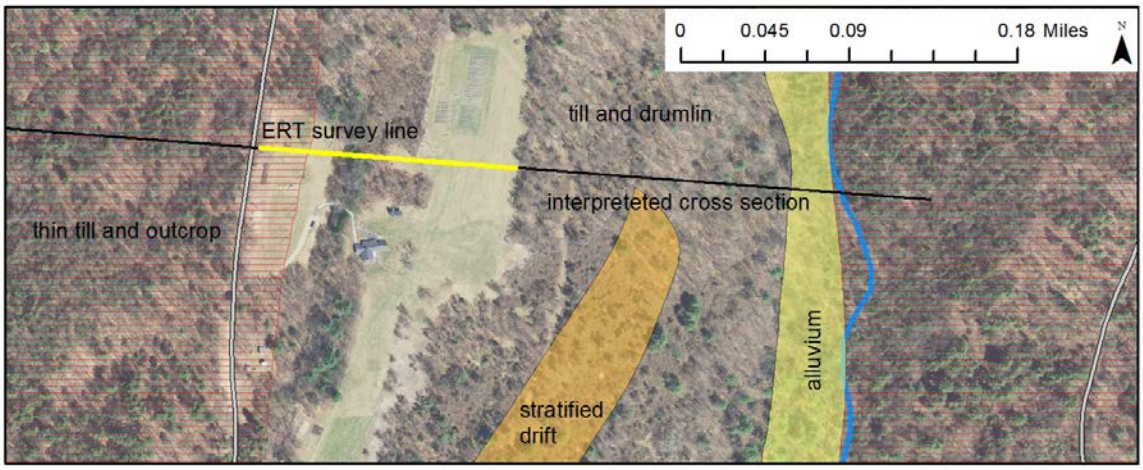

Figure 7: Location of ERT survey transect (yellow line) completed at the MacLeish Field Station and the transect of inferred subsurface geology extending to Jimmy Nolan Brook (black line). Figure from Isaacson, in progress.

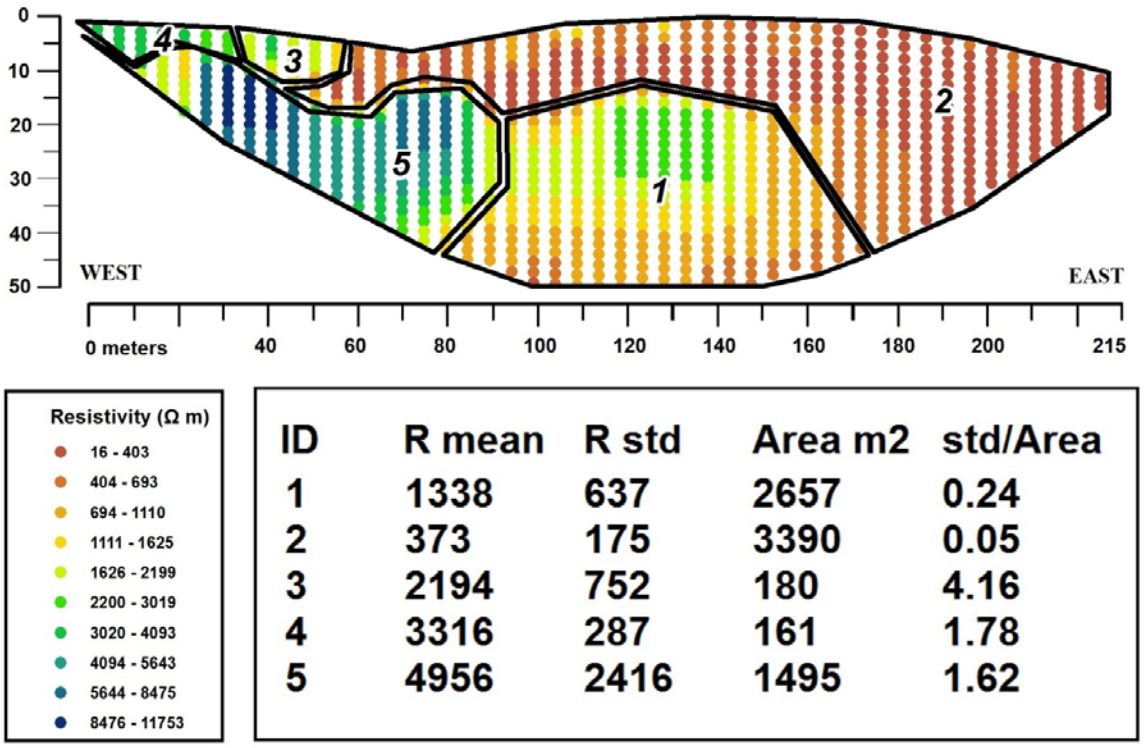

ID	R mean	R std	Area m2	std/Area
1	1338	637	2657	0.24
2	373	175	3390	0.05
3	2194	752	180	4.16
4	3316	287	161	1.78
5	4956	2416	1495	1.62

Figure 8: Modelled resistivity values shown in cross section for the ERT Survey completed at the MacLeish Field Station. The polygon areas have been interpreted from the modeled data. The calculated mean and standard deviation of the modeled resistivity values are provided. Figure and interpretation from Isaacson, in progress.

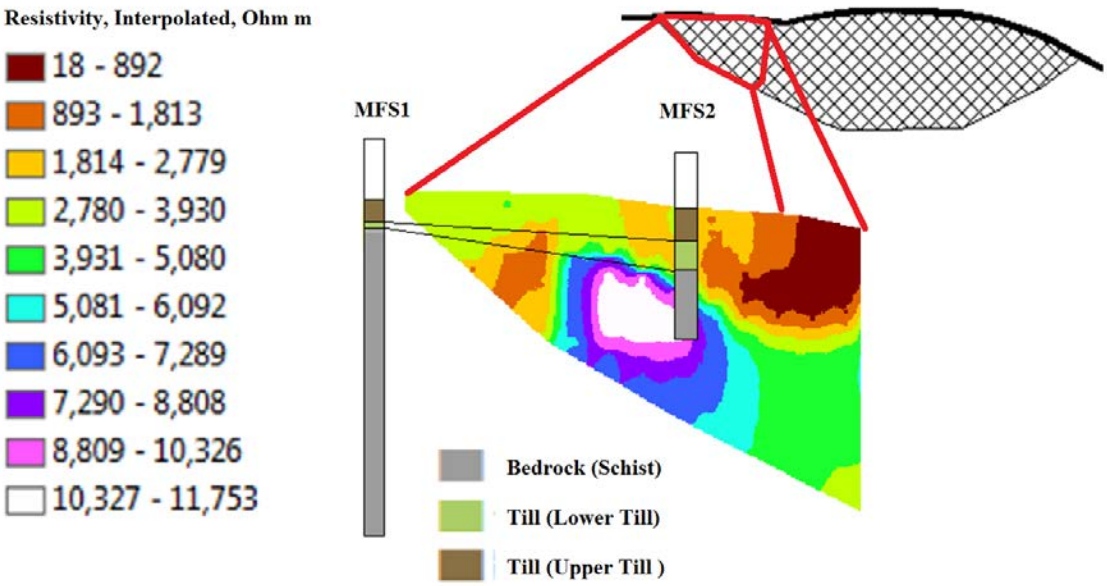

Figure 9: Modeled resistivity values of the western portion of the ERT survey completed at the MacLeish Field Station, with the general geologic interpretation of MFS-1 and MFS-2 overlain. Wells MFS-1 and MFS-2 are located approximately 40 meters apart. Figure and interpretation from Isaacson, in progress.

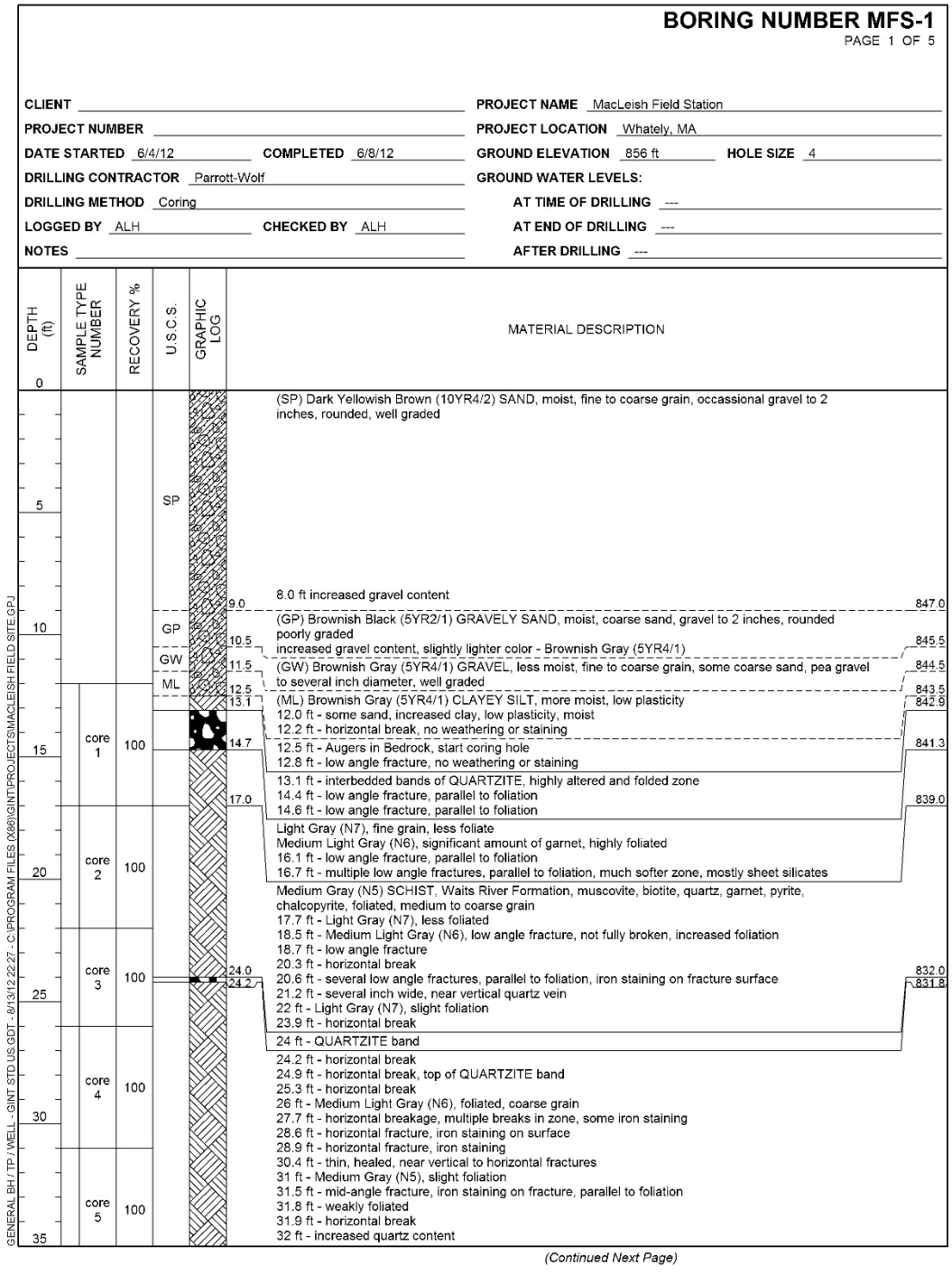

Figure 10: Core log developed from the drilling of open borehole bedrock well MFS-1 at the MacLeish Field Station in Whately, Massachusetts.

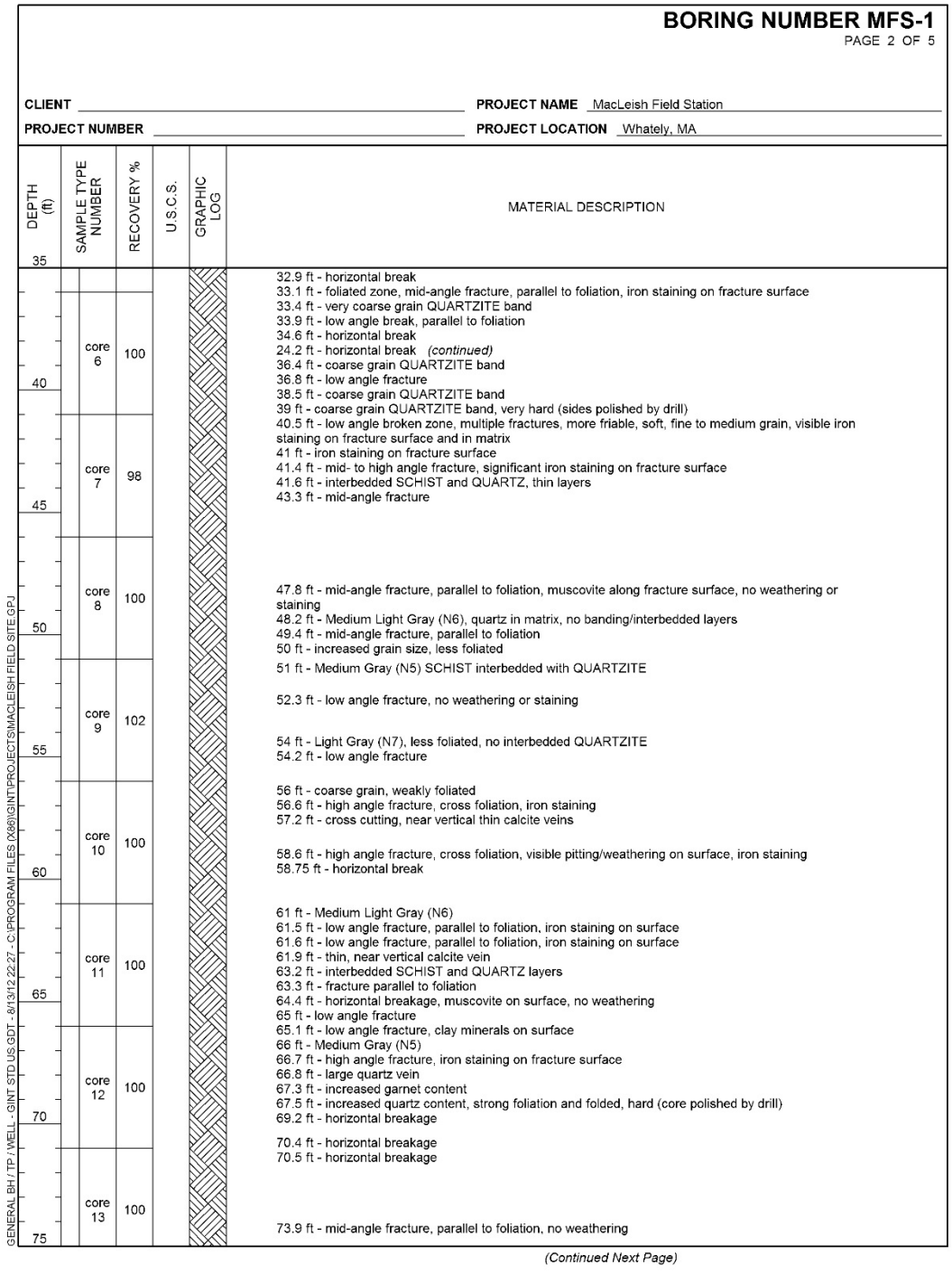

Figure 10 (continued): Core log developed from the drilling of open borehole bedrock well MFS-1 at the MacLeish Field Station in Whately, Massachusetts.

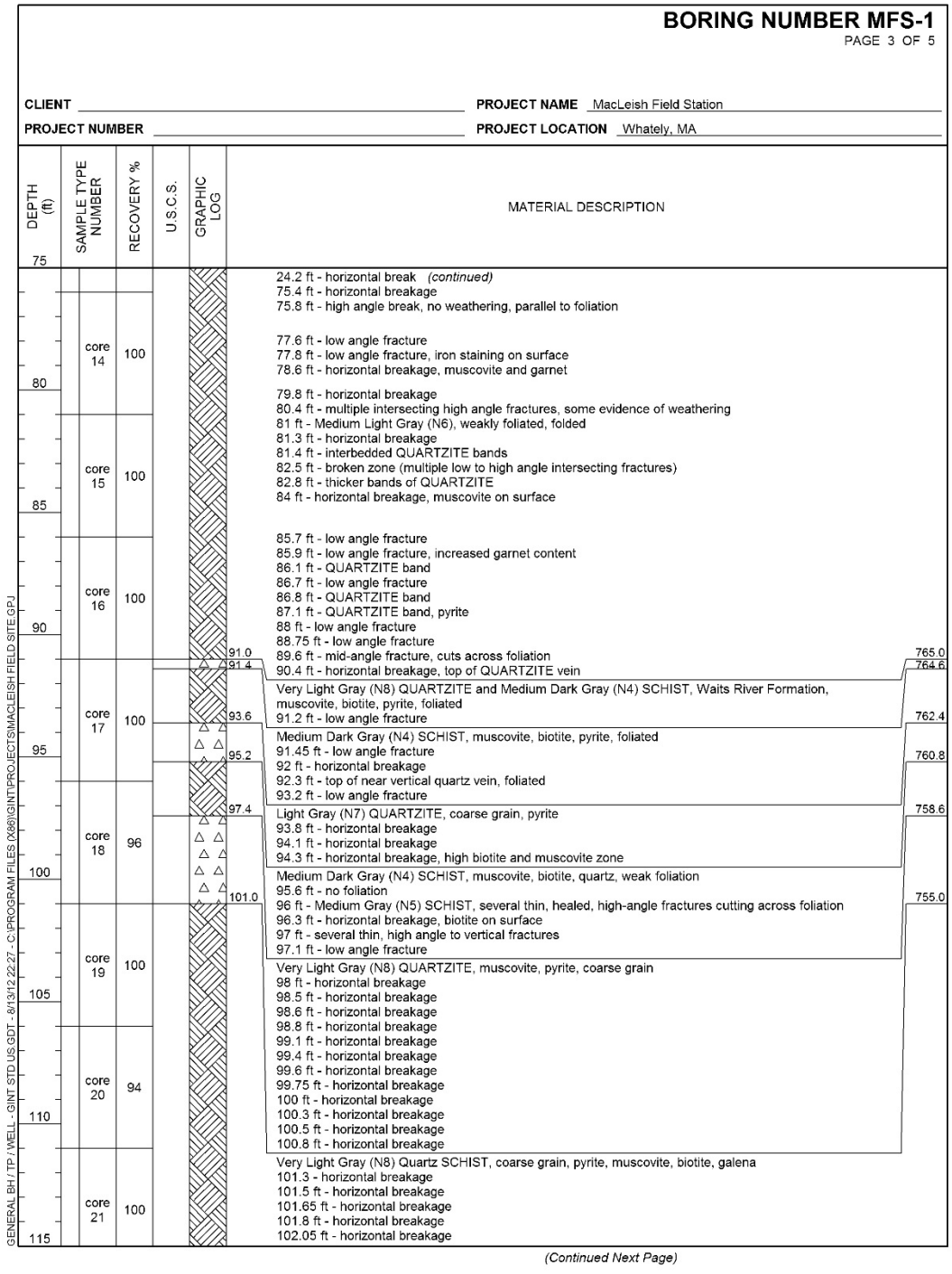

Figure 10 (continued): Core log developed from the drilling of open borehole bedrock well MFS-1 at the MacLeish Field Station in Whately, Massachusetts.

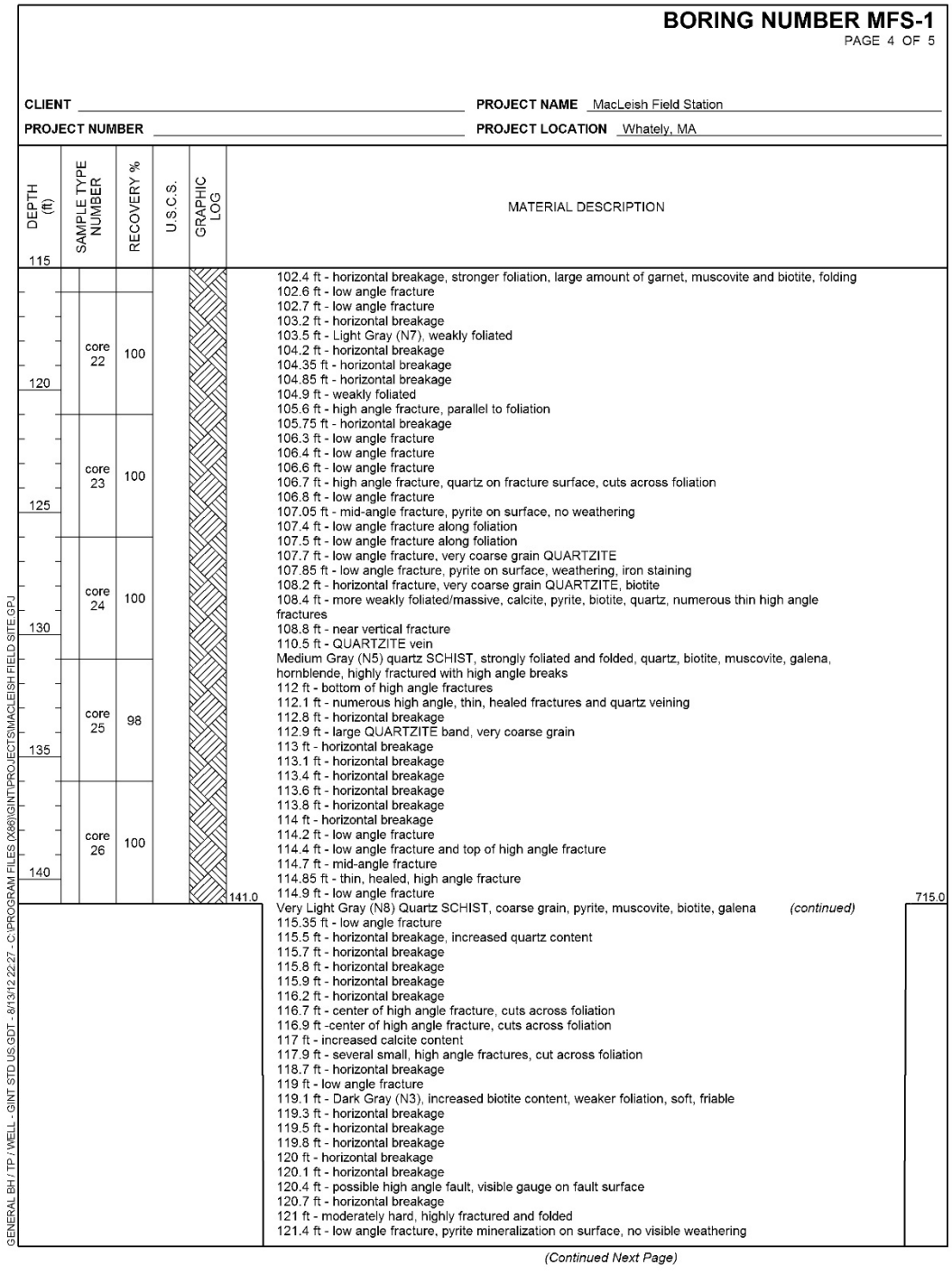

Figure 10 (continued): Core log developed from the drilling of open borehole bedrock well MFS-1 at the MacLeish Field Station in Whately, Massachusetts.

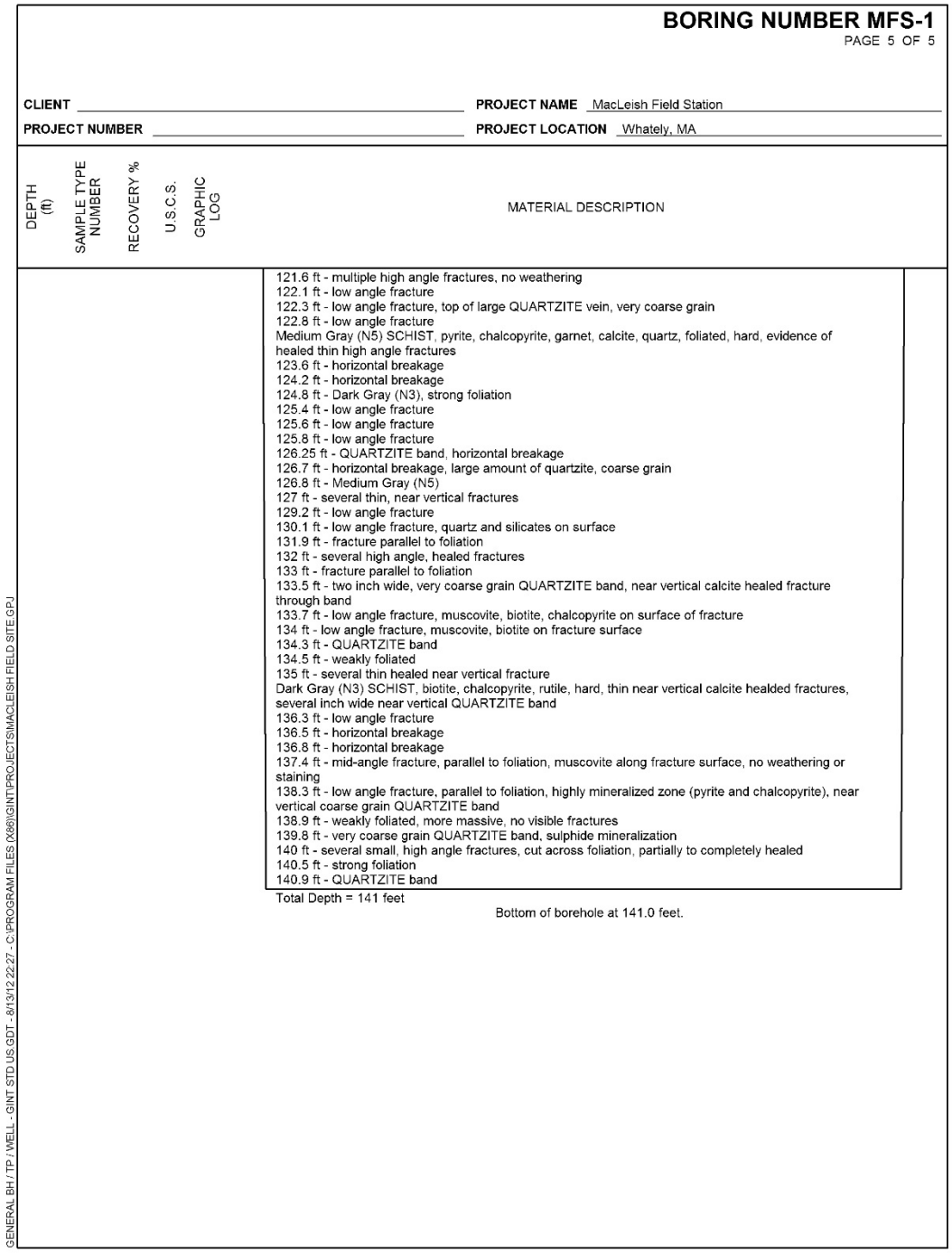

Figure 10 (continued): Core log developed from the drilling of open borehole bedrock well MFS-1 at the MacLeish Field Station in Whately, Massachusetts.

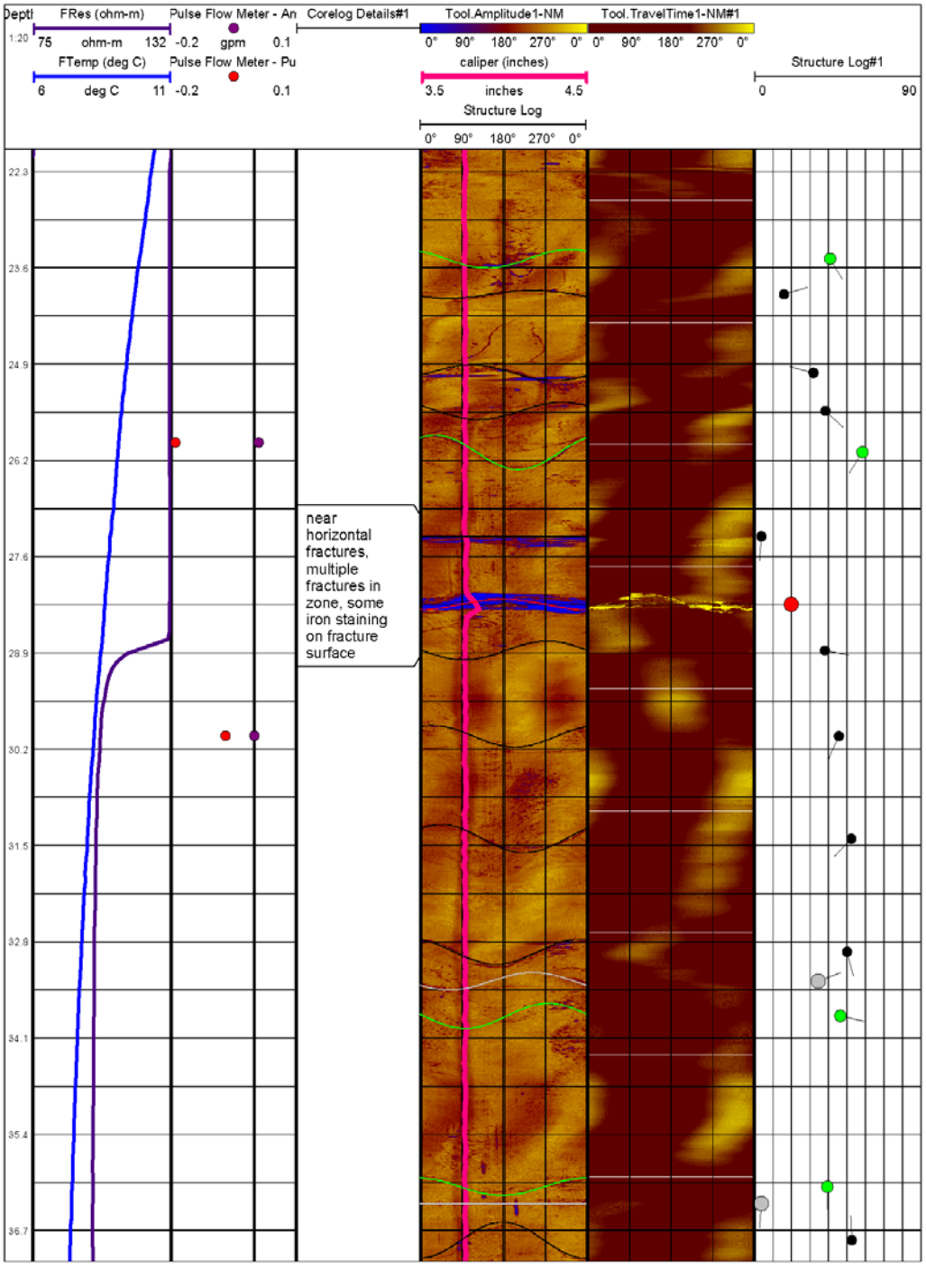

Figure 11: Compiled downhole geophysical test results from open borehole bedrock well MFS-1 at the MacLeish Field Station in Whately, Massachusetts.

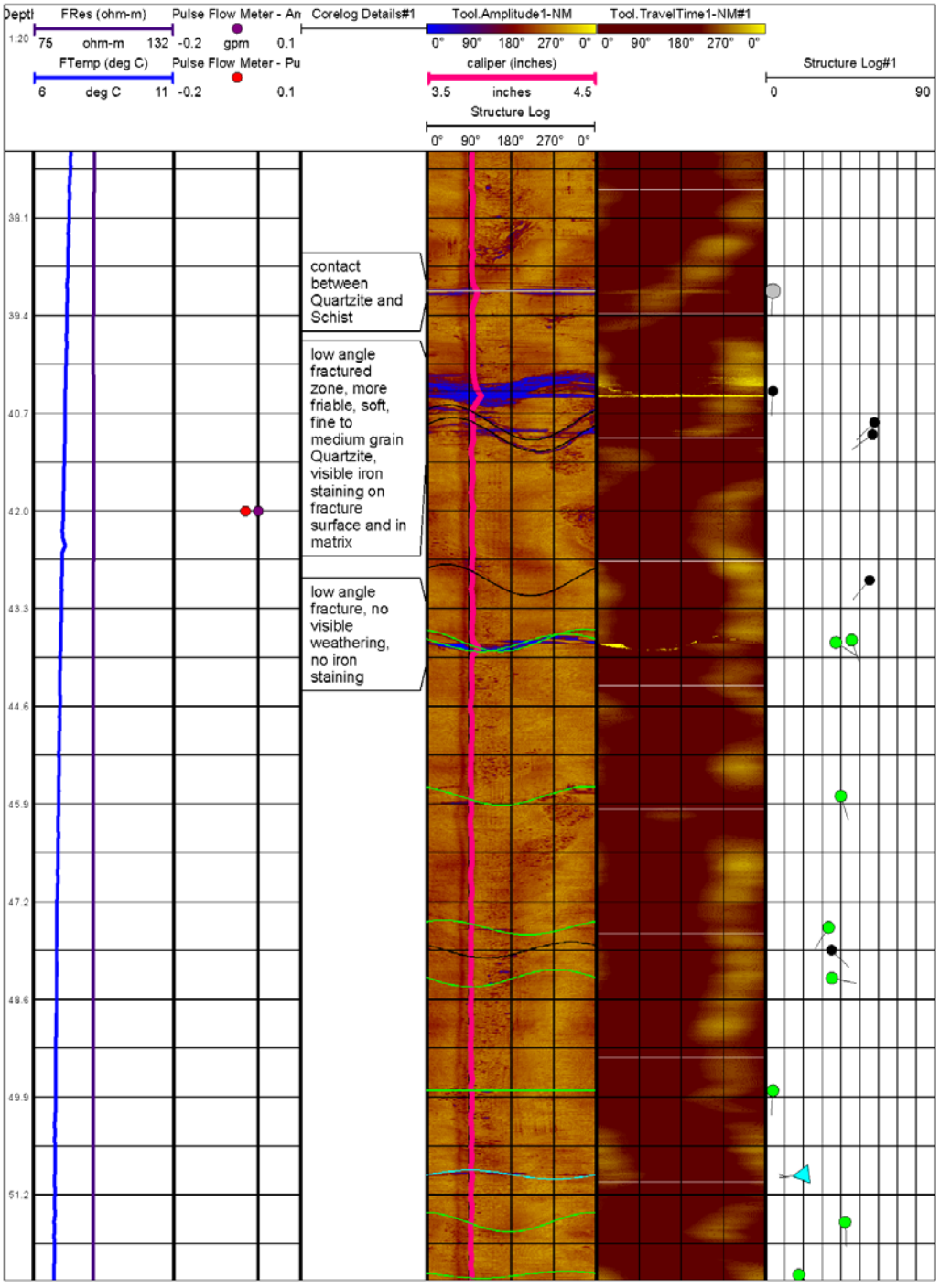

Figure 11 (continued): Compiled downhole geophysical test results from open borehole bedrock well MFS-1 at the MacLeish Field Station in Whately, Massachusetts.

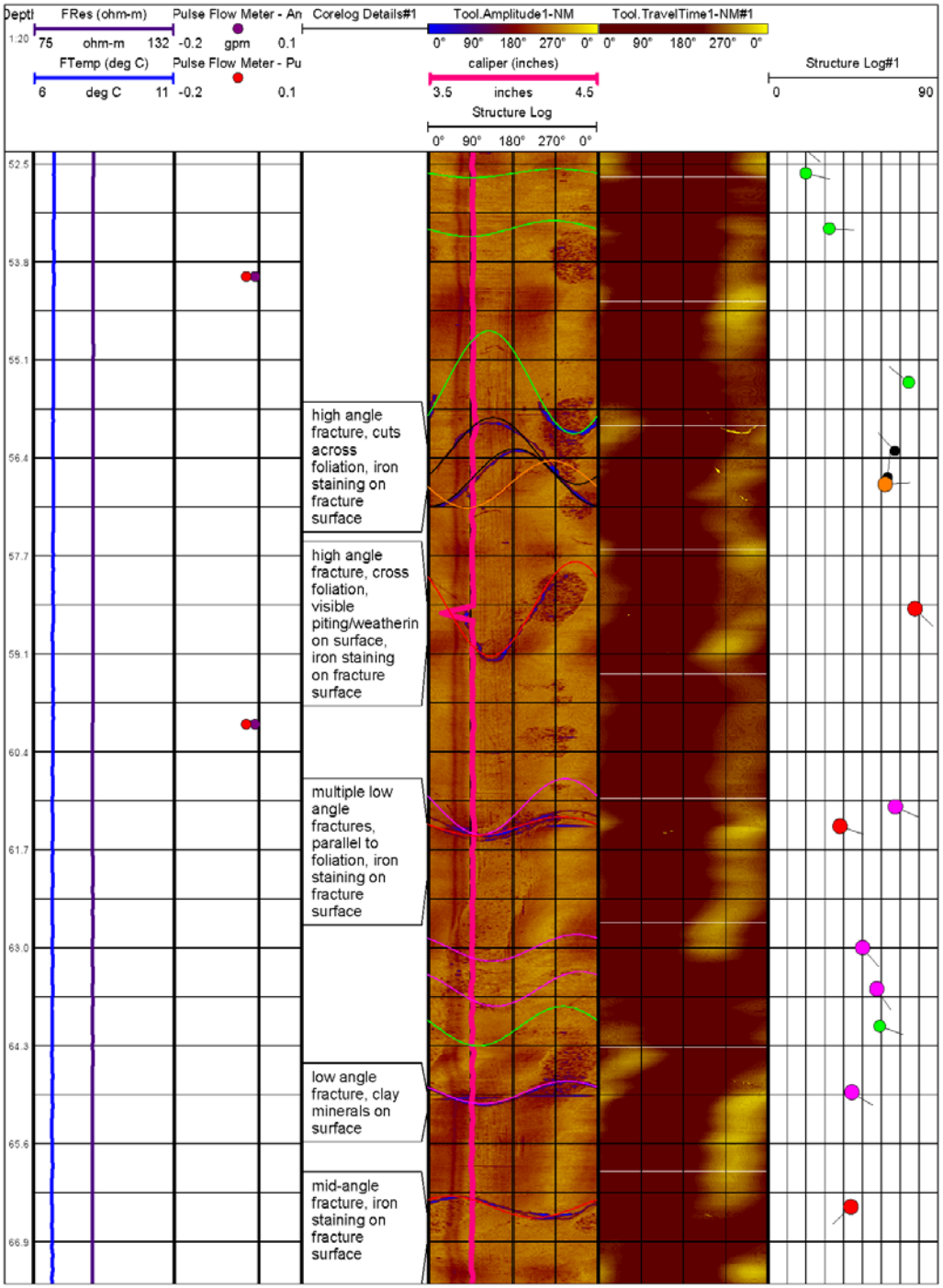

Figure 11 (continued): Compiled downhole geophysical test results from open borehole bedrock well MFS-1 at the MacLeish Field Station in Whately, Massachusetts.

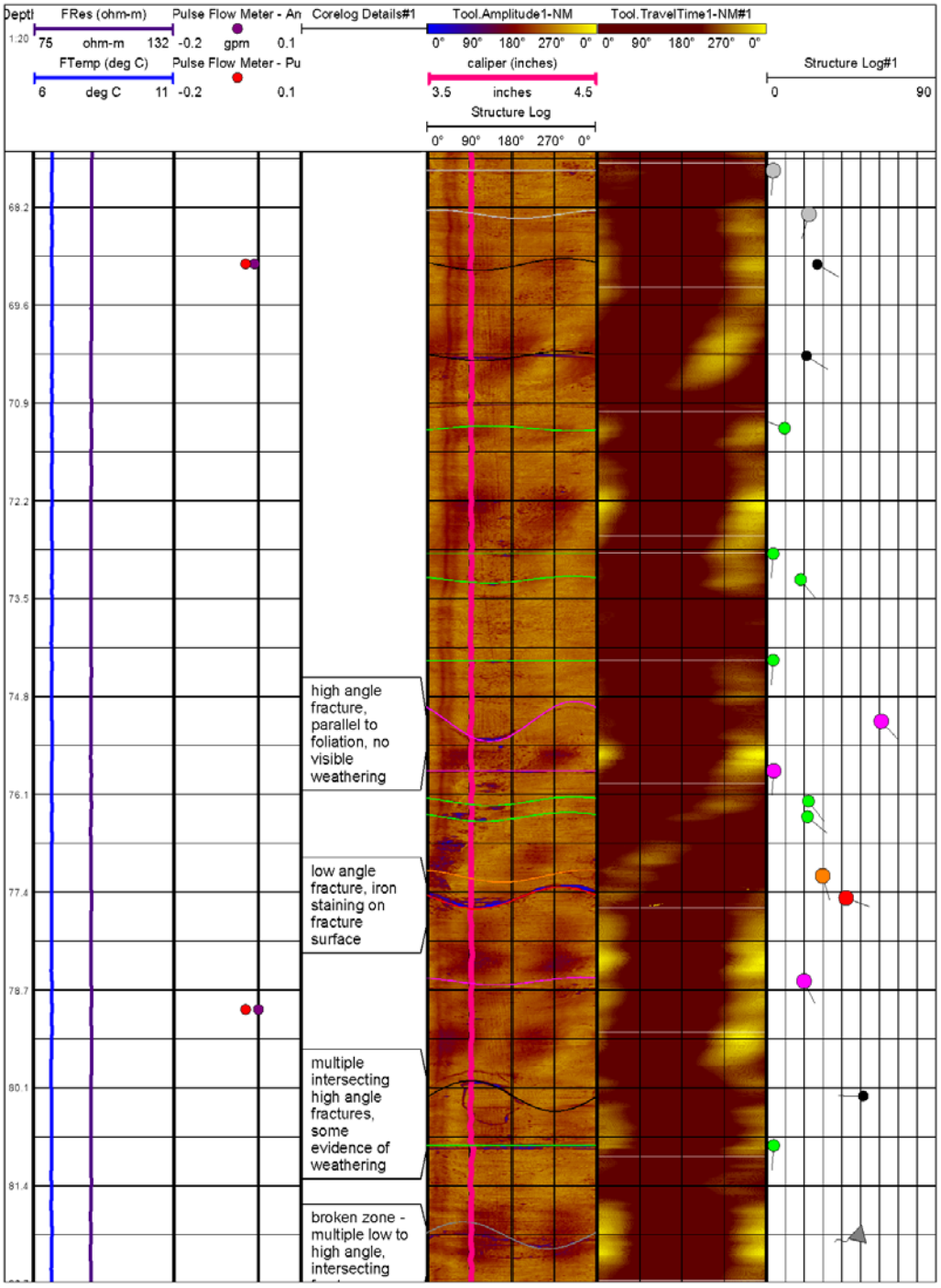

Figure 11 (continued): Compiled downhole geophysical test results from open borehole bedrock well MFS-1 at the MacLeish Field Station in Whately, Massachusetts.

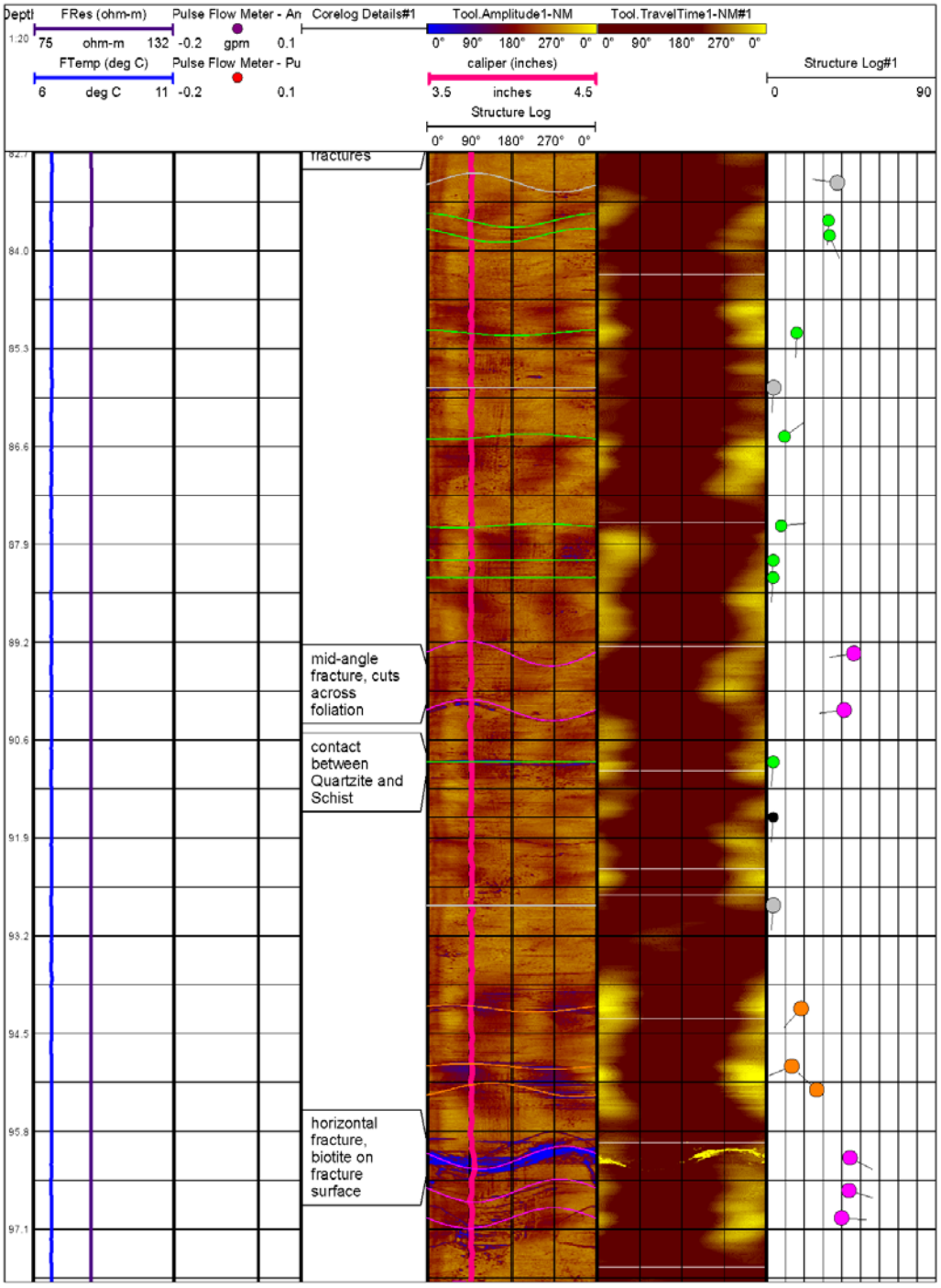

Figure 11 (continued): Compiled downhole geophysical test results from open borehole bedrock well MFS-1 at the MacLeish Field Station in Whately, Massachusetts.

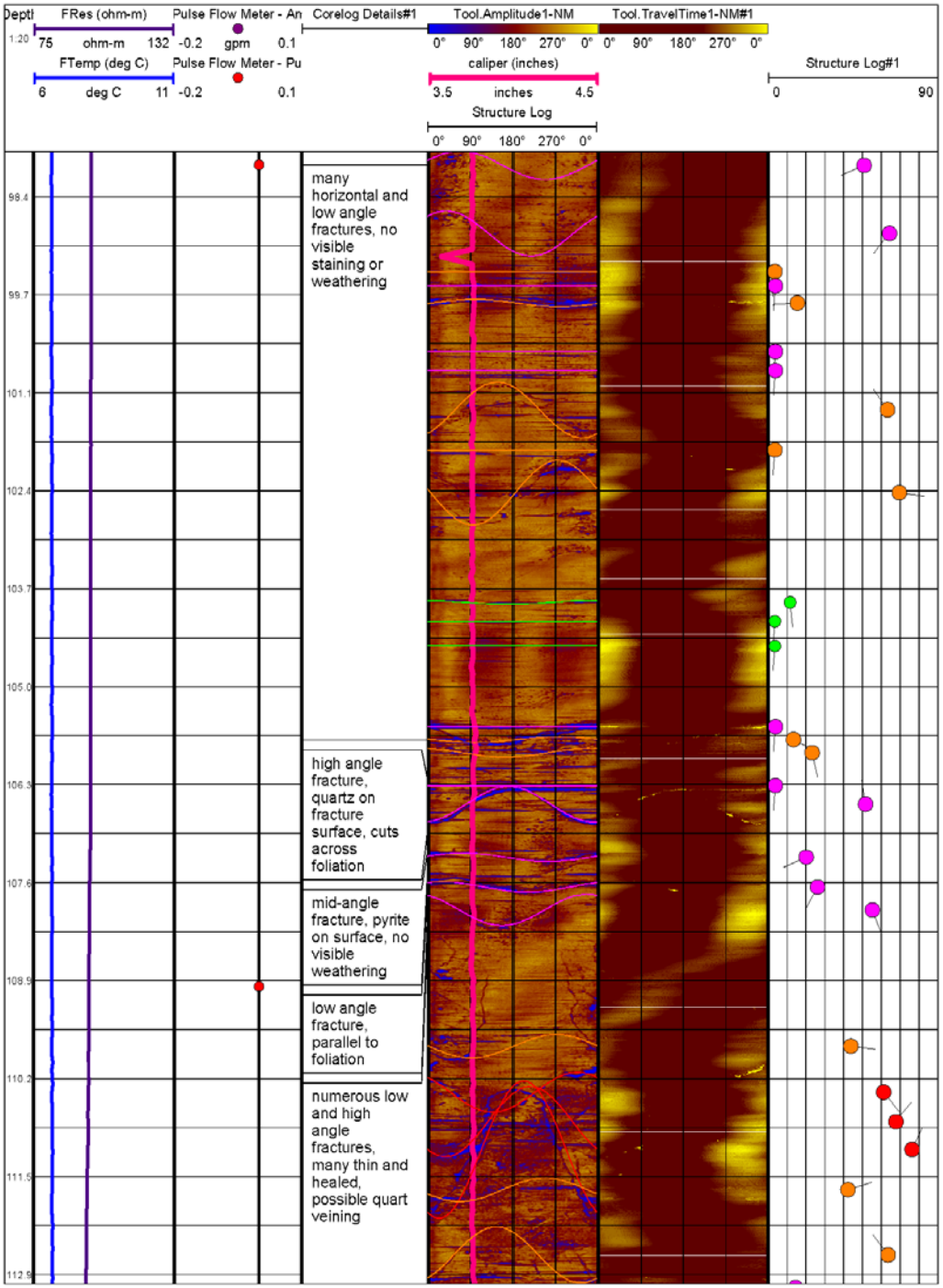

Figure 11 (continued): Compiled downhole geophysical test results from open borehole bedrock well MFS-1 at the MacLeish Field Station in Whately, Massachusetts.

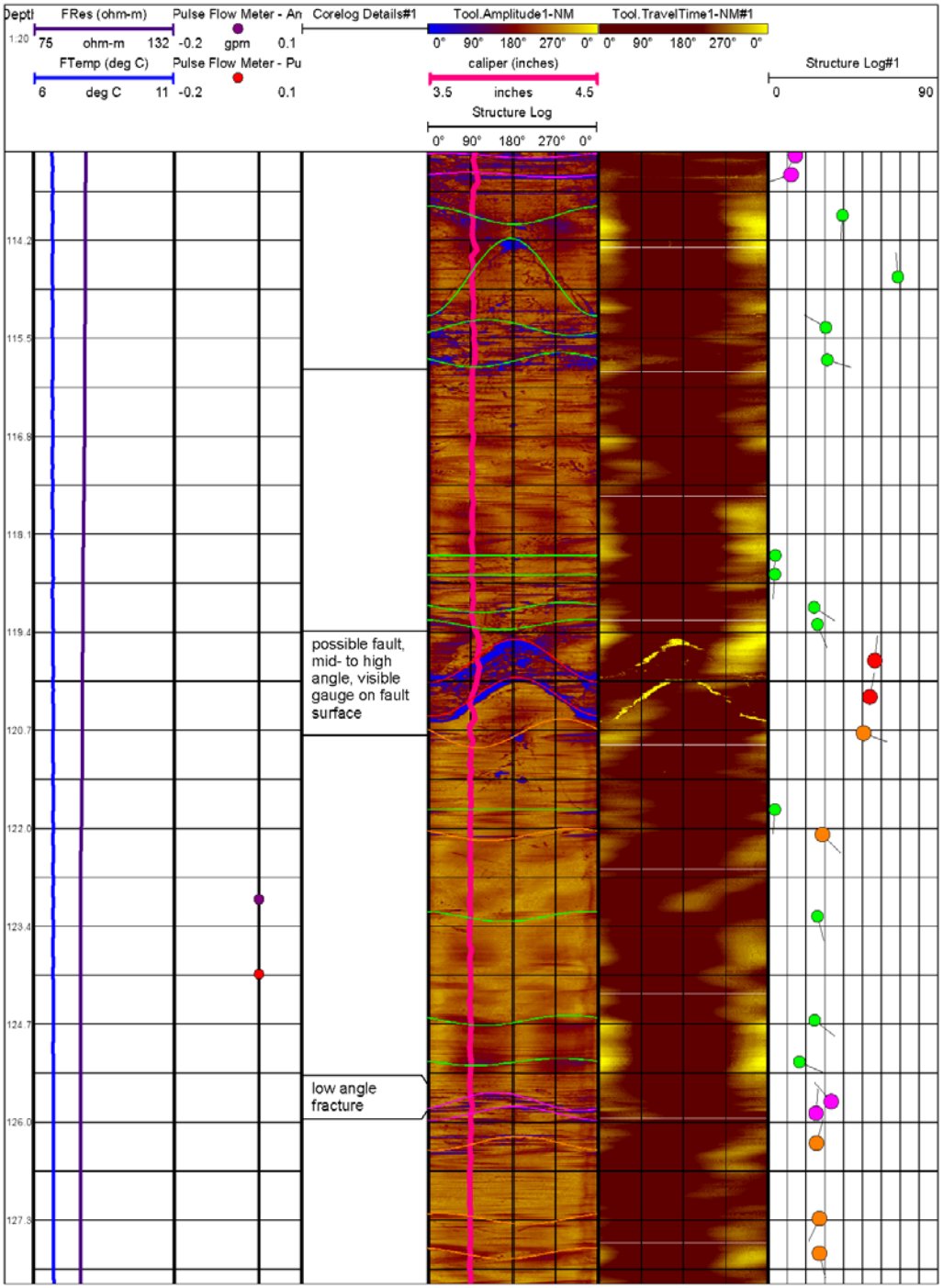

Figure 11 (continued): Compiled downhole geophysical test results from open borehole bedrock well MFS-1 at the MacLeish Field Station in Whately, Massachusetts.

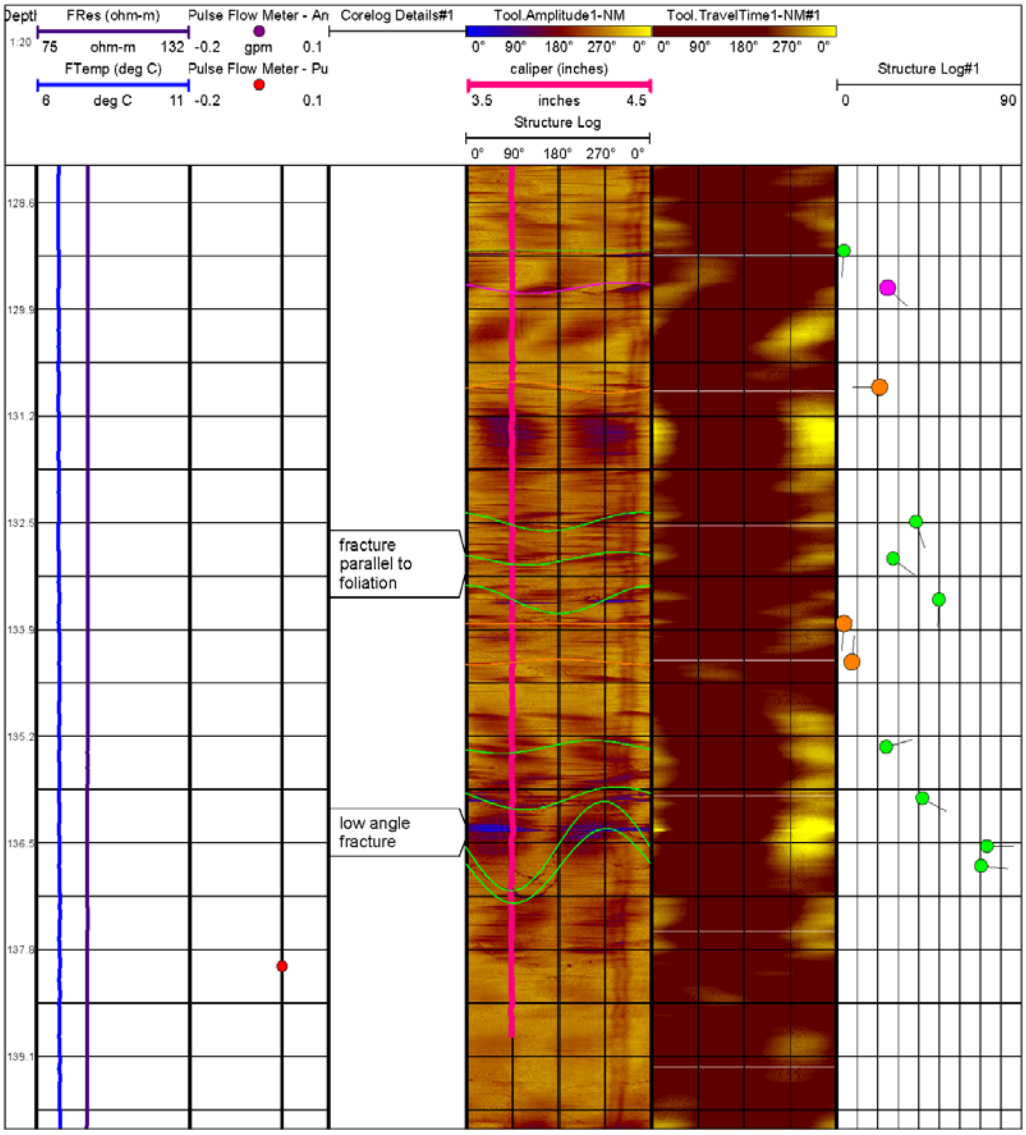

Figure 11 (continued): Compiled downhole geophysical test results from open borehole bedrock well MFS-1 at the MacLeish Field Station in Whately, Massachusetts.

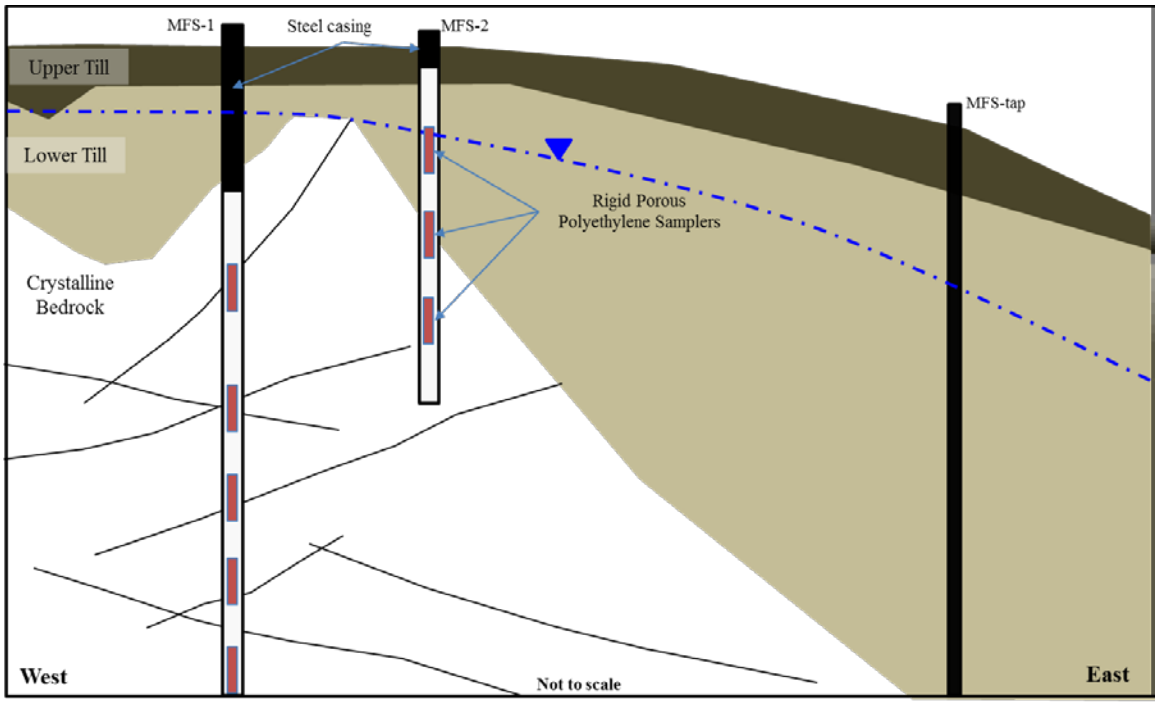

Figure 12: Conceptual Model of the MacLeish Field Station hydrogeologic condition and detail of RPP deployment in Wells MFS-1 and MFS-2.

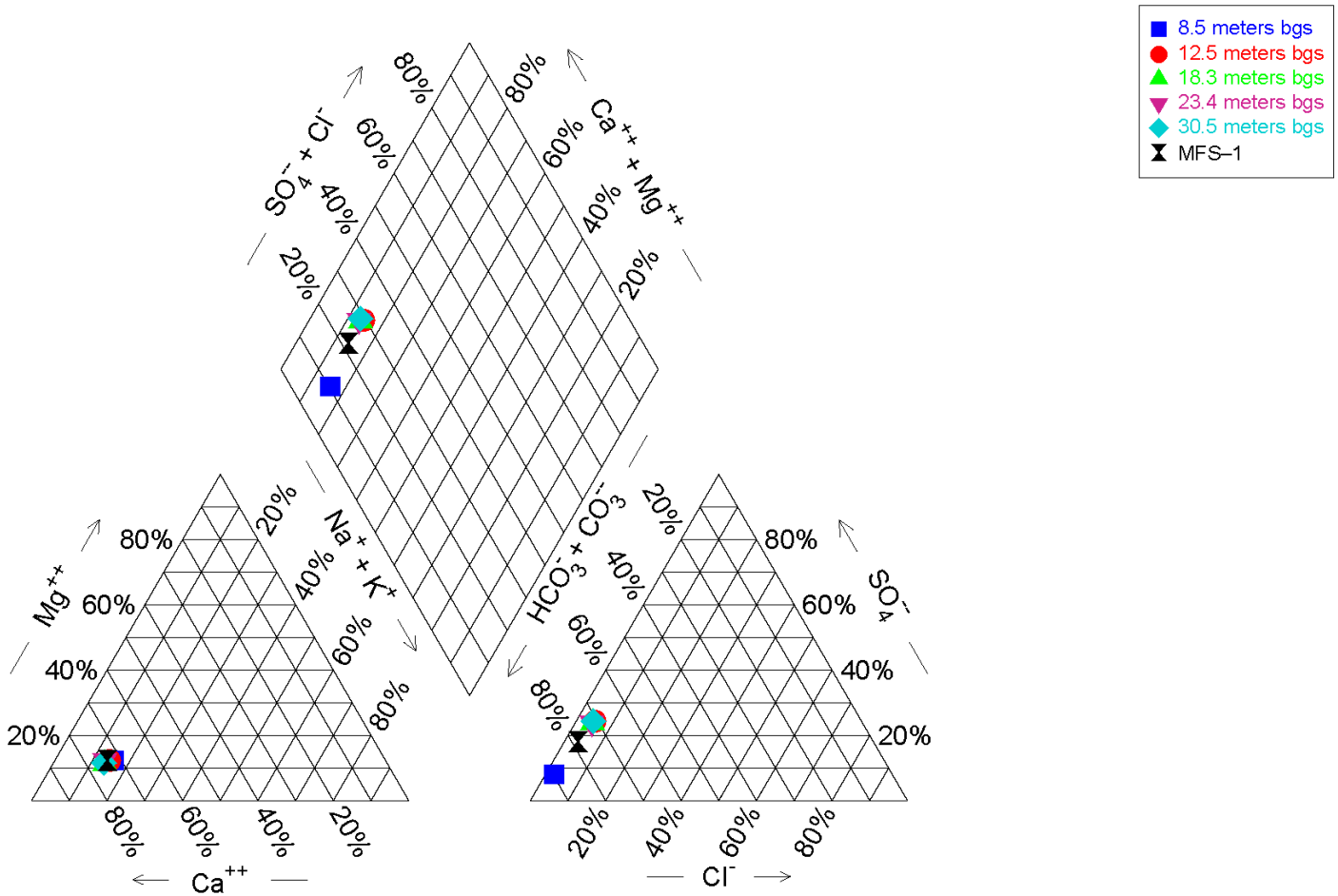

Figure 13: Piper diagram of average concentrations measured in MFS-1 and average concentrations from the discrete interval samples.

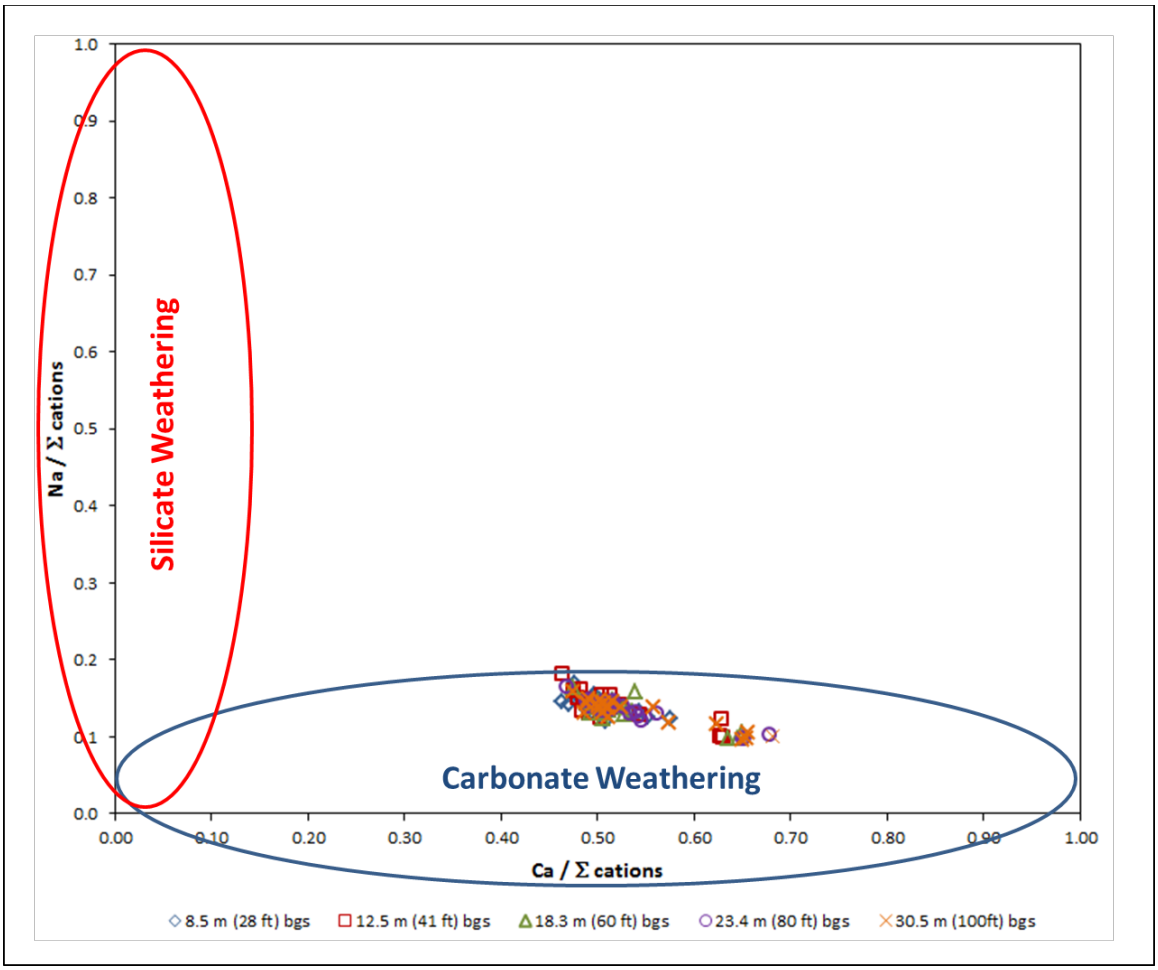

Figure 14: Comparison of normalized sodium and calcium concentrations from Well MFS-1 to determine the dominant weathering reactions controlling the groundwater quality.

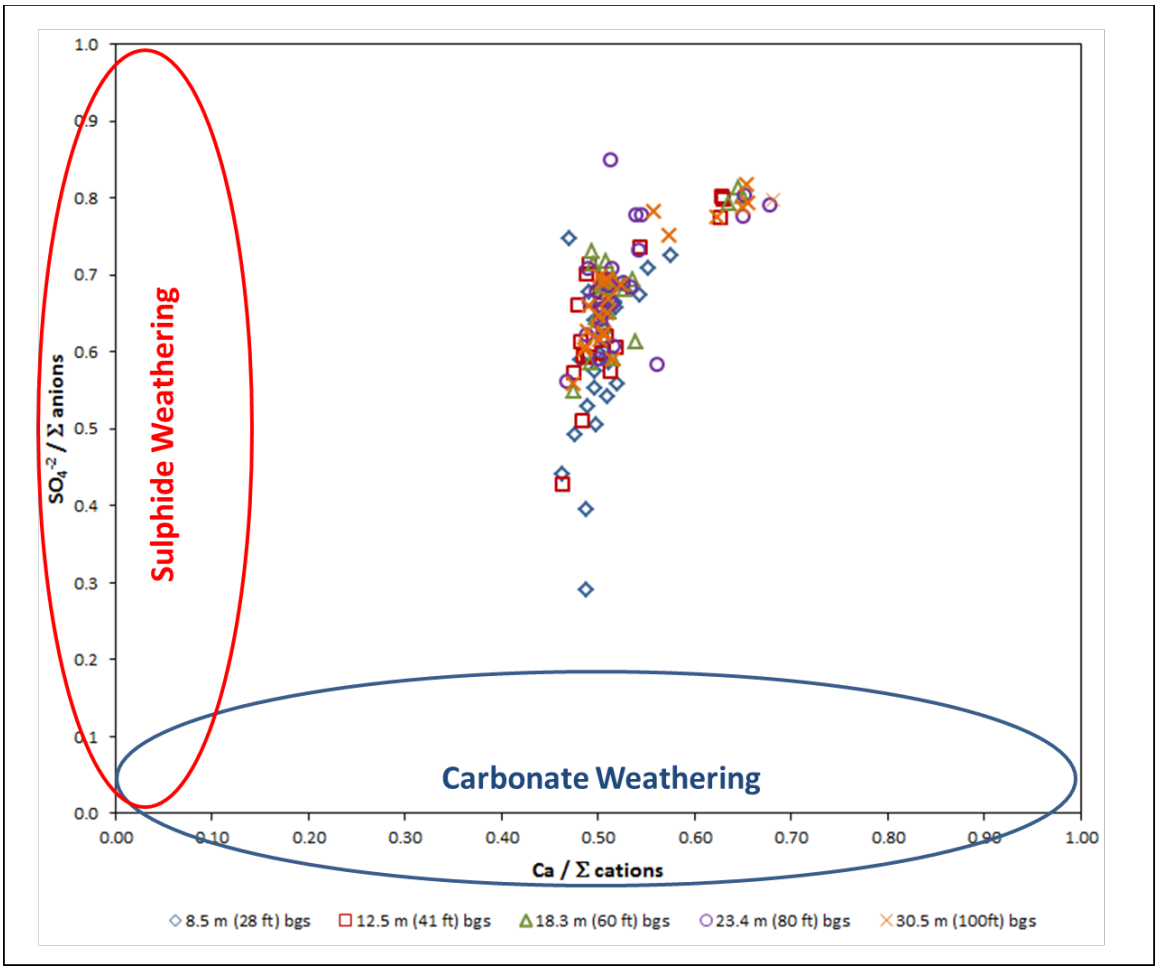

Figure 15: Comparison of normalized sulphate and calcium concentrations from Well MFS-1 to determine the dominant weathering reactions controlling the groundwater quality.

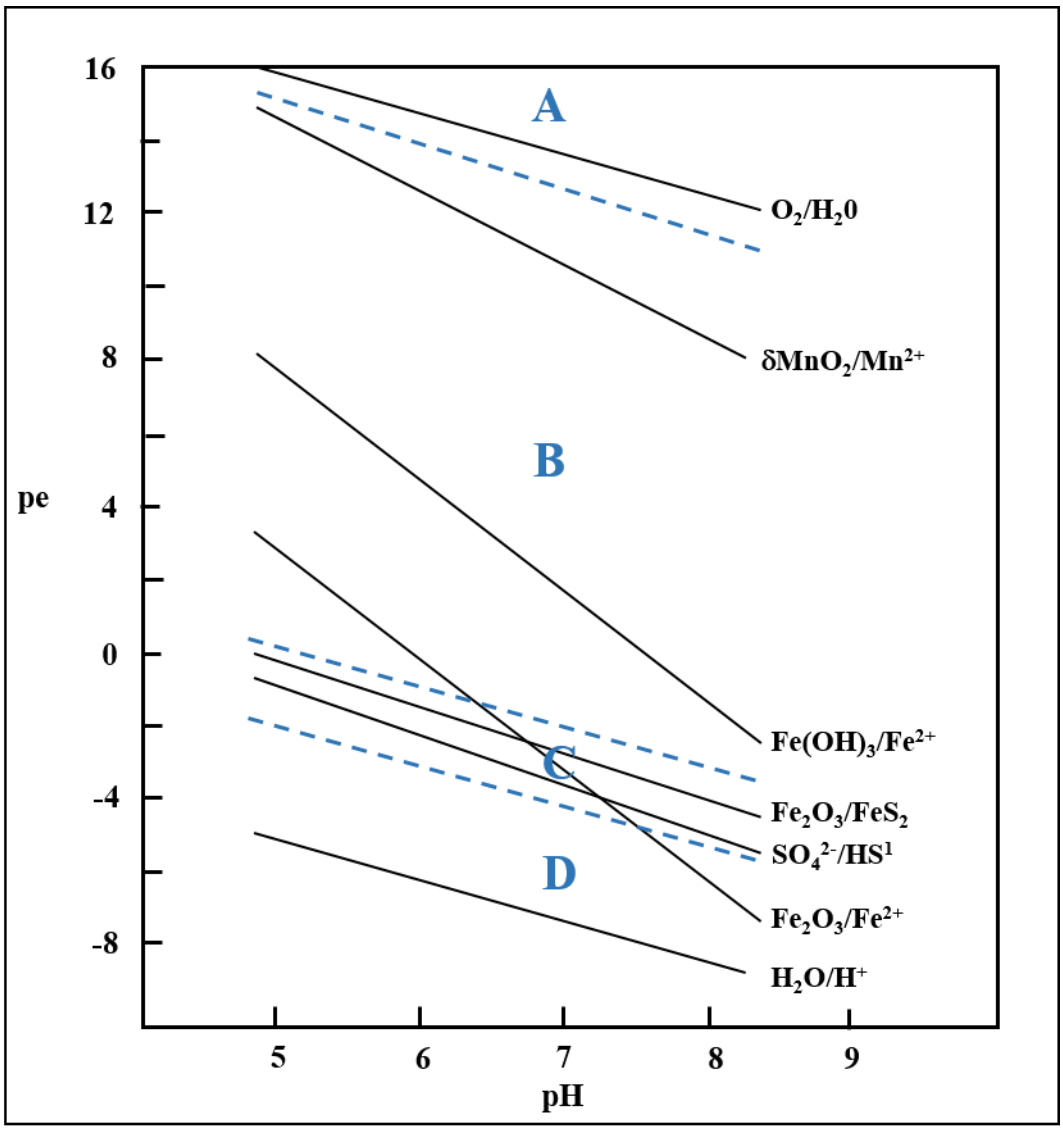

Figure 16: pe versus pH diagram of typical groundwater oxidation-reduction pairs. Zone A corresponds to groundwater with free oxygen, Zone B corresponds to groundwater with no free oxygen but no sulphate reduction, Zone C is groundwater without free oxygen and sulphate reduction, and Zone D is fully reducing conditions (adapted from Drever, 2002).

Figure 17: Iron staining on the RPP samples after two years deployed in Well MFS-1 (top) and lack of iron staining on RPP samplers deployed in MFS-2 (bottom) over the same period.

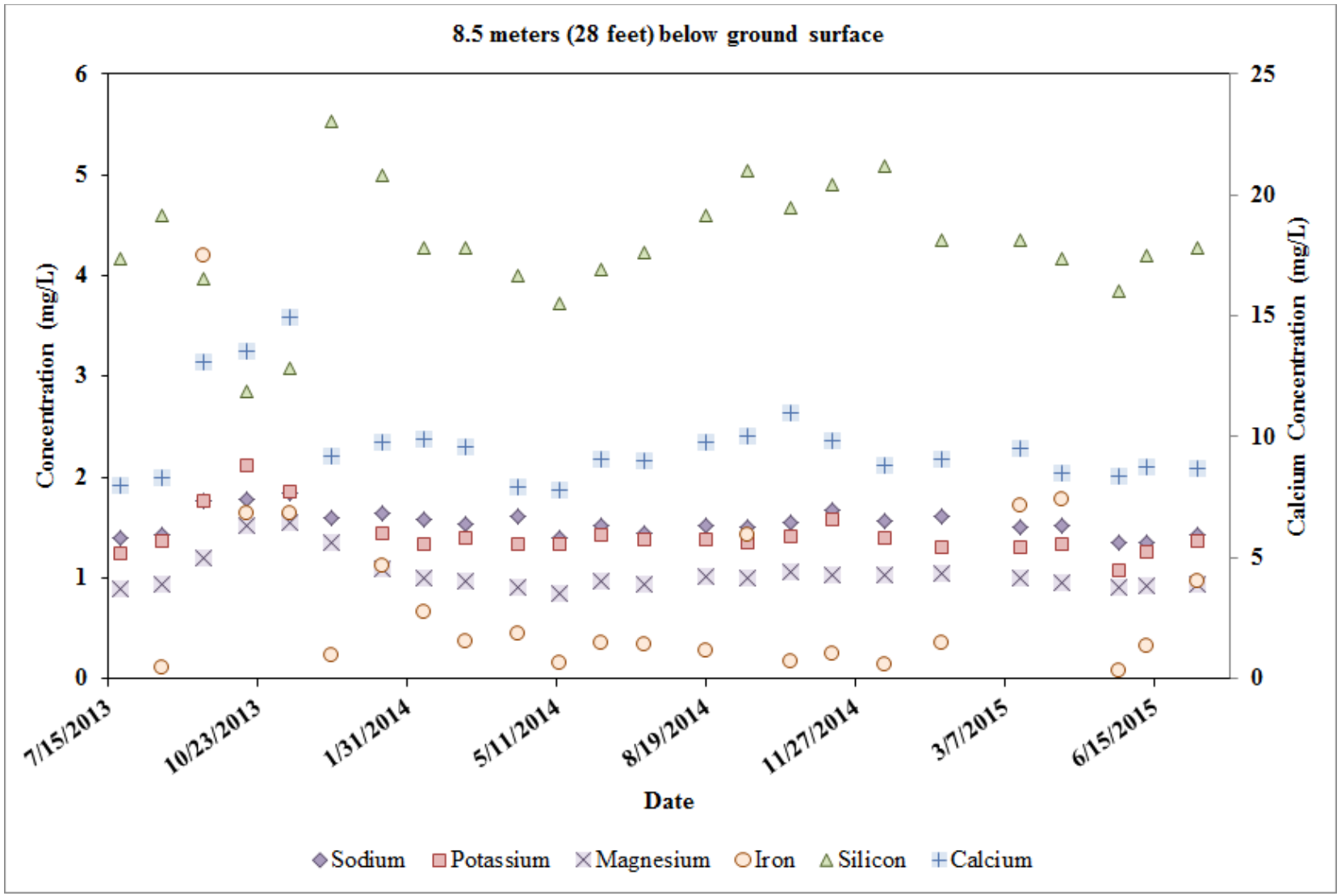

Figure 18: Monthly dissolved concentrations measured at discrete interval 8.5 meters (28 feet) bgs within open borehole Well MFS-1.

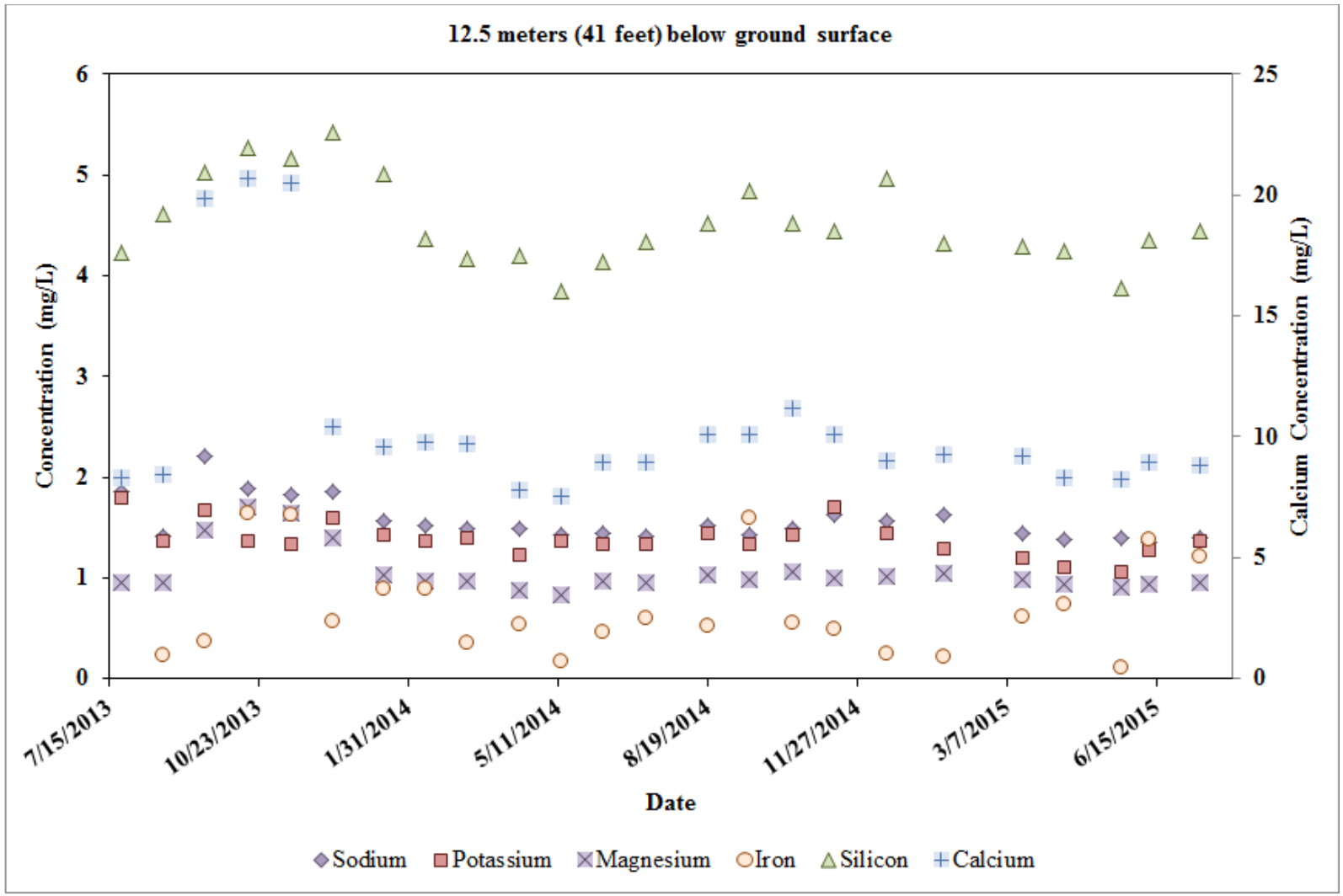

Figure 19: Monthly dissolved concentrations measured at discrete interval 12.5 meters (41 feet) bgs within open borehole Well MFS-1.

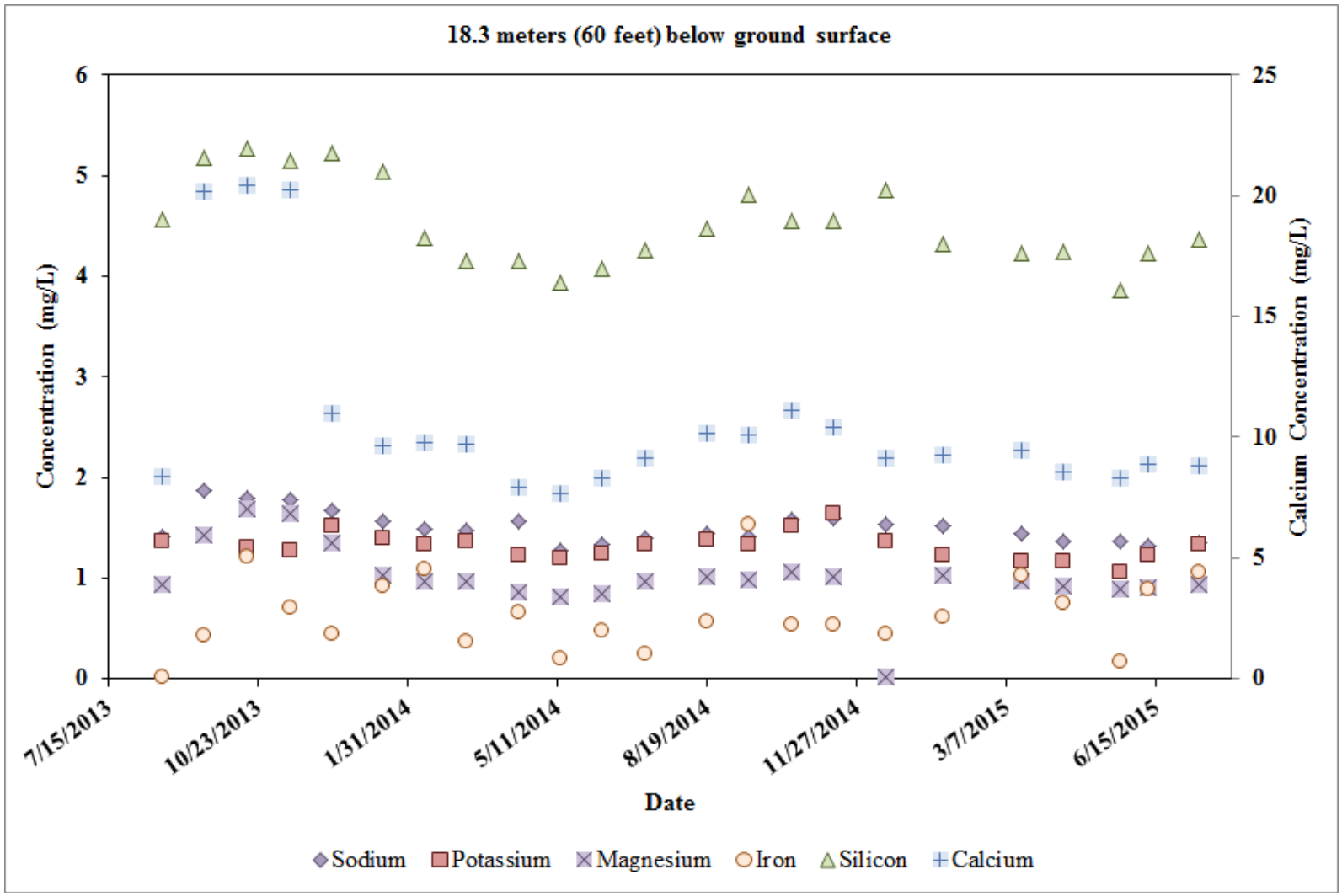

Figure 20: Monthly dissolved concentrations measured at discrete interval 18.3 meters (60 feet) bgs within open borehole Well MFS-1.

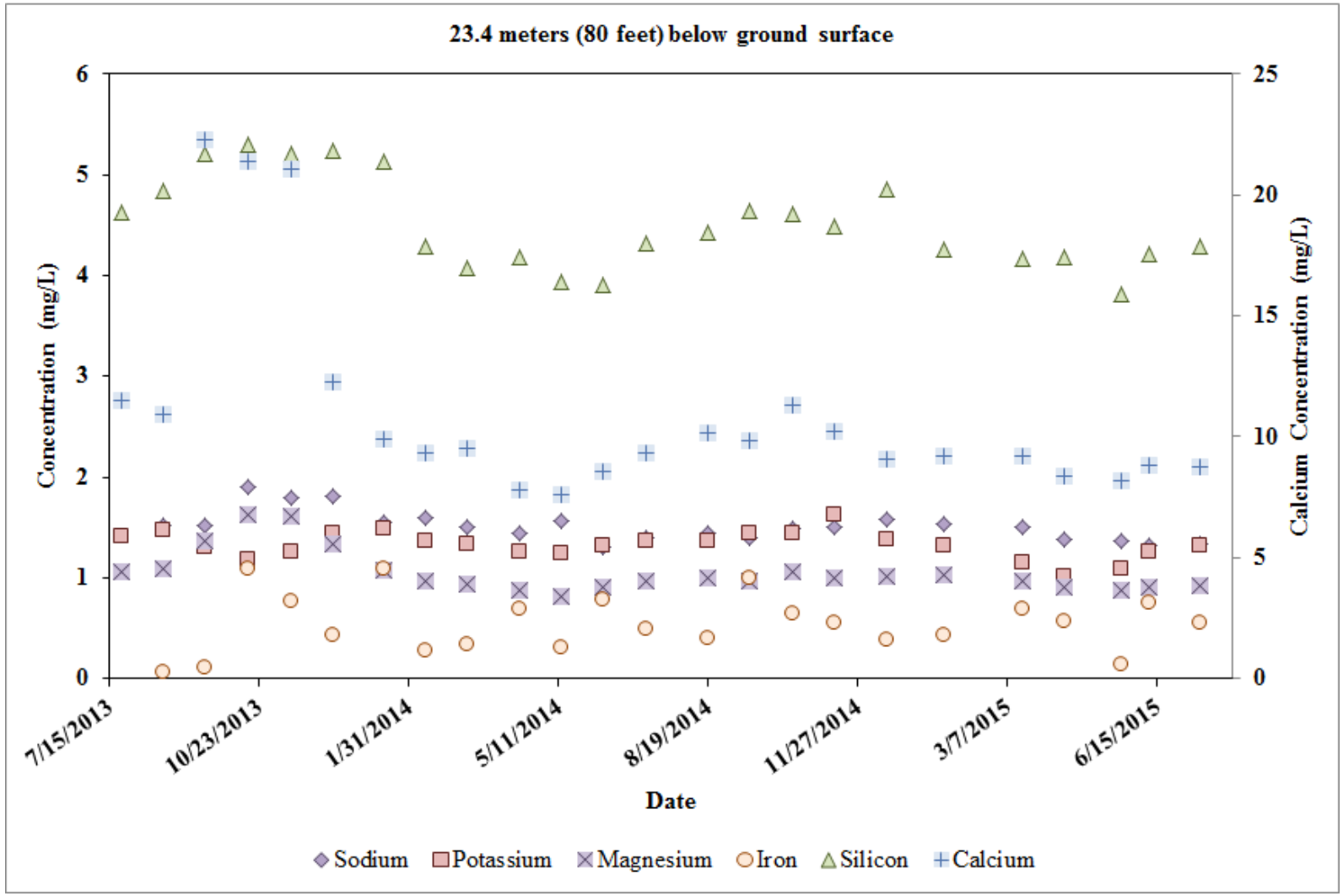

Figure 21: Monthly dissolved concentrations measured at discrete interval 23.4 meters (80 feet) bgs within open borehole Well MFS-1.

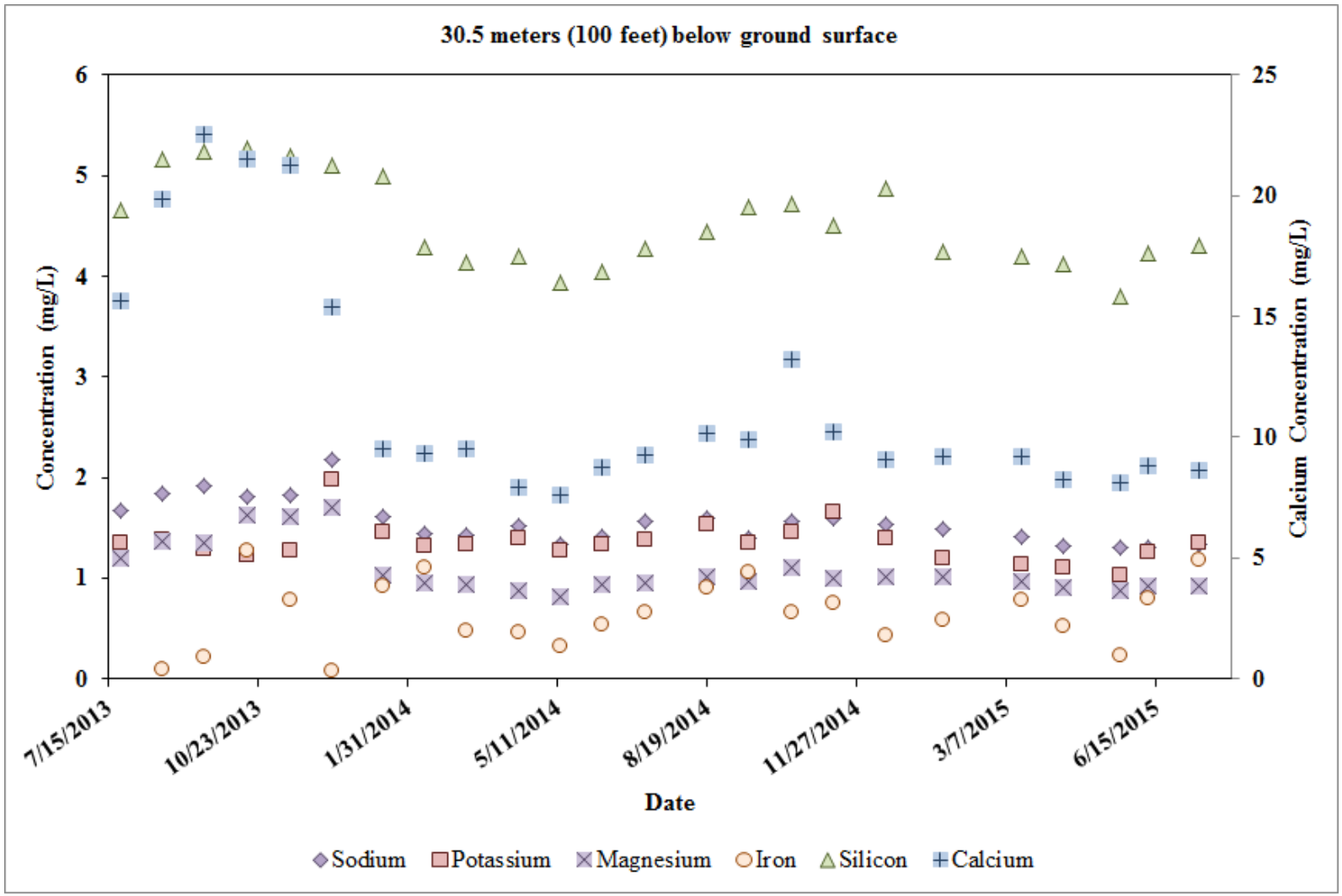

Figure 22: Monthly dissolved concentrations measured at discrete interval 30.5 meters (100 feet) bgs within open borehole Well MFS-1.

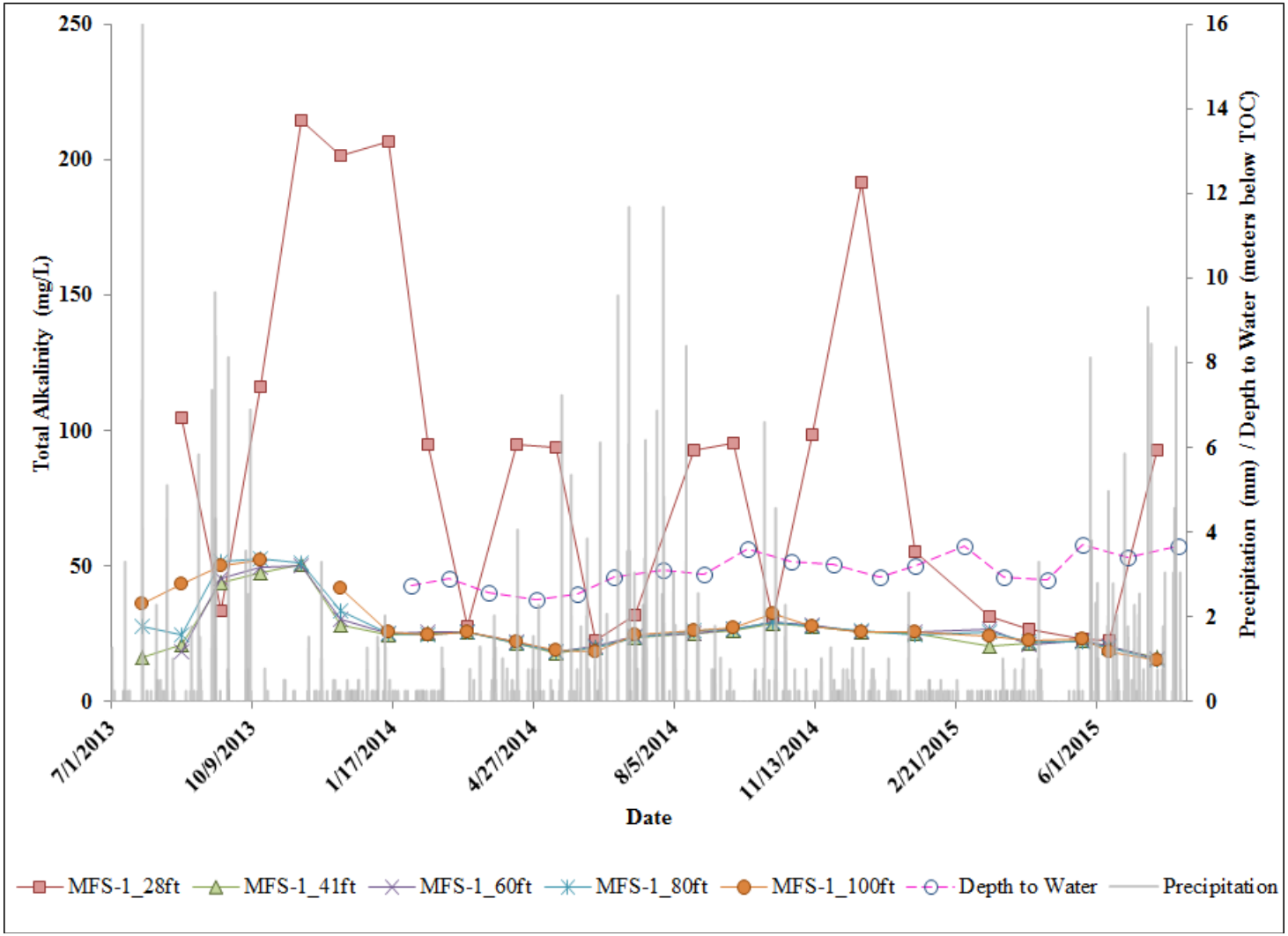

Figure 23: Total alkalinity and depth to water measured in Well MFS-1 compared with precipitation data from the MacLeish Field Station meteorological station.

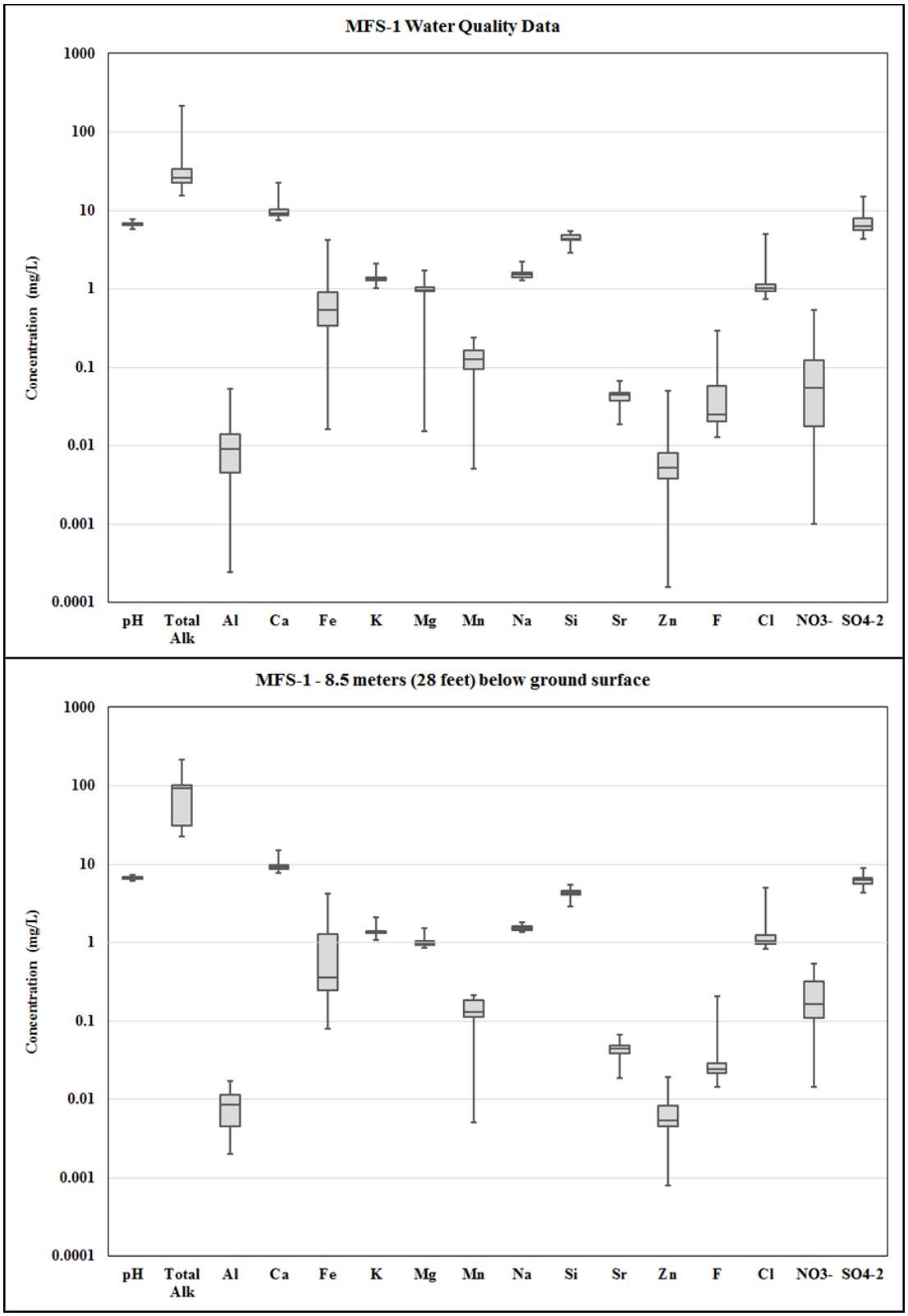

Figure 24: Box and whicker plots of the entire dataset collected from Well MFS-1 (combined dataset from all discrete interval samples collected) and the datasets collected at the five discrete intervals sampled along the water column.

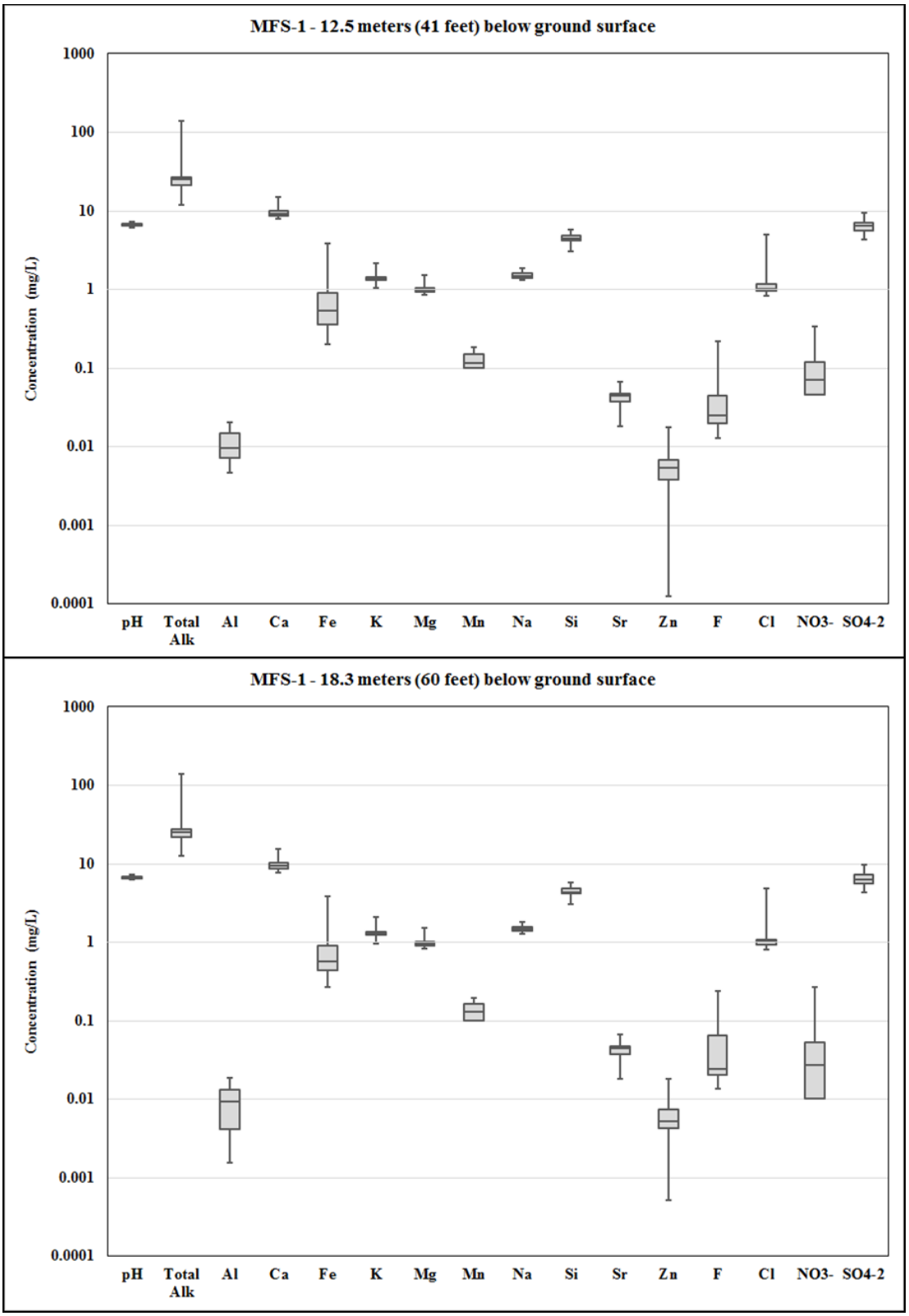

Figure 24 (continued): Box and whicker plots of the entire dataset collected from Well MFS-1 (combined dataset from all discrete interval samples collected) and the datasets collected at the five discrete intervals sampled along the water column.

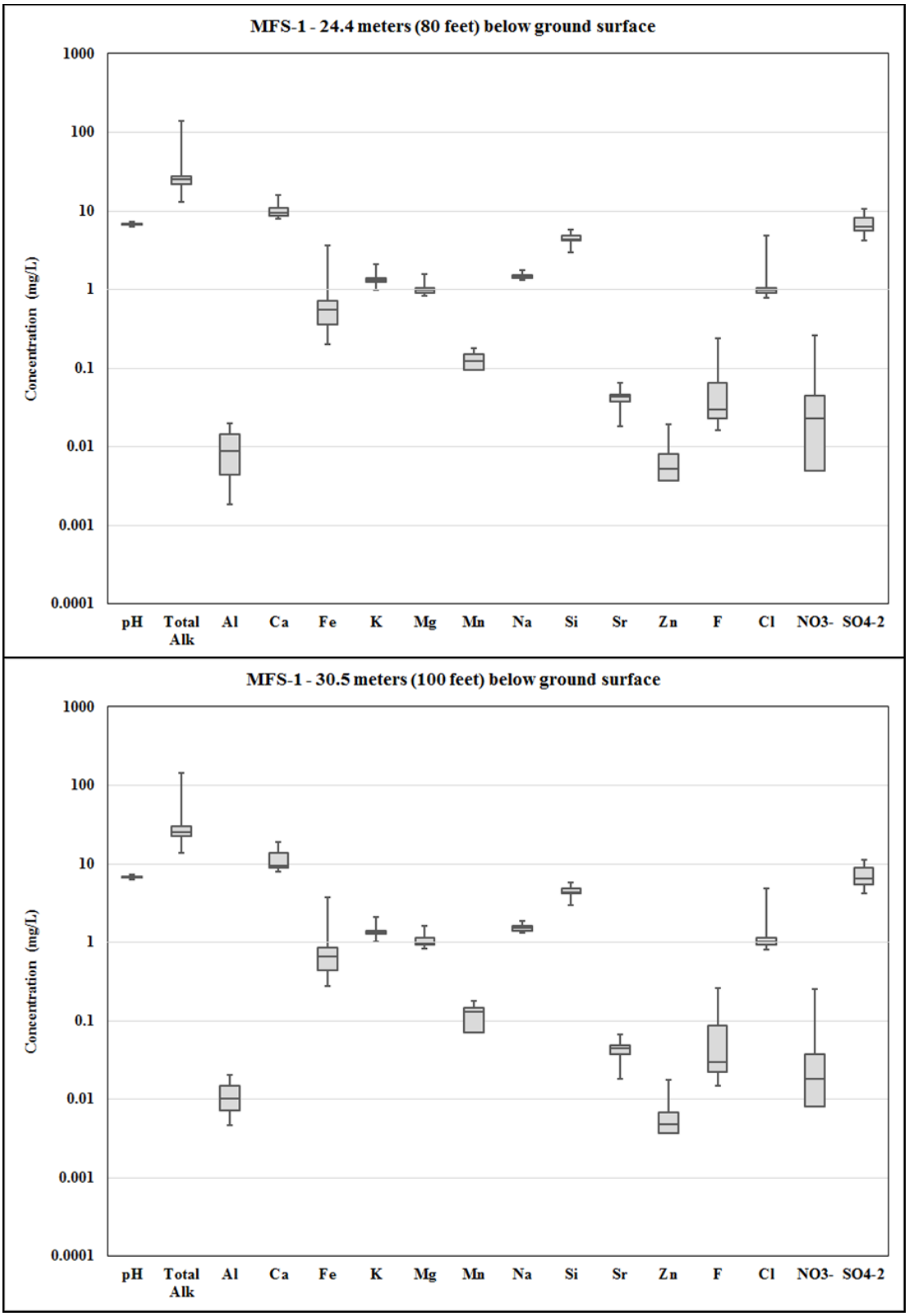

Figure 24 (continued): Box and whicker plots of the entire dataset collected from Well MFS-1 (combined dataset from all discrete interval samples collected) and the datasets collected at the five discrete intervals sampled along the water column.

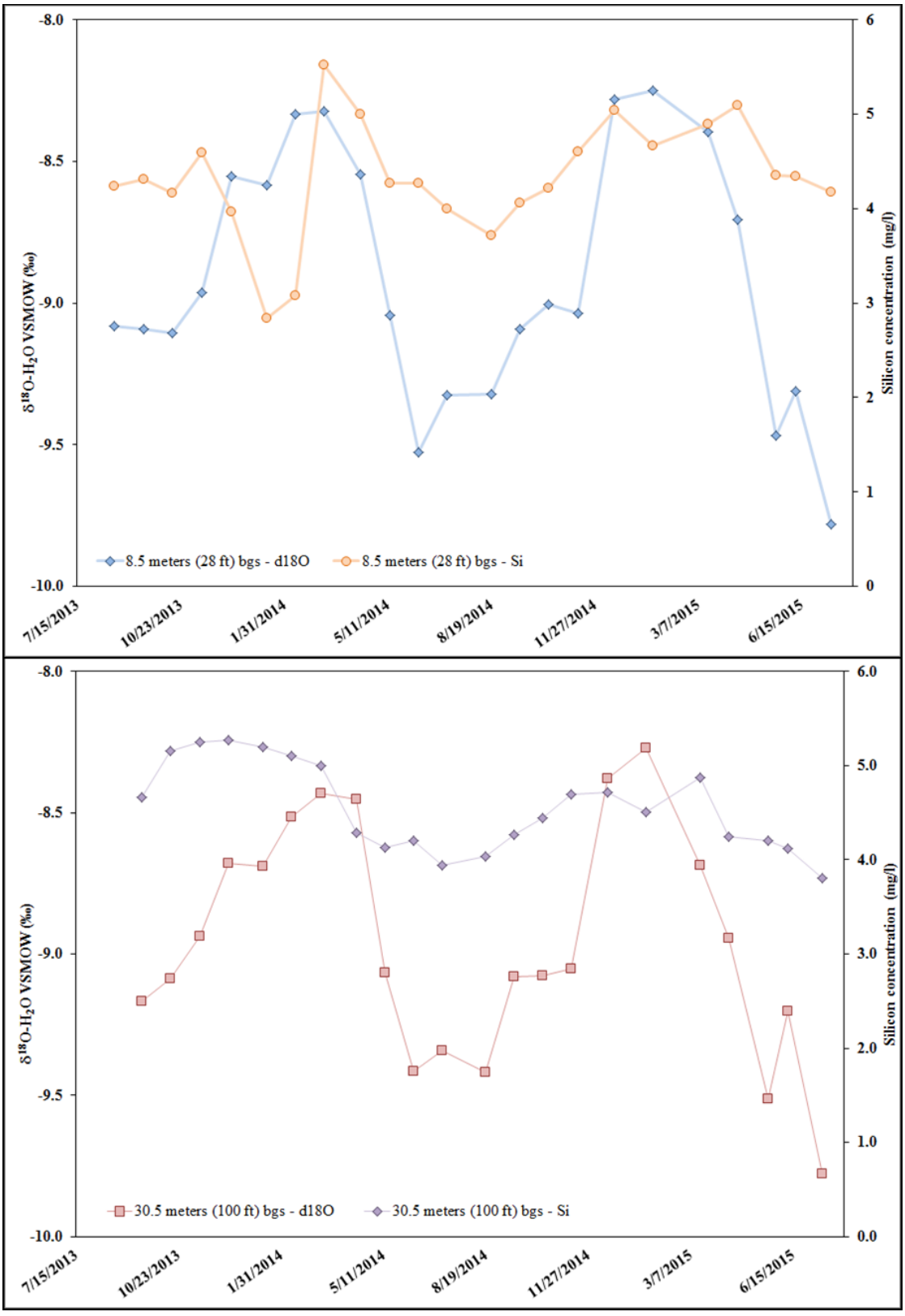

Figure 25: Silicon and $\delta^{18}O$-H_2O concentration time series plot showing the seasonal weathering response to changes in recharge.

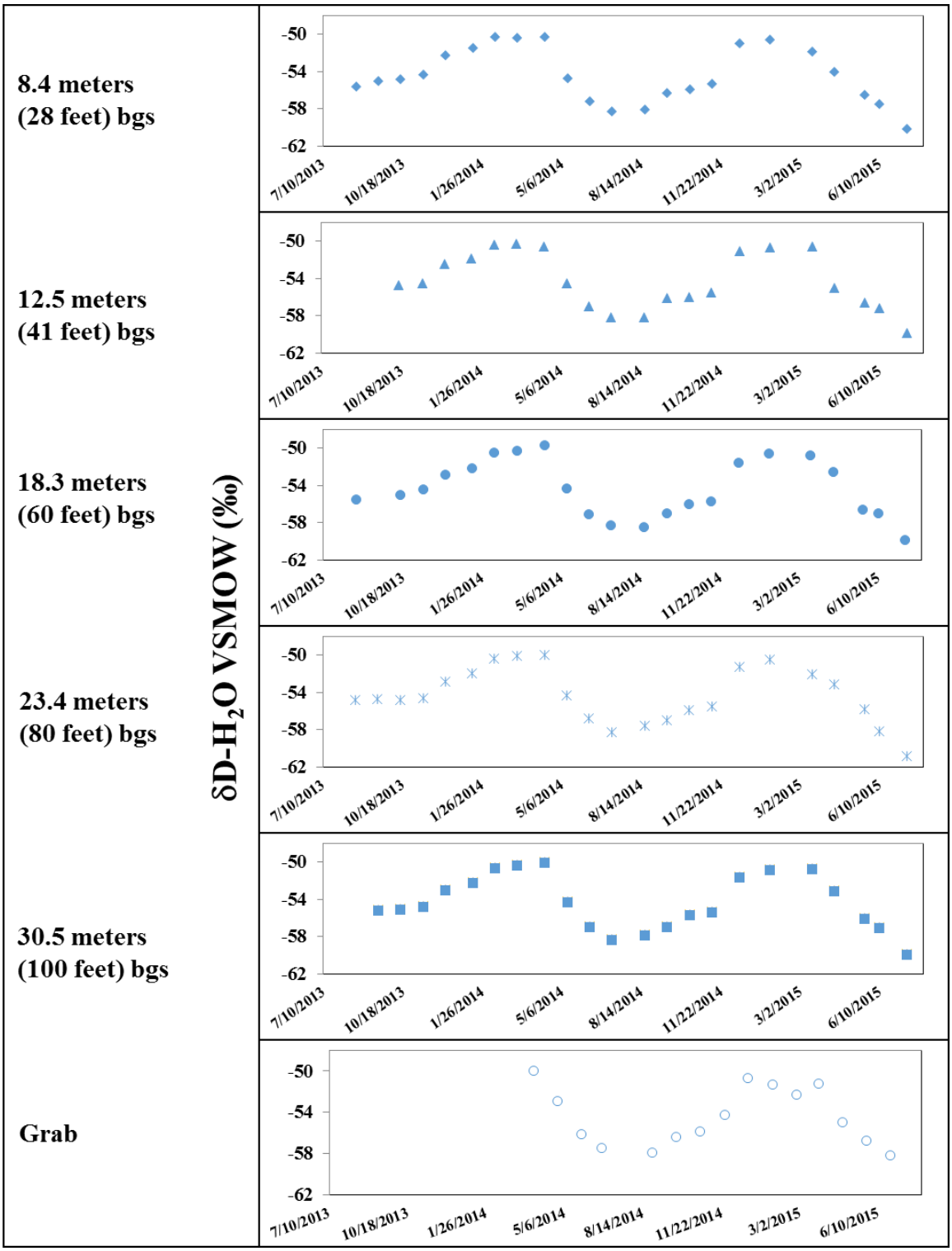

Figure 26: Monthly deuterium concentrations measured at discrete intervals within open borehole Well MFS-1. Also shown are the deuterium measurements from the USGS grab sampling and the average ambient temperature.

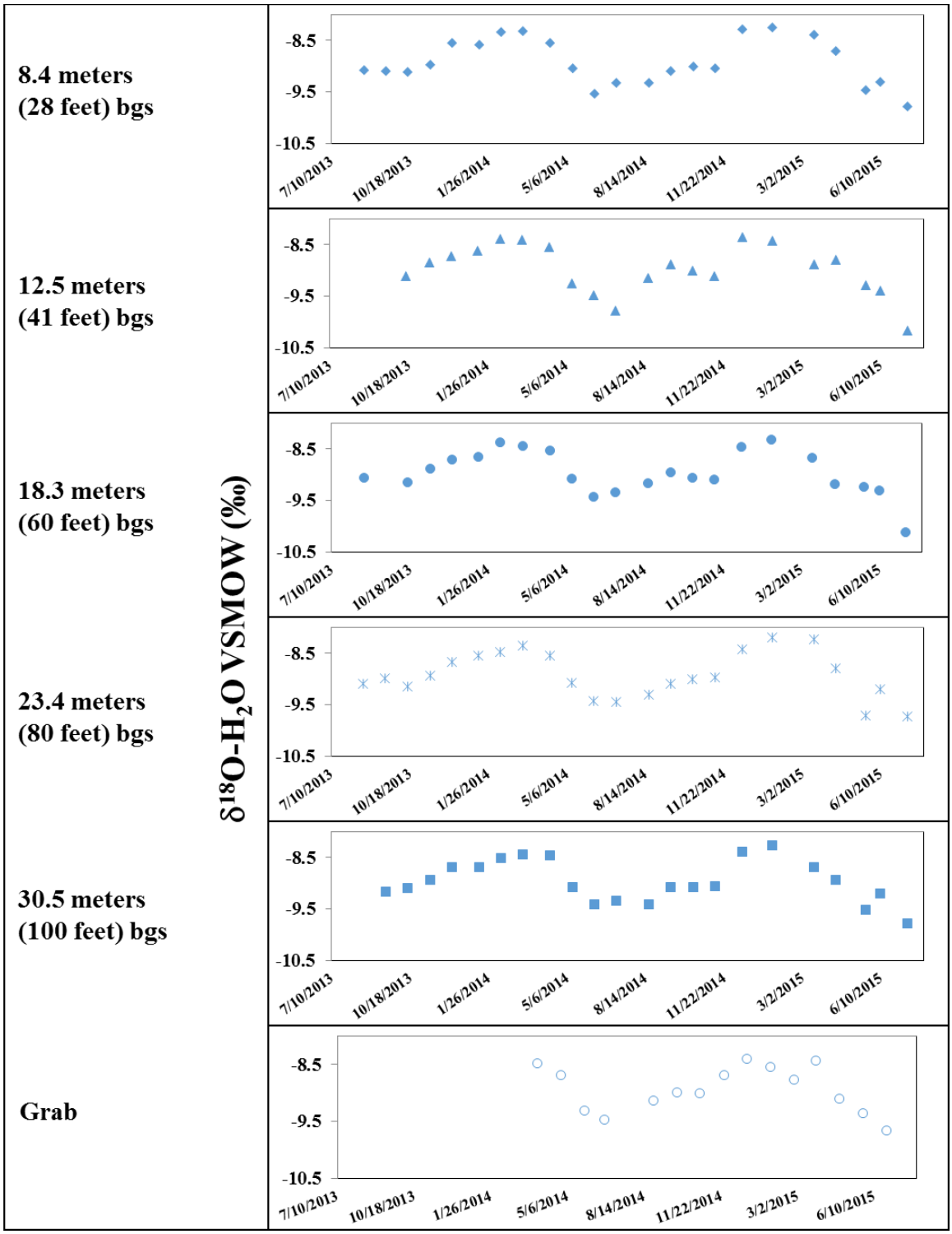

Figure 27: Monthly oxygen-18 concentrations measured at discrete intervals within open borehole Well MFS-1. Also shown are the deuterium measurements from the USGS grab sampling and the average ambient temperature.

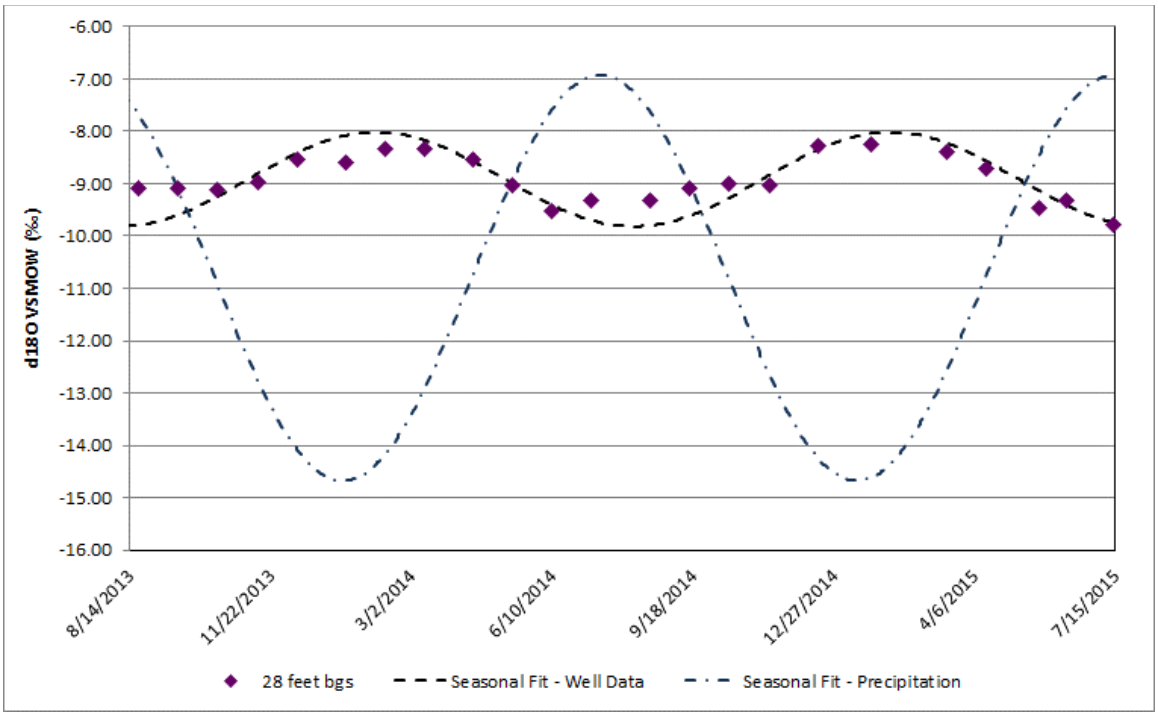

Figure 28: Monthly oxygen-18 concentrations measured in Well MFS-1 at 8.5 meters (28 feet) below ground surface fitted to the sine function representative of precipitation oxygen-18 values. Also provided is the sine function of the local precipitation.

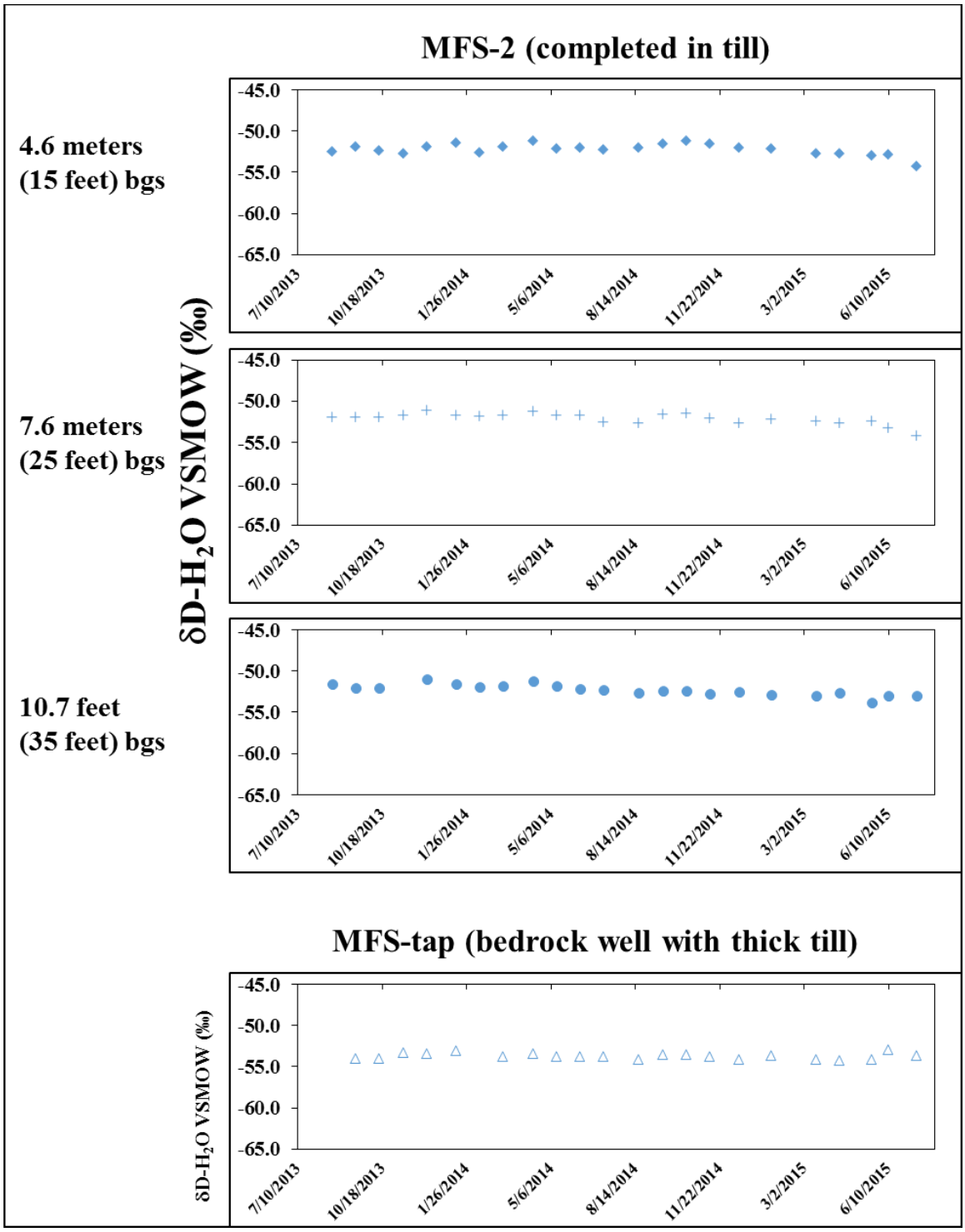

Figure 29: Monthly deuterium concentrations measured at discrete intervals within shallow till/bedrock contact Well MFS-2 and deep bedrock water supply well MFS-tap.

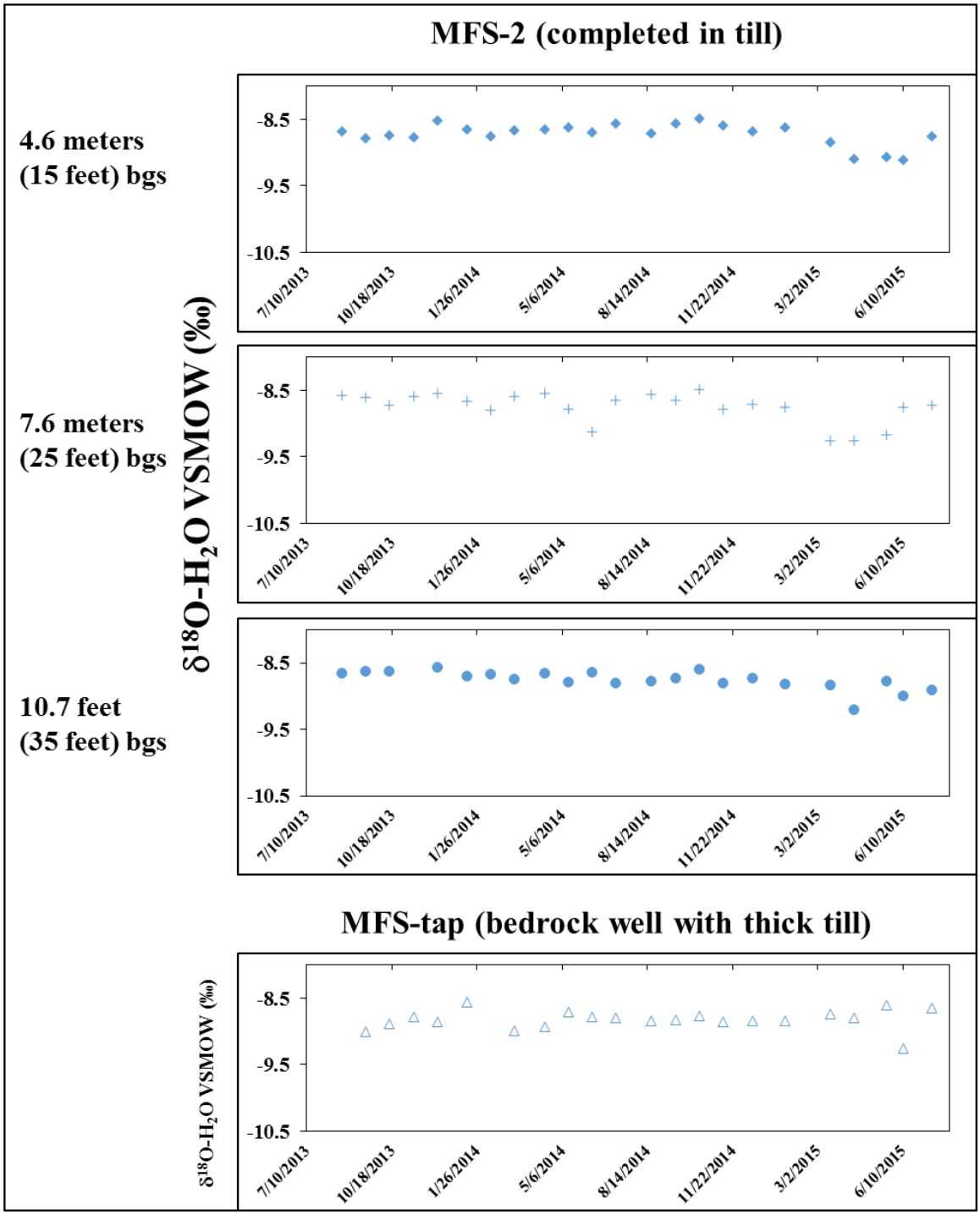

Figure 30: Monthly oxygen-18 concentrations measured at discrete intervals within shallow till/bedrock contact Well MFS-2 and deep bedrock water supply well MFS-tap.

CHAPTER 3

SIMULATION OF NATURAL WEATHERING REACTIONS AND WHAT IT CAN TELL US ABOUT RED STAINING AT THE SINGLE FRACTURE SCALE

One of the greatest challenges with understanding rock weathering and its influence on groundwater quality in New England is the young nature of the landscape. The most recent period of glaciation altered the landscape of New England and likely changed the hydrologic flow regime of the groundwater system as recently as within the last 10,000-20,000 years. This makes weathering and geochemical studies in New England unique from research being conducted in similar geologic settings further south along the Eastern United States (e.g., the Shale Hills Critical Zone Observatory, Blue Ridge Mountains, etc.), where a large saprolitic unit has formed. Beyond the maximum southern extent of the glacial advances the saprolitic unit overlying the bedrock can be used to understand the mechanisms and time associated with natural weathering; however, in glacially impacted environments such as New England, this saprolitic unit has been removed and replaced with a till deposit that may not be representative of local bedrock, so less information is available from the geology regarding natural rock weathering.

Weathering reactions within fractured bedrock aquifers are a function of the fluid residence time and flow within the fractures (Maher, 2010). Modeling has shown that the geochemical weathering reactions within individual fractures are controlled by residence time and concentration gradients, rather than reaction kinetics; the work of Maher (2010), Navarre-Sitchler et al. (2011), and Steffel et al. (2005) highlights the importance of residence time, rather than physical structure as a controlling mechanism of weathering reactions. The work of Pacheco and Alencoao (2006) shows that a predictable series of parent minerals and daughter minerals will be present along a flow path, suggesting that

identification of these mineral sequences may also be correlated to longer flow paths. In addition, the connectivity of the fractures within the aquifers may be able to be defined by identifying specific minerals or sequences of minerals along the flow path.

Groundwater in New England is also young, with water having been part of the groundwater system for less than 50 years since recharge (Flanagan et al., 2011). Through the amplitude attenuation method applied to the $\delta^{18}O$-H_2O data collected from Well MFS-1, the MRT of the water in this well is 0.7 years. Therefore, the time period considered relevant for weathering reactions and chemical transport in the NECRA is between 0 and 10,000 years. This range of ages represents the period of the current configuration of the hydrologic system in New England, and is expected to incorporate the likely water ages and water-rock interaction times represented by the bulk groundwater measurements from the NECRA. Based on saprolite formation rates measured in the Sierra Nevada Range (5.6 centimeters [cm]/1,000 years; Helgeson, 1969) and in the Southern Blue Ridge Mountains (3.8 cm/1,000 years; Velbel, 1985), approximately 30 cm (one foot) of saprolite or soil has be able to develop through natural weathering of the bedrock or till since the end of the last glacial period in New England. If the geologic setting and weathering rates in New England are analogous to those in the southern Blue Ridge Mountains, a saprolatization rate of approximately 3 cm/1,000 years is assumed to be representative.

Because the groundwater data collected from Well MFS-1 only represents one location along a crystalline rock aquifer flow path, geochemical and oxygen transport modeling is needed to better understand the specific mineralogy and weathering reactions controlling the groundwater quality. It can be impractical to collect data from field and laboratory measurements, so modeling is often relied on to provide insight into system

scale dynamics (Ogilvie et al., 2006). The modeling completed for this study simulates the diffusive and advective transport of oxygen along a single fracture and into the adjacent rock matrix and the mineral weathering reactions representative of the system based on inverse modeling using the groundwater data of MFS-1 and MFS-tap.

3.1 Inverse Modeling of the MacLeish Field Station Weathering Reactions

As presented on Figures 14 and 15, the dominant mineral groups weathering, based on the MFS-1 groundwater data, are carbonates and sulphides. Though the data does not show silicate weathering as a significant contributor, Berkley (1999) found anorthite dissolution is a representative reaction for surface waters near MFS-1. Using the water quality data from MFS-1 and MFS-tap, the computer code PHREEQC version 3.3.3 (Parkhurst and Appelo, 2015), a reaction path chemical equilibrium model supplied by the USGS, in combination with the Lawrence Livermore National Laboratory (LLNL) and PHREEQ thermodynamic databases, were used to perform inverse geochemical modeling. PHREEQC is able to simulate complex geochemical processes to produce the final chemical speciation of a system by accounting for dissolution and precipitation of solids to/from solution, the mixing chemistry of multiple waters (including between the active flow zone and a stagnant zone such as the rock matrix), and estimate the chemical make-up of the system over time. Each geochemical model has its advantages and disadvantages. Other models specialize in particular aspects of a chemical system, such as ion-exchange, surface complexation, advection, and dispersion, but PHREEQC is capable of simulating each of these in the same solver, which has been validate and verified by the USGS and through many years of application to a broad range of geochemical problems: inverse geochemical modeling, using PHREEQC, has been applied to studies focused on solute transport in fractured rock (Dai, 2006; Lipson et al., 2007), chemical reactions controlling

water chemistry (Ledesma-Ruiz et al., 2015; Acero et al., 2015), the chemical evolution of water (Tallini et al., 2014; Saravanan et al., 2015; Sharif et al., 2008; Soumya et al., 2011). Sharif et al. (2008) also noted more than ten other studies utilizing geochemical inverse modeling to develop an understanding of how groundwater chemically evolves as it is transported through the aquifer.

Inverse modeling using PHREEQC can determine the most likely mineral reactions based on two water samples located along the same flow path. The modeling code assumes that the first water sample mixes with other solutions and reacts with the minerals to produce a solution that has the composition of the second water sample (Parkhurst and Appelo, 2015). The approach used by the PHREEQC code is based on the mole-balance approach (Plummer and Back, 1980), which has been used in other geochemical modeling software (Parkhurst et al., 1982; Plummer et al., 1991; Plummer et al., 1994). The method utilized by the PHREEQC software expands on the previous inverse modeling methods of other geochemical models by introducing additional mole-balance equations for consideration of mechanisms such as evaporation, dilution, isotopic speciation, etc. and consideration of uncertainties in the water quality data (Parkhurst and Appelo, 2015). The mole-balance equation solved by PHREEQC is:

$$\sum_{q}^{Q} c_q \alpha_q (T_{m,q} + \delta_{m,q}) + \sum_{p}^{P} c_{m,p} \alpha_p + \sum_{r}^{R} c_{m,r} \alpha_r = 0 \quad (8)$$

where, Q is the number of aqueous solutions in the model, q represents the aqueous solution, m represents the element valence state, T is the total moles of each element, δ is the uncertainty term (can be positive or negative), c is the coefficient of master species, α is the mixing fraction or mole transfer coefficient, P is the total number of reactive phases,

and R is the total number of redox reactions (Parkhurst and Appelo, 2015). This formulation of the mole-balance equation considers uncertainty and redox reactions for all defined elements and valance states; previous inverse geochemical models did not include an uncertainty term that accounts for the charge imbalance of the water solutions used as the simulation basis.

For this study, the data from MFS-1 and MFS-tap were used as the two representative water samples. For the purposes of this modeling, it was assumed that the MFS-1 water would evolve to the MFS-tap water due to water-rock interactions in the aquifer. There is insufficient data available to confirm that these two wells are on the same flow path, but the two wells are in the same geologic unit and in close proximity. Evaluation of the groundwater data collected shows that the water from MFS-tap is more evolved and has a longer residence time than MFS-1 (see Chapter 2). The groundwater data has the same suite of chemical parameters available from each location over the same period of time. The data from MFS-1 is an average of the data collected from the 8.5 meter (28 feet) bgs discrete interval sample over the period of testing. As discussed in Chapter 2, this fracture and sampling location within MFS-1 represents the hydraulically active zone of the well, where the water is most representative of expected natural groundwater chemistry at this location along the flow path. A second solution representing MFS-1 was developed using the average of all samples collected during the second year of sampling. Focusing specifically on the second year of groundwater data removes the chemical changes that occurred due to the system perturbation related to lime addition and averaging the data from each of the discrete interval depths provides a chemistry representative of the entire water column. The MFS-tap data used in the inverse model is the average of all

measurements from this well over the testing period. In addition to the two water samples, an initial set of minerals must be selected, from which the model will try to resolve the chemistry evolution through changes in moles of each element due to precipitation or dissolution reactions (Table 4). The initial minerals included were selected because of being identified in the core samples, as in the case of biotite and muscovite, or because the speciation of the water solution within PHREEQC showed the mineral was at or above saturation (Sharif et al., 2008; Tallini et al., 2014; Ledesma-Ruiz, 2015).

The two databases used for this modeling contain difference minerals and were utilized to consider a broader range of potential reactions. The model using the PHREEQ database includes albite, anorthite, calcite, dolomite, chlorite, kaolinite, pyrite, siderite, quartz, gibbsite, and goethite. The PHREEQ database does not include any muscovite or biotite minerals, which are present throughout the MFS-1 core. The LLNL database includes these minerals, so it was also used for the inverse modeling, with the initial minerals albite, anorthite, calcite, dolomite, kaolinite, pyrite, siderite, quartz, gibbsite, goethite, muscovite, and phlogopite were selected. The LLNL database does not include chlorite, which is part of the PHREEQ database and is expected to be a secondary mineral of the system. The minerals modeled and their chemical formulas are provided in Table 4. Oxygen and carbon dioxide are also included in the inverse model calculations to provide a better understanding of the dissolution or consumption of these weathering agents and how this and the mineralogy relate to red staining.

3.2 Simulation of Oxygen Flow through a Single Fracture

Both oxygen and carbon dioxide can play important roles in mineral weathering, and the presence of red staining can be interpreted as oxygen being transported with the water, if it is assumed to be iron oxide sourced by current flows. However, many mineral

weathering reactions are oxygen consuming (e.g., Reactions 1), which can be an important factor in weathering reactions (Stumm and Morgan, 1996) and the source of dissolved oxygen in water recharging the aquifer. The presence of red staining on fracture surfaces, if assumed to be iron oxide, could support the conclusion that dissolved oxygen in groundwater is driving the oxidation reactions of iron present in the rock or that iron oxide is being precipitated on the fracture surface. The groundwater data discussed in Chapter 2 shows that the iron being transported along the fracture is limited in free oxygen until encountering an air-water interface, such as the well or oxygenated water in the diffusion samplers, and that iron oxide is not likely precipitated on the fracture surfaces due to the water transport currently occurring. Therefore, in addition to the inverse geochemical modeling, oxygen transport along a single fracture in a saturated crystalline bedrock system was simulated.

The software used to investigate diffusion controlled oxygen fate and transport is VADOSE/W, a variably saturated finite-element modeling platform developed by Geo-Slope International (Geo-Slope, 2014). This software can consider flow of water in both the saturated and unsaturated zones, while also considering diffusion controlled heat and oxygen transport; heat transport was not simulated in this model. VADOSE/W has been widely applied to study oxygen transport for acid rock drainage problems in the mining industry, through the investigation of oxygen diffusion and consumption through closure covers (Demers et al., 2009; Song and Yanful, 2011) and ground-atmosphere interactions (Rajeev et al., 2012), but there is limited application to saturated zone transport problems because it is often assumed that the primary transport mechanism will be from air phase oxygen to free oxygen in solution (Binning et al., 2007; Kim and Benson, 2004), which

does not occur in the saturated zone. The governing equation solved by VADOSE/W is a modified form of Fick's second law as derived for a one-dimensional domain (Geo-Slope, 2014; Mbonimpa et al., 2003):

$$\frac{\partial}{\partial t}(\theta_{eq} C) = \frac{\partial}{\partial y}\left(D_{eff}\frac{\partial C}{\partial y}\right) - K_r C \tag{9}$$

where, C is the concentration of oxygen in pores, θ_{eq} is the equivalent diffusion porosity defined as (θ_a + H θ_w), θ_a is the volumetric air content, θ_w is the volumetric water content, H is the dimensionless form of Henry's equilibrium constant, D_{eff} is the effective diffusion coefficient, and K_r is the effective reaction rate coefficient. It should be noted that this equation does not include an advective transport term, and as with most oxygen transport models it assumes that oxygen transport in the subsurface is driven by diffusion (Binning et al., 2007; Kim and Benson, 2004). Oxygen has limited solubility in water, with average dissolved oxygen concentrations of 10 mg/l for water in equilibrium with atmospheric levels of oxygen (Drever, 2002).

As discussed in Chapter 2, the presence of organic matter or mineral weathering reactions can quickly consume this small amount of oxygen to low levels within a few meters of the recharge zone (Krauskopf, 1967; Deutsch, 1997; Sidborn et al., 2010). Kim and Benson (2004) found that advective transport of free oxygen in solution represents as little as 1% of the oxygen transport in an unsaturated system. Binning et al. (2007) found advective transport to be a more significant contributor to oxygen in an unsaturated system, representing approximately 23% of the total flux of oxygen, but still was not a dominant source of oxygen. The advective transport modeling built on the water transport and oxygen diffusion modeling by using CTRAN/W (Geo-Slope, 2012), another software code within the GeoStudio package. This allowed the same model geometry and parameters to

be applied to both transport mechanisms. Additionally, the fluid transport simulated in VADOSE/W is used as the basis for the advective transport simulated with CTRAN/W. For this study, diffusion and advective oxygen transport were simulated assuming no retardation or consumption along the single fracture transport pathway to estimate the range of transport distances that can be represented by these end member transport mechanisms (diffusion and advection). The governing equation for the advective transport modeling is the basic advection-dispersion equation (Geo-slope, 2012):

$$\frac{\partial C}{\partial t} = D \frac{\partial^2 C}{\partial x^2} - v \frac{\partial C}{\partial x} \tag{10}$$

where, D is the hydrodynamic dispersion coefficient, C is the concentration, and v is the average linear velocity, as calculated in VADOSE/W.

The size of the model domain simulated is 1,000 meters in the lateral direction and 150 meters in the vertical direction (Figure 31). Three finite element regions were assigned to represent two zones of competent bedrock over- and underlying a single, hydraulically active fracture. The boundary conditions used in this modeling are total fluxes to represent the flow of water and oxygen into the hydraulically active fracture, initial water table at an elevation of 150 meters to simulate saturated conditions within the competent bedrock and hydraulically active fracture, heads assigned at 150 meters on left side of model and 149 meters on the right side to simulate a groundwater gradient of 0.001 meters per meter (m/m) across the model domain, and a temperature profile to simulate the groundwater at 12°C throughout the entire model domain. The diffusion controlled oxygen transport can be simulated as a concentration or a gas flux applied as a model boundary condition. The goal of this modeling is to investigate the transport of oxygen through a single fracture, so an

oxygen flux was used and assigned to the entrance of the fracture (the left side of the model), as well as along the first ten meters of the fracture to ensure simulation of the transport of oxygen into the rock matrix adjacent to the fracture. The model was run in a forward predictive mode to simulate the change in oxygen concentration along the fracture and into the competent rock, over the simulated model periods.

The hydraulic conductivity used to represent the competent rock is 2×10^{-10} meters per second, which is a representative value for an unfractured igneous or metamorphic rock (Domenico and Schwartz, 1990). The hydraulic conductivity for the hydraulically active fracture was calculated from the MRT for Well MFS-1 (Chapter 2). The exact location of the entrance to the hydraulically active fracture is not known, but based on the system response to the lime addition in the western field at the MacLeish Field Station, the location is near the central portion of this field. Using this assumed location, the estimated travel distance along the fracture intersecting Well MFS-1 is between 15 and 30 meters (50 and 100 feet) and the calculated MRT is 243 days, which gives a range of hydraulic conductivities between 7.2×10^{-7} meters per second and 1.4×10^{-6} meters per second. An average value of 1.1×10^{-6} meters per second was used in this modeling, which is in the range of conductivities for fractured rock (Domenico and Schwartz, 1990). An effective porosity of 1.5% was assigned to the competent bedrock regions and a porosity of 30% was assigned to the hydraulically active fracture which has an aperture of one centimeter. For the advective transport model, a dispersion coefficient of 100 meters was used. Dispersion coefficients are typically in the range of 0.1 to 100 meters and are related to the scale of the problem being simulated, with 0.1 meters representing a laboratory scale system and 100 meters representing an aquifer scale system (Geo-Slope, 2012). Multiple

simulation periods were used to evaluate the changes in oxygen transport under different residence times. The simulations were run for the periods of one day, ten days, 100 days and ten years.

The model setup described above represents the conditions of the MacLeish Field Station, which is consistent with values representative of fractured and competent crystalline rock. But to understand the oxygen transport across the broader range of conditions that could be encountered in a crystalline rock aquifer, a series of sensitivity analysis models were also run. These models adjusted one parameter at a time to determine which parameters the model is most sensitive to, and to understand the changes in the oxygen transport across the range of values representative of crystalline rock. Table 5 presents a summary of the parameters adjusted and tested as part of the sensitivity analysis. The sensitivity analysis models utilized the ten year simulation period for each of the model runs.

3.3 Results and Discussion

3.3.1 Potential Weathering Reactions Controlling the Evolution of Groundwater at the MacLeish Field Station

There are several assumptions that are inherent to inverse geochemical modeling: the two groundwater solutions represent the same flow path, dispersion and diffusion are not significant transport mechanisms, weathering reactions have reached steady state in the system, and the initial mineral phases provided to the model are present in the aquifer (Zhu and Anderson, 2002). For this study, it was assumed that the two solutions represent waters on the same flow path, but this could not be confirmed with the data collected and reviewed for this study. Because the solutions may not represent a single flow path, this could result in mineral weathering reactions being simulated that are not necessarily representative of

the system. It also cannot be confirmed that diffusion and dispersion of not significant contributors to fluid transport, but because the inverse modeling is being applied to simulate flow along fractures, it is reasonable to assume that advection is the primary transport mechanism. As described earlier in this chapter, the current hydrologic and thus weathering system have only been in the current configuration for approximately 10,000 years, but based on weathering rates in similar systems, this should be a sufficient amount of time to develop a steady state condition. The initial mineralogy assigned to the inverse simulations provides a starting point for the model to calculate the combinations of minerals that could cause the evolution of the water represented by the two entered solutions, but also serves to constrain the model results, along with the assigned error tolerance (Sharif et al., 2008).

The initial solutions representing the two waters being evaluated were first speciated in PHREEQC to determine the mass balance of the solutions and to evaluate the saturation indices. The two databases calculated similar mass balances for the two solutions (15.6% error for MFS-1 water and -0.1% error for MFS-tap). The sample from MFS-1 has a higher mass balance error than the water from MFS-tap, which could be related to depth of the water in the well. MFS-tap is a much deeper well and the construction appears to be such that it is not open to atmospheric conditions, leading to a more stable redox state. The Well MFS-1 has a more variable redox state due to its shallow depth and the degree of mixing that is occurring within the well based on the groundwater data discussed in Chapter 2. A second solution was considered for Well MFS-1 that only used the data from the second year of testing. This data is less variable and resulted in a slightly lower mass balance error of 9.2%. The saturation indices calculated from the two solutions show that

aluminum oxide, iron oxide, and potassium silicates are the minerals that are at or over saturation, so these were the initial minerals selected for the inverse modeling.

During the model simulations, the model adjusts the mineralogy, dissolution, and precipitation and reports the resulting combinations. The PHREEQ database simulations result in 289 models (combinations of weathering reactions), 70 of which contain the minimum mineralogy needed for the provided water chemistry, highlighting that the results are not unique. Thirteen of the models resulted in a maximum error of 2% and a sum of residuals of 0.09, the lowest error of the simulations, and were therefore considered to be valid (Table 6). Ledesma-Ruiz et al. (2015) noted the issue of non-unique results and that changing the initial minerals used or a different the model, can result in different combinations of weathering reactions. The LLNL database models found 465 models and 84 with the minimum mineralogy. Three of the models from this simulation were considered valid based on the lowest error (9%) and sum of residuals (0.21) (Table 7). The sum of residuals resulting from the LLNL model is higher than the PHREEQ model.

Simulations with both databases found that small amounts of albite, pyrite, and goethite dissolution and siderite precipitation are occurring. The 16 models considered to be valid from both databases based on the lowest resulting error, showed variable weathering reaction possibilities for the other minerals. The majority of the PHREEQ models were dominated by quartz and gibbsite dissolution with either anorthite or dolomite precipitation. If anorthite is being precipitated, carbon dioxide is generated. Five of the models simulated kaolinite precipitation with carbon dioxide consumption. The LLNL models were less consistent in the representation of mineral weathering. The first model shown on Table 7 shows that quartz and gibbsite dissolution are the dominant reactions,

along with kaolinite precipitation and carbon dioxide consumption, consistent with the PHREEQ database models. However, the second and third model show calcite, gibbsite, and phlogopite dissolution are dominant reactions and the source of carbon dioxide consumption, with dolomite and muscovite precipitating. Phlogopite (biotite group mineral) and muscovite are important minerals in the Waits River-Gile Mountain Province, and are not part of the PHREEQ database, so the second model from the LLNL simulation is considered to be the best representation of the mineralogy at the MacLeish Field Station, but the reactions are not realistic under typical groundwater conditions.

One of the challenges in developing an inverse model, is that not all of the system processes are not being evaluated. The inverse modeling using PHREEQC is heavily dependent on the thermodynamic database being used with the modeling code. Because inverse modeling is not considering a flow path or water-rock contact time for the weathering reactions, the results of the simulations are based on the data in the thermodynamic database. The inverse modeling was rerun using the second water solution from MFS-1 that did not include the alkalinity perturbation, but this did not result in a change in the dominant reactions being identified. Adjustments to the acceptable model error and a setting that allows the minerals to provide or consume water during the reactions was also tested to obtain a more constrained and realistic set of weathering reactions. However, these changes resulted in more non-unique combinations and an increase in the overall error of the solutions. Because the assumptions inherent to this type of model could not be precisely applied to this dataset, there are some inconsistencies between the weathering reactions being simulated and those that are likely to occur in a shallow groundwater system that cannot be resolved.

3.3.2 Oxygen Transport through a Single Fracture – Is There Sufficient Oxygen Transport to Support Oxide Formation?

The mineralogy determined to be present and reactions controlling the groundwater samples collected as part of this study would be expected to consume oxygen. Evidence from the groundwater testing (iron and manganese concentrations in groundwater and the iron precipitation occurring in the well) shows that the system is limited in free oxygen, so the simulation of oxygen transport was expected to show limited transport along the fracture. The boundary conditions assigned to the model established a groundwater flow regime that is saturated throughout the majority of the model domain and that has a direction of flow from left to right (Figure 32). The hydraulically active fracture is simulated with a one centimeter aperture, but only an effective porosity of 30% to account for fracture surface roughness rather than simulating the flow as if it were through a pipe. The flow of water into the hydraulically active fracture also includes the flow of oxygen (one gram per cubic meter [g/m^3]), which transports the oxygen into the model domain. An oxygen flux is also assigned to the fracture surface for the first ten meters beyond the fracture entrance to ensure simulation of the flow of oxygen into the competent rock region of the model, representing matrix diffusion.

The results of the oxygen diffusion transport modeling are represented by the color profile shown on Figures 33 and 34, where blue represents zero oxygen and red is the highest concentrations. Each of the baseline models using the parameters representative of the MacLeish Field station, but simulated for different transport times are presented on Figure 33, and the results from just the one day model and ten year model are presented on Figure 34. The majority of the model domain, including both the competent rock and the hydraulically active fracture, has a resulting oxygen concentration of zero (blue color). The

model simulating a period of one day resulted in oxygen diffusion 1.3 meters beyond the oxygen source (11.3 meters from the fracture entrance) in the direction of flow along the fracture and 1.6 meters into the rock matrix, though the concentration decreases rapidly away from the hydraulically active fracture. Extending the period of simulation to ten years only resulted in slightly greater distances of transport, 1.8 meters beyond the oxygen source along the fracture and approximately two meters into the competent rock. A 100 year simulation period model showed only minimal additional oxygen transport distance beyond that simulated in the ten year model though the flux at the leading edge of the oxygen plume increases with time.

The velocity of the water transporting the oxygen was set equivalent to the hydraulic conductivity of the hydraulically active fracture and no consumption or retardation was included to ensure as much advective oxygen transport as possible. While the diffusion transport of oxygen represents the shortest possible transport distances that would be expected, the advective transport models are intended to simulate the maximum transport distance along the fracture length. Figure 35 presents the results of the advective transport model for each of the baseline models. After one day, the oxygen is transported only transported slightly more than five meters, which is within the zone of the boundary condition and may not be representative of actual transport along the fracture. By ten days, the oxygen has transported a total of 27 meters along the fracture length, or 17 meters beyond the extent of the oxygen flux model boundary conditions. The transport distance continues to increase over the 100 day and ten years models, showing a transport distance of greater than 500 meters is possible over a ten year period (Figure 35).

The sensitivity analysis focused on the diffusion transport model and the results showed similar conditions to the baseline model. Oxygen transport was limited to a short distance past the application of the flux boundary condition. The baseline model resulted in the shortest transport distance, while the modeling using high hydraulic conductivity of the fracture resulted in the longest transport distance. However, regardless of the model scenario simulated, the transport distance beyond the boundary condition location was generally less than two meters due to diffusion transport, confirming that oxygen transport could be limited to the zone of recharge where oxygen water is entering the system if diffusion is the primary transport mechanism for oxygen. The flux rate of oxygen at the leading edge of the plume did show sensitivity to changes in the hydraulic conductivity and porosity (Figure 36). Increasing the hydraulic conductivity of the fracture or the rock increases the flux at the leading edge of the plume, while changes to the rock porosity decrease the flux rate. The greatest increase in the flux was observed with an increase in the porosity of the fracture (Figure 36). The models simulating higher porosity in the rock matrix (competent rock unit of model) did show sensitivity to the transport distance into the rock matrix. Increasing the porosity of the competent rock to 10% increased the distance oxygen was transported into the rock matrix by approximately 0.5 meters. Based on this result, near the zone of recharge where water is expected to be most oxygenated, oxidation reactions could be occurring in the rock matrix adjacent to the fracture.

One of the goals of the oxygen transport modeling was to determine if a relationship could be developed between the distance of oxygen transport into the rock matrix and the transport time. This would provide a means to determine the amount of time that water had been transported through the hydraulically active fractures. However, based on these

modeling results, the transport of oxygen due to diffusion requires less than one day to penetrate more than one meter into the competent rock, which is beyond the typical distance of weathering rinds or red staining observed on and adjacent to fractures. The advective transport also shows that significant transport distances can be achieved over relatively short periods of time. These two transport mechanisms represent the shortest and longest transport distances, but as discussed in Chapter 2, oxygen consumption generally decreases free oxygen in the statured zone within meters of the recharge zone, likely resulting in a transport distance much shorter than the advective distances simulated. Therefore the depth of oxygen penetration or observed mineral oxidation cannot be correlated to a transport time because the transport of oxygen occurs so readily in the absence of reactions or will be limited where significant reactions exist.

3.4 Conclusions

For the red staining present on hydraulically active fractures to be representative of oxidation due to free oxygen being transported in the current groundwater system, the transport of oxygen would need to be along a significant distance of the fracture, as observed through the advective transport modeling. However, diffusion tends to be the dominant transport mechanism for oxygen in the saturated zone and oxygen consumption can readily occur do to organic matter or weathering reactions, so it is likely to be limited before these distances can be achieved. The groundwater data collected from MFS-1 does not contain high concentrations of iron in solution, though iron oxide precipitate was observed in the well and on the RPP samplers (Figure 17). If the red staining observed on fracture surfaces and in the adjacent rock matrix is iron oxide, it would suggest that the water being transported through the fracture has free oxygen available and its deposition is due to the current flow regime. Though some free oxygen appears to available in the water

transporting along the hydraulically active fractures, the groundwater data shows that it is limited which is not consistent with the red staining on the fractures being deposited due to the current flow regime. This is consistent with the results of other studies based on observed measurements of the oxidation state of near fracture mineralogy not the lack of an iron source in the current groundwater system (Drake et al., 2008; Drake and Tullborg, 2006; Smith and Roychoudhury, 2013; Mathurin et al., 2014).

The results of the inverse geochemical modeling provide the potential mineralogy and weathering reactions responsible for the water quality measured at the MacLeish Field Station. The results of the modeling are not unique and many possible combinations of minerals and reactions could be represented by the system. Albite, pyrite, and goethite dissolution and precipitation of siderite were found to be minor weathering reactions contributing to the weathering products in groundwater, regardless of the basis of the modeling. The more dominant mineral weathering reactions in the system were simulated to be calcite, gibbsite, phlogopite dissolution and dolomite and muscovite precipitation. These reactions are the source of the sodium, sulphate, iron, calcium, and alkalinity being observed. Though these reactions are consistent with the water chemistry of the two solutions, the model does not contain a time component or transport pathway, so these may not be realistic in a shallow groundwater system.

Table 4: Starting mineralogy used in the inverse geochemical modeling

Mineral	Chemical Formula
Albite	$NaAlSi_3O_8$
Anorthite	$CaAl_2Si_2O_8$
Calcite	$CaCO_3$
Chalcopyrite	$CuFeS_2$
Dolomite	$CaMg(CO_3)_2$
Gibbsite	$Al(OH)_3$
Goethite	$FeO(OH)$
Kaolinite	$Al_2Si_2O_5(OH)_4$
Muscovite	$KAl_2(AlSi_3O_{10})(OH)_2$
Phlogopite	$KMg_3(AlSi_3O_{10})(OH)_2$
Pyrite	FeS_2
Siderite	$FeCO_3$
Quartz	SiO_2

Table 5: Summary of Parameter Adjustments for Model Sensitivity Analysis

Parameter	Baseline	Sensitivity Model 1	Sensitivity Model 2	Source
Competent Rock Hydraulic Conductivity	3×10^{-14} m/sec	2×10^{-10} m/sec	2×10^{-12} m/sec	Domenico and Schwartz, 1990 Table 3.2
Competent Rock Porosity	1.5%	10%	5%	Domenico and Schwartz, 1990 Table 2.1
Fracture Hydraulic Conductivity	1×10^{-6} m/sec	3×10^{-4} m/sec	8×10^{-9} m/sec	Domenico and Schwartz, 1990 Table 3.2
Fracture Effective Porosity	30%	10%	60%	

Table 6: PHREEQ database simulated weathering reactions responsible for the water quality measured at the MacLeish Field Station

	1	2	3	4	5	6	7	8	9	10	11	12	13
	Moles Transferred												
Albite	1.40E-04	1.40E-04	1.40E-04	1.40E-04	1.40E-04	1.40E-04	1.40E-04	1.40E-04	1.40E-04	1.40E-04	1.40E-04	1.40E-04	1.40E-04
Anorthite	-2.55E+01		-2.78E+01	-3.47E+01		-2.78E+01	-1.73E+01	-1.51E+01	-1.70E-03	-2.78E+01	-3.70E+01	4.87E-04	
Calcite	2.55E+01	4.87E-04	2.78E+01		5.44E-04	2.78E+01	3.47E+01	6.56E+01	2.19E-03	2.78E+01			-1.21E-03
Dolomite	5.75E-05	5.75E-05		3.47E+01		1.06E-03	-1.73E+01	-5.05E+01	5.75E-05		3.70E+01	5.75E-05	1.76E-03
Chlorite(14A)			1.15E-05	-6.94E+00	1.15E-05	-2.01E-04	3.47E+00	1.01E+01		1.15E-05	-7.40E+00		-3.40E-04
Kaolinite	2.09E+01	-5.55E+01	2.78E+01	4.16E+01	-5.55E+01	2.78E+01			-5.55E+01	2.78E+01	4.81E+01	-5.55E+01	-5.55E+01
Pyrite	8.04E-05	8.04E-05	8.04E-05	8.04E-05	8.04E-05	8.04E-05	8.04E-05	8.04E-05	8.04E-05	8.04E-05	8.04E-05	8.04E-05	8.04E-05
Siderite	-1.20E-03	-1.20E-03	-1.20E-03	-1.20E-03	-1.20E-03	-1.20E-03	-1.20E-03	-1.20E-03	-1.20E-03	-1.20E-03	-1.20E-03	-1.20E-03	-1.20E-03
Quartz	9.13E+00	1.11E+02		6.94E+00	1.11E+02		2.43E+01		1.11E+02	-2.13E-04		1.11E+02	1.11E+02
Gibbsite	9.13E+00	1.11E+02	2.13E-04		1.11E+02		2.78E+01	1.01E+01	1.11E+02		-7.40E+00	1.11E+02	1.11E+02
Goethite	1.13E-03	1.13E-03	1.13E-03	1.13E-03	1.13E-03	1.13E-03	1.13E-03	1.13E-03	1.13E-03	1.13E-03	1.13E-03	1.13E-03	1.13E-03
CO2(g)	-2.55E+01	1.70E-03	-2.78E+01	-6.94E+01	1.76E-03	-2.78E+01		3.53E+01		-2.78E+01	-7.40E+01	2.19E-03	

Note: negative values represent precipitation and positive values are dissolution. The pink highlighted cells are the dominant precipitation reactions in the model and gray highlighted cells are the dominant dissolution reactions.

Table 7: LLNL database simulated weathering reactions responsible for the water quality measured at the MacLeish Field Station

	1	2	3
	Moles Transferred		
Albite	1.40E-04	1.40E-04	1.40E-04
Calcite	5.76E-04	5.55E+01	8.33E+01
Dolomite	-4.90E-05	-5.55E+01	-8.33E+01
Kaolinite	-5.55E+01	-2.24E-04	2.78E+01
Pyrite	8.04E-05	8.04E-05	8.04E-05
Siderite	-1.21E-03	-1.21E-03	-1.21E-03
Quartz	1.11E+02		-5.55E+01
Gibbsite	1.11E+02	3.70E+01	
Goethite	1.13E-03	1.13E-03	1.13E-03
Muscovite		-1.85E+01	-2.78E+01
Phlogopite	3.55E-05	1.85E+01	2.78E+01
CO2(g)	1.83E-03	5.55E+01	8.33E+01

Note: negative values represent precipitation and positive values are dissolution. The pink highlighted cells are the dominant precipitation reactions in the model and gray highlighted cells are the dominant dissolution reactions.

Table 8: Summary of Sensitivity Analysis Model Results - Measure of the Oxygen Transport Distance Beyond the Flux Boundary Condition

Model Scenario	Oxygen Transport Distance Beyond Boundary Condition (meters)
Baseline	1.79
Competent Rock - Average Hydraulic Conductivity	1.99
Competent Rock - High Hydraulic Conductivity	1.93
Competent Rock - Average Porosity	1.84
Competent Rock - High Porosity	1.84
Fracture - Low Hydraulic Conductivity	1.94
Fracture - High Hydraulic Conductivity	2.05
Fracture - Low Effective Porosity	1.82
Fracture - High Effective Porosity	2.03

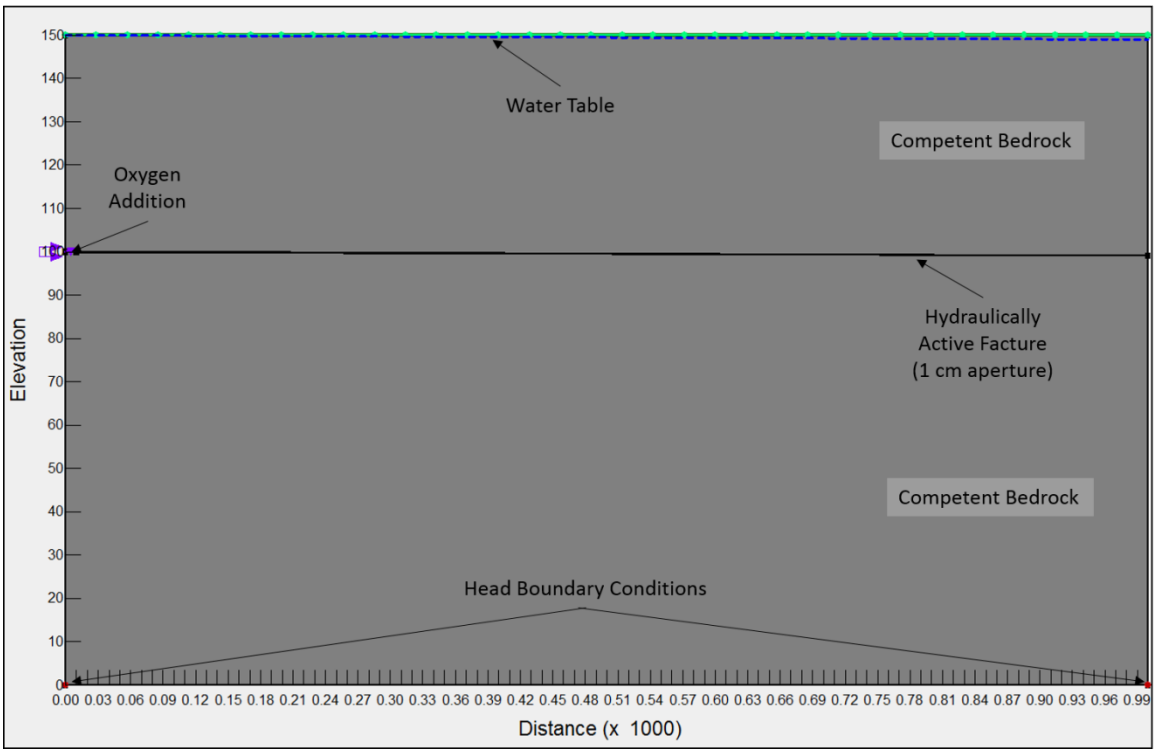

Figure 31: Model construction and conceptual model for simulation of flow and oxygen transport through a single fracture under saturated conditions.

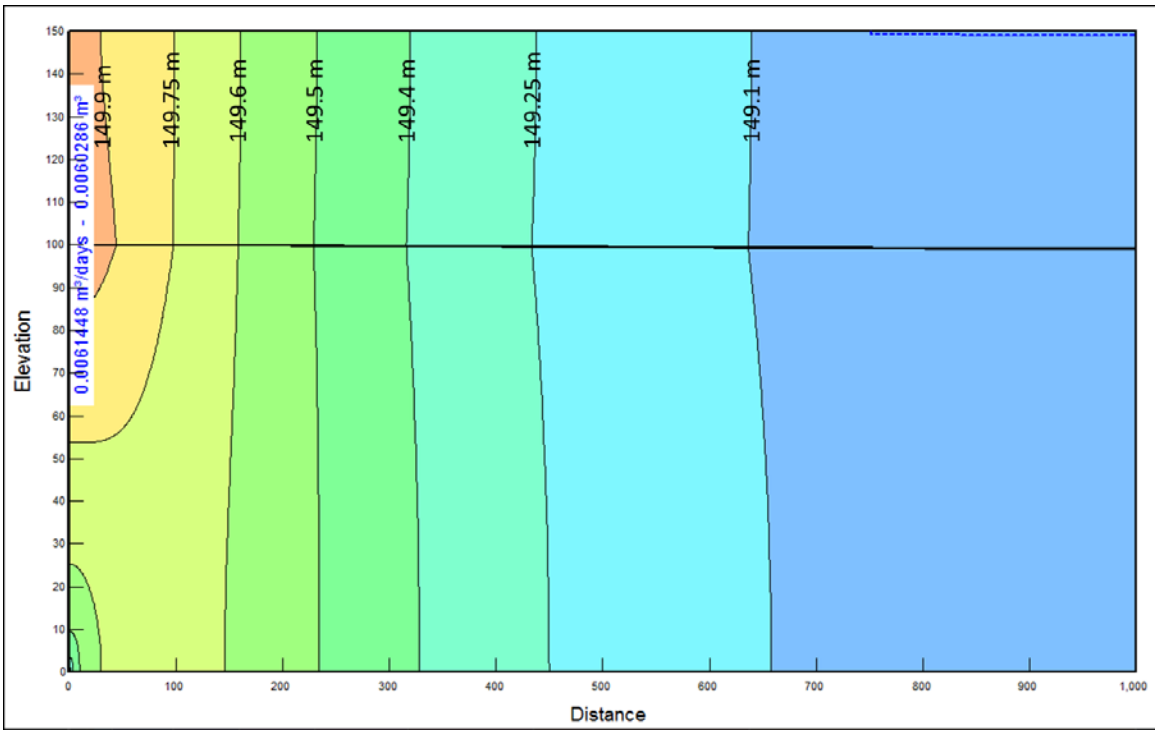

Figure 32: Simulated total head (black numbers and color contour), average linear velocity and total volume of flow over the simulation period (blue numbers), and the location of the water table (blue dashed line) from one day VADOSE/W model of oxygen transport system water flow dynamics.

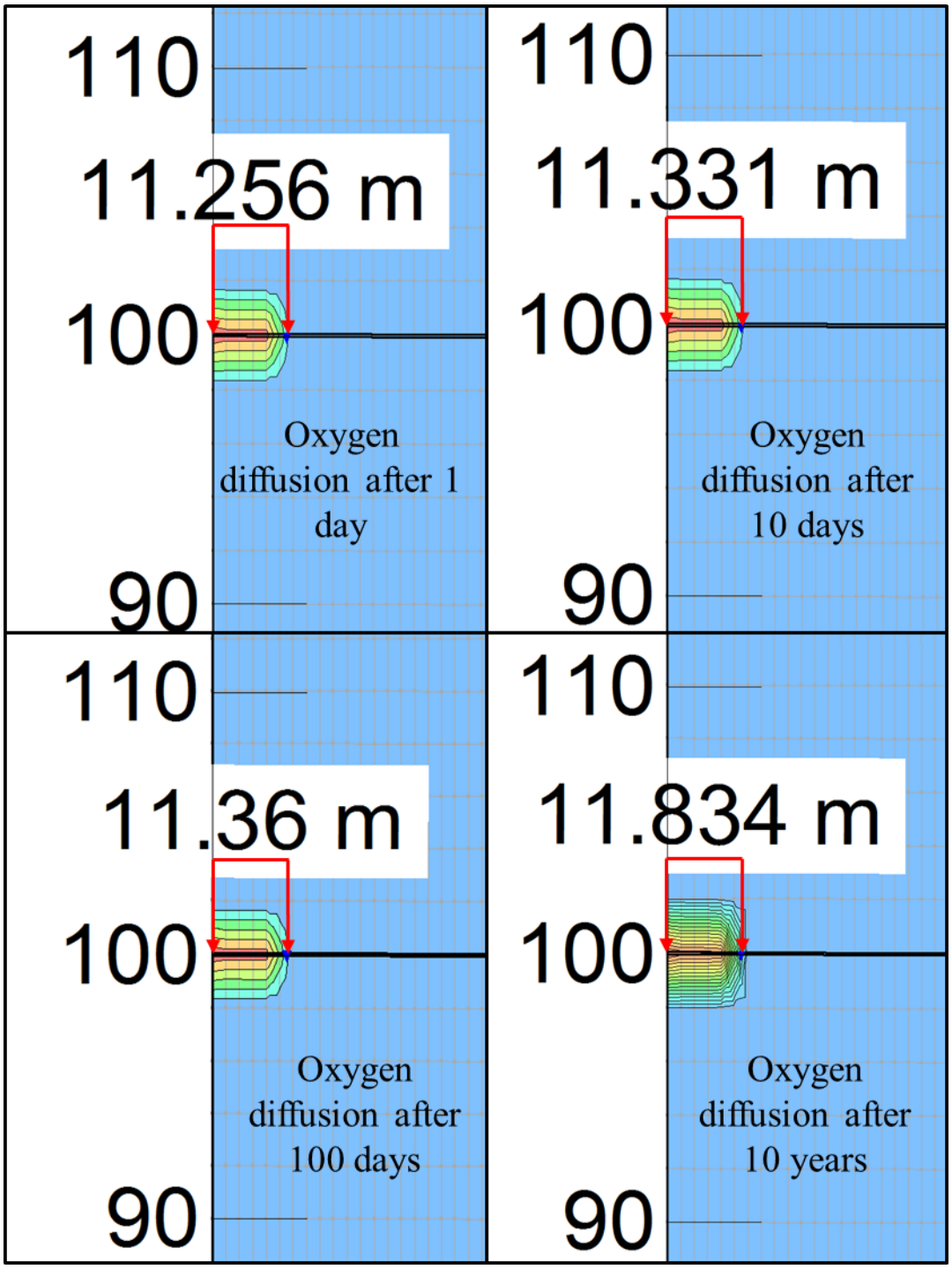

Figure 33: Simulated results of oxygen transport through a single one centimeter fracture in a saturated bedrock aquifer after one day, ten days, 100 days, and ten years, with measurement of the lateral (along fracture) diffusion transport distance.

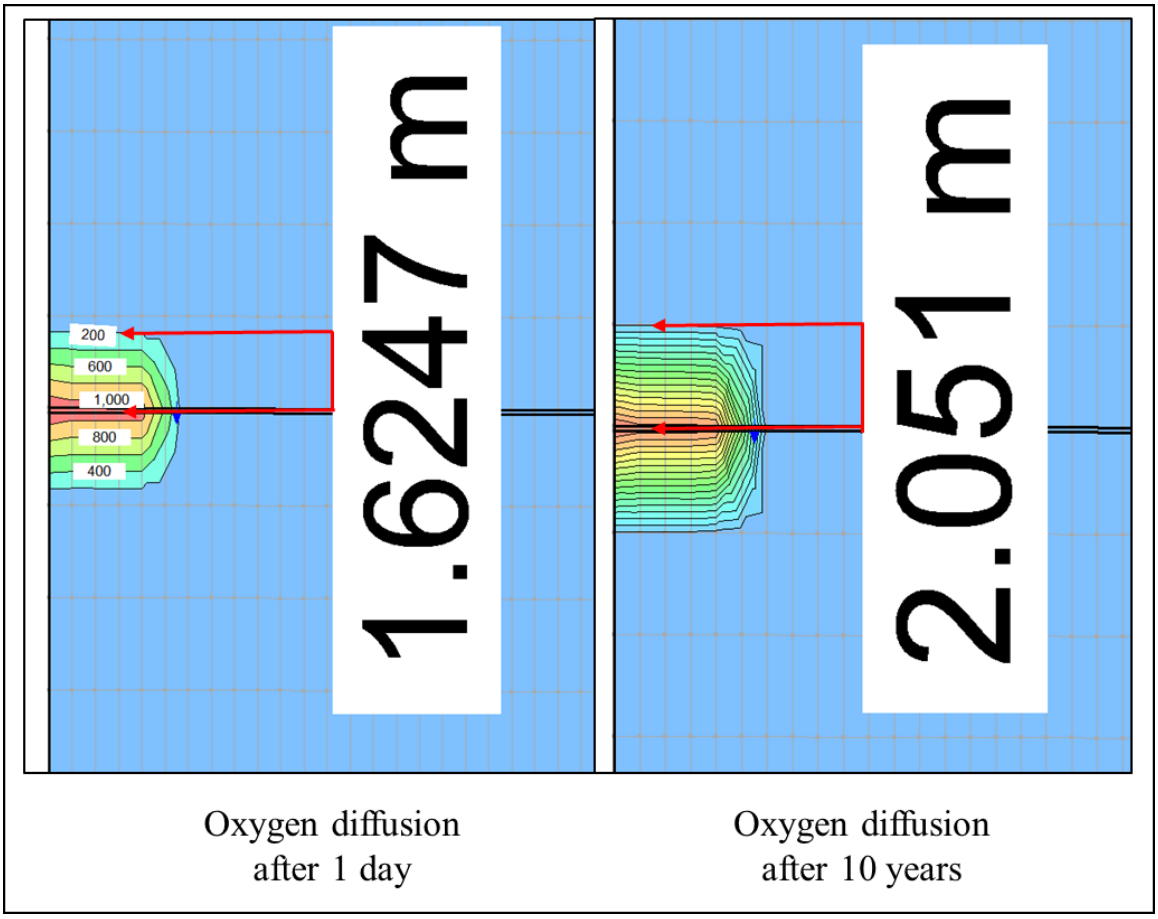

Figure 34: Simulated results of oxygen transport through a single one centimeter fracture in a saturated bedrock aquifer after one day and ten years, with measurement of the matrix diffusion distance.

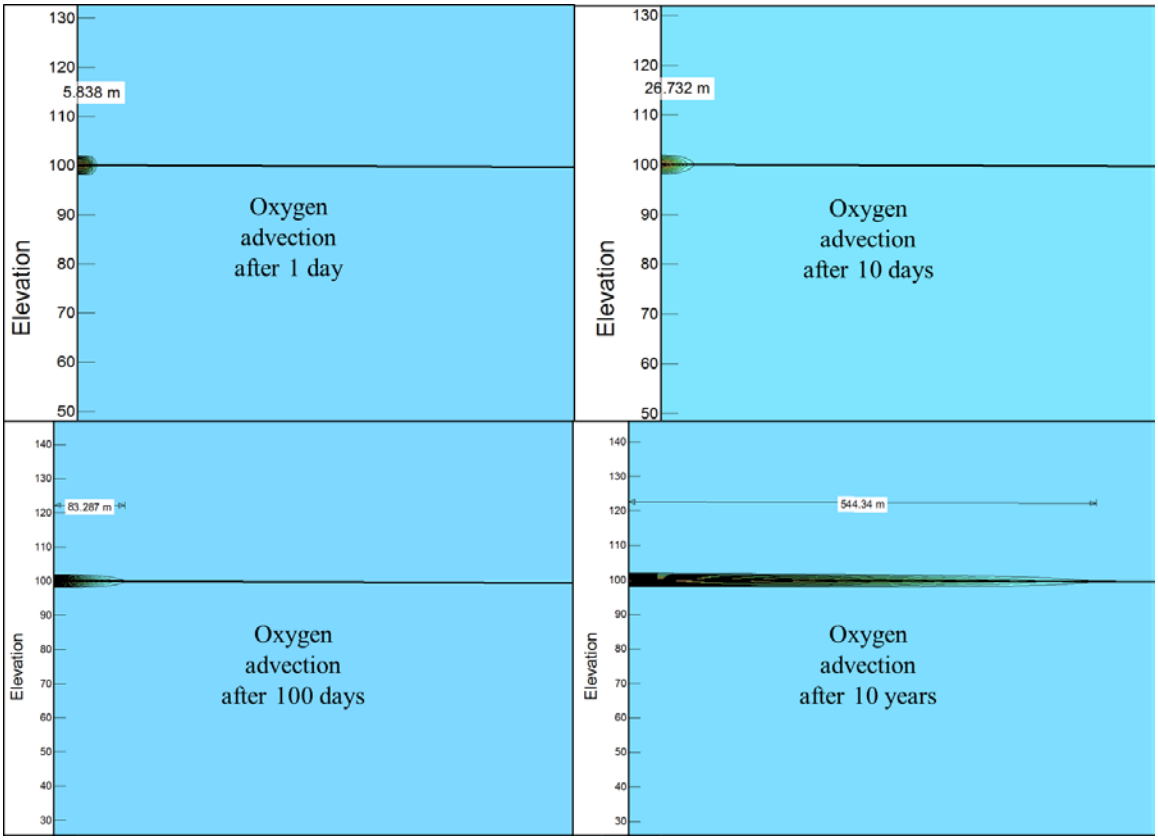

Figure 35: Simulated results of oxygen transport through a single one centimeter fracture in a saturated bedrock aquifer after one day, ten days, 100 days, and ten years, with measurement of the lateral (along fracture) advective transport distance.

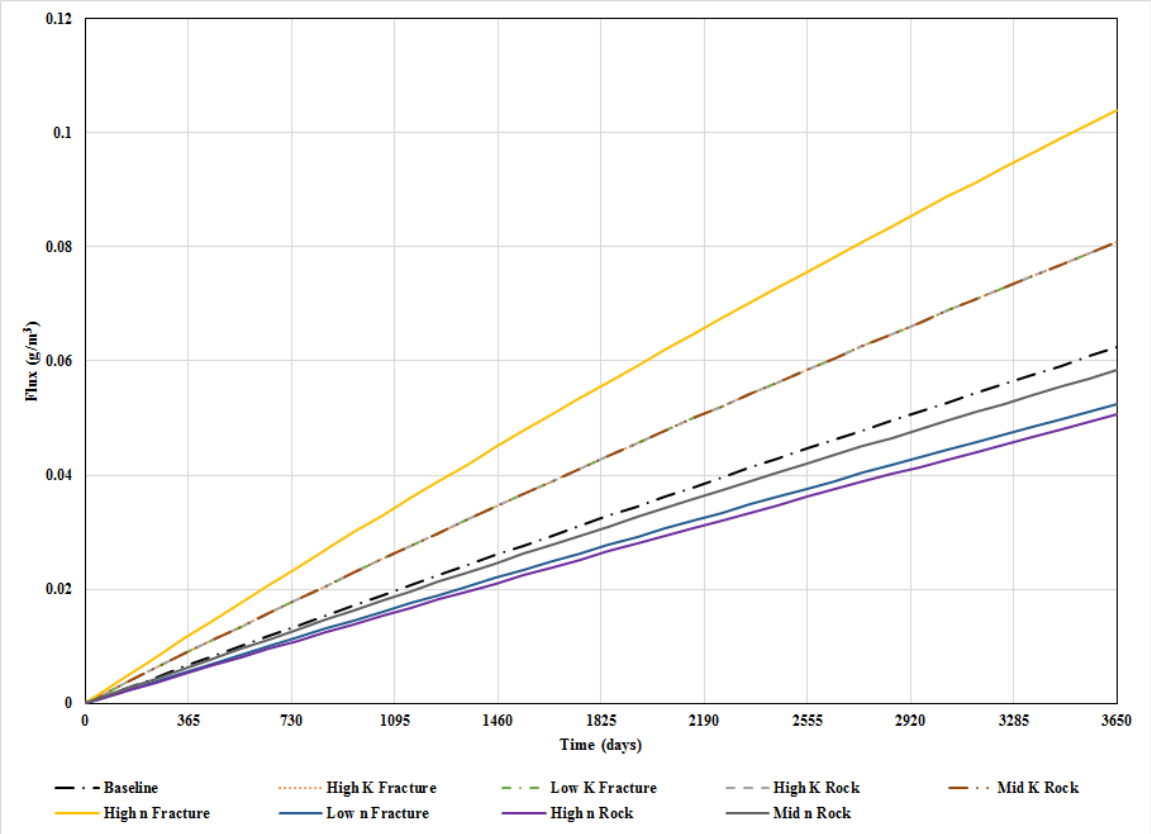

Figure 36: Sensitivity analysis results plotted as a comparison of oxygen flux rates at the leading edge of the plume being transported along the open fracture.

CHAPTER 4

THE COMPOSITION OF RED STAINING AS OBSERVED IN CORE SAMPLES AND GEOCHEMICAL EVIDENCE OF CURRENT AND PAST ADVECTIVE FLOW

When installing groundwater monitoring wells, performing initial characterization activities in new locations, or during mineral exploration activities, it can be common practice to collect core samples during the drilling. It would be expected that clear interpretations about the hydrogeologic system could be made from the rock samples collected, but rock core has been shown to have limited use for providing information on the hydrologic setting or advective flow conditions in fractured bedrock aquifers. The degree of weathering is often noted on borehole logs based on the amount of red staining or surface coating present, and scales have been developed around these indicators (Ehlen, 2002). However, as previously noted the presence of red staining or fracture coatings may not be indicative of current weathering conditions and the current hydrologic flows. Red staining has been shown to be the result of past alteration or weathering events, and testing is rarely completed to confirm (Drake et al., 2008). The most likely source of the red staining is iron rich minerals hosted in the pores of secondary minerals (Drake and Tullborg, 2006). Drake et al. (2008) found that the source of the red staining was not current water flow and weathering reactions, but was due to hydrothermal alteration, and in particular the alteration of plagioclase. The site investigated by Drake and Tullborg (2006) and Drake et al. (2008) represents a deep geologic system that has experienced multiple fracture reactivation episodes, as well as glaciation/deglaciation and transgression/regression cycles, which have been recorded in the fractures and groundwater (Tullborg et al., 2008). The rocks of New England have experienced similar fracture

reactivation episodes during the three orogenic events impacting the east coast of the United States, and have experienced glaciation/deglaciation events, which may also play a role in the current hydraulically active fractures and can be observed in the core samples.

Several projects have investigated the possible connection between water quality and red staining/fracture coatings (Smith and Roychoudhury, 2013; Mathurin et al., 2014). These studies focused on the limited information available on the mobilization of iron and other metals relative to the whole rock composition, and how the fracture coatings limit the frayed edge sites and thus the exchange capacity of the rock with the groundwater. As described in the modeling discussed in Chapter 3, simulations of oxygen transport due to diffusion shows it is limited to the first few meters of the fracture, and though advective transport can increase this distance to more than 100 meters, but still could be limited by organic matter or mineral weathering reactions. The Mathurin et al. study (2014) assumed that the high temperature alteration sourced coatings and low temperature fracture coatings are the same, but this was not confirmed. Perhaps a more appropriate conclusion is that the fracture staining resulted during prior hydrothermal events and the current flow system is utilizing zones of past weakness for paths of advective flow.

4.1 Methods

The groundwater data from Well MFS-1 (Chapter 2) concluded that the iron being transported in the system is in a primarily in the reduced form (ferrous [Fe^{2+}]) and does not support a conclusion that current water flow is the source of red staining as an iron oxide due to the lack of free oxygen (Chapter 2). Rock core samples were collected during the drilling of Well MFS-1 at the MacLeish Field Station (Chapter 2) to provide rock for analysis and evaluation as part of this study. In total, 39 meters (128.5 feet) of core was collected from borehole MFS-1 using 1.5 meter (five foot) drilling runs, from 3.8 meters

(12.5 feet) to 43 meters (141 feet) bgs. Near 100 percent core recovery was achieved over the entire core length of the borehole. A log of the core collected from borehole MFS-1 is provided as Figure 10. The core collected from MFS-1 was tested using X-ray fluorescence (XRF), spectrophotometry, microscopy, and electron microprobe analysis to examine the changes in elemental composition at, adjacent to, and away from active and inactive fractures.

4.1.1 Rock Core Sample Preparation

The borehole for Well MFS-1 was drilled using a CME-55 HSA rig, and bedrock was cored using an HQ-sized drill bit (Figure 37). The core resulting from this drilling is approximately 63.5 millimeters (2.5 inches) in diameter, and 39 meters (128.5 feet) in length; an additional four meters of drilling was completed in the unconsolidated till deposits overlying the crystalline bedrock but no samples were collected of this material. A more complete description of the installation of the Well MFS-1 and the downhole geophysical testing completed is provided in Chapter 2.

The core log prepared for MFS-1 (Figure 10) and the results of the groundwater sample collection were used to guide the selection of core samples for testing. The initial focus for sample selection was on fractures noted as having red staining or weathering evident on the fracture surface. The downhole geophysical testing was used to identify the zone from 8.2 to 8.7 meters (26.9 to 28.5 feet) bgs as the zone of hydraulically active fractures, which was confirmed by the water quality testing (Chapter 2). The group of samples with staining on the fracture surface was divided into samples near a hydraulically active zone of the well and those associated with inactive zones of the well. The interval of core between 8.2 meters and 9.1 meters (26.9 feet and 29.1 feet) bgs, which is from the identified hydraulically active zone shown in Figure 38. A third group of samples was

selected that represents core that has no red staining or coatings on fracture surfaces. Two of the samples from the third group of samples are located outside of the zone of advective flow and one sample is in the zone of advective flow. The three groups of samples selected for testing are summarized in Table 9.

The initial sample preparation methods used were intended to limit damage to the core samples to allow for further samples to be prepared and more quantitative testing to be utilized later in the study. Initially, each piece of core selected for further testing was split in half along the long axis with a rock saw using a diamond blade (Figure 39). One half of the split core was returned to the core box for archive and the other half was lightly polished using a series of progressively higher grit polishing wheels to remove saw marks, while limiting the shine of the cut surface. This balance of a smooth but light polished surface is necessary to limit the measurement error of the core scanners, which can be sensitive to reflection and surface roughness (Blum, 1997).

4.1.2 Thin Section Preparation

Standard and high polished thin sections were prepared by Quality Thin Sections of Tucson, Arizona. Billets were cut from the split core samples for submission to the laboratory for thin section preparation. Samples for thin section preparation were selected from the samples summarized in Table 9, and positioned so that microscopic and electron microprobe analysis would be focused on areas of the core at and adjacent to the fracture surface, and when possible, extending in to the unaltered portion of the rock matrix away from the fracture. Several samples were also focused on the rock matrix, away from any fracture surfaces. In total 11 thin section samples were prepared and five of the samples were prepared as high polished sections to allow for quantitative methods of analysis to be employed using the electron microprobe (Table 10).

4.1.3 Core Scanning Techniques

Core scanning techniques provide insight into the composition of the rock and the red staining observed on the fractures and in the rock matrix adjacent to the fractures. The first analytical testing of the core included magnetic susceptibility and color spectrophotometry using the UMass Amherst Quaternary Laboratory Geotek Multi-Sensor Core Logger (MSCL). The core samples were scanned dry because water has been noted to affect the reflectance measurements using similar instruments (Mix et al., 1992; Blum, 1997). For the magnetic susceptibility measurements, the Bartington Point sensor was utilized to obtain measurements every two millimeters along the length of the cut face of the split core. The magnetic susceptibility of common minerals, such as quartz, calcite, hematite, and pyrite, have been documented and this data in combination with other more quantitative analyses can be used to map the geochemical characteristics along the length of the core. Similarly, the color spectrophotometry results can be used to identify the chemical composition along the core. Hunt et al. (1971) documented the spectral features of many common minerals and studies since have documented means to process the data for more quantitative uses, including Deaton and Balsam (1991), who provided a rapid method for determining accurate iron concentrations through the first derivative of the spectral reflectance data. The use of these scanning techniques allows for rapid and nondestructive determination of lithologies present and their oxidation state (Mix et al., 1992), and have been shown to reduce the need for more conventional analysis methods (Reeves and Smith, 2009).

Elemental analysis of the core samples was completed using an ITRAX^{TM} XRF core scanner at the UMass Amherst. The XRF core scanner analyzes the elemental composition at a 100 micrometer (µm) resolution, allowing identification of small

geochemical variations along a length of core. For this study, the rock near the fracture surface, within the stained matrix adjacent to the fracture, and the unaltered matrix away from the fractures could be analyzed as part of a continuous scan to look for variations between these zones. The geochemical data resulting from the ITRAX™ scan provides a semi-quantitative summary of the elements present along the analyzed zone of the core. XRF is considered to be a semi-quantitative technique, especially for geologic applications, because light elements (which make up the majority of the Earth's crust) cannot be analyzed. The element distribution can be interpreted along with the Geotek MSCL and optical microscopy results, to determine the minerals present, and for this study, particular attention was paid to minerals and element patterns that are important in weathering reactions (plagioclase, biotite, and chlorite) (Pacheco and Alencoao, 2006).

In total, seven sections of core were analyzed using both the Geotek MSCL and the ITRAX™ XRF core scanners (3.7 to 3.9 meters bgs, 4.5 to 4.6 meters bgs, 8.2 to 8.4 meters bgs, 8.5 to 8.7 meters bgs, 8.7 to 8.8 meters bgs, 8.8 to 8.9 meters bgs, and 8.9 to 9.0 meters bgs [12.2 to 12.7 feet bgs, 14.6 to 15.0 feet bgs, 26.9 to 27.7 feet bgs, 27.8 to 28.5 feet bgs, 28.7 to 28.9 feet bgs, 28.9 to 29.1 feet bgs, and 29.2 to 29.5 feet bgs]). The samples from 3.7 to 3.9 meters (12.2 to 12.7 feet) bgs and 4.5 to 4.6 meters (14.6 to 15.0 feet) bgs were selected as control samples (sample group 3); these samples showed no indication of red staining. It could not be determined if the breaks were naturally occurring or mechanical breaks due to drilling because they are parallel to the foliation of the rock. Additionally, these two samples are located in a portion of the borehole that is within the steel casing of the well at a depth just below the measured water level in Well MFS-1, so no imaging of this portion of the borehole was completed. The remaining samples analyzed using these

techniques focused on the interval of the borehole that is hydraulically active, and the fractures at 8.4 meters, 8.5 meters, 8.7 meters, and 8.8 meters (27.7 feet, 27.8 feet, 28.5 feet, 28.7 feet, 28.9 feet) bgs each have red staining on the fracture surface. These fracture angles are not parallel to the rock's foliation so they are considered to be naturally occurring and not drilling induced mechanical breaks. Figure 40 presents pictures of each of the samples from the hydraulically active zone and Figure 41 presents pictures of the two control samples.

4.1.4 Cross-Polarized Light Microscopy

Optical microscopy using a cross-polarized light microscope was employed to image the 11 thin section samples for this study (Table 10). The optical work was completed at the UMass Amherst Department of Geosciences optical microscopy laboratory, using a digital imaging station with a Wild macroscope, to view and image the thin section samples. This is a contact enhancing technique that highlights variability and anisotropies in mineral structures. Observation were made to the millimeter scale using cross-polarized light.

4.1.5 Electron Microprobe Analysis

Electron microprobe analysis is a method for analyzing small solid samples using an X-ray spectrum for quantification of elemental composition (Reed, 1996). This technique is another non-destructive method that can provide a great deal of information rapidly while allowing additional testing later. Microprobe analysis was used to generate "element maps", which are two-dimensional arrays of elemental composition, mapped over the entire surface of the sample. If this method is used in concert with a known standard, quantification can be achieved to within one percent accuracy and detection limits of 50 parts per million (ppm) are generally applicable (Reed, 1996). The microprobe analysis

completed on the MFS-1 samples was not calibrated to a standard so semi-quantitative analysis was completed for this study.

Microprobe analysis was completed at the UMass Amherst Electron Imaging and Compositional Microanalysis Facility. Elemental composition maps were generated from the five high polished thin sections (Table 10). Each sample was carbon coated prior to X-ray microanalysis via wavelength dispersive spectrometry (WDS). Image maps of the elements aluminum, silicon, calcium, potassium, and iron were generated.

4.1.6 Fourier Transform Infrared Spectrometry

Fourier Transform Infrared Spectrometry (FT-IR) is a form of infrared spectroscopy that passes radiation through a sample (transmitted) to create a molecular signature of the sample. The molecular signature created by each molecule structure is unique, making this method useful for identifying unknown materials. The scanning methods used in this study can provide semi-quantitative indication of the mineralogy and elemental composition of the rock, but cannot precisely determine the forms of iron. Therefore, FT-IR was used to determine the form of the iron present in the thin section samples from areas adjacent to the hydraulically active fractures. Additionally, iron precipitate from the well was collected to determine the structure of this iron for comparison. If the red staining is being sourced from the current system as the iron precipitate is, it would be expected that they would be of similar forms.

4.2 Results and Discussion

Hydrothermal fluid transport through fractures results in the alteration of minerals and has been found to result in the repositioning of iron present in the solid phase mineralogy (Drake et al., 2008). Research has shown that the presence of red staining, or what is interpreted as iron oxide, is not a good indicator of the presence of oxygen (Smith

and Roychoudhury, 2013; Mathurin et al., 2014). Moreover, it could be an indicator of increased potassium related to K-metasomatism (Drake et al., 2008), the presence and mechanics of which are still being studied, but could represent hydrothermal fluids, low temperature alkaline saline waters, or other water sources (Ennis et al., 2000), providing limited value in understanding the past or current hydrologic system.

Paleohydrogeologic studies have tried to use fracture mineralogy and analysis of weathering rinds to develop an understanding of the changes to the hydrogeologic system over time (Tullborg et al., 2008). These studies require a significant amount of data covering multiple disciplines (high quality rock core; knowledge of the mineralization history associated with the fracture; the environmental evolution of the setting; high quality chemistry data; and a conceptual model of the geochemical system), which may not be readily available for most locations (Tullborg, et al., 2008). The paleohydrogeologic study presented by Tullborg et al. (2008) is related to the research being completed for the Swedish high level radioactive waste disposal facility, which has been an actively studied system for more than 20 years, providing an ideal dataset for such an analysis. Additionally, the deep nature of the system being studied and the broad range of groundwaters of differing chemistries that have been recorded in the rock, allowed for the mineralization of the fractures to be correlated with historic water conditions (Tullborg et al., 2008). For this study, the bedrock aquifer is much shallower than that studied for the high level radioactive waste facility in Sweden, allowing greater influence of past glacial advances and retreats, which can change the hydrologic flow regime through mobilization of fines (Mathurin et al., 2014). However, examination of the rock core collected from borehole MFS-1 and its mineralogy, the elemental composition can still provide insights into the current location

of advective flow in the hydrogeologic systems and how it may relate to past fracture activation events.

4.2.1 Geologic History and Formation of Major Fracture Sets

The rocks of the Waits River-Gile Mountain Province have a long geologic history (Table 11) that has involved several tectonic scale events that have imparted four dominant fractures sets on the Waits River-Gile Mountain Province. The rocks of the Waits River-Gile Mountain Province were deposited in the partially closed basin of the Iapetus Ocean after the Taconic Orogeny (480 - 455 ma). During the Acadian Orogeny, Avalon collided, closing the Iapetus Ocean and metamorphosing the sedimentary deposits. Additionally, doming occurred which contributed to the orientation of the foliation and mineralogy that developed in the rock (Hatch et al., 1988). The rocks of the Waits River-Gile Mountain Province are moderately to strongly foliated, creating planes of weakness in the rock. The fractures observed today that are the result of this geologic event are primarily striking E-W and N-S, with dip angles less than 45º, and many are less than 25º (tadpole plots of Figure 11). Manda et al. (2008) identified this type of fracture as Foliation Parallel Fractures (FPFs), which were not a dominant set in eastern Massachusetts where their study was based. These fractures represent planes of weakness in the rock fabric.

The rocks of the Waits River-Gile Mountain Province observed to be present at the surface today were previously deeply buried (Figure 42), but due to erosion, uplift and glaciation (Table 11) these rocks are now at the surface. This has removed a significant amount of weight and confining stress from the rocks, allowing unloading joints or fractures to develop along the previously imparted planes of weakness. The fractures that have been identified as hydraulically active are FPFs. Two other fracture sets associated with tectonic scale events (Table 11) are also present striking NE-SW and NW-SE. The

tectonic fracture sets are more steeply dipping than the FPF, with angles greater than 25º and many between 45º and 60º; these sets were also identified by Manda et al. (2008). The fractures observed in the borehole of MFS-1 (Figure 11) are evenly distributed between the two types of fractures (FPF and tectonic) and the red staining is present on both types of fractures and those that are active in the current hydrologic system, as well as those that are not.

4.2.2 Sample Color as a Measure of Red Staining

The magnetic susceptibility and color measurements collected using a Geotek MSCL or similar instrument have been shown to be able to be correlated to specific mineralogy (Geotek, 2014). The results of the magnetic susceptibility scan of the core from MFS-1 did not show any clear mineral signals. The methods described for using magnetic susceptibility data to determine mineralogy are intended for sediment core samples and not rock core. Using the scanner to evaluate crystalline rock core is likely to result in measurements of multiple minerals at each location due to the fine grained nature of the rock mineralogy compared to the grain size distribution and analysis of sediment cores. The resulting data is therefore representative of multiple closely spaced minerals within the matrix of the rock, and thus provides limited value in characterizing the rock mineralogy for this study. It was assumed that if the red staining of the rock is composed of iron oxide, the measured magnetic susceptibility measurements at or adjacent to the fracture would be higher than areas without the red staining. The magnetic susceptibility data did not show any discernable patterns relative to the red staining or higher measured values at or near fractures with red staining.

Color measurements were collected along the center line of the cut core face using the Geotek MSCL. As noted above, this instrumentation and many assumptions for the

data processing techniques are heavily focused on sediment samples rather than rock. However, it is assumed that application of these techniques to a scanned rock sample is within the acceptable use of the methods. Specifically, iron rich sediments and oxidized iron have been shown to be detectible using spectrophotometry at weight percent concentrations of less than 0.1% (Barranco et al., 1989), and iron tends to have significant impacts on the color spectrum of the sample, even at very low concentrations (Mix et al., 1992; Blum, 1997).

Visual inspection of the core from MFS-1 shows red staining in the rock matrix, adjacent to the red stained fractures. It is expected that red staining can be identified through spectral analysis as colors representative of iron and/or oxides. The measurements collected using spectrophotometer with the MSCL are colors that correspond to the uniform color space CIELAB, which has the components L*, measure of luminosity, a*, measure of reddish (positive values) and greenish (negative values) colors, and b*, measure of yellowish (positive values) and bluish (negative values) colors (X-Rite, 2007). The CIELAB system was established in 1931 by the International Commission on Illumination to provide a standardized method to assign color values (X-Rite, 2007). This standard color system has been interpreted such that the measured L*, a*, and b* values can be used to quantify mineral or elemental compositions in the samples analyzed. In general, silicates and carbonates are naturally transparent in the visible light spectrum, so they cannot be easily identified through color measurements (Hunt et al., 1971). Oxides have an opposite behavior and can be used to quantify the composition of scanned core, and in particular the iron oxide content (Hunt et al., 1971; Guimaraes et al., 2013).

Guimaraes et al. (2013) studied sediment colors of samples derived from Amazon wetlands, and established that iron rich sediments have L* values greater than or equal to 24, a* values greater than or equal to 4, and b* values equal to or greater than 10. Figure 43 presents the L*, a*, and b* values collected from the seven MFS-1 core samples scanned with the Geotek MSCL. As shown on Figure 43, none of the core samples scanned with the spectrophotometer exhibited these characteristics, though visible red staining in the rock matrix is present. The L* values measured are greater than 24 for each of the core samples scanned, including the control samples and portions of the core not associated with red stained fractures. The a* values are all lower than 4 and the b* values are below 10 for all seven samples scanned, and most are negative suggesting a blue hue rather than the yellow hue which would be indicative of iron oxide. If iron is present in the rock, as visual inspection suggests, it is not in sufficient quantity to cause a color shift of the sample (i.e., less than 0.1% [Barranco et al., 1989]), it is small isolated iron minerals trapped between the grains of other minerals (Drake and Tulborg, 2006; Drake et al., 2008), or the red staining is not iron oxide as has been assumed. Bigham et al. (1978) found that iron oxide in soils was present in finely divided particles and can be difficult to measure, though they seem to have a disproportionate influence on the soil and soil water quality. This could explain the visual identification of red staining, but no spectral reflectance data suggesting it is present in measurable concentrations. Natural iron oxides are also known to have high substitution potential (aluminum for the iron), which would change the color spectrum and particle size of the oxides (Bigham et al., 1978).

In addition to the standard CEILAB colors measured by the spectrophotometer, the reflectance associated with visible and near infrared wavelengths ranging from 360 to 740

nanometeres (nm) is also measured. The ratio of the reflectance values at the 700 nm to the 400 nm wavelengths can be used to identify "characteristic signatures" of the sediment (Guimaraes et al. 2013). The ratio of 700 nm to 400 nm, or Q7/4 as termed by Guimaraes et al. (2013), was determined to be between 6 and 11 for iron rich sediments, with an associated L* value in the range of 10 and 45. Figure 44 presents the Q7/4 for each of the core samples scanned with the spectrophotometer. The Q7/4 values for each of the core samples scanned is between 0.8 and 1.5, which is well below the threshold of 6 that would support the presence of iron rich material in the samples. The ratio of the red spectrum (595 to 700 nm) to blue spectrum (400 to 515 nm) reflectance has also been shown to identify the presence of oxides or sulphides (Mix et al., 1992); red/blue spectrum ratio values of greater than 1.5 are associated with oxides or sulphides. Figure 45 presents plots of the red/blue ratio for the MFS-1 core samples. The patterns of these plots are similar to those from the Q7/4 analysis, and only show two locations where oxides or sulphides are likely to be present (i.e., the red/blue ratio is greater than 1.5), at 4.6 meters (15.0 feet) bgs and at 8.8 meters (28.9 feet) bgs. Although a significant amount of red staining appears to be present on the fractures of the core obtained from Well MFS-1, and is observed to be in the rock matrix adjacent to the fracture, the spectrophotometry data does not support that this red staining is iron rich or an iron oxide. The spatial scale of this scanning method may not be fine enough to quantify the disseminated red staining in the rock adjacent to the core and appears to have been primarily measuring the gray colored rock matrix.

4.2.3 Changes in Mineral Chemistry Adjacent to and Away from the Fracture Surface

As with the Geotek MSCL, the ITRAX^{TM} XRF scanning has the benefit of being a non-destructive testing method that allows for the rapid and continuous determination of

whole rock geochemistry along a cut core face (Gauthier et al., 2012). The same seven samples analyzed with the Geotek MSCL were also scanned using the ITRAX™ along a line centered on the cut face of each sample. The XRF data was collected every 100 μm, and thus provides a much finer resolution dataset compared to the MSCL data collected every two millimeters. Figures 46 to 52 present an image of the core sample, the approximate location of the centerline, and the associated XRF results for aluminum, silicon, potassium, calcium, and iron. The core samples with visible red staining in the matrix adjacent to a fracture surface and the extent of that staining are noted, as well.

Potassium and iron concentrations followed the same patterns (increases and decreases in parts per million concentration [ppm]) over each of the core samples, regardless of the sample's position relative to hydraulically active fractures in the borehole, a fracture, or the rock matrix. Aluminum followed the same pattern of increases and decreases along the core samples as potassium and iron, except along the sample from 8.9 to 9.0 meters (29.2 to 29.5 feet) bgs. The sample from 8.9 to 9.0 meters (29.2 to 29.5 feet) bgs does not have an aluminum concentration decrease by more than an order of magnitude starting at a position of approximately 100 millimeters, as is observed in the iron and potassium measurements from this sample. In the image of this sample, a large white mineral is present at the position which is associated with the abrupt chemical changes. The white mineral has increasing calcium and low silicon concentration which has been interpreted as a marble vein, not associated with an open or active fracture zone. Excluding core sample 8.9 to 9.0 meters (29.2 to 29.5 feet) bgs, which does not show a discernable pattern, the silicon concentrations measured follow an inverse pattern to the iron and potassium concentrations, though the amplitude of the silicon variations is much smaller.

Calcium concentrations do not correlate with changes in aluminum, silicon, potassium, or iron.

In the portions of the core where red staining was observed to be present in the rock matrix adjacent to a fracture (8.4 meters, 8.5 meters, 8.7 meters, 8.8 meters, and 8.9 meters [27.7 feet, 27.8 feet, 28.5 feet, 28.7 feet, and 28.9 feet] bgs) the aluminum, calcium, potassium, and iron are well correlated and have a similar order of magnitude change in concentration. The core sample ending at 8.4 meters (27.7 feet) bgs (Figure 48) and the core sample ending at 8.5 meters (27.8 feet) bgs (Figure 49) are separated by a broken zone that also had red staining when collected (Figure 10). These samples represent opposite sides of the same fracture and are in the zone of advective flow; therefore, similar chemical concentrations and variability would be expected to be observed on either side of a hydraulically active fracture. The XRF measured concentrations of aluminum, calcium, potassium, and iron increase from the rock matrix toward the fracture surface on both sides of the zone at 8.4 to 8.5 meters (27.7 to 27.8 feet) bgs (Figures 48 and 49). A decrease in the element concentrations is shown at the fracture at 8.5 meters (27.8 feet) bgs (Figure 49), but due to the measurement position near the edge of the sample this could be representative of sample error associated with the uneven edge of the sample surface and not a depletion chemically at the fracture. An increase in aluminum, calcium, potassium, and iron was also measured moving from the rock matrix toward the fracture surface through a visibly stained portion of the core toward 8.7 meters (28.5 feet) bgs (Figure 49). The sample from 8.7 to 8.8 meters (28.7 to 28.9 feet) bgs has visible red staining at both ends of the sample and in the adjacent rock matrix, but a less clear pattern of concentration changes (Figure 50). The concentrations of aluminum, calcium, and potassium at 8.7

meters (28.7 feet) bgs (Figure 50) have a similar pattern to the concentrations measured through the stained matrix and fracture at 8.5 meters (27.8 feet) bgs (Figure 49), but with a smaller magnitude of change. A decrease in concentration is shown approaching the fracture at 8.7 meters (28.7 feet) bgs. The matrix approaching the fracture at 8.8 meters (28.9 feet) exhibited the least amount of red staining within the rock matrix and a decreasing trend in aluminum, silicon, calcium, potassium, and iron concentrations from the rock matrix toward the fracture. The thickness of each of the zones of stained matrix, where changes in chemical composition are also observed, is in the range of 10 to 25 millimeters from the fracture surface, which is consistent with weathering rinds measured on basalts (Navarre-Sitchler et al., 2011).

4.2.3.1 Element Mapping and Current Hydrogeologic System

The results of the XRF analysis are considered to be semi-quantitative and need to be verified with other element quantification methods such as elemental mapping using the electron microprobe. Five high polished thin sections were mapped using the electron microprobe (Table 10), resulting in element concentration images for aluminum, silicon, calcium, potassium, and iron. The thin section samples from 8.4 meters (27.7 feet) and the two samples from 8.7 meters (28.5 feet and 28.7 feet) bgs correspond to the same portion of the core as the samples analyzed with the Geotek MSCL and ITRAX^{TM} XRF scans. The high polished section from 9.6 meters (31.5 feet) bgs is near a fracture with red staining that is outside of the zone of advective flow and the sample from 17.3 meters (56.6 feet) bgs is from the rock matrix, in a less foliated zone, not associated with red staining.

The elemental mapping results in a grayscale image that represents the relative concentrations of the elements being measured; dark colors are associated with high concentrations and light colors represent low concentration. A color profile (high to low

concentration: black, blue, purple, red, orange, yellow, white) was assigned to the element maps to make small variations in the chemical composition more visible. Figures 53 to 57 present the element maps for the five high polished thin section samples from MFS-1. The elemental maps of the five samples from MFS-1 show the dominant lithology present is carbonate, associated with the high concentrations of calcium and limited silicon throughout each of the samples. This is consistent with the predicted mineralogy based on inverse modeling (Chapter 3). The Waits River-Gile Mountain geology is described as interbedded marble and quartzite schist; the samples of MFS-1 are predominantly associated with a marble zone. The zones of the section maps with the high calcium concentrations also have high iron concentrations. The marble has been identified as weathering brown (Hatch et al., 1988) which would indicate that iron is present in the carbonate mineralogy, consistent with the element maps of the MFS-1 samples and the inverse modeling.

Iron concentrations are high throughout each of the section maps, but are significantly lower in the garnets in the less foliated zone (Figure 57), than the garnets near the hydraulically active fractures, which do not have reduced iron (Figure 53). The predominant silicate minerals present in the samples are biotite, mica, and garnet. Throughout the thin sections the highest silicon concentrations are associated with lower measured concentrations of aluminum and potassium. Microscopy showed that biotite is the silicate mineral being observed in the elemental maps; biotite can be a good reservoir of ferrous iron. Biotite dissolution reactions can result in the release of aluminum, potassium, iron, magnesium, and silicon, though they are quite slow. The elemental maps show a decrease in the potassium toward the fracture surface at 8.4 meters and 8.7 meters

(27.7 feet and 28.5 feet) bgs (Figures 53 and 54). Early in the weathering process, potassium is released fastest compared to the other elements in the framework of the biotite and ferrous iron is retained by the solid structure (Malmstrom and Banwart, 1997). The XRF results closest to the fractures at 8.5 meters, 8.7 meters, and 8.8 meters (27.8 feet, 28.7 feet, and 28.9 feet) bgs all show sharp decreases in aluminum, potassium, and iron. Based on these multiple observations, biotite weathering, releasing potassium, magnesium (based on water quality data), and silicon, is a dominant reaction representing the location of Well MFS-1 along the reaction path.

4.2.3.2 Garnets in Thin Section – Past Fracture Activity and the Current Hydrogeologic System

Metamorphic rocks are generally assumed to retain the chemical composition of the unmetamorphosed sediments because it is an isochemical process, though in schists the concentrations of mafic minerals may be higher than the original sediments (Krauskopf, 1967; Turekian and Wedepohl, 1961; Shelley, 1993). Paleohydrogeologic studies have also found that current hydraulically active fractures may be the reactivation of previous fractures or zones of weakness, so investigating previous indications of fluid and fracture activity can provide insight into the current system.

Garnets were observed to be present throughout the core and the thin sections created from the MFS-1 core. The presence of garnets is commonly associated with prograde metamorphic crystallization that is water assisted or results in the release of water, which can transport reaction products away from the crystals (Shelley, 1997). The garnets present in the MFS-1 samples are representative of a greenschist facies and show several of the classic signatures of this alteration environment (Shelley, 1993): occur in quartz rich zones; S-shaped trails of quartz and opaque minerals; and garnets, mica, quartz, and

feldspars have replaced finer grained clays, micas, and quartz (Figure 58), so they can be used to interpret the prior condition of the system under a hydrothermal flow regime.

The most highly altered garnet is closest to the current hydraulically active fracture (Figure 58), which based on the orientation of the fractures and the angle of the fracture relative to the rock foliation are FPF (Figure 11). The elemental mapping of the garnet closest to the fracture at 8.4 meters (27.7 feet) bgs is depleted in potassium and aluminum (Figure 53). A second garnet is present on the same thin section (Figure 58), but away from the hydraulically active fracture, and is less depleted in potassium and aluminum (Figure 53). All of the garnets observed in this thin section are irregularly shaped and spaced. Garnets are observed to be present throughout the thin section samples, including those not mapped with the microprobe. The number of garnets is observed to increase and the uniformity in their size and spacing improve away from the current hydraulically active fractures of borehole MFS-1. The ordered arrangement of crystals in space resulting from hydrothermal alteration occurs if diffusion is controlling the growth of the crystal, while heat flow controlled growth results in irregular spacing (Shelley, 1997). Based on the regular distribution of garnets in the sample from 17.3 meters (56.6 meters) bgs (Figure 57), the minerals in this portion of the rock grew as a result of diffusion and were not in direct contact with the hydrothermal fluid. The fractures in the proximity of these garnets are consistent with the tectonic sets and thus would not have been present during the metamorphic period when the garnets developed. The highly altered garnets that are irregularly spaced and near the fracture at 8.4 meters (27.7 meters) bgs grew in close proximity to the flow of the hydrothermal fluids (Figure 53).

The garnets present are likely not contributing significantly to the weathering products being measured in the groundwater samples, but the garnets provide a clear indication of the fluid flow through the rock fractures during past metamorphic events. Using the garnet distribution and alteration as indications of past hydraulic activity, the fractures located at 8.4 meters (27.7 feet) bgs were previously in a zone of hydraulic activity and transported hydrothermal fluid during the period of metamorphism. In addition to them having signs of near fluid alteration, these fractures are parallel to the rock foliation indicating planes of weakness. The location of the past hydrothermal activity is consistent with the current hydraulically active fractures of the system providing which have been reactivated due to the unloading of the units from above them and removal of the stress.

The red staining on the fracture surfaces is to be present on fractures from both sets of fractures (FPF and tectonic). Not all fracture surfaces show signs of iron staining. Looking at the core log and the fracture orientation along with the understanding of the relationship between the fracture sets and their history, it does not appear that the iron staining can be attributed to any one event or source. Some of the staining appears to be related to the oxidation of sulphide minerals, and these samples have become stained black over time in the core box. Other areas of staining could be associated with the past hydrothermal flow that appears to have occurred through some of the fractures. Therefore, it does not appear that the iron staining can conclusively be determined to be sourced from the current hydrologic system.

4.2.3.3 Form of Iron Present in Rock Matrix and Well Precipitate

The core scanning and element mapping provide some evidence that the iron present is in small quantities and may be between mineral grains, making measurement of it difficult. The overall high iron content of many of the minerals present also makes

isolating the different forms somewhat challenging. This has led to an inconclusive understanding of the relationship of the current hydrologic system to the source of red staining on fracture surfaces and it composition. The FT-IR is a good tool for identifying differences in molecule bonding, so it can identify the different iron minerals, as well as the iron precipitate in the well. Figure 59 provides a summary of the FT-IR scans completed. The top scan is from the iron precipitate collected from the well and the low scans are of individual minerals identified in the thin section sample of red stained rock matrix. The iron precipitate is an amphorous iron ($Fe(OH)_{3(a)}$) based on the results of the FR-IR scan. Figure 60 presents the FT-IR scan of the iron precipitate from MFS-1, and an inset image of a scan of ferrihydrite and orange precipitate (Clark, 1999). The scale of the inset images is reverse to the FT-IR scans and the FT-IR scans are showing absorbance and the inset are providing reflectance, but the patterns can be used to identify main characteristics, such as the wavelength associated with the peak of the curve. The peak of the curve for the iron precipitate collected from MFS-1 is at 1μm, which is consistent with orange precipitate, or $Fe(OH)_{3(a);}$ or ferrihydrite, the peak is shifted from 1μm. This is consistent with the visual observations in the well (Figure 17) and the groundwater chemistry discussed in Chapter 2, confirming that much of the iron remains in solution until it enters the well where oxygen is introduced, quickly oxidizing the iron in solution, causing it to come out of solution in the borehole.

It has been suggested by other data in this study that the red staining present on the fractures and in the rock matrix adjacent to the fracture surface is not indicative of current hydrologic conditions and advective flow. If the current system is the source of the red staining it would be expected that the minerals would be an iron oxide similar to the iron

precipitate. The FT-IR scans of minerals located in the rock matrix directly adjacent to the hydraulically active fracture at 8.7 meters (28.7 feet) bgs in Well MFS-1, which is red stained were used to determine if the oxide minerals were consistent with the iron precipitate of the current system. Three minerals, biotite, an oxide mineral, and between biotite and quartz grains, were scanned (Figure 59 and 61). The biotite provides a scan of an individual mineral with a reduced form of iron. Some red staining appeared to be present between grains of silicate minerals, but the scan showed that this location is a blend of the two silicates (biotite and quartz).

Few oxide minerals were identifying using microscopy, but an individual grain was able to be scanned. Figure 61 shows the resulting scan and an inset picture hematite and goethite scans (Clark, 1999) for comparison. The FT-IR scan has been exaggerated 2x in the y-direction to make the peaks more visible. It appears from a comparison of the size of the peaks and the pattern, that the oxide mineral present in the sample is hematite (Fe_2O_3). Hematite minerals can be sourced from the precipitation of iron out of water, but it is more typical of volcanic activity. This would suggest that the source of the hematite in the samples in not the current hydrologic system, but could be associated with the original sedimentary deposits and the following metamorphic event. The basin in which the minerals would have been deposited was partially closed and stagnant, suggesting that low oxygen conditions may have been dominant, leading to reduced forms. During the later metamorphic events, oxidation and redistribution of the iron present formed the hematite, which is the source of the red staining being observed today. This is consistent with the observations made by Drake et al. (2008) that the iron staining is related to hydrothermal alteration and represents a redistribution of the iron present in the rock. It also confirms

that it should not be assumed that red staining is an indication of current oxygen or advective flow conditions within a fractured rock aquifer.

4.3 Conclusions

The hydraulically active fractures of Well MFS-1 are all associated with red staining on the fracture surface and in the matrix of the rock adjacent to the fracture. Red staining is commonly assumed to be associated with iron oxide, but the results of this study are not conclusive. The spectrophotometry data did not show that the red staining is iron rich or oxides are present in the rock based on measured color and reflectance data. The groundwater sampling of Well MFS-1 found that ferrous iron is the dominant form of iron in the system. Biotite which is a prominent mineral in the MFS-1 core, can provide a reservoir of ferrous iron and a source of potassium, magnesium, and silicon in groundwater.

The elemental mapping of the rock samples from MFS-1 using XRF and electron microprobe further shows high iron concentrations throughout the rock, not just at the fracture surface. The fractures in the advective zone also shows lower potassium and aluminum concentrations toward the fracture surface, which could be an indication of the disequilibrium created when water is continually flushed over the surface and weathering is not controlled kinetically. Other observations about the rock, such as the presence and nature of garnet crystals show that the current zone of advective flow in Well MFS-1 was previously active during a period of hydrothermal activity and the FT-IR scan shows that the red staining is likely hydrothermally sourced. More work is needed to fully understand the source of red staining and its relationship to hydraulic activity in fractured bedrock aquifers, but it has been shown in this study that the broad assumption that it represents iron oxide staining resulting from current hydrologic flows or that is represents a zone of free oxygen is not correct. It should also not be assumed that the current fluid system is the

source of the red staining without investigating the paleohydrogeologic history and past hydrothermal events.

Table 9: Core sample intervals selected for testing and associated sample group based on the observation of staining on the fracture surface and presence of advective flow near sample location.

Core Interval (meters below ground surface)	Core Interval (feet below ground surface)	Staining present?	Near zone of advective flow?	Sample Group
3.7 to 3.9	12.2 to 12.7	no	no	3
4.5 to 4.6	14.6 to 15.0	no	no	3
8.2 to 8.4	26.9 to 27.7	no at 26.9 feet yes at 27.7 feet	yes	2 1
8.5 to 8.7	27.8 to 28.5	yes	yes	1
8.7 to 8.8	28.7 to 28.9	yes	yes	1
8.8 to 8.9	28.9 to 29.1	yes at 28.9 feet no at 29.1 feet	yes	1 2
8.9 to 9.0	29.2 to 29.5	no	yes	3
9.4 to 9.6	31.0 to 31.5	yes	no	2
9.6 to 9.7	31.5 to 31.9	yes	no	2
17.1 to 17.3	56 to 56.6	yes	no	2
17.3 to 17.4	56.6 to 56.9	yes	no	2

Note:

Sample group 1 = red staining present on fracture surface and near zone of advective flow
Sample group 2 = red staining present on fracture but not near advective flow
Sample group 3= no red staining (control samples)

Table 10: Thin sections prepared from MFS-1 core.

Sample Number	Sample Depth (meters bgs)	Thin Section	High Polished Thin Section
MFS1-27.7ft	8.4	X	X
MFS1-27.8ft	8.5	X	
MFS1-28.5ft	8.7	X	X
MFS1-28.7ft	8.7	X	X
MFS1-28.7ft-D	8.7	X	
MFS1-28.9ft	8.8	X	
MFS1-29.0ft	8.9	X	
MFS1-29.2ft	8.9	X	
MFS1-31.5ft	9.6	X	X
MFS1-56.6ft	17.3	X	X
MFS1-56.9ft	17.3	X	

Table 11: Major regional and localized geologic history

Time	Major Geologic Event	Local Geologic Event
800 - 600 ma	Iapetus Ocean formed	
480 - 455 ma	Taconic Orogeny; partial closure of ocean	Stagnant basin forms
440 - 400 ma	Taconics erode	Sediments deposited in marine basin
390 - 360 ma	Avalon collides, closing Iapetus Ocean; Acadian Orogeny	Rocks metamorphosed, rocks folded, foliation/weakness established
290 - 270 ma	Alleghenian Orogeny	Tectonic fracturing
200 - 150 ma	Rifting of Pangea	Tectonic fracturing
100 - 20 ma	Erosion	Unloading of Waits River-Gile Mountain Province
20 - 2 ma	Uplift	Unloading of Waits River-Gile Mountain Province
2 ma - 12 ka	Glaciation	Erosion, deposition, unloading

Figure 37: Drilling rods and HQ-sized (96 millimeter outer and 63.5 millimeter inner diameter) rock coring bit used to drill borehole MFS-1 at the MacLeish Field Station in Whately, MA.

Figure 38: Core from the interval of 8.2 to 9.1 meters (27 to 30 feet) below ground surface. Iron staining was identified on the fracture surfaces in this interval and downhole geophysical testing supported that advective flow into the well is likely occurring along one of the fractures in this zone. Note the broken zone between 8.4 and 8.5 meters (27.5 and 28 feet) below ground surface with significant iron staining on the broken surfaces of the rock.

Figure 39: Rock saw using water and diamond blade to cut core samples along the long axis for geochemical testing.

Figure 40: Core samples from hydraulically active portion of well selected for testing using core scanning with Geotek MSCL and ITRAX™ XRF.

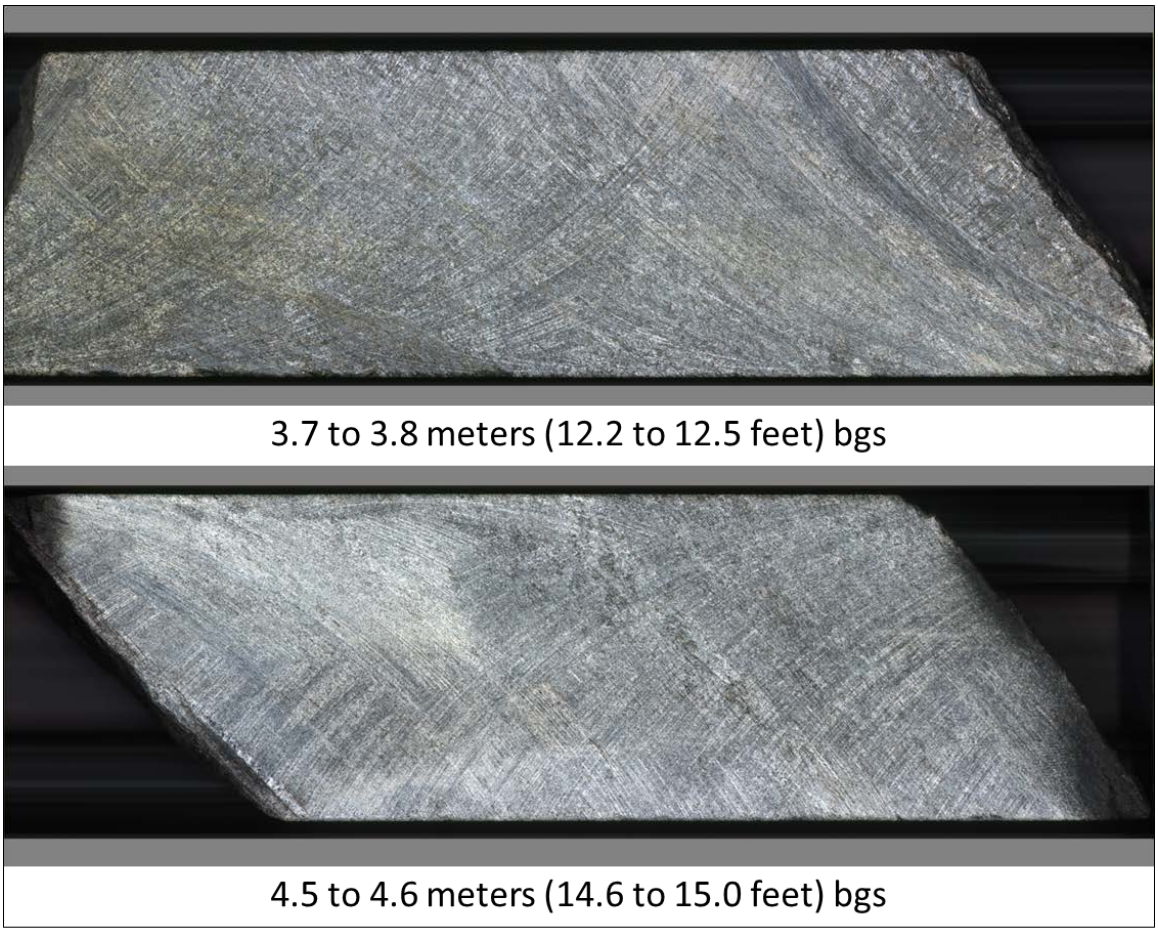

Figure 41: Control core samples from borehole MFS-1 selected for testing using core scanning with Geotek MSCL and ITRAX™ XRF. These samples showed no indications of red staining on the fracture surface and are not associated with a zone of hydraulic activity in the well.

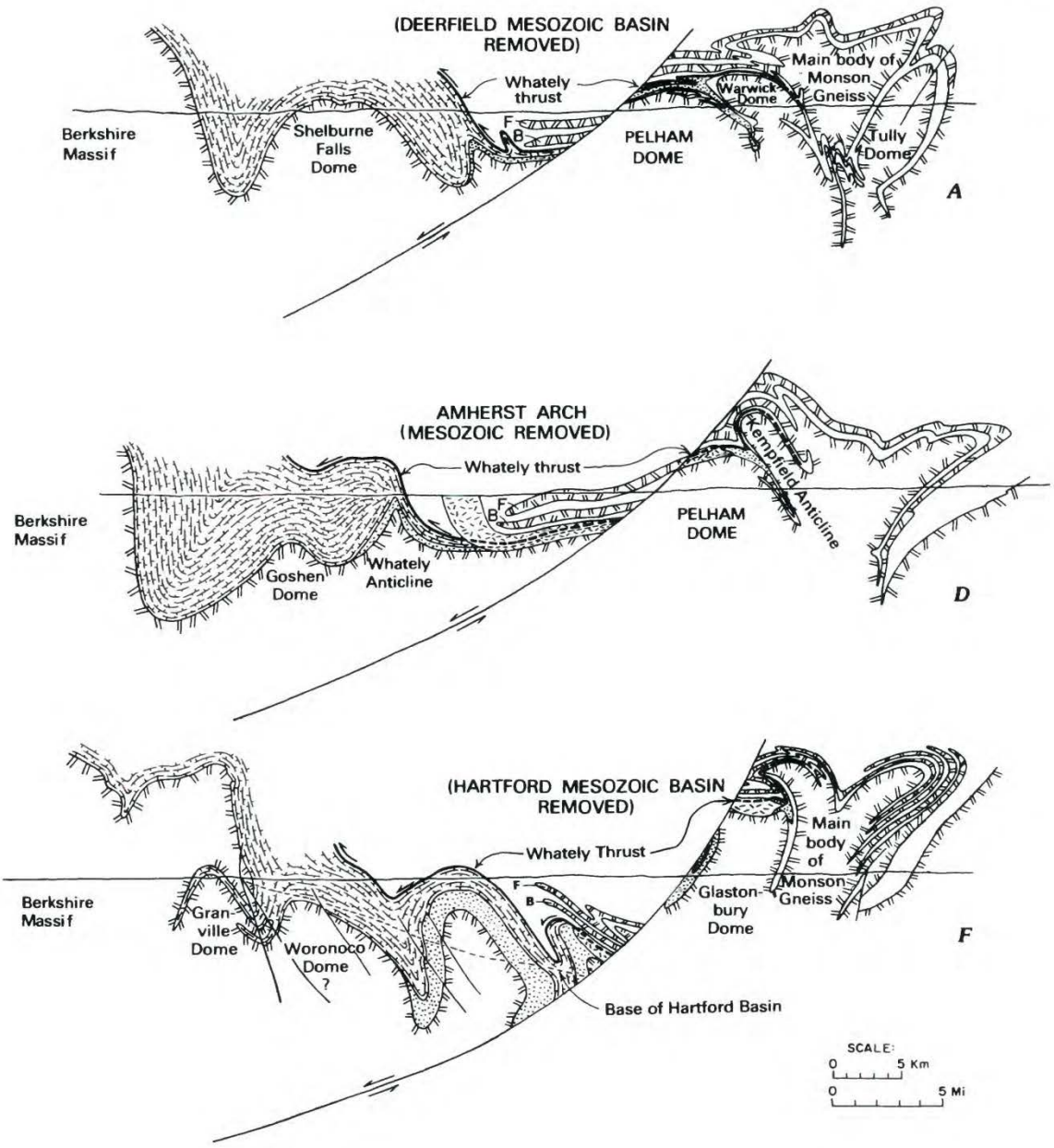

Figure 42: Three geologic sections of the Whately Thrust and Devonian age rocks from Hatch et al., 1988 (north, central, and southern locations). The rocks of the Waits River-Gile Mountain, along with the Goshen Formation and Putney Volcanics are represented by the brick line pattern overlying the stippled pattern of the Erving Formation and underlying the Littleton Formation (no pattern). The current ground surface is marked by the horizontal line.

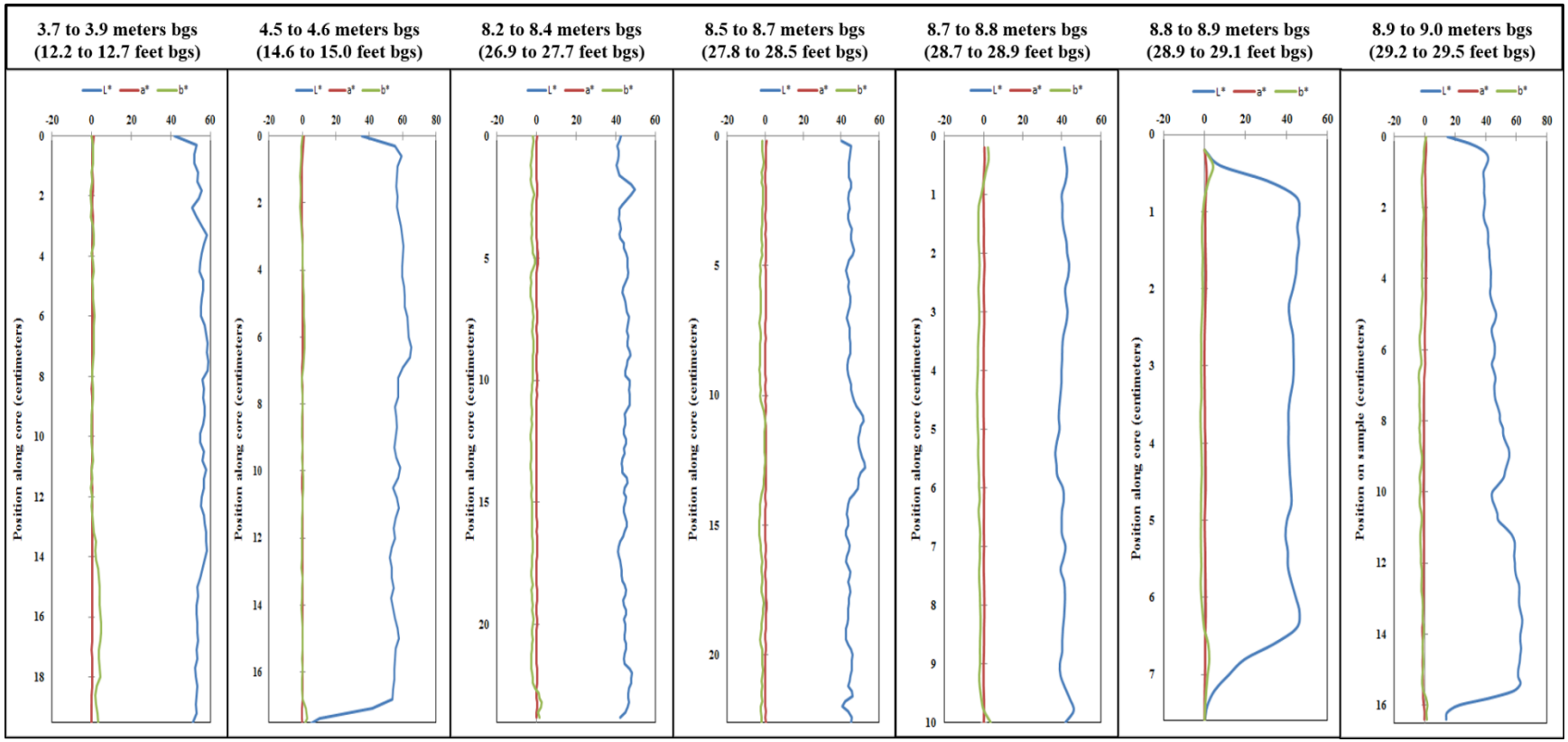

Figure 43: Color measurements collected using a Geoteck MSCL spectrophotometer. Colors are based on the uniform color space CIELAB system, where L* is the measure of luminosity, a* is the measure of reddish (positive values) and greenish (negative values) colors, and b* is the measure of yellowish (positive values) and bluish (negative values) colors.

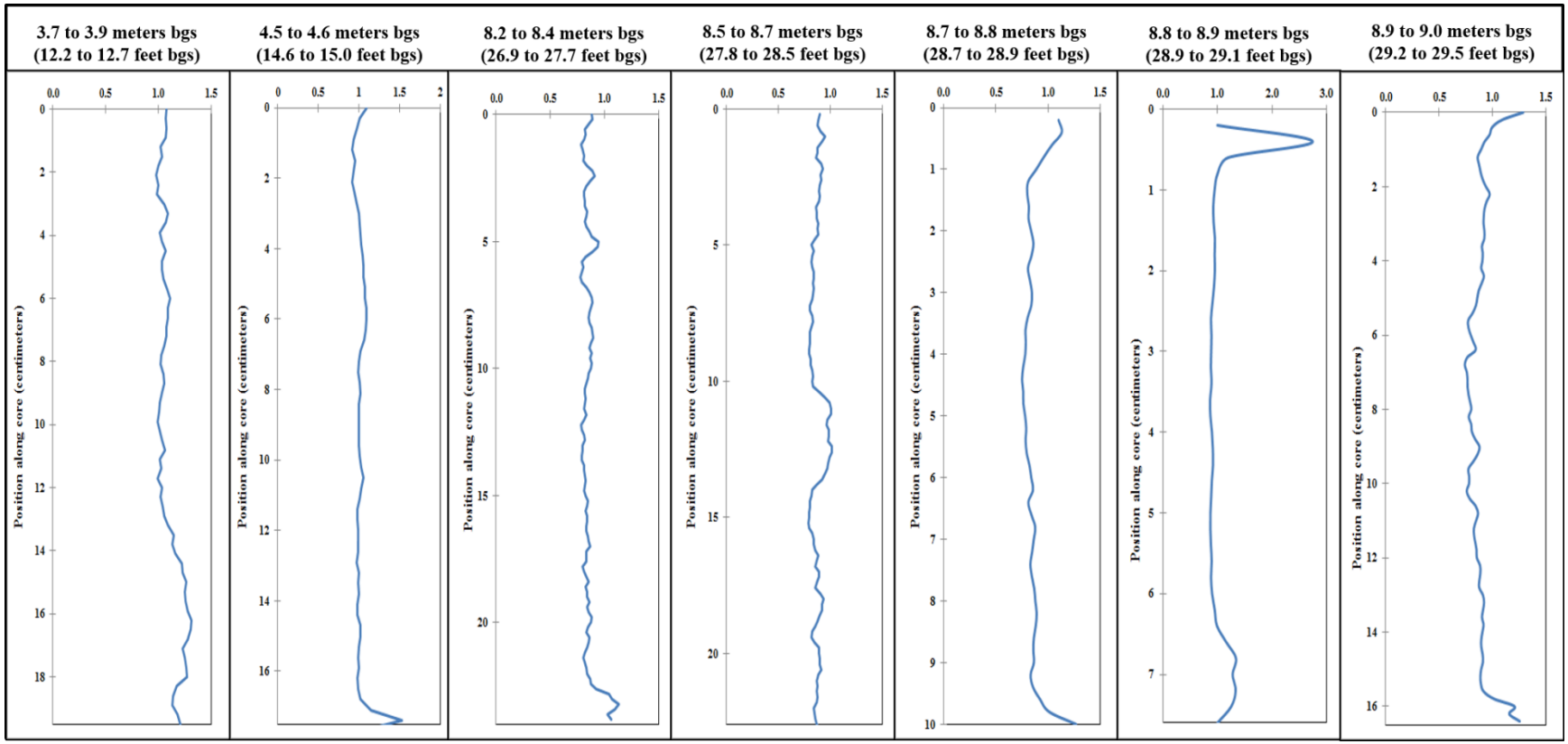

Figure 44: Q7/4 ratio of spectral reflectance data obtained from Geoteck MSCL spectrophotometer. The Q7/4 value is a ratio of the reflectance at the 700 nm wavelengths to the reflectance at the 400 nm wavelength.

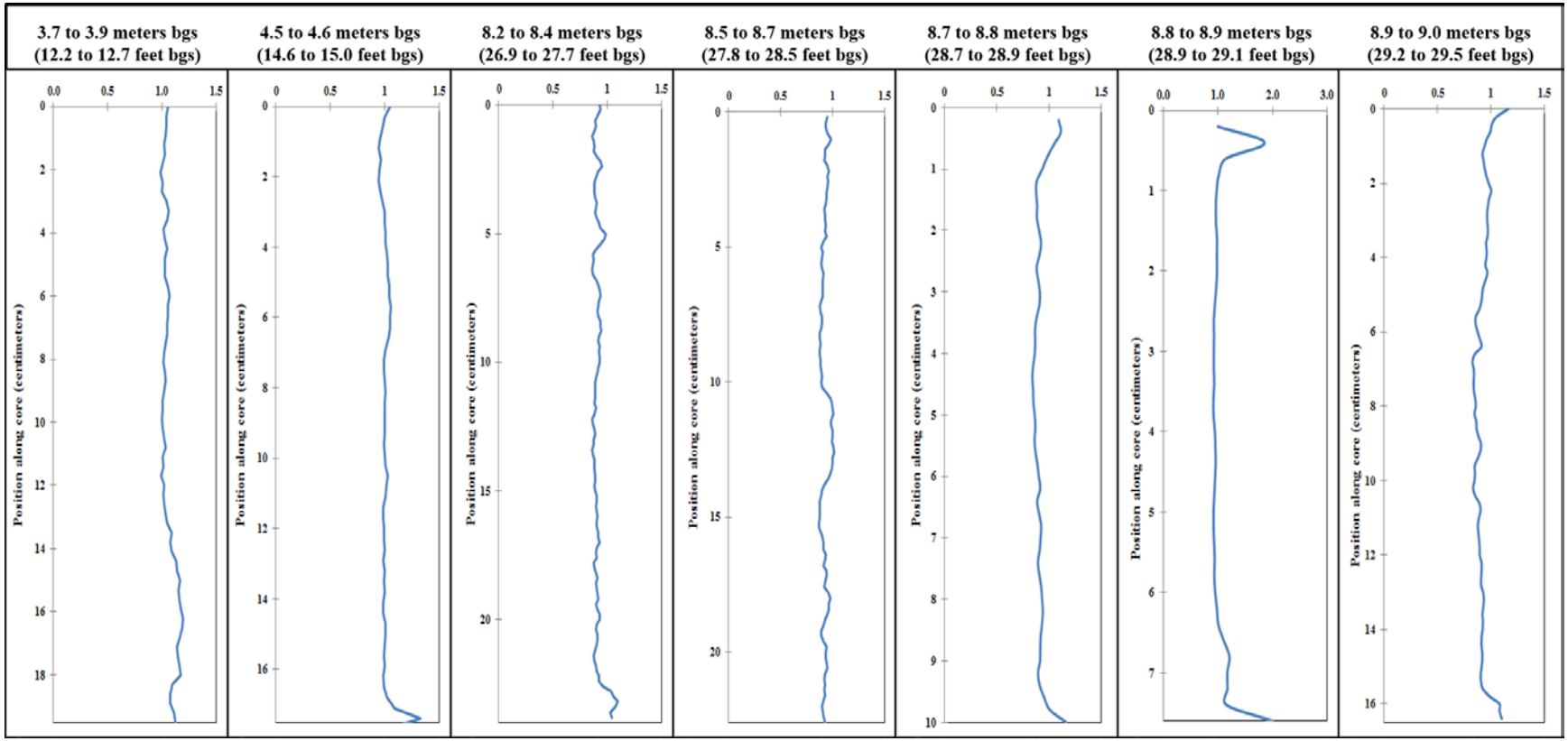

Figure 45: Red/blue ratio of spectral reflectance data obtained from Geoteck MSCL spectrophotometer. Red/blue values greater than 1.5 are indicative of the presence of oxides or sulphides.

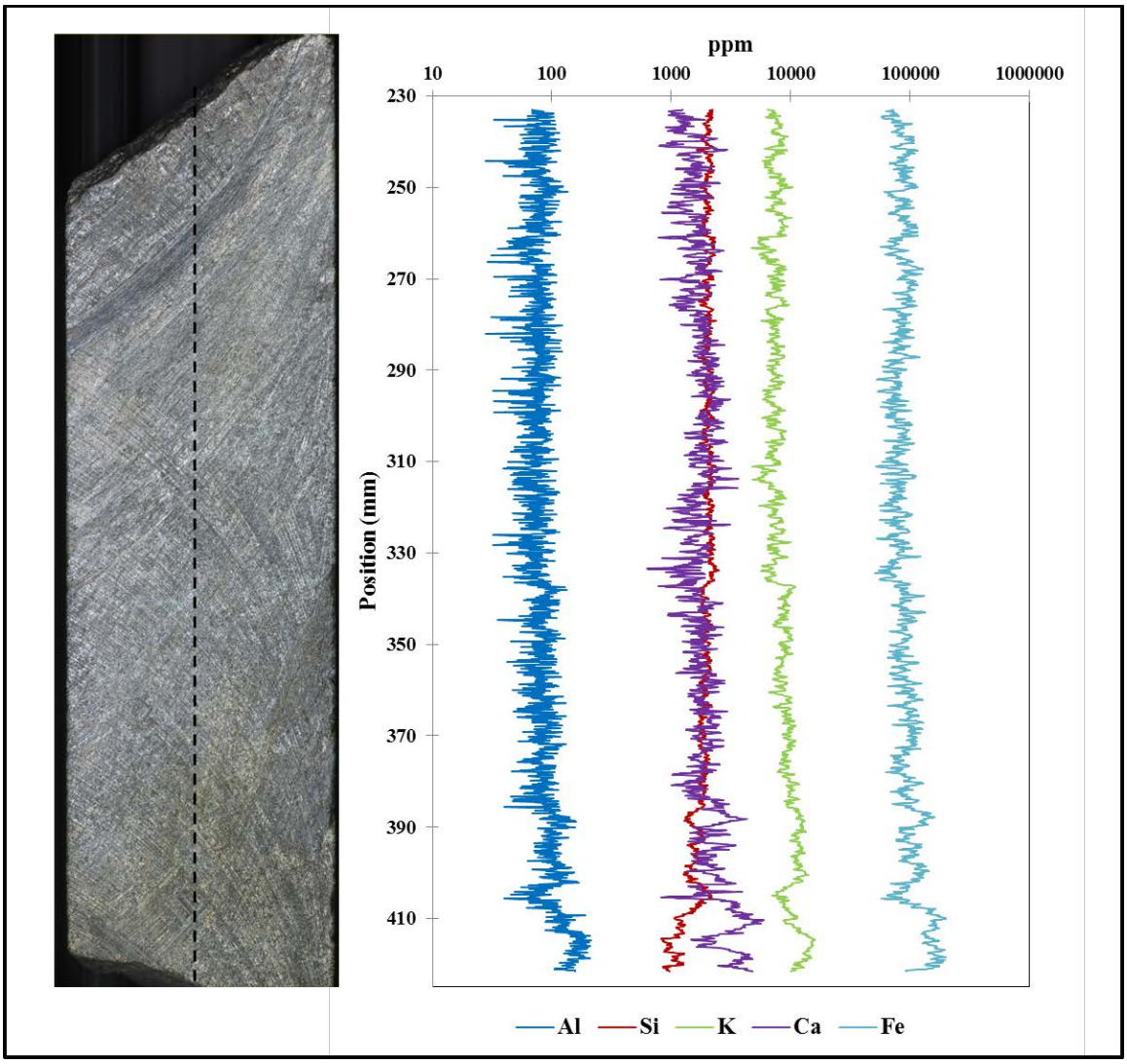

Figure 46: XRF potassium, silicon, and iron intensities measured along core from 3.7 to 3.8 meters (12.2 to 12.7 feet) below ground surface. Image of core with scale provided to show location of measurements along split core sample.

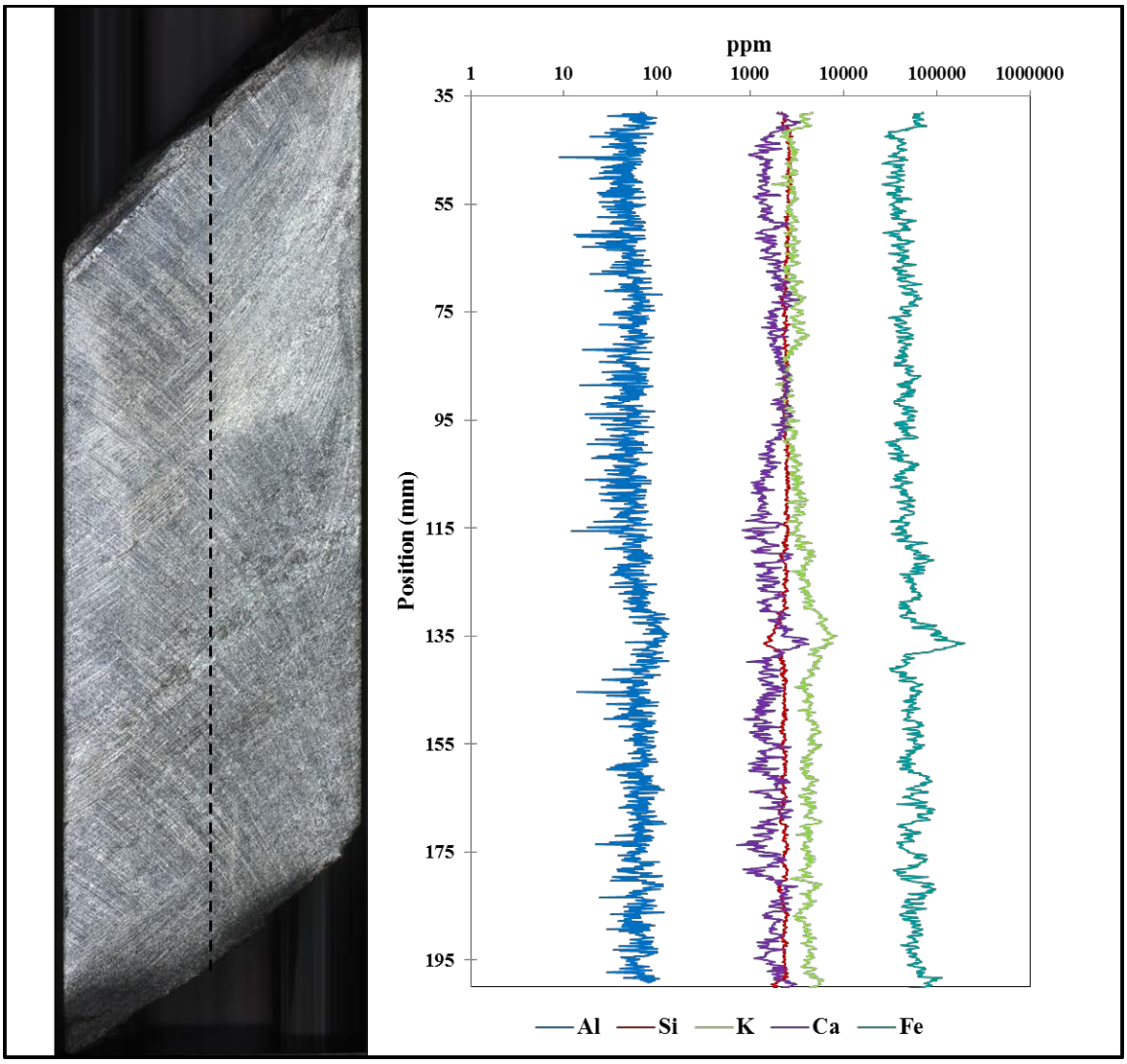

Figure 47: XRF potassium, silicon, and iron intensities measured along core from 4.5 to 4.6 meters (14.6 to 15.0 feet) below ground surface. Image of core with scale provided to show location of measurements along split core sample.

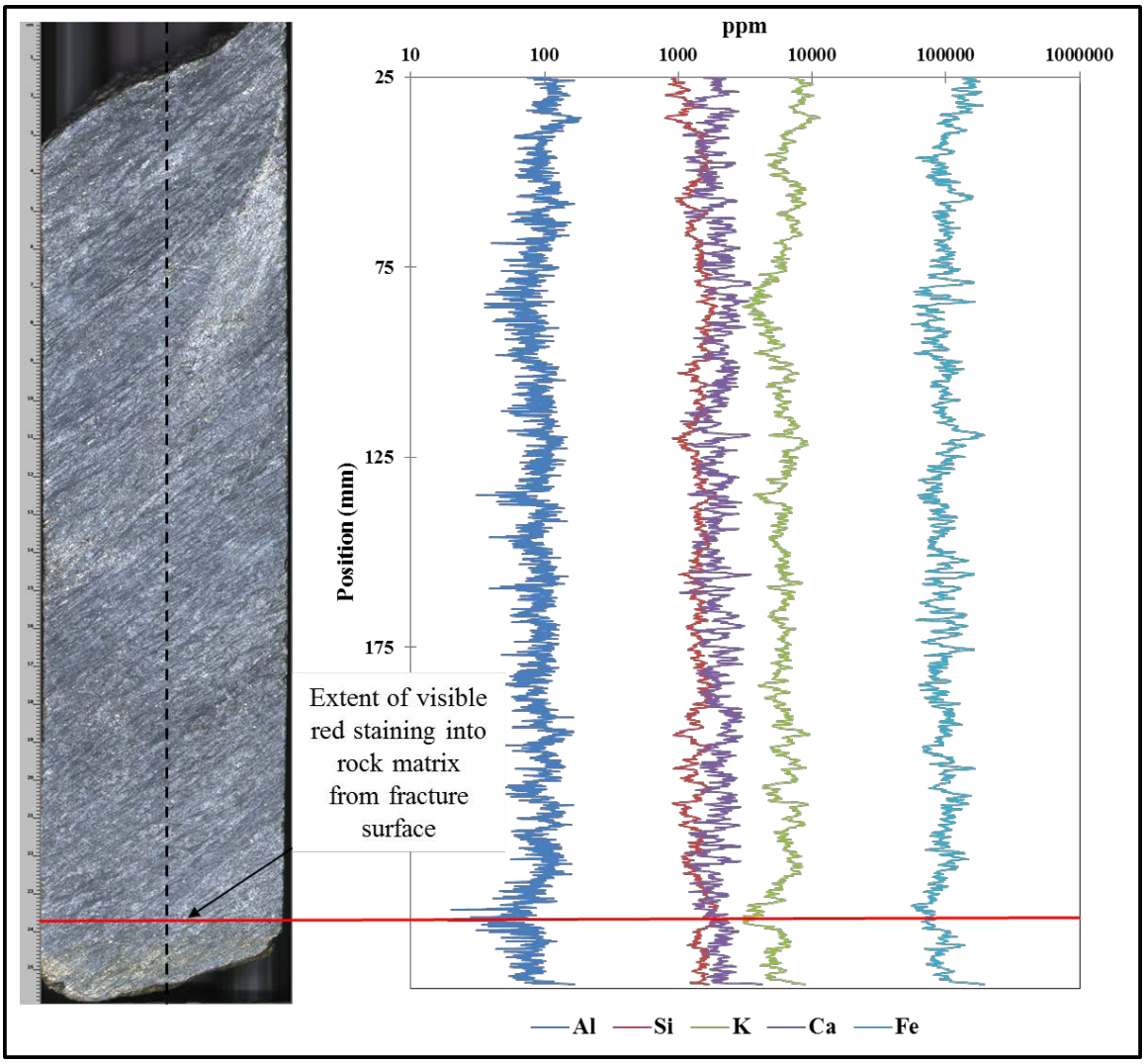

Figure 48: XRF aluminum, silicon, calcium, potassium, and iron intensities measured along core from 8.2 to 8.4 meters (26.9 to 27.7 feet) below ground surface. Image of core with scale provided to show location of measurements along split core sample.

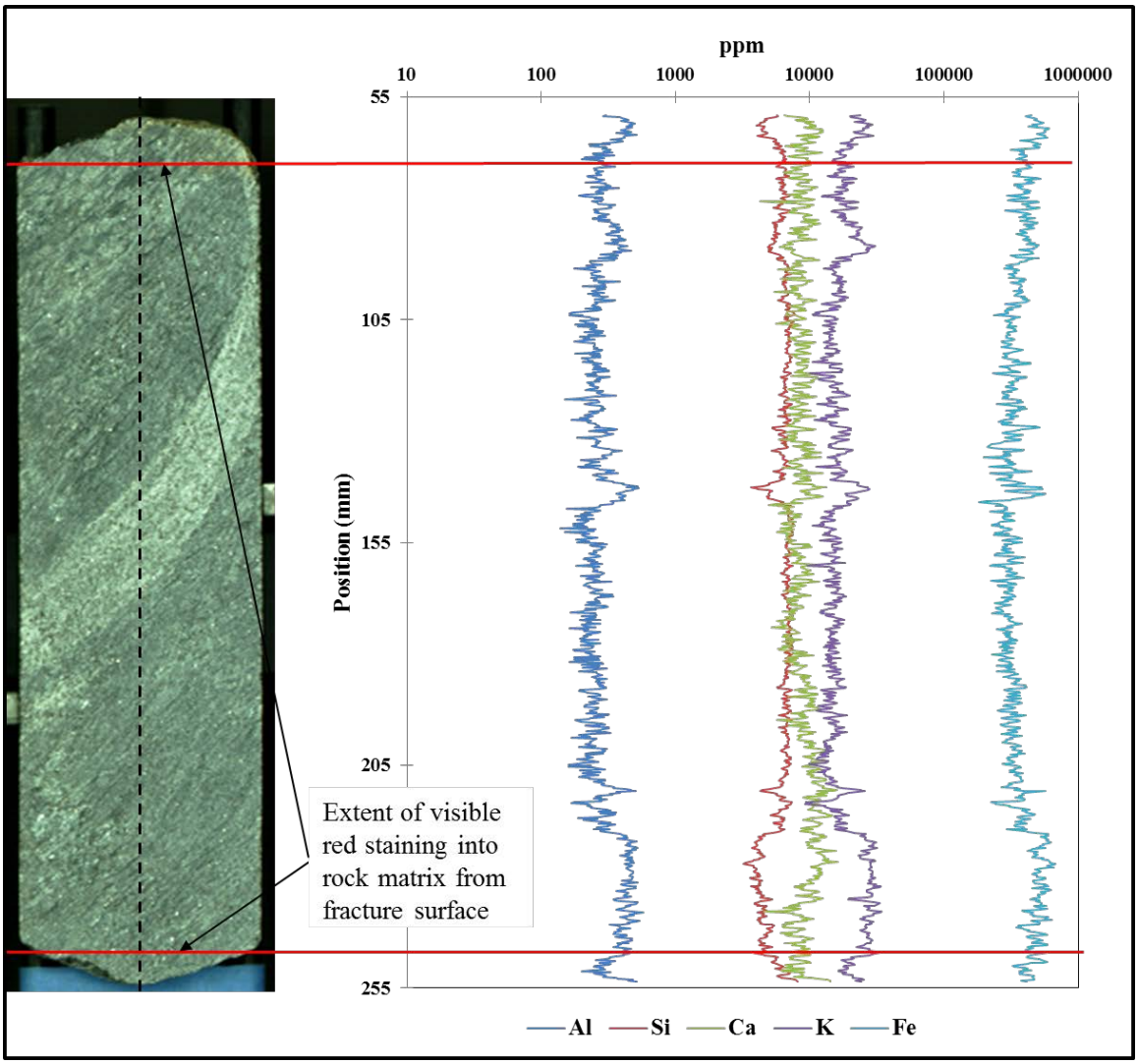

Figure 49: XRF aluminum, silicon, calcium, potassium, and iron intensities measured along core from 8.5 to 8.7 meters (27.8 to 28.5 feet) below ground surface. Image of core with scale provided to show location of measurements along split core sample.

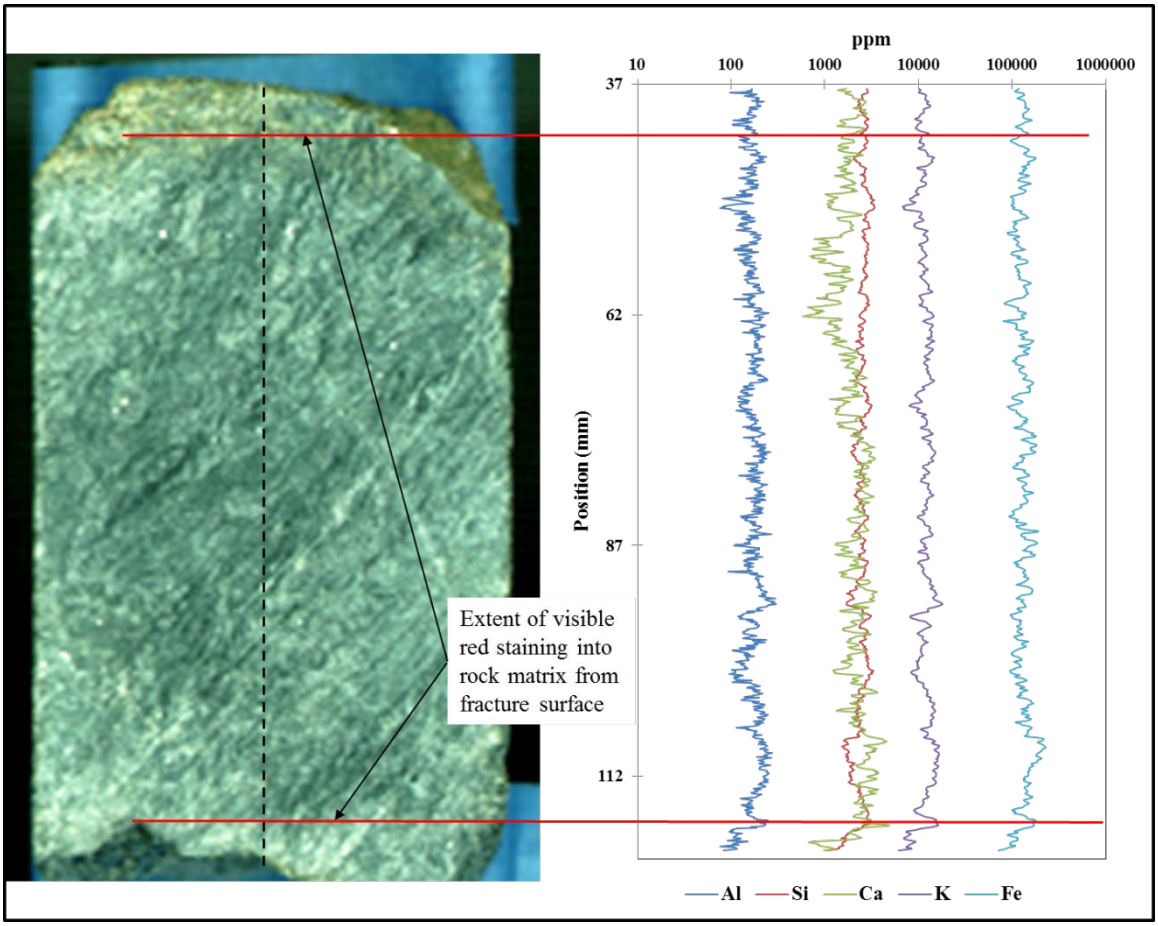

Figure 50: XRF aluminum, silicon, calcium, potassium, and iron intensities measured along core from 8.7 to 8.8 meters (28.7 to 28.9 feet) below ground surface. Image of core with scale provided to show location of measurements along split core sample.

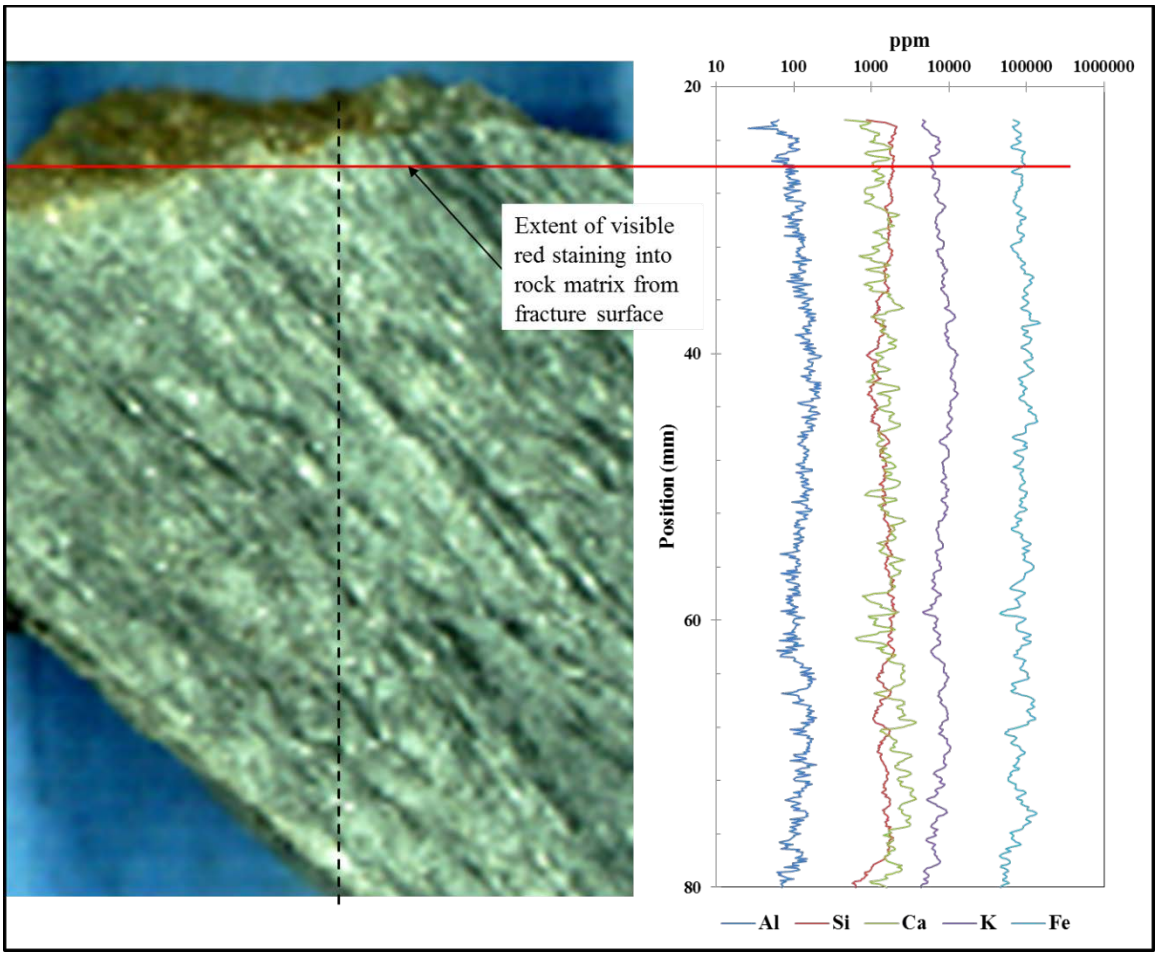

Figure 51: XRF aluminum, silicon, calcium, potassium, and iron intensities measured along core from 8.8 to 8.9 meters (28.9 to 29.1 feet) below ground surface. Image of core with scale provided to show location of measurements along split core sample.

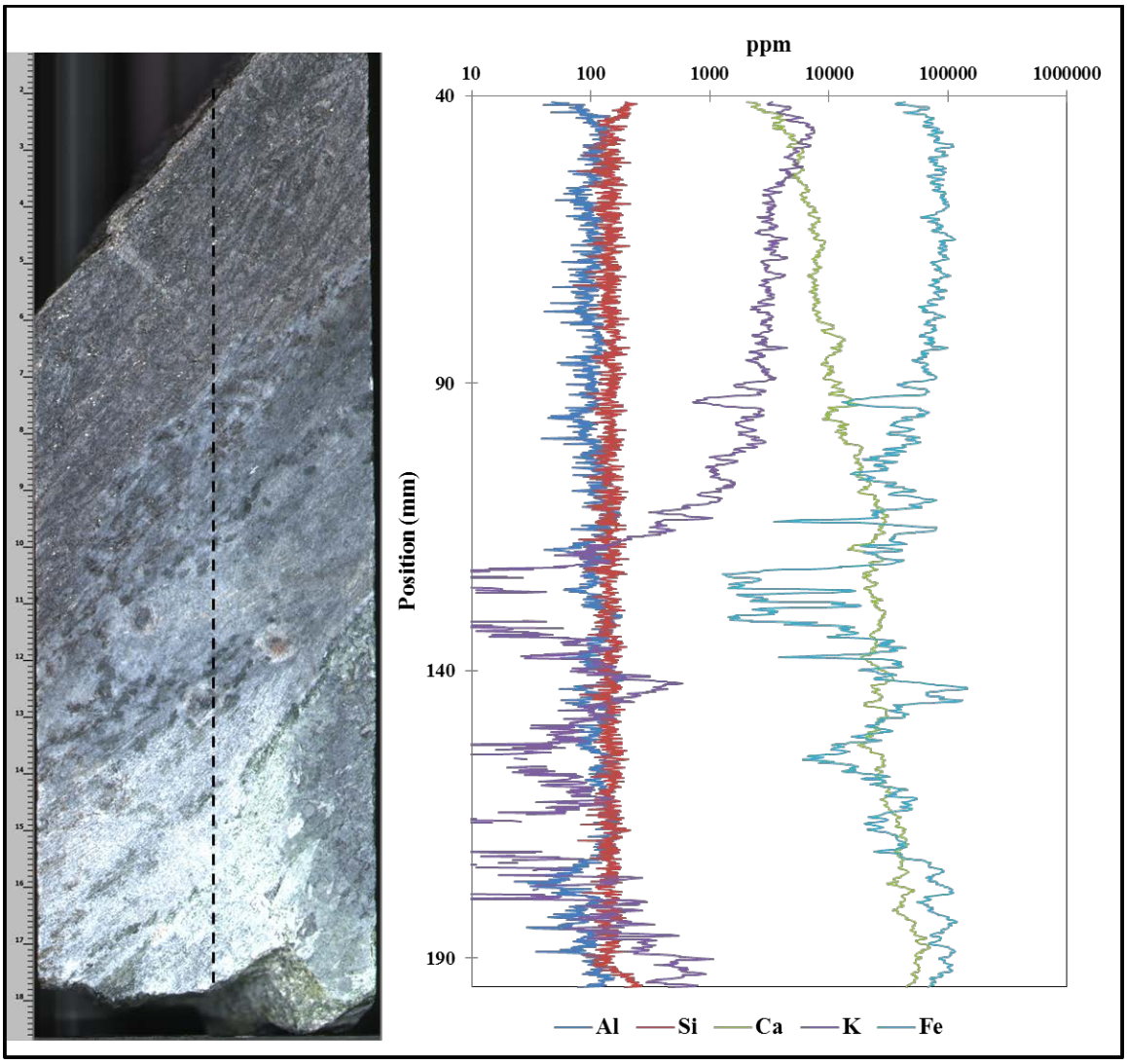

Figure 52: XRF aluminum, silicon, calcium, potassium, and iron intensities measured along core from 8.9 to 9.0 meters (29.2 to 29.5 feet) below ground surface. Image of core with scale provided to show location of measurements along split core sample.

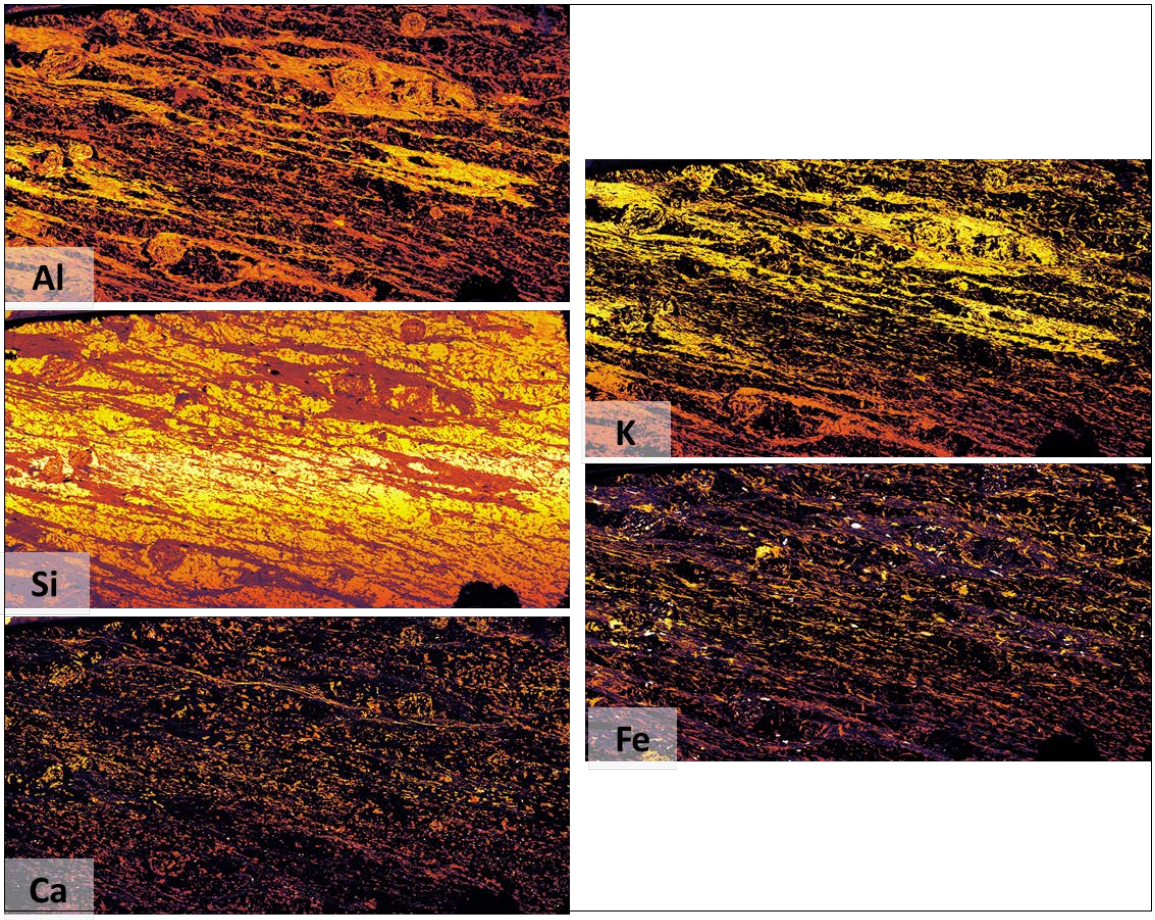

Figure 53. Element mapping of thin section sample from 8.4 meters (27.7 feet) below ground surface. The top edge of each image corresponds to a fracture surface with red staining in the zone of hydraulic activity. The bottom edge of the image corresponds to a zone of no staining within the rock matrix.

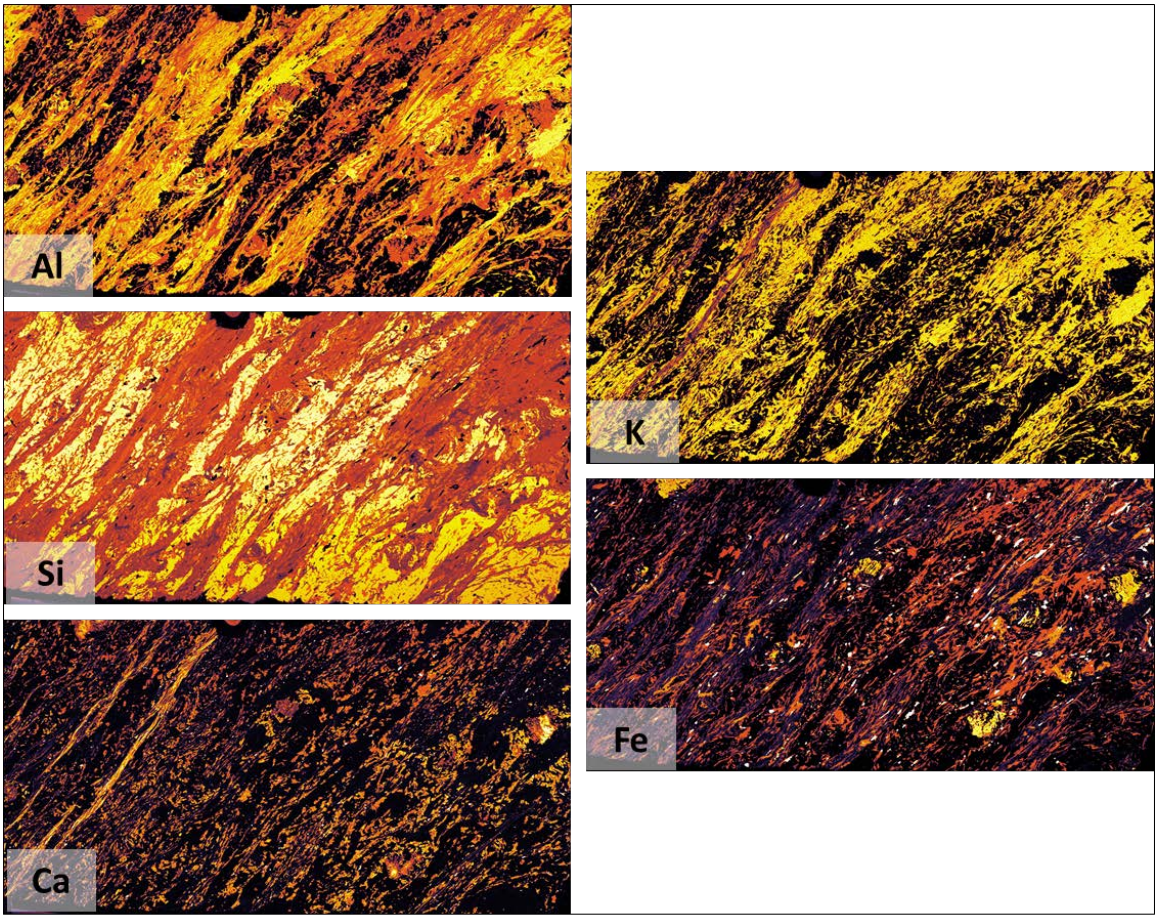

Figure 54: Element mapping of thin section sample from 8.7 meters (28.5 feet) below ground surface. The bottom edge of each image corresponds to a fracture surface with red staining in the zone of hydraulic activity and the top edge is toward the rock matrix.

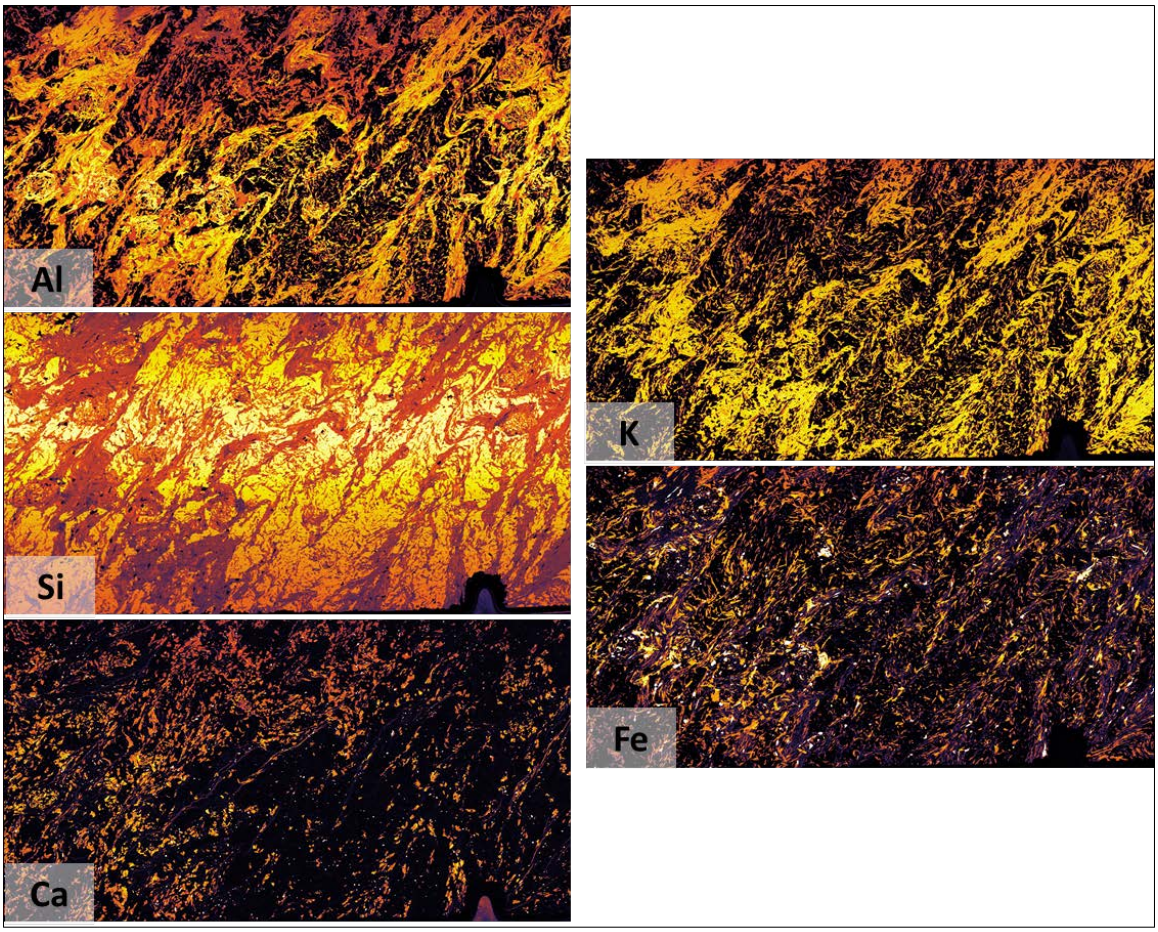

Figure 55: Element mapping of thin section sample from 8.7 meters (28.7 feet) below ground surface. The top edge of each image corresponds to a fracture surface with red staining in the zone of hydraulic activity and the bottom edge is toward the rock matrix.

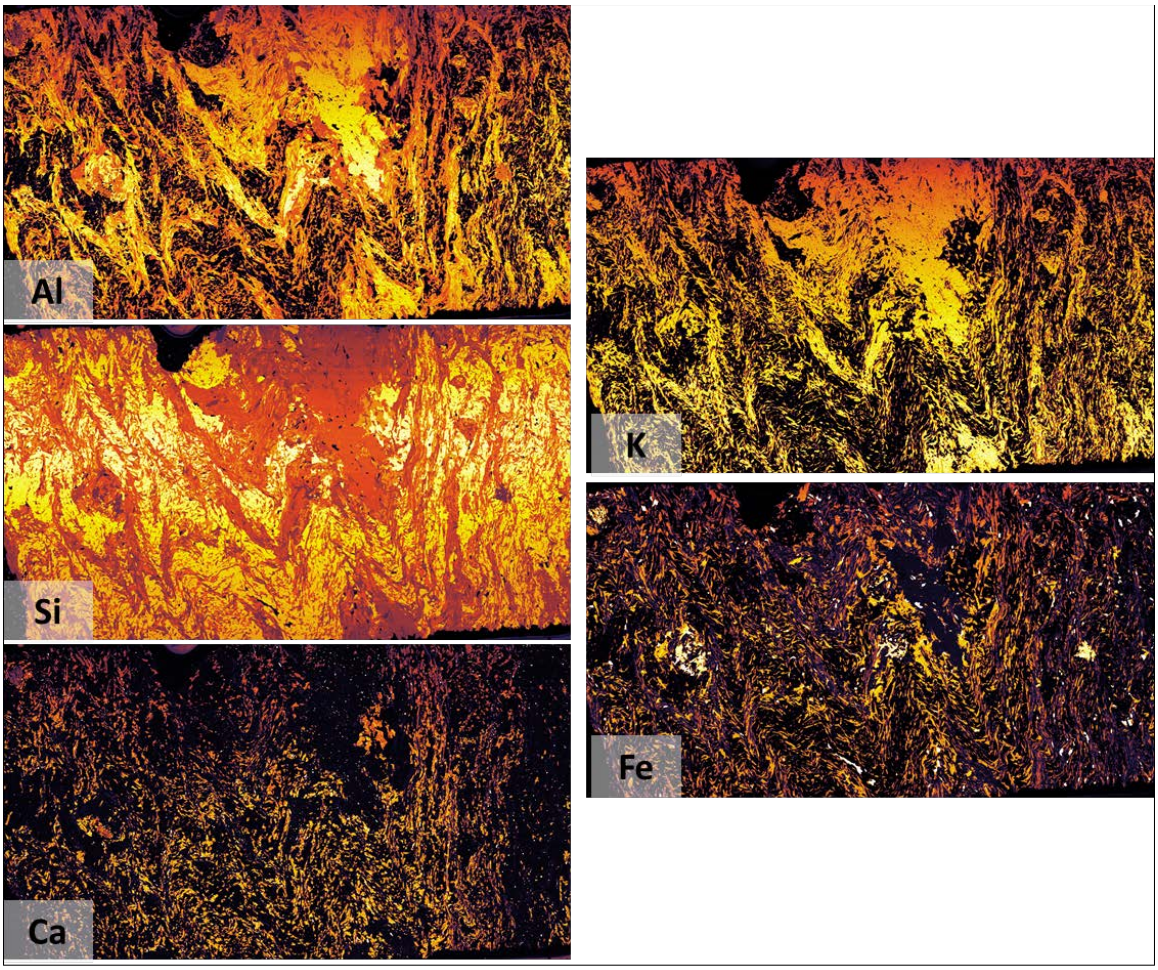

Figure 56: Element mapping of thin section sample from 9.6 meters (31.5 feet) below ground surface. The bottom and left edges of each image are toward a fracture surface with red staining. This sample is from outside of a zone of hydraulic activity.

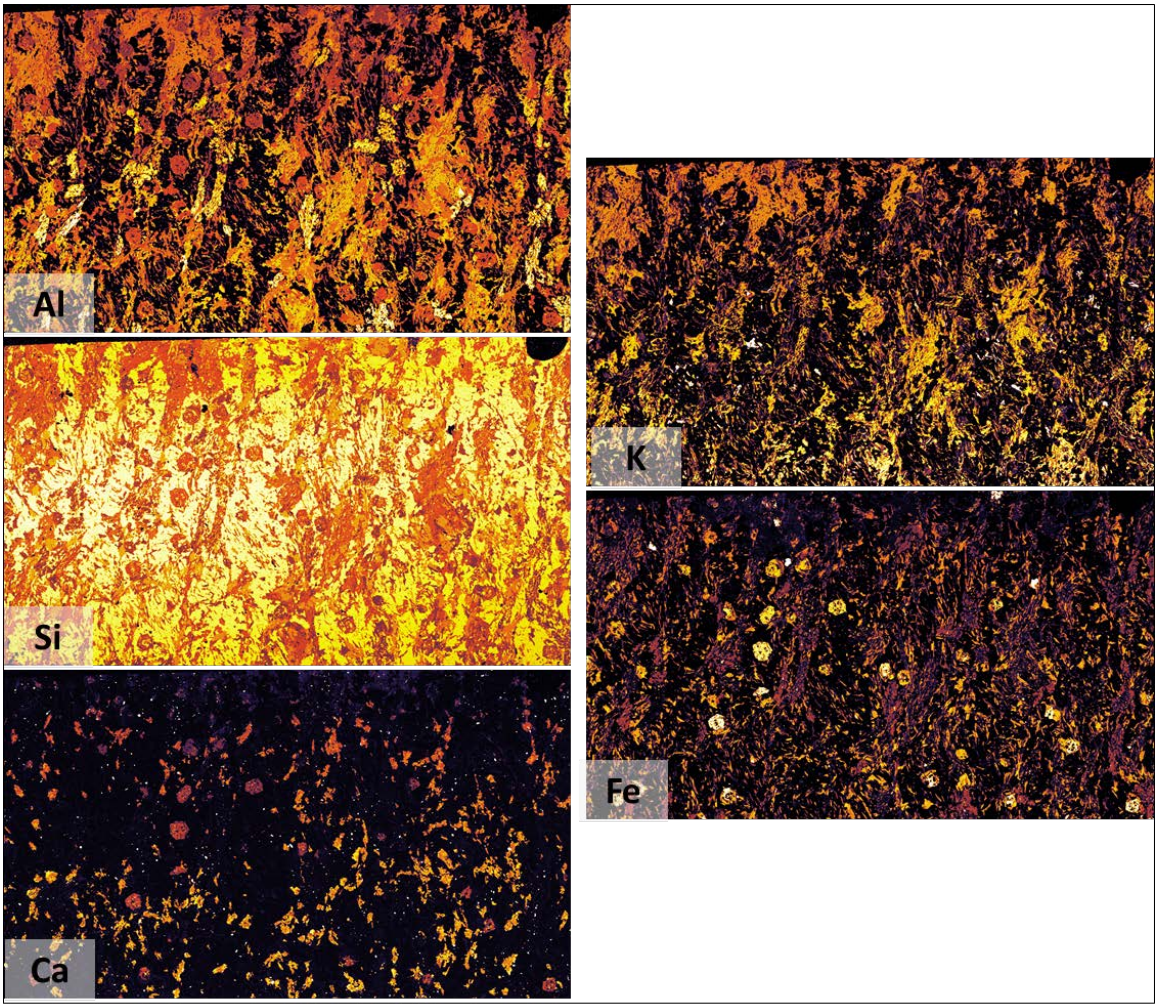

Figure 57: Element mapping of thin section sample from 17.3 meters (56.6 feet) below ground surface. This sample is from within the rock matrix away from a zone of hydraulic activity. Some staining was noted to exist on fractures cutting across foliation in this zone of the borehole.

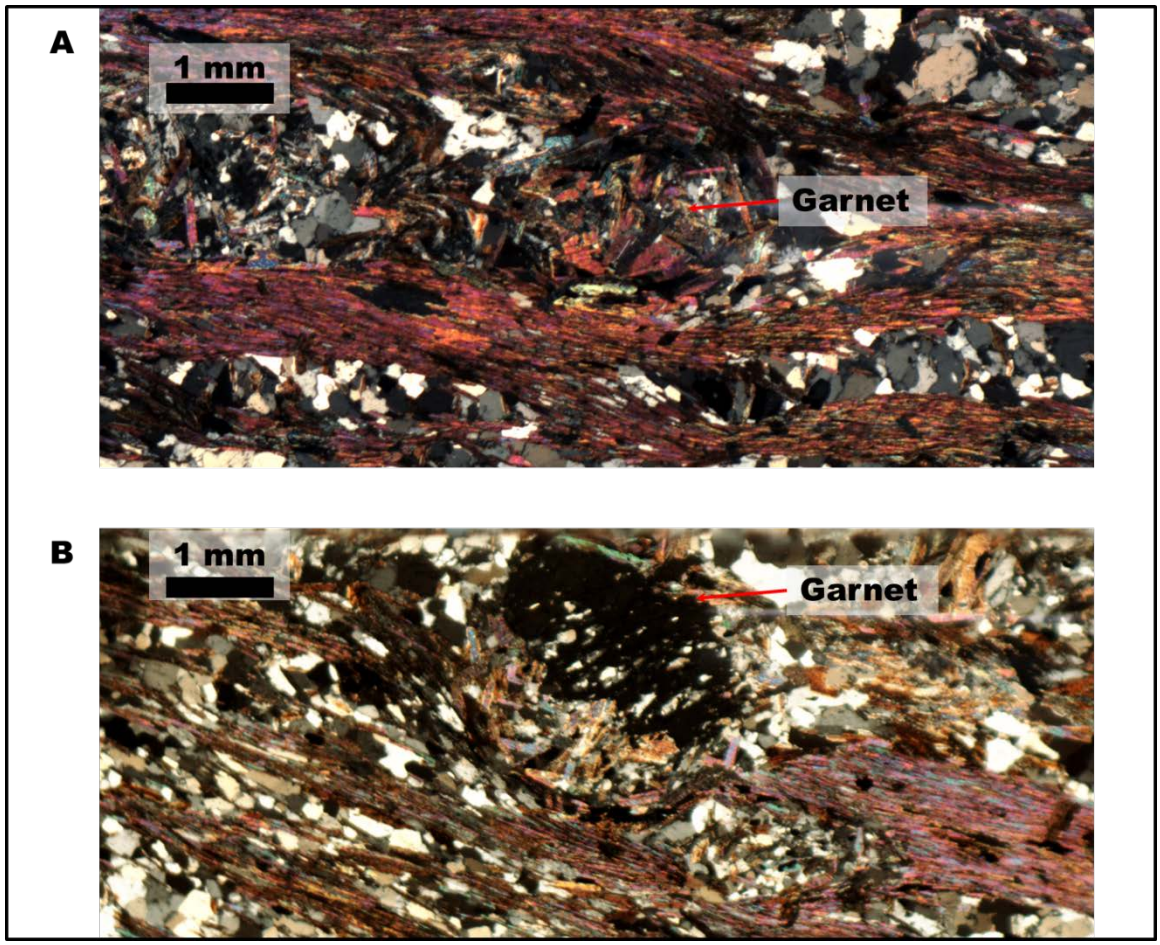

Figure 58: A. Psuedomorph garnet near fracture surface at 27.7 feet below ground surface. B. Unaltered irregularly grown garnet in matrix near same fracture at 27.7 feet bgs.

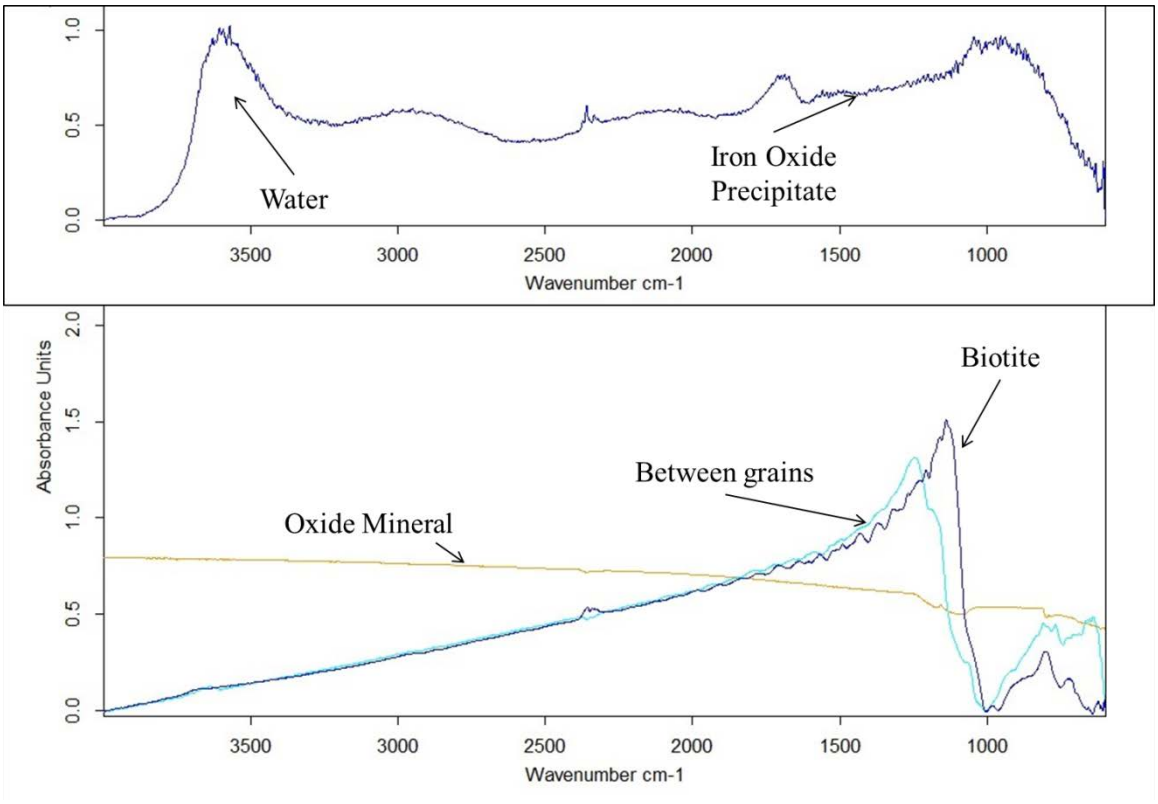

Figure 59: FT-IR scans of iron precipitate from Well MFS-1 and minerals in rock adjacent to hydraulically active fracture.

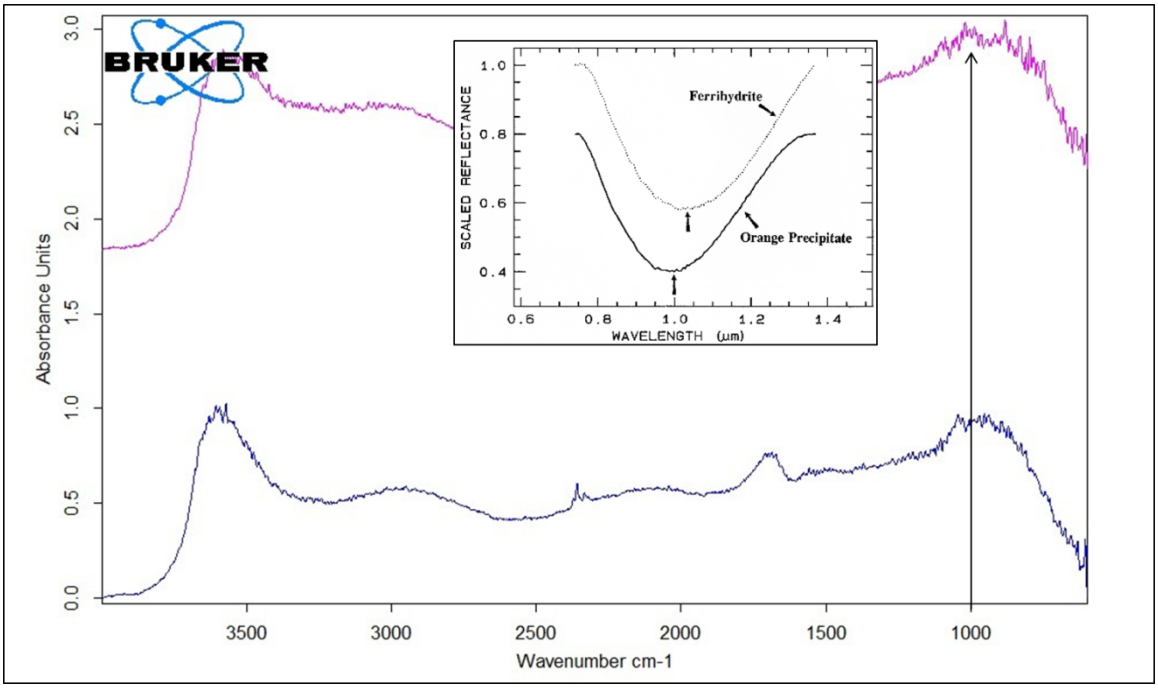

Figure 60: FT-IR scans of iron precipitate collected from samplers placed in Well MFS-1. The two scans are of the same sample which have been offset, the blue with atmospheric air present during scan and the purple after flushing with nitrogen gas. The inset (from Clark [1999]) provides reflectance of orange precipitate (amorphous iron hydroxide) and ferrihydrite for comparison of peaks.

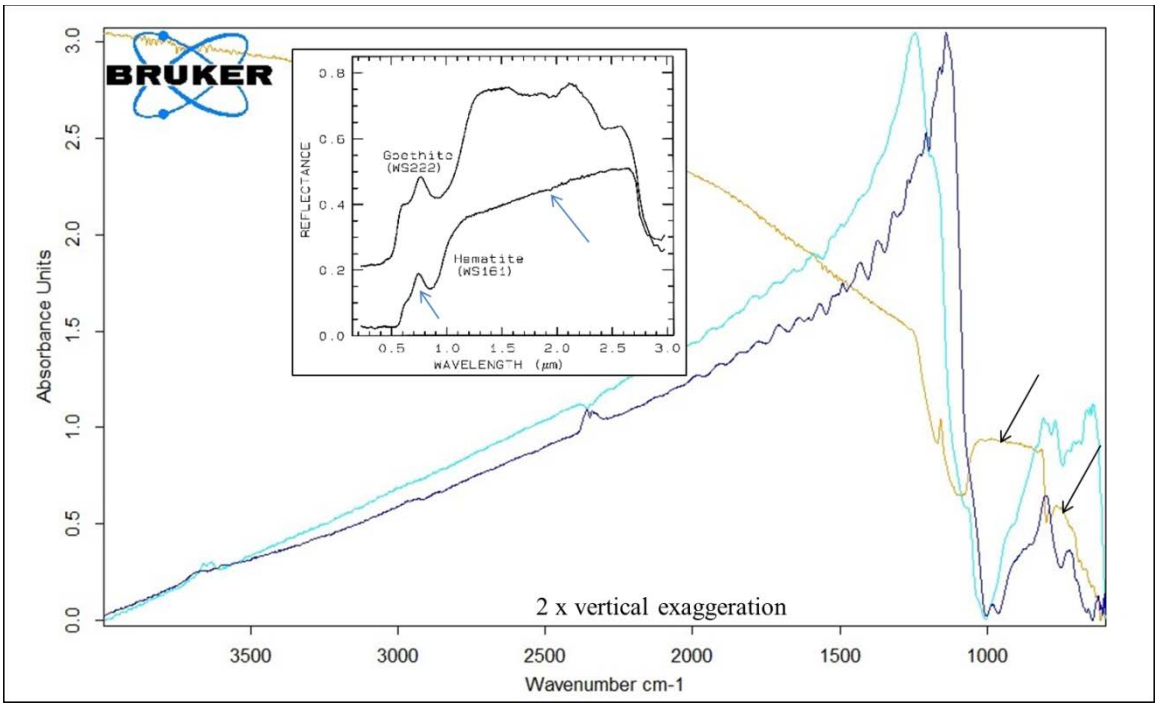

Figure 61: FT-IR scans of iron minerals present in rock adjacent to hydraulically active fracture from Well MFS-1. The blue line is a biotite grain, the aqua line is a mineral between biotite and quartz, and the brown is an iron oxide mineral. The inset provides IR spectrums for hematite and goethite (from Clark [199]) for comparison to the oxide mineral pattern.

CHAPTER 5

CONCLUDING REMARKS

The goals of this study are centered on the connection between the geochemistry of the geologic units in a crystalline bedrock aquifer and the groundwater quality in the aquifer, in an effort to improve our understanding of these systems and to provide additional characterization tools. Fractured bedrock aquifers present many challenges, including low porosity, preferential flow through the fractures, diffusion into and out of the rock matrix, that make characterization and development of water resources in these setting difficult. Effective development of resources from fractured bedrock aquifers requires identifying the small percentage of hydraulically active fractures and their connection to the broader hydrogeologic system. The framework for this study and answering the associated research questions was based on the presence of red staining on the surface of fractures and in the matrix of the rock adjacent to the fracture and its chemical composition.

It was hypothesized that the fracture coating/red staining of a hydraulically active fracture is thinner than a hydraulically inactive fracture due to the disequilibrium between the fracture and the water moving past the fracture surface. This hypothesis was proven to not be true. There was no discernable pattern related to the presence of red staining on the fracture surface and the presence of a zone of advective flow. The fractures were determined to be associated with four sets, two associated with the rock fabric (E-W and N-S oriented FPF) and two sets associated with tectonic stresses (NE-SW and NW-SE oriented sets) (Figure 11 and Table 11). All of the fracture sets have some fractures with staining on the fracture surface and some fractures without. Fractures outside of the hydraulically active zone were observed to have red staining (Chapter 4), though there was

less observed red staining in the matrix adjacent to inactive fractures. The matrix associated with hydraulically active fractures exhibited a zone of red staining adjacent to the fracture and that extended up to 25 millimeters into the matrix. However, based on the oxide mineral identified (hematite), the source of that red staining is more likely to be high temperature alteration than low temperature precipitation. Therefore, it has been concluded that the red staining on the fracture surface is not indicative of advective flow under the current hydrologic condition.

The source of the red staining was also investigated using the hypothesis that the red staining in the matrix associated with a hydraulically active fracture is the result of oxygen present in the water that is diffused into the rock matrix, oxidizing the iron present in the rock. The groundwater data collected and observations from Well MFS-1 (Chapter 2), as well as the simulated transport of oxygen along a single fracture (Chapter 3) do not fully support this hypothesis. The groundwater data suggests that it is limited in free oxygen and may be between the Zones A and B as shown on Figure 16, where there is some oxygen available, but it is readily consumed by higher redox elements, such as manganese. The iron in the groundwater system therefore is primarily in the reduced form (ferrous), which is readily precipitated out of solution in the well due to the oxygen interface at the borehole or the diffusion samplers. The modeling of oxygen transport highlighted the short transport distances of oxygen in a fractured bedrock setting when diffusion is dominant. Advective transport of oxygen can be quite long (Figure 35), but only if no reactions are consuming the oxygen supplied with the recharge water. When weathering reactions such as those represented by the mineralogy present at the MacLeish Field Station, oxygen consumption would be expected to further limit the amount transport within a fractured bedrock aquifer.

Therefore the conclusion could be that the current groundwater system is not the source of the red staining due to the lack of oxygen transport.

The results of the rock core testing partially support the hypothesis that hydraulically active fractures host both dissolution and precipitation reactions due to departure from equilibrium, where inactive fractures will be subject to only precipitation. The elemental changes (aluminum, calcium, iron, and potassium) measured along the core of hydraulically active fractures showed increases toward the fracture which can be concluded to represent precipitation (Chapter 4). Approximately half of the samples from the zone of hydraulically active fractures also showed a decrease in elemental concentration (aluminum, calcium, and potassium) both from the XRF measurements and the element map from the electron microprobe, supporting the conclusion that dissolution is also occurring from the fracture surface. The water quality measurements collected from Well MFS-1 are representative of the weathering of the minerals observed to be present in the bedrock (Chapter 2), also supporting the conclusion that dissolution reactions are occurring as water is transported along the fracture surface. The reason this hypothesis is only partially proven is related to the inactive fractures. No pattern of geochemical characteristics were observed from the fractures in inactive zones of the well from either the rock core samples or the water quality testing.

The final hypothesis of this study tried to better relate the residence time of groundwater in the system to the geochemical observations from the rock. Specifically, it was hypothesized that the depth of the red staining and rate of diffusion of oxygen into the rock can be used to determine the minimum amount of time that the fracture has been actively transporting water. This hypothesis was also shown to not be true based on the

results of this study. The modeling showed that oxygen transport by diffusion is so fast that it reaches nearly its maximum depth into the rock matrix within one day. Therefore, the rate of diffusion of oxygen into the rock matrix and the associated oxidation of ferrous to ferric iron provides no indication of the amount of time water has been advectively flowing through the specific fractures. Under advective transport conditions the oxygen would also be expected to flow significant distances over a very short period of time, or to be limited by reactions shortly after entering the saturated portion of the system, also not providing a reliable way to relate transport distance to amount of time of transport. Based on the observations from the rock core, it was concluded that the presence of red staining in the matrix may not be due to the current hydrologic system, but is due to past hydrothermal flow within the system.

APPENDIX A

STIFF DIAGRAMS OF MFS-1 DISCRETE INTERVAL SAMPLING

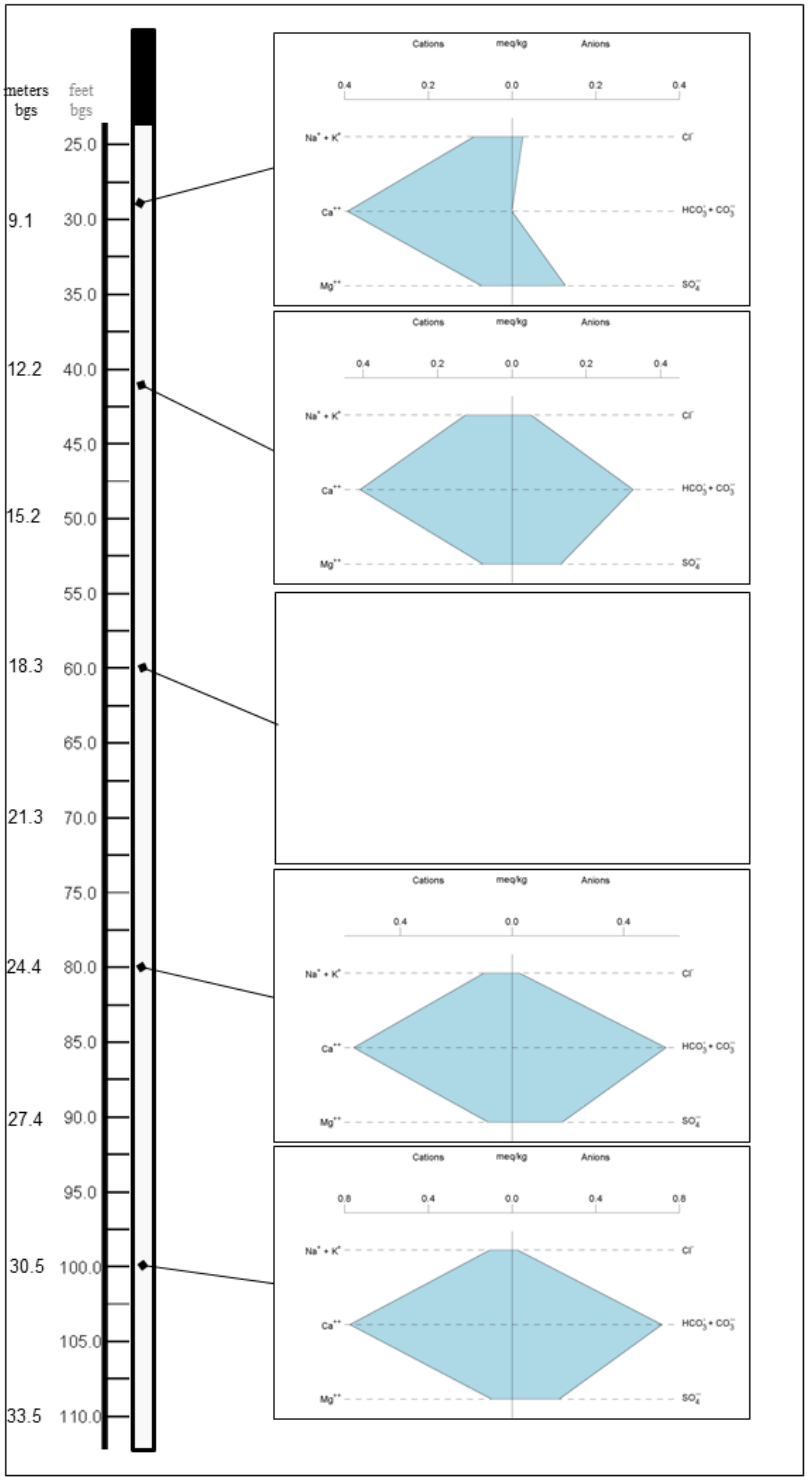

Figure A1: Stiff diagram for July 2013 discrete interval sampling of open borehole well MFS-1, located at the Smith College Ada & Archibald MacLeish Field Station, in Whately, Massachusetts. Note that no sampler was deployed at a depth of 60 feet and total alkalinity was not measured for the 28 foot depth due to an insufficient quantity of sample.

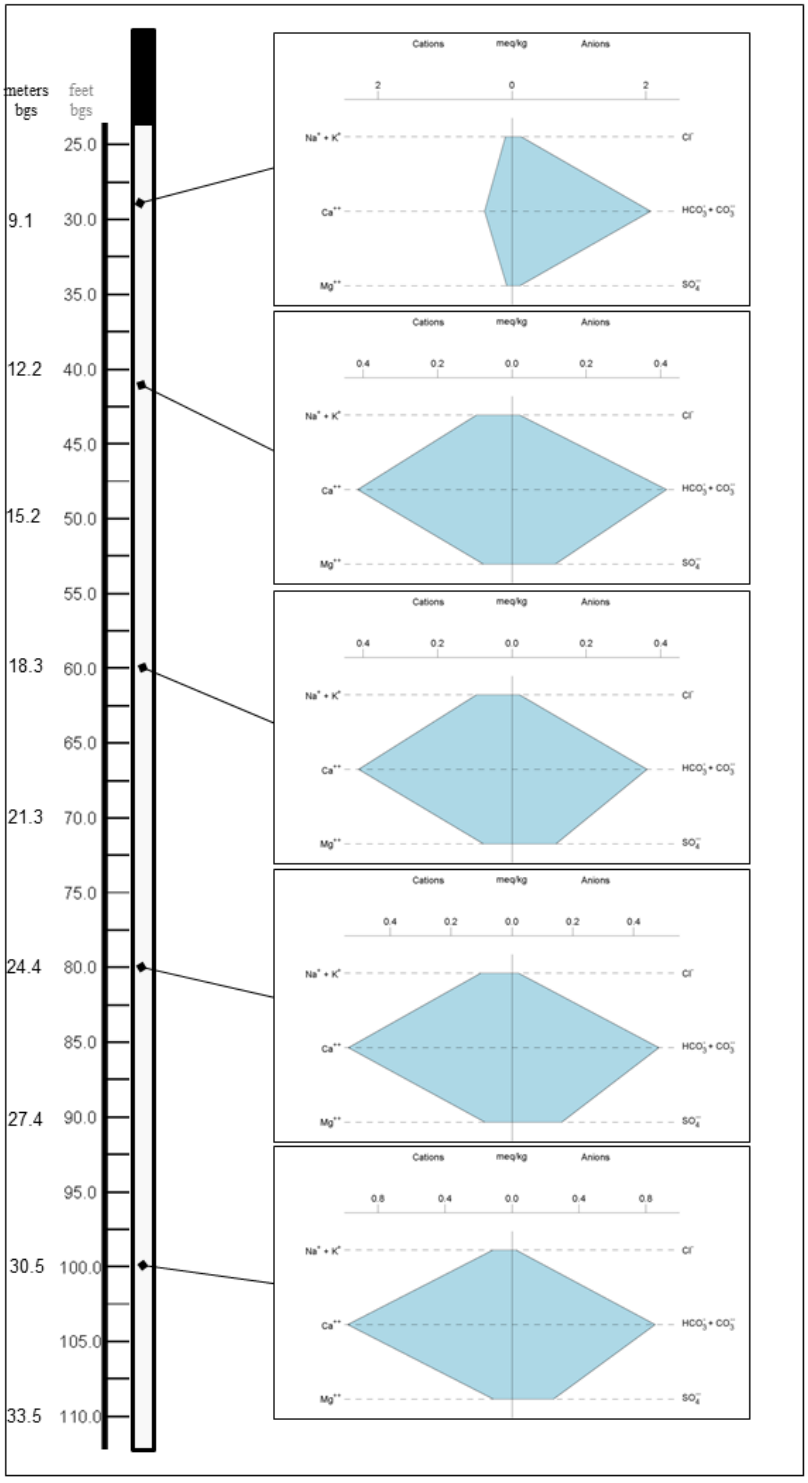

Figure A2: Stiff diagram for August 2013 discrete interval sampling of open borehole well MFS-1, located at the Smith College Ada & Archibald MacLeish Field Station, in Whately, Massachusetts.

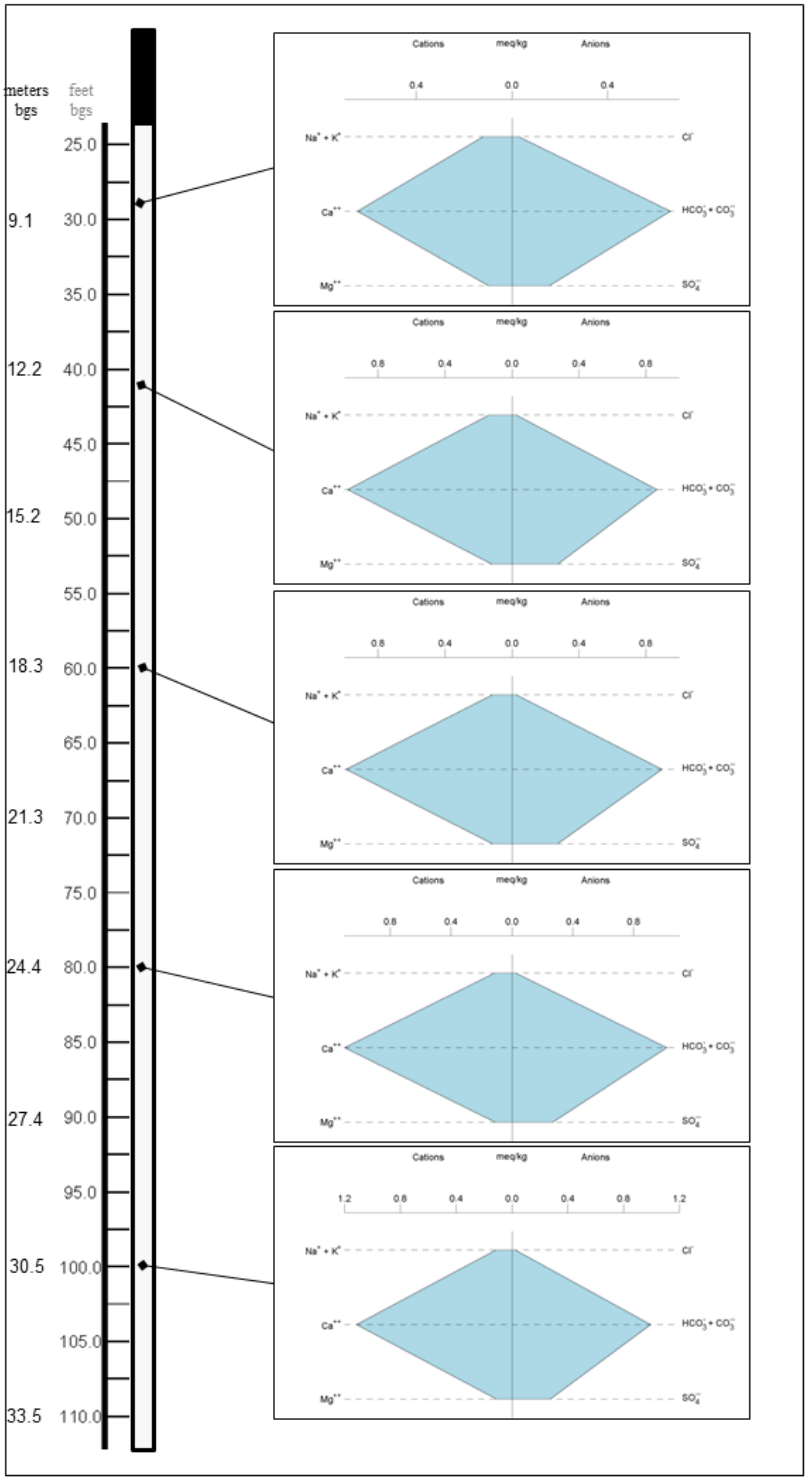

Figure A3: Stiff diagram for September 2013 discrete interval sampling of open borehole well MFS-1, located at the Smith College Ada & Archibald MacLeish Field Station, in Whately, Massachusetts.

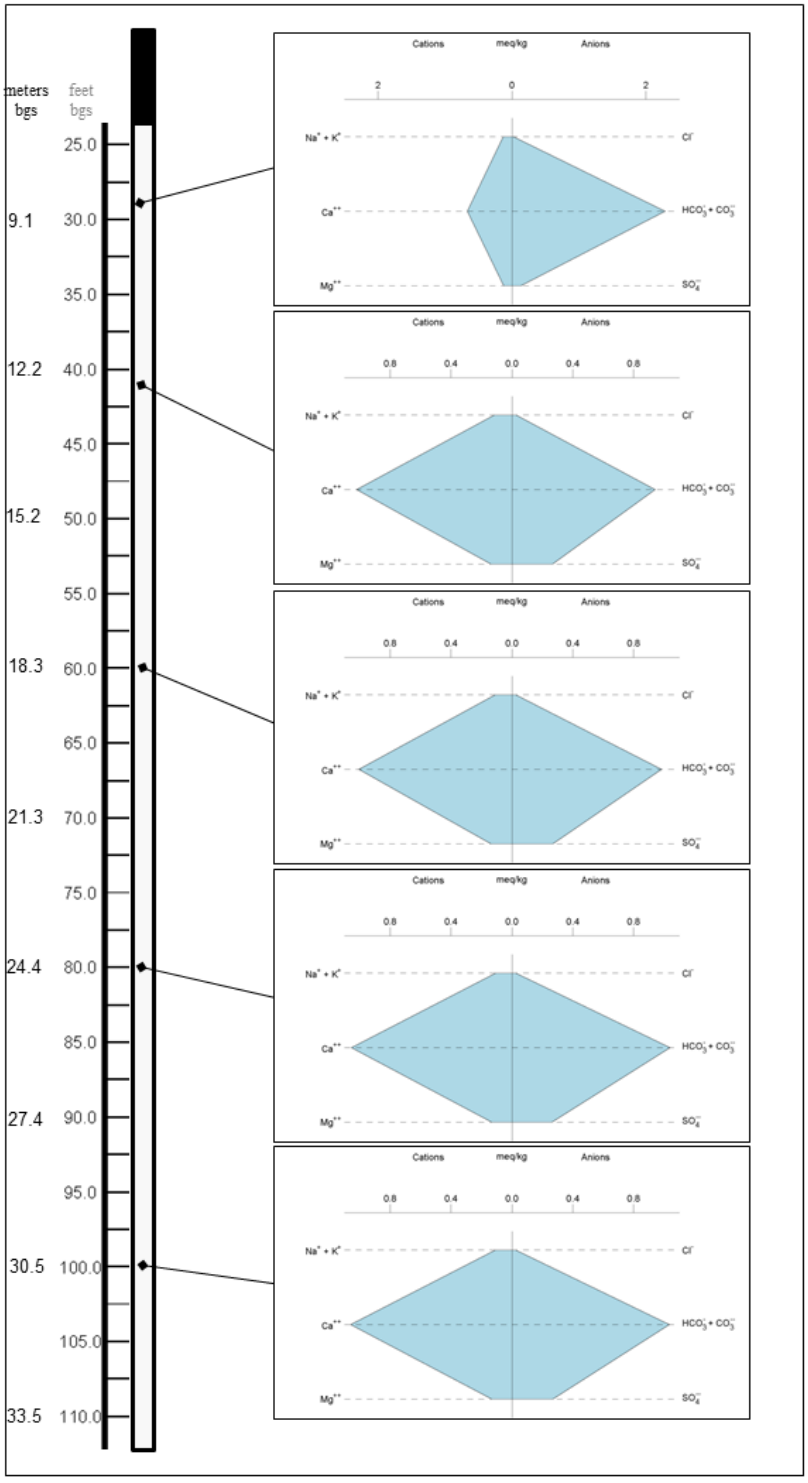

Figure A4: Stiff diagram for October 2013 discrete interval sampling of open borehole well MFS-1, located at the Smith College Ada & Archibald MacLeish Field Station, in Whately, Massachusetts.

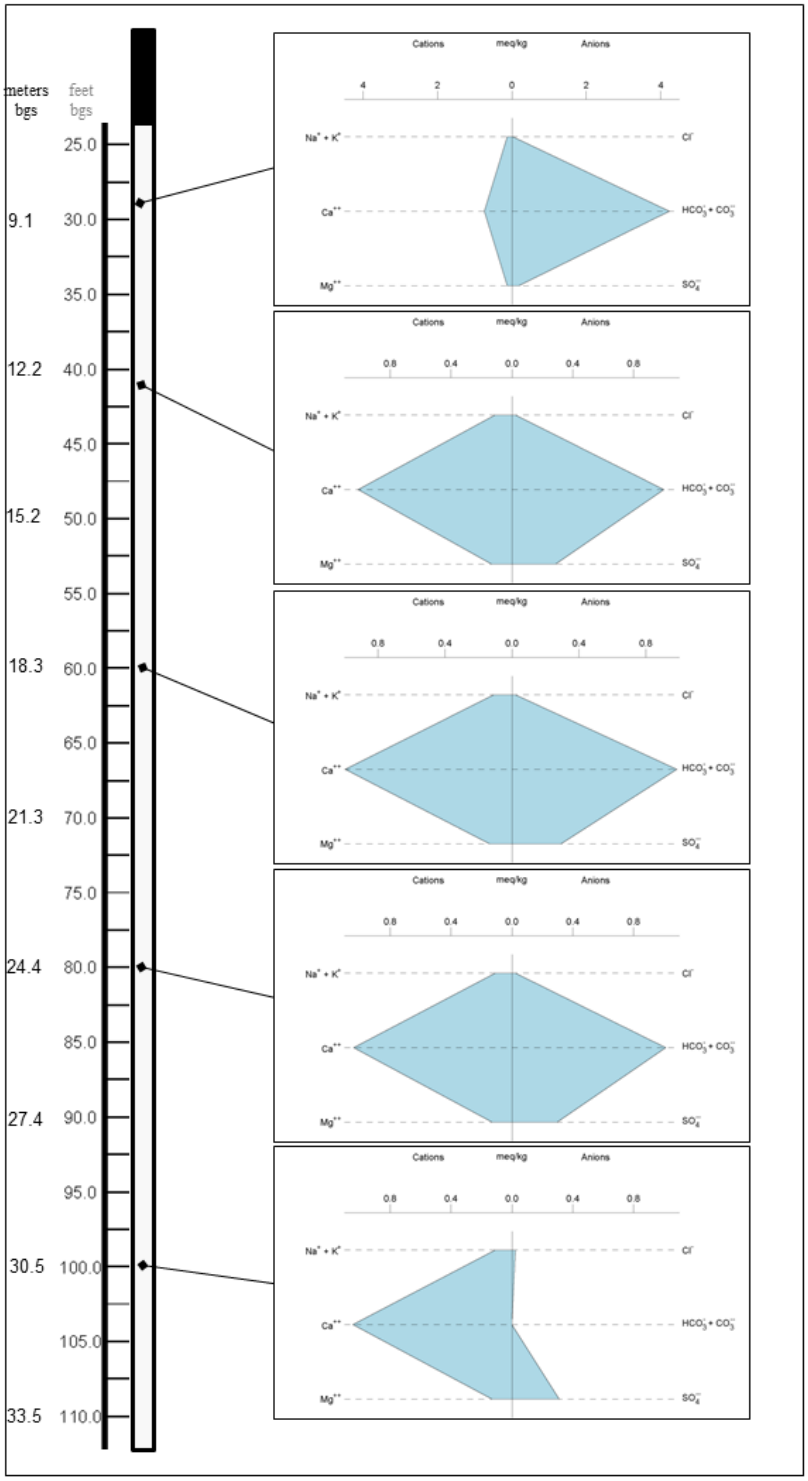

Figure A5: Stiff diagram for November 2013 discrete interval sampling of open borehole well MFS-1, located at the Smith College Ada & Archibald MacLeish Field Station, in Whately, Massachusetts. Note that total alkalinity was not measure for the 100 foot depth due to an instrument error.

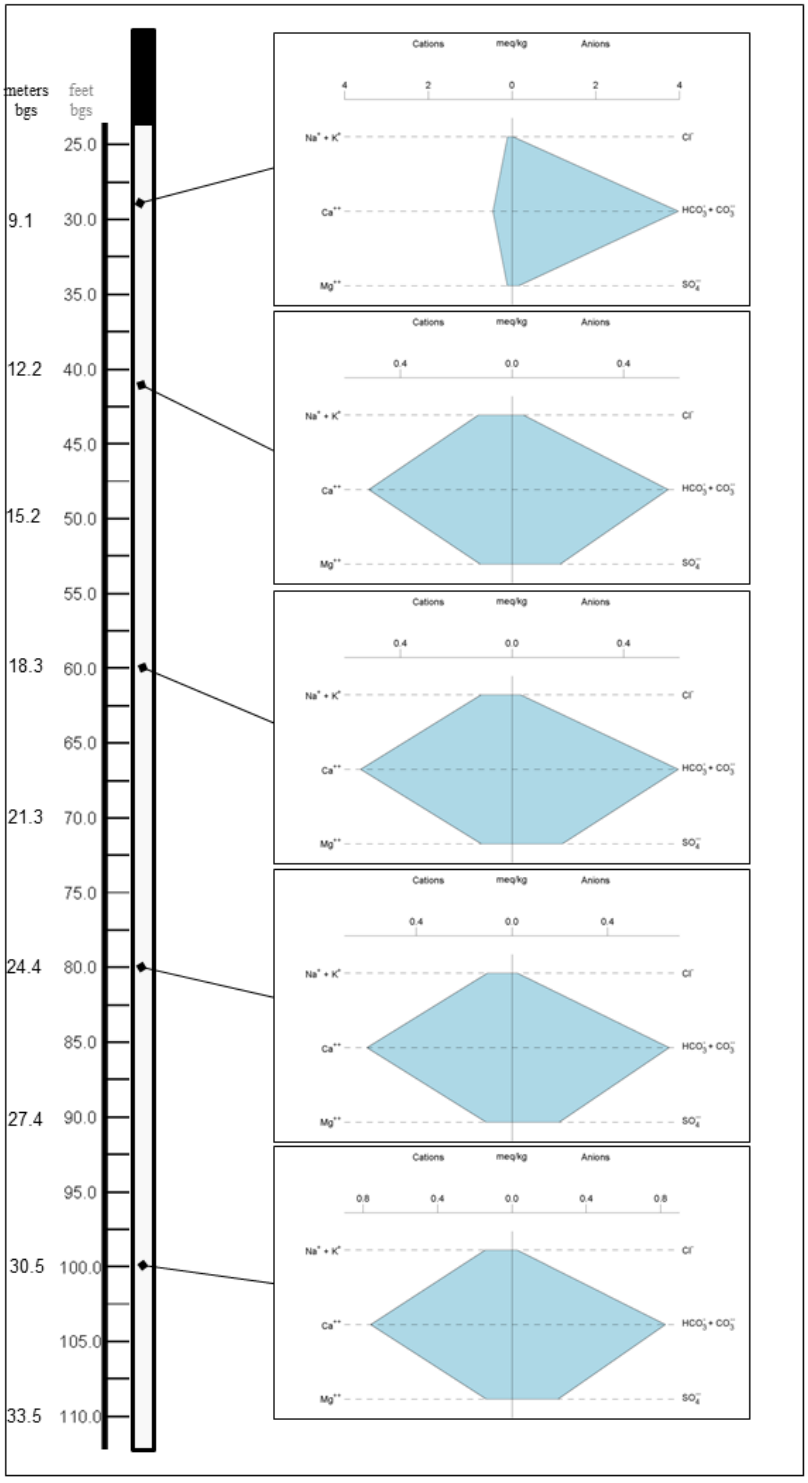

Figure A6: Stiff diagram for December 2013 discrete interval sampling of open borehole well MFS-1, located at the Smith College Ada & Archibald MacLeish Field Station, in Whately, Massachusetts.

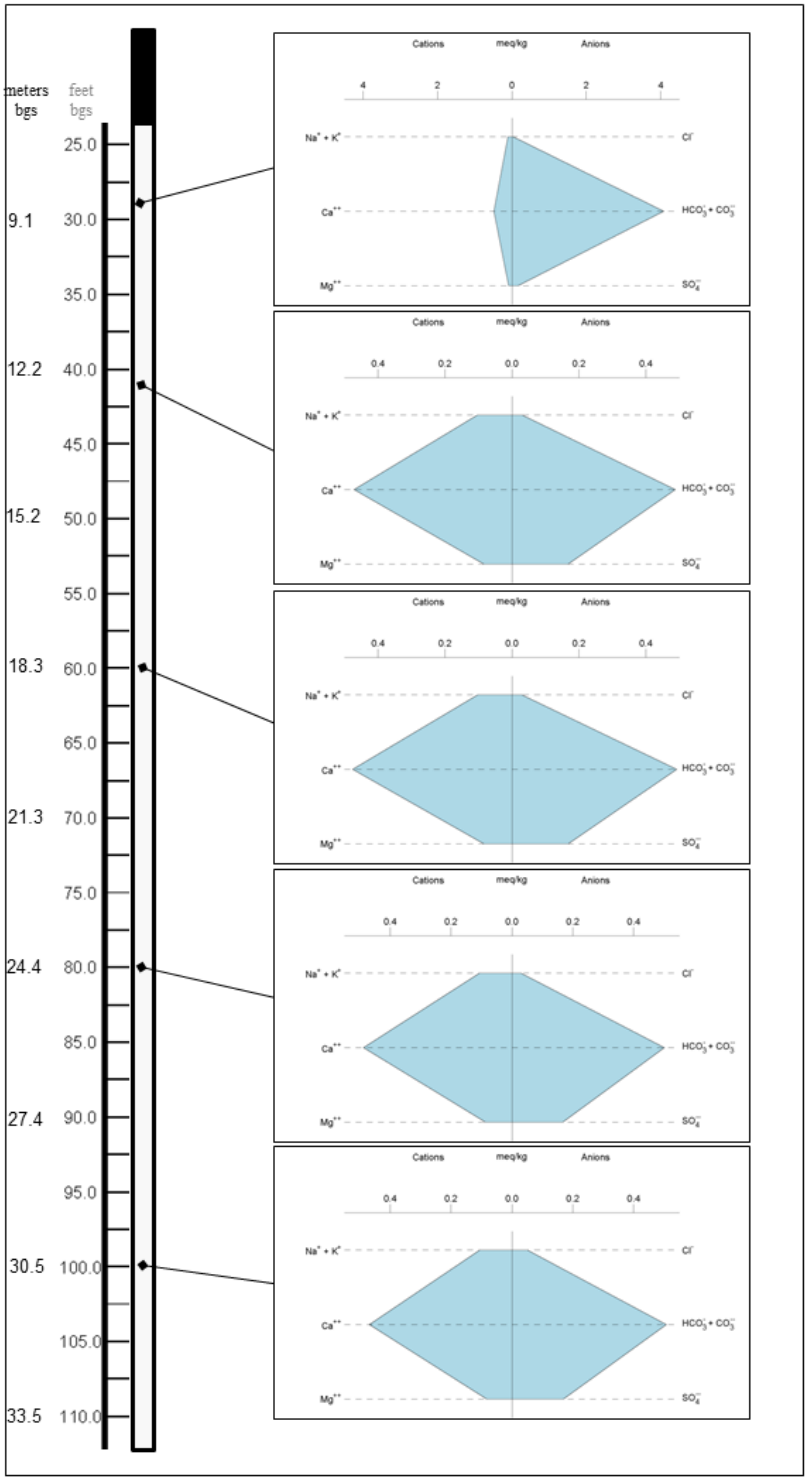

Figure A7: Stiff diagram for January 2014 discrete interval sampling of open borehole well MFS-1, located at the Smith College Ada & Archibald MacLeish Field Station, in Whately, Massachusetts.

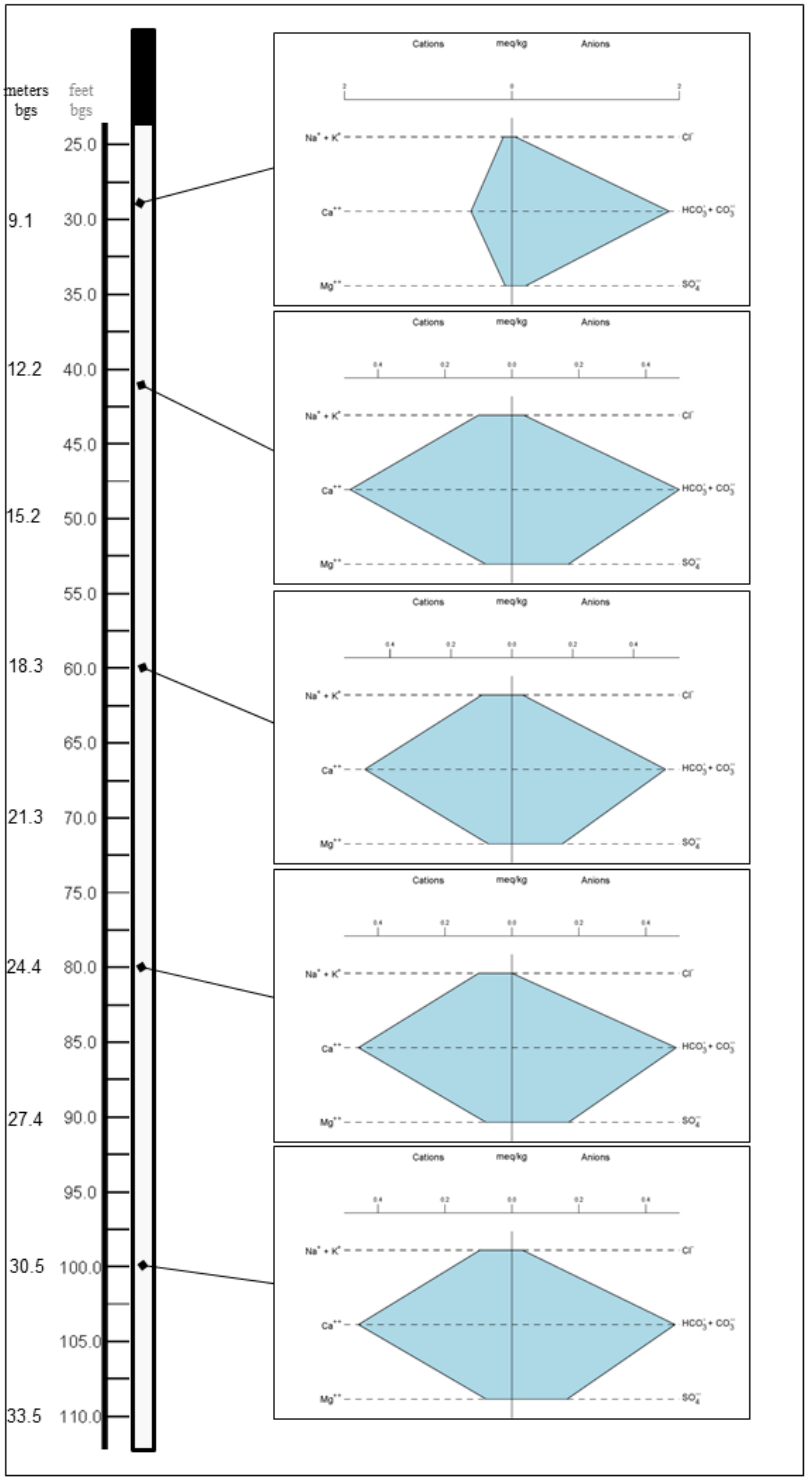

Figure A8: Stiff diagram for February 2014 discrete interval sampling of open borehole well MFS-1, located at the Smith College Ada & Archibald MacLeish Field Station, in Whately, Massachusetts.

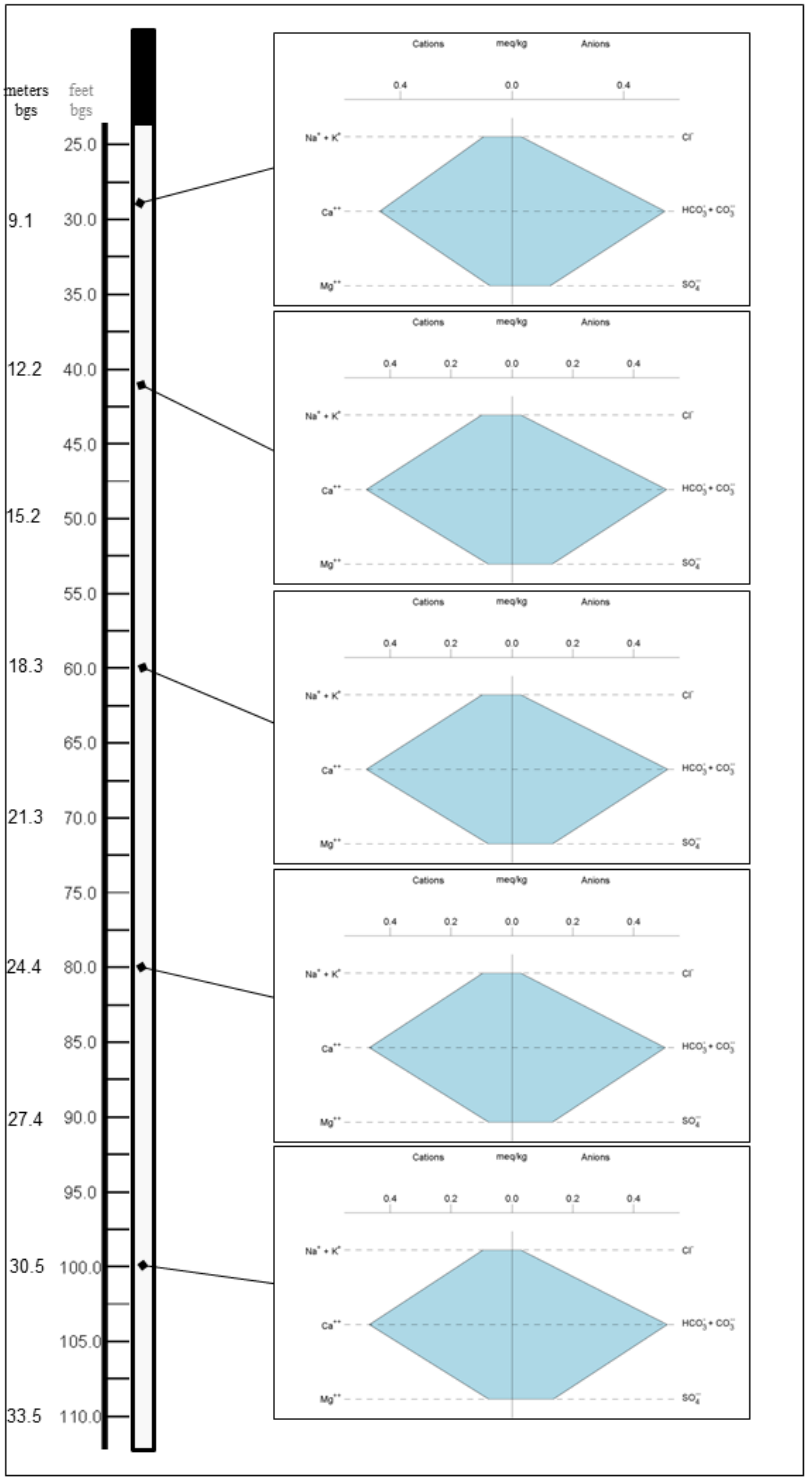

Figure A9: Stiff diagram for March 2014 discrete interval sampling of open borehole well MFS-1, located at the Smith College Ada & Archibald MacLeish Field Station, in Whately, Massachusetts.

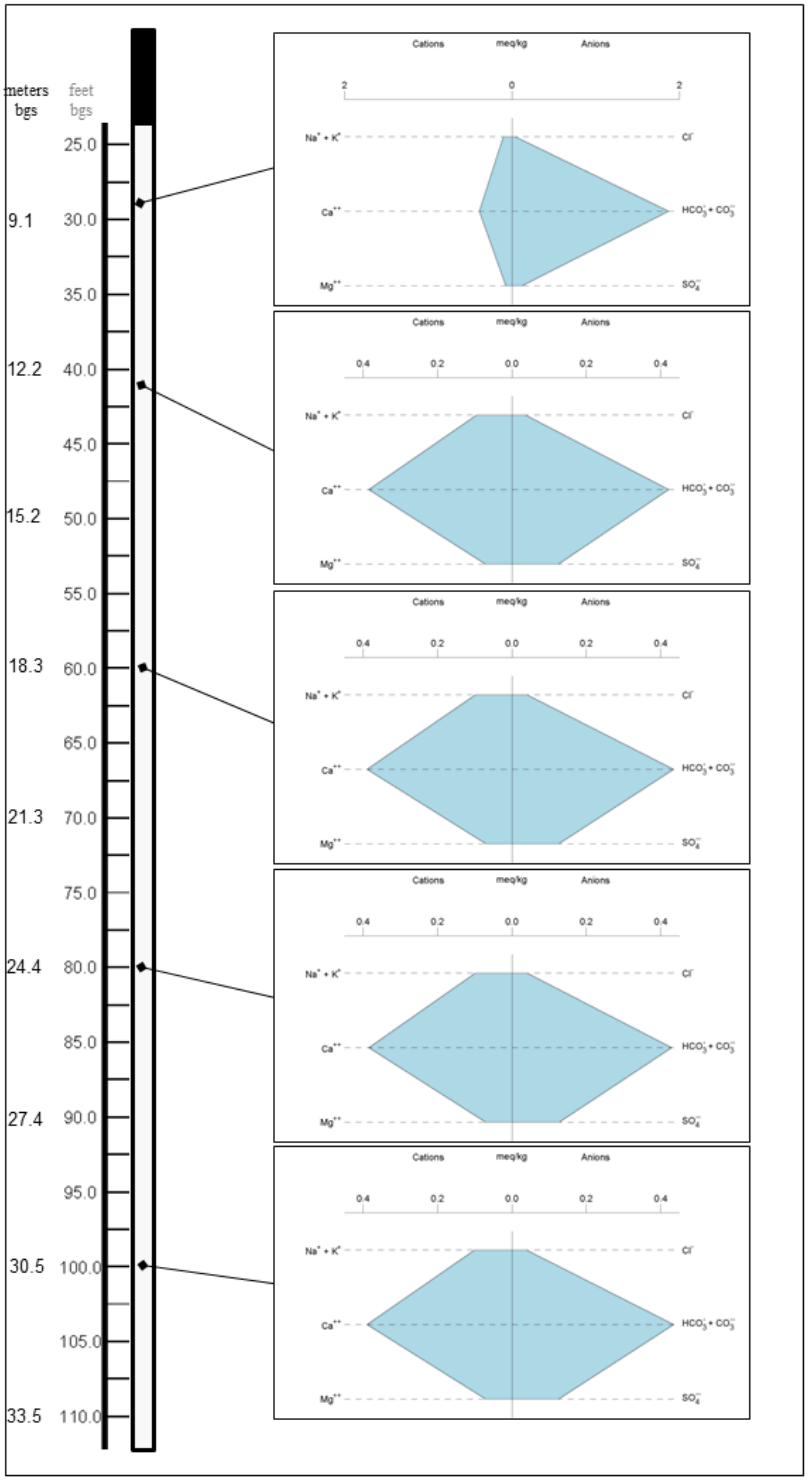

Figure A10: Stiff diagram for April 2014 discrete interval sampling of open borehole well MFS-1, located at the Smith College Ada & Archibald MacLeish Field Station, in Whately, Massachusetts.

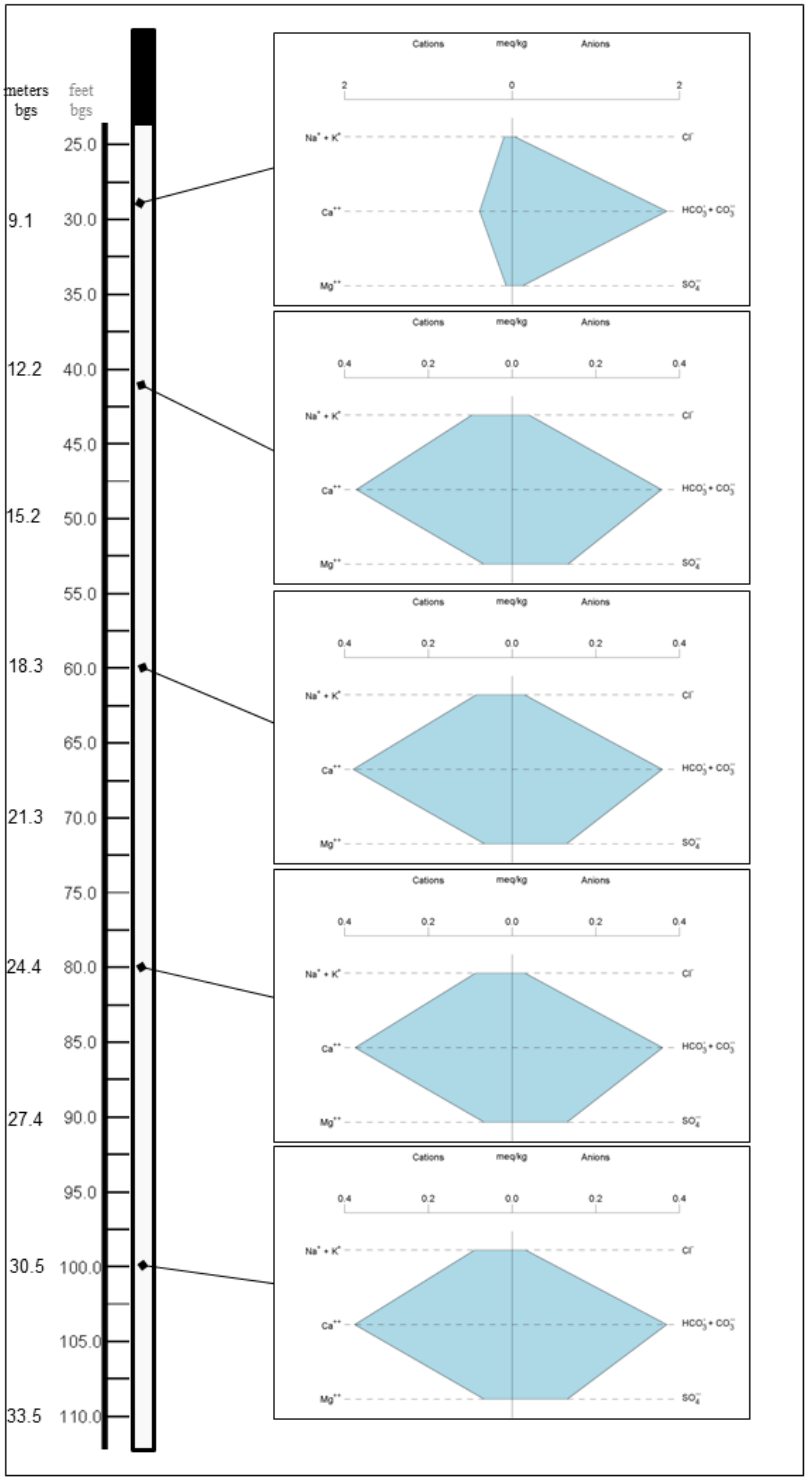

Figure A11: Stiff diagram for May 2014 discrete interval sampling of open borehole well MFS-1, located at the Smith College Ada & Archibald MacLeish Field Station, in Whately, Massachusetts.

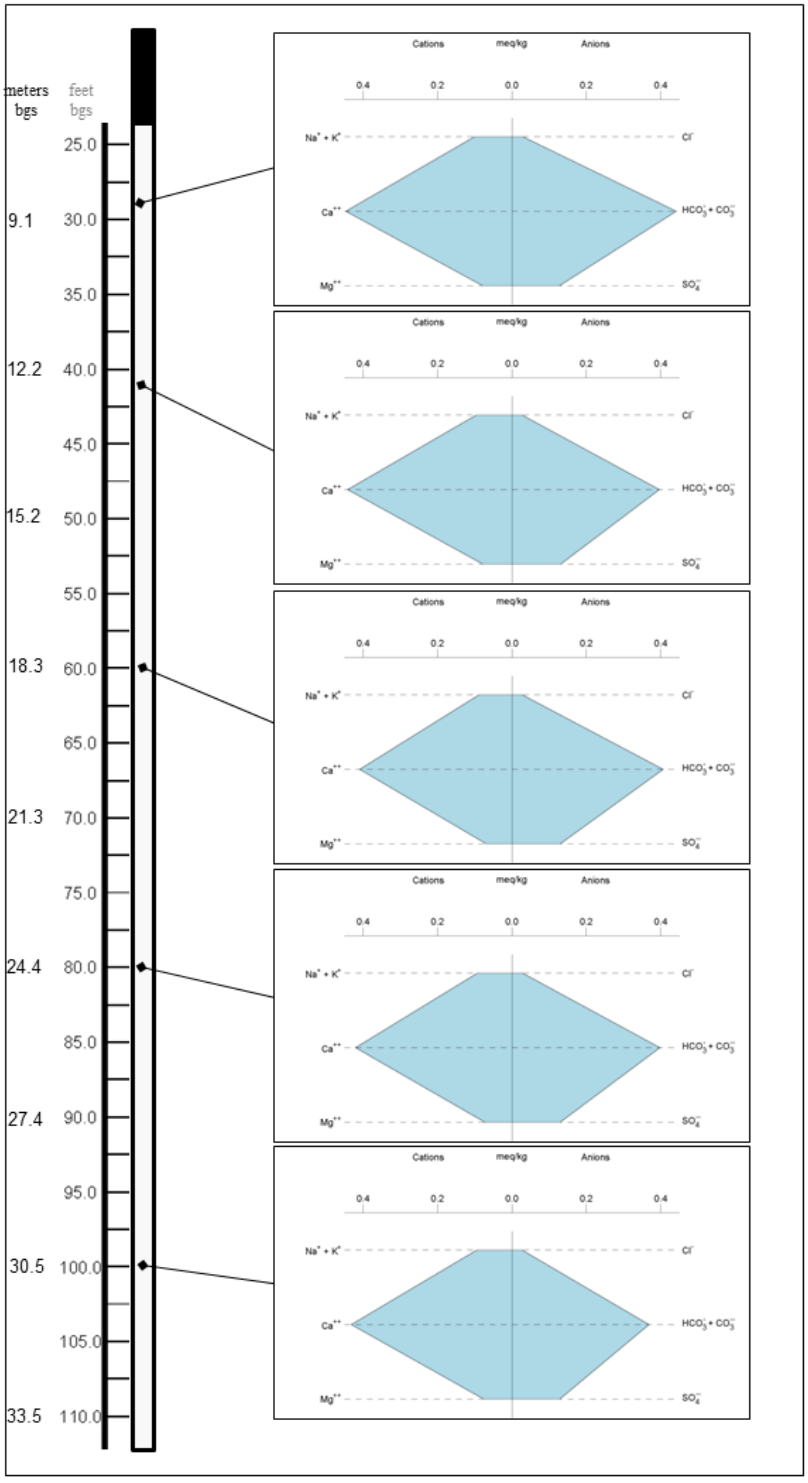

Figure A12: Stiff diagram for June 2014 discrete interval sampling of open borehole well MFS-1, located at the Smith College Ada & Archibald MacLeish Field Station, in Whately, Massachusetts.

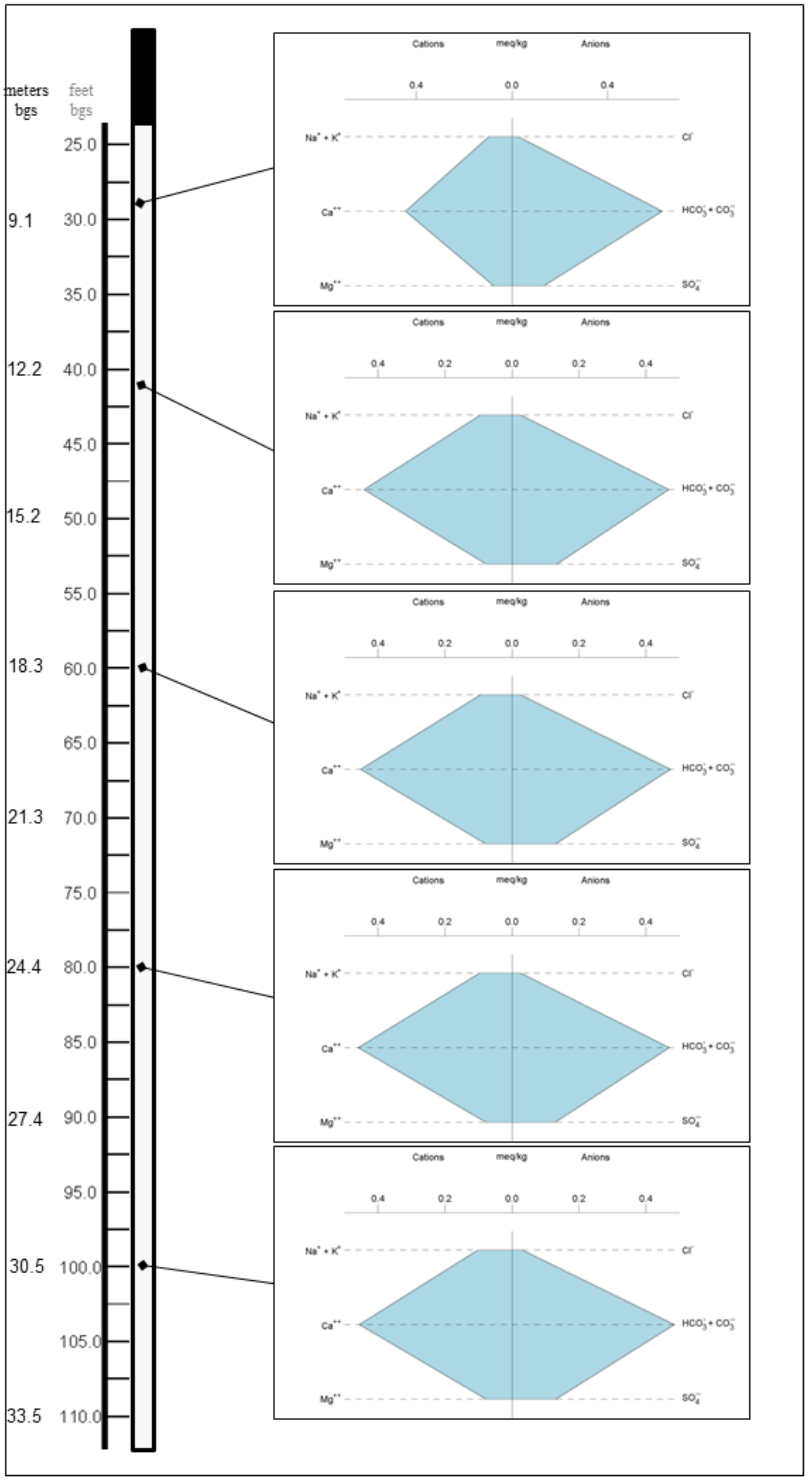

Figure A13: Stiff diagram for July 2014 discrete interval sampling of open borehole well MFS-1, located at the Smith College Ada & Archibald MacLeish Field Station, in Whately, Massachusetts.

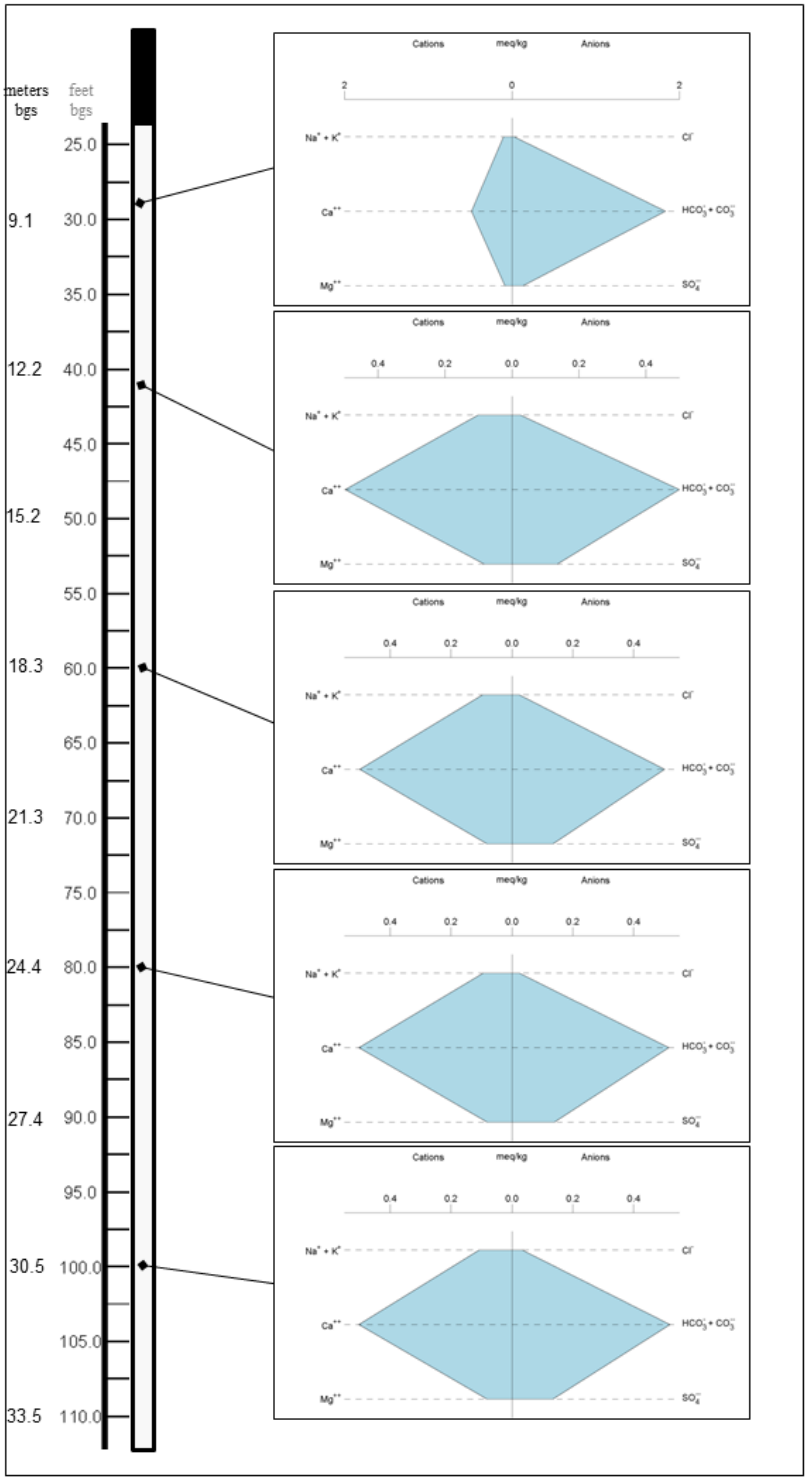

Figure A14: Stiff diagram for August 2014 discrete interval sampling of open borehole well MFS-1, located at the Smith College Ada & Archibald MacLeish Field Station, in Whately, Massachusetts.

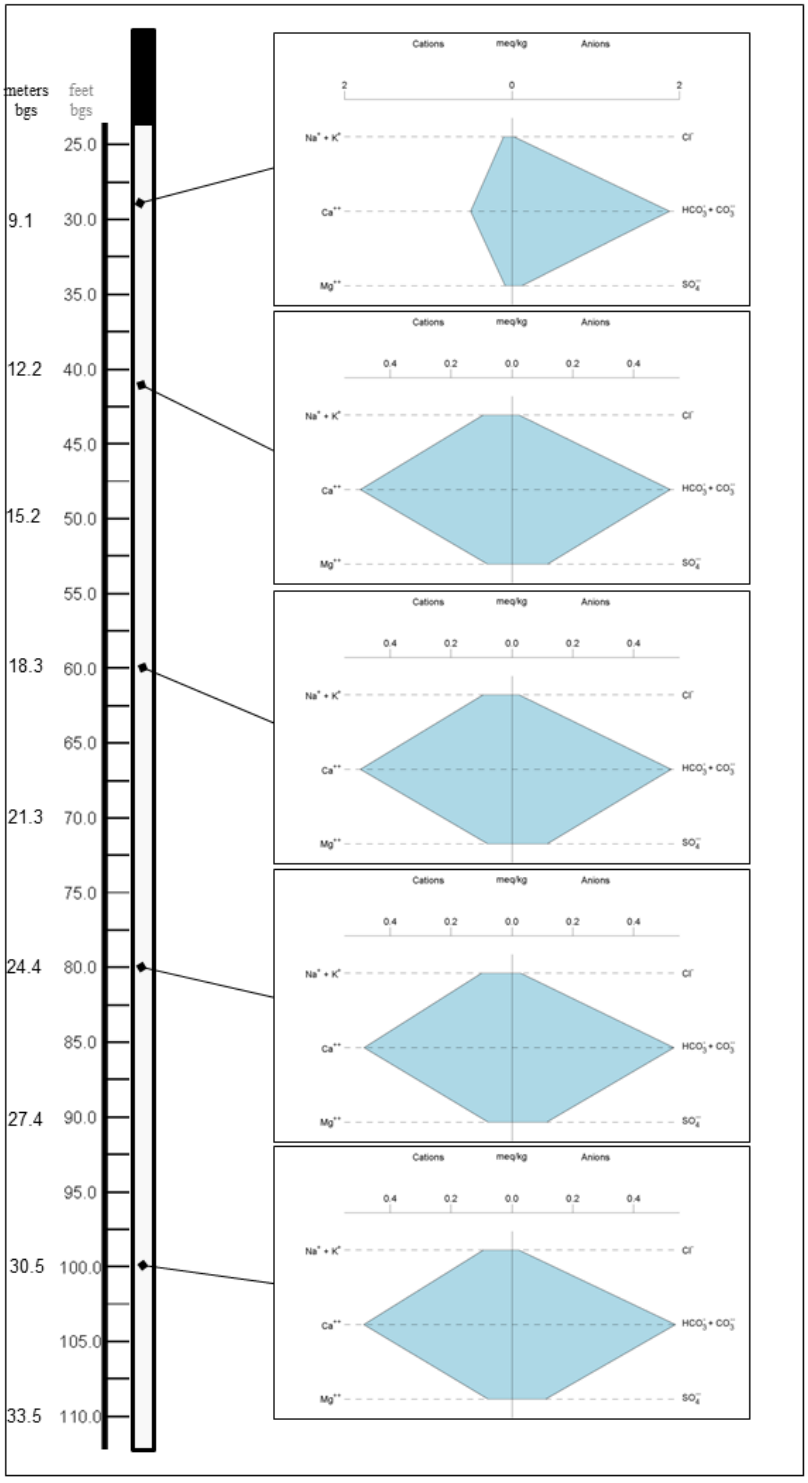

Figure A15: Stiff diagram for September 2014 discrete interval sampling of open borehole well MFS-1, located at the Smith College Ada & Archibald MacLeish Field Station, in Whately, Massachusetts.

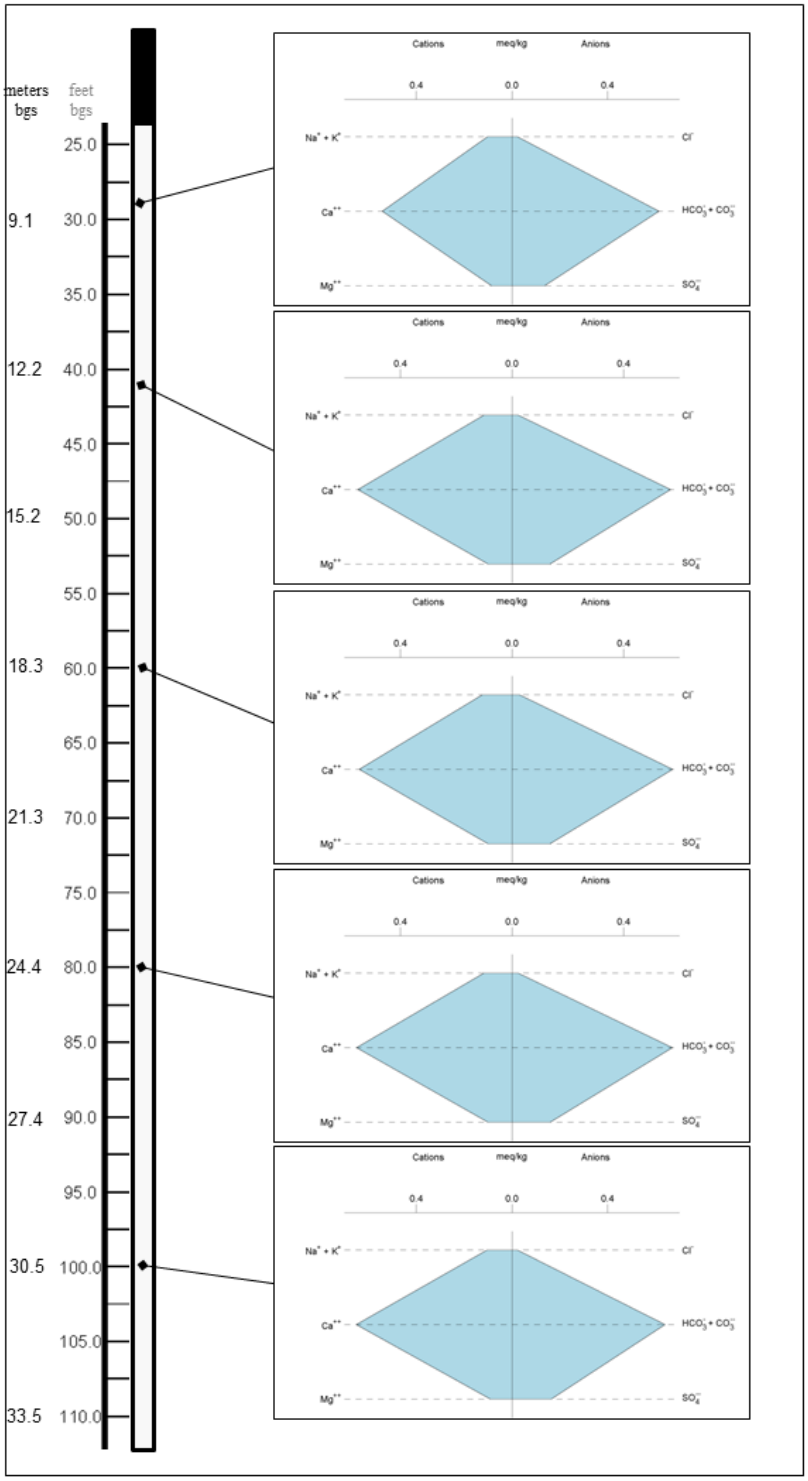

Figure A16: Stiff diagram for October 2014 discrete interval sampling of open borehole well MFS-1, located at the Smith College Ada & Archibald MacLeish Field Station, in Whately, Massachusetts.

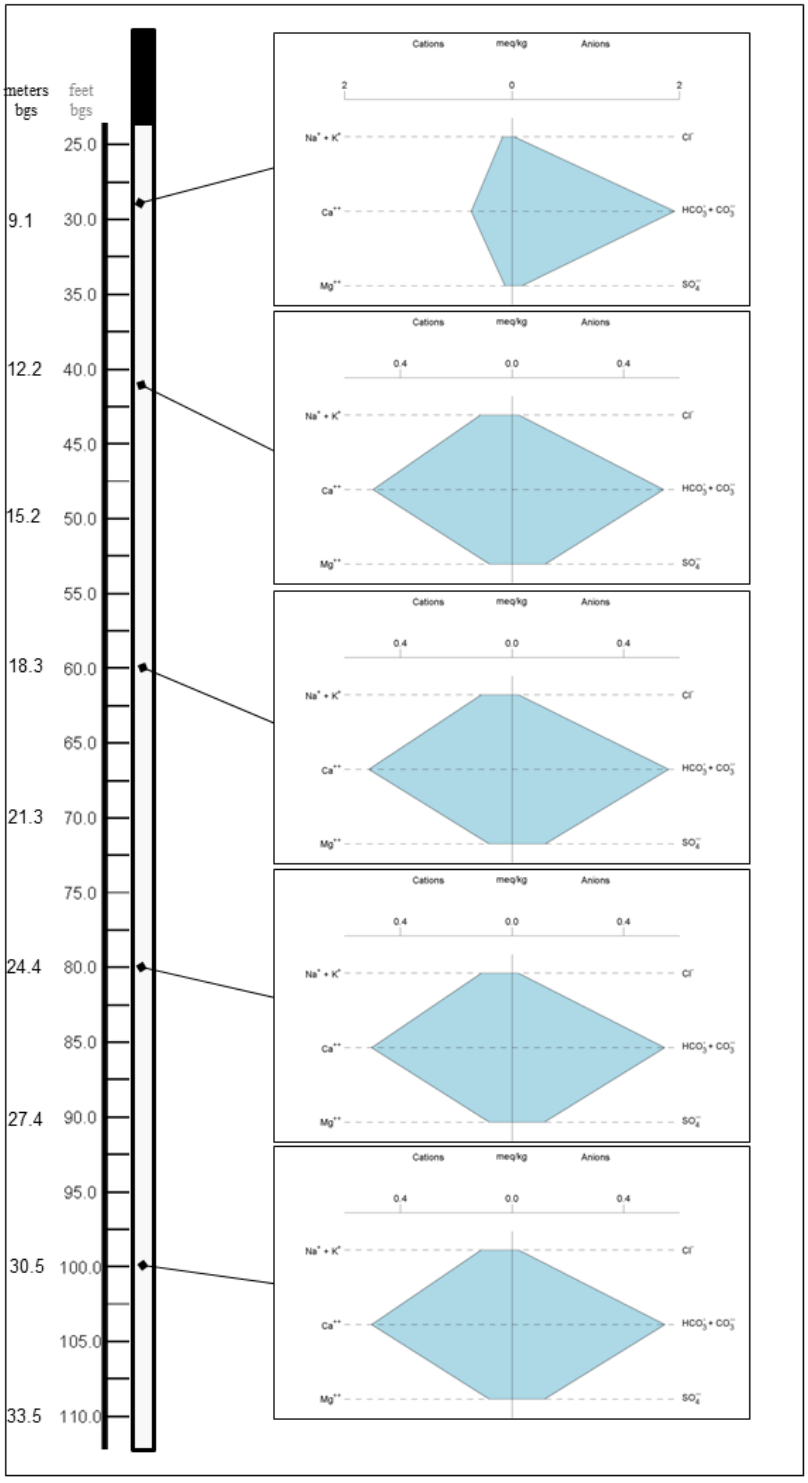

Figure A17: Stiff diagram for November 2014 discrete interval sampling of open borehole well MFS-1, located at the Smith College Ada & Archibald MacLeish Field Station, in Whately, Massachusetts.

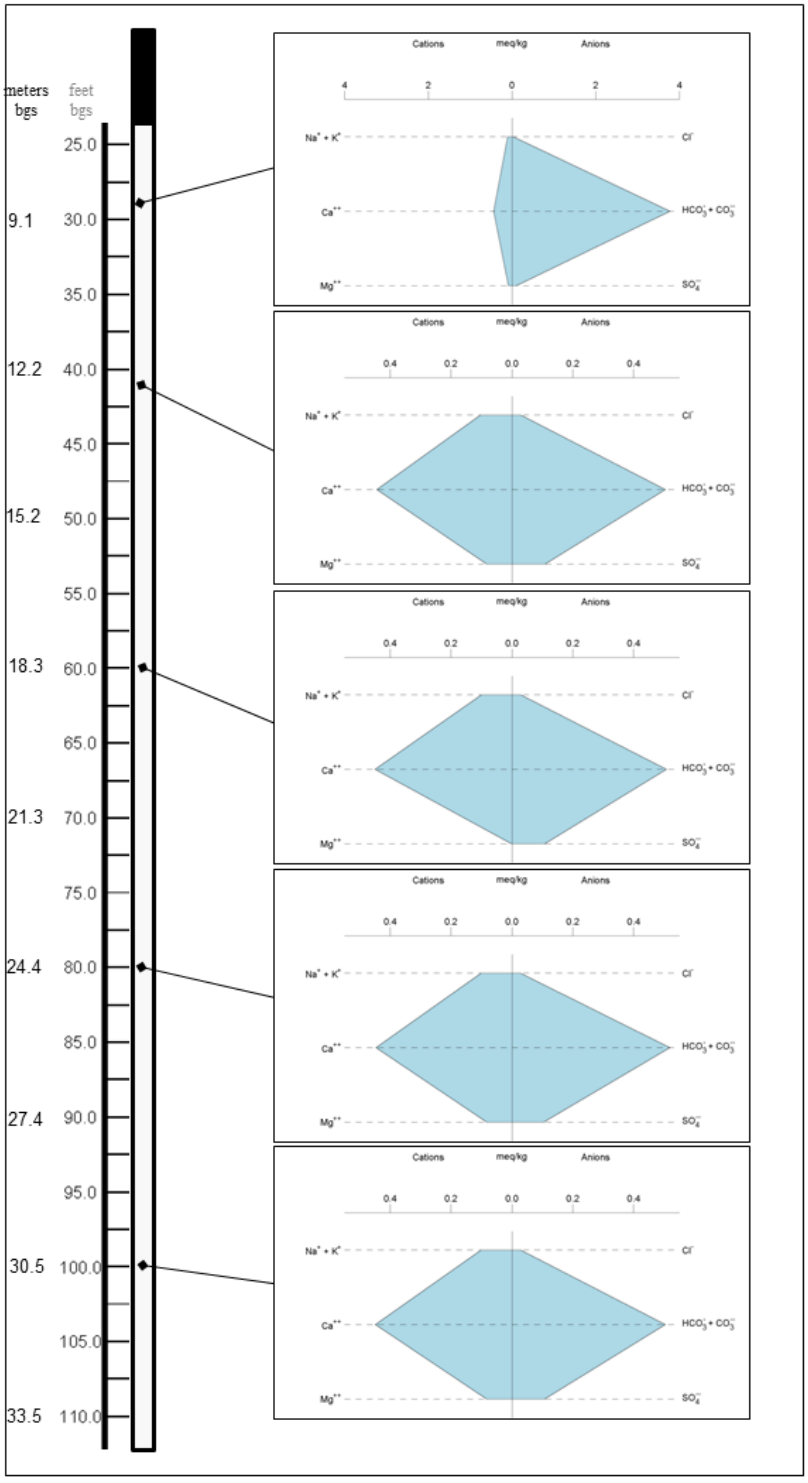

Figure A18: Stiff diagram for December 2014 discrete interval sampling of open borehole well MFS-1, located at the Smith College Ada & Archibald MacLeish Field Station, in Whately, Massachusetts.

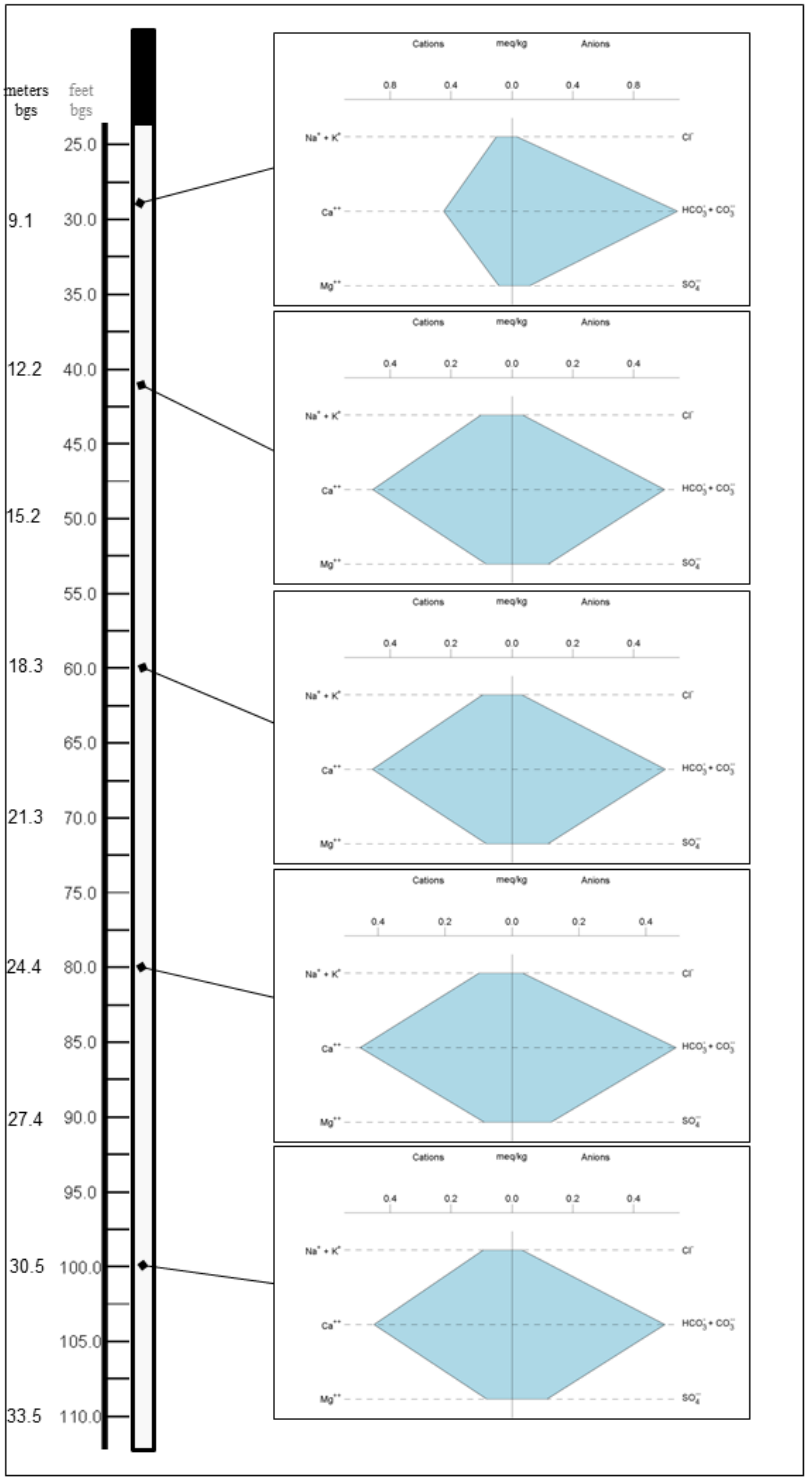

Figure A19: Stiff diagram for January 2015 discrete interval sampling of open borehole well MFS-1, located at the Smith College Ada & Archibald MacLeish Field Station, in Whately, Massachusetts.

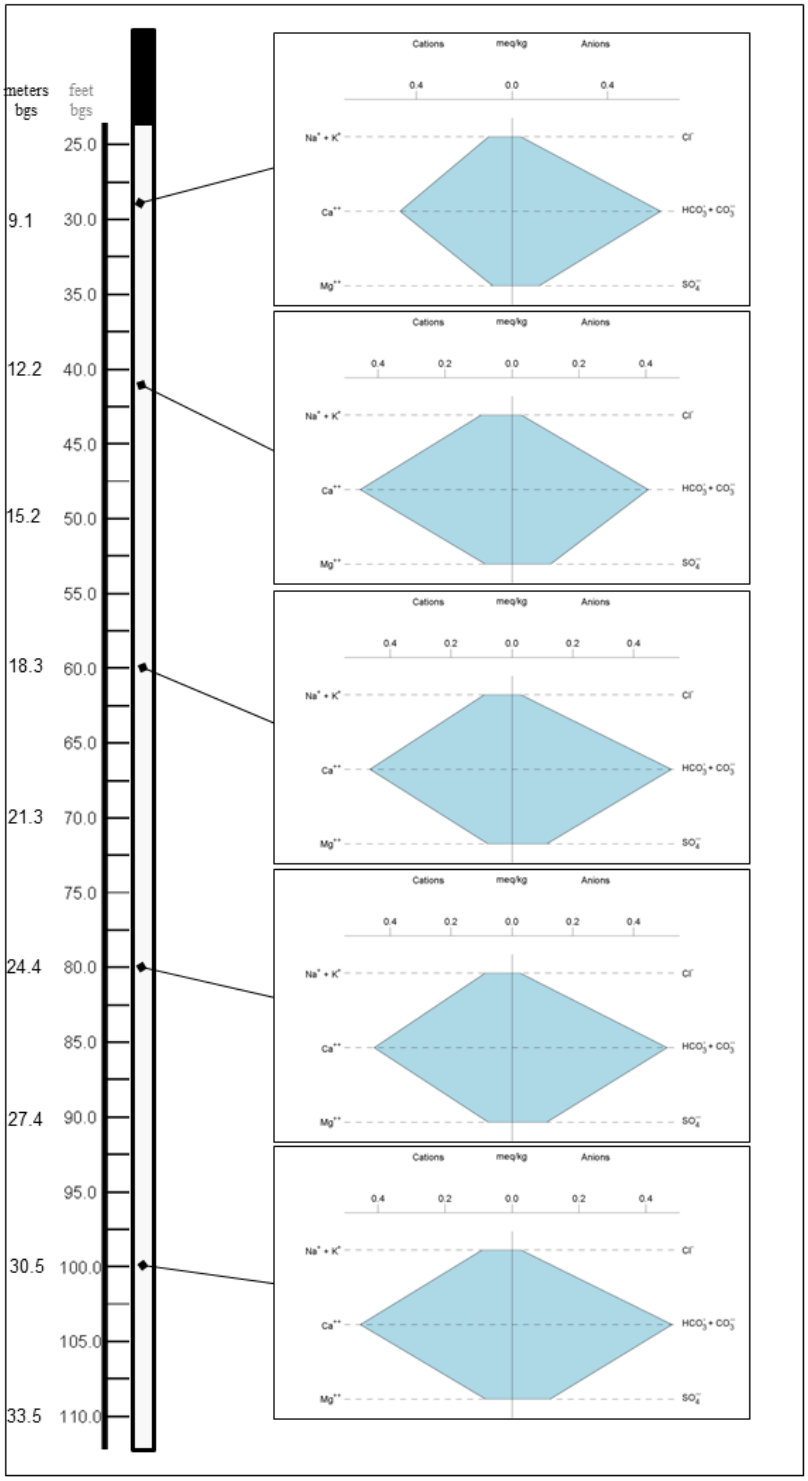

Figure A20: Stiff diagram for March 2015 discrete interval sampling of open borehole well MFS-1, located at the Smith College Ada & Archibald MacLeish Field Station, in Whately, Massachusetts.

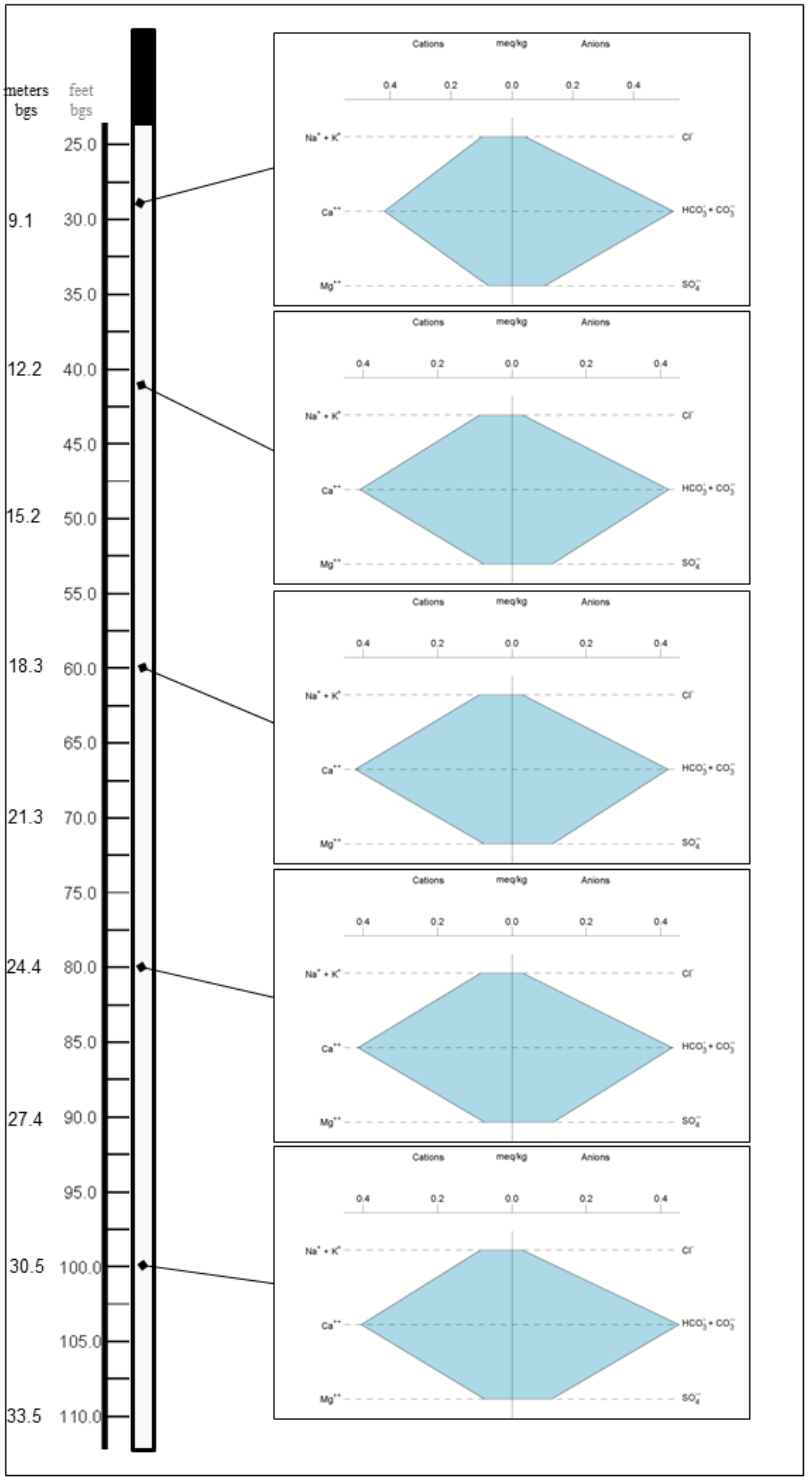

Figure A21: Stiff diagram for April 2015 discrete interval sampling of open borehole well MFS-1, located at the Smith College Ada & Archibald MacLeish Field Station, in Whately, Massachusetts.

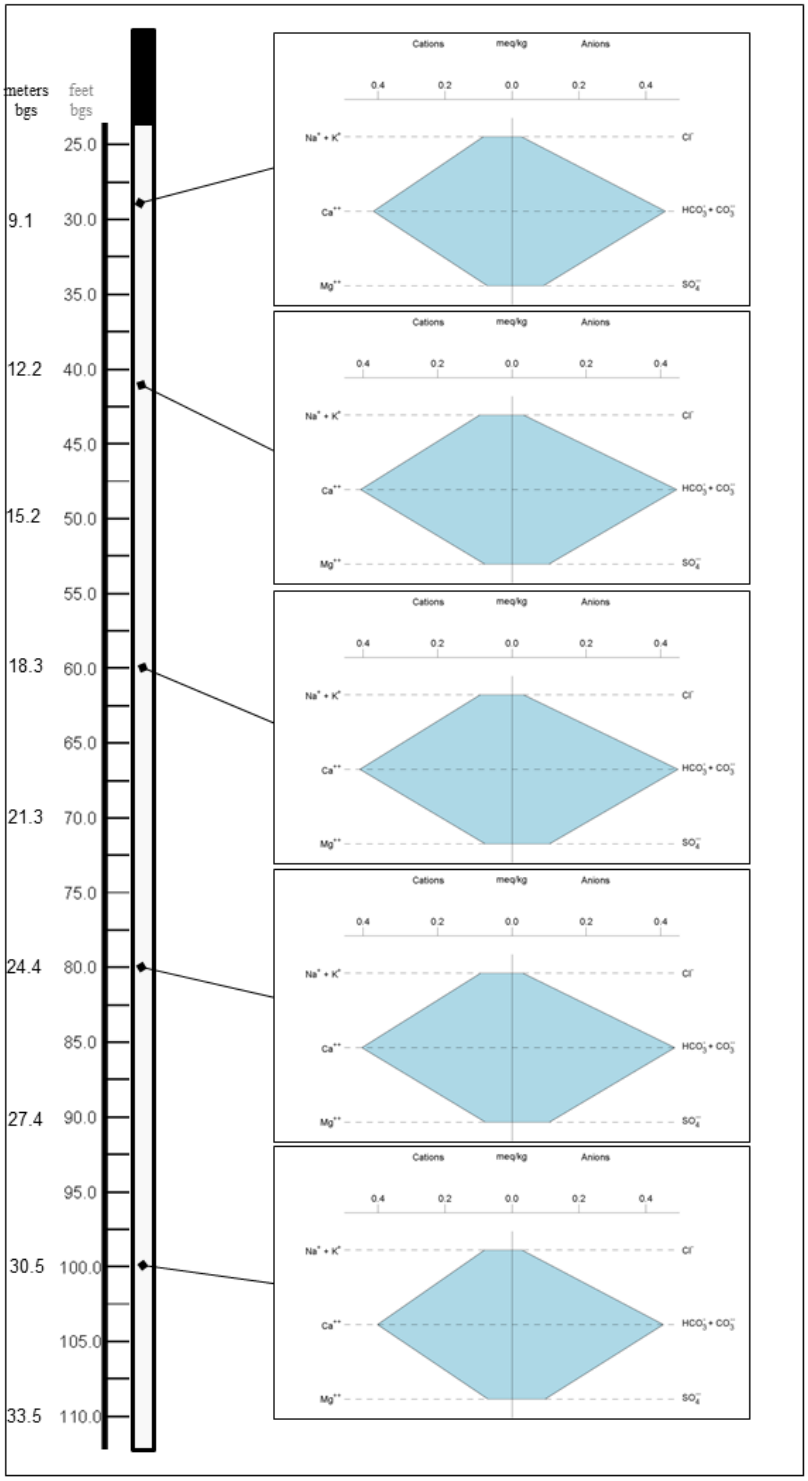

Figure A22: Stiff diagram for May 2015 discrete interval sampling of open borehole well MFS-1, located at the Smith College Ada & Archibald MacLeish Field Station, in Whately, Massachusetts.

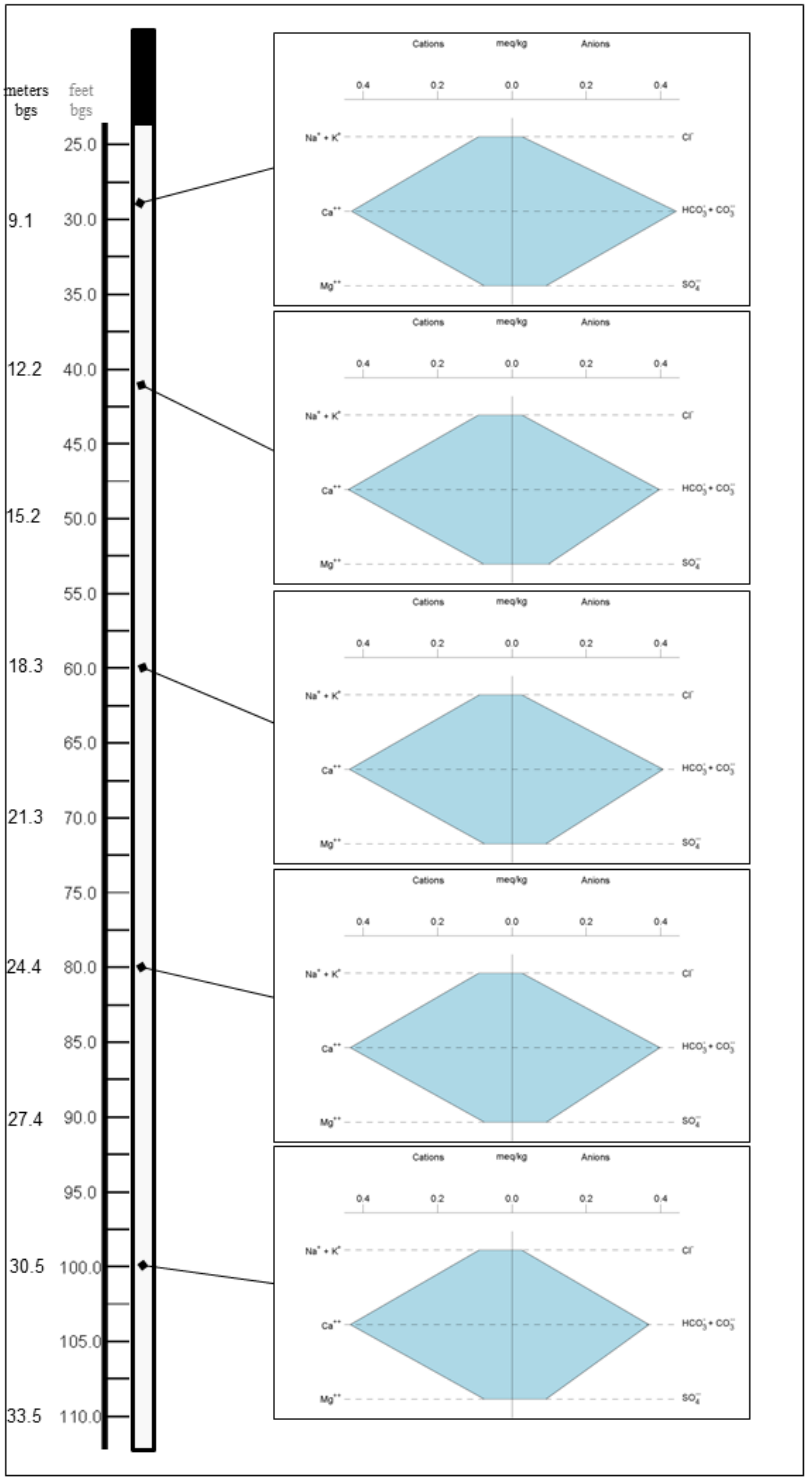

Figure A23: Stiff diagram for June 2015 discrete interval sampling of open borehole well MFS-1, located at the Smith College Ada & Archibald MacLeish Field Station, in Whately, Massachusetts.

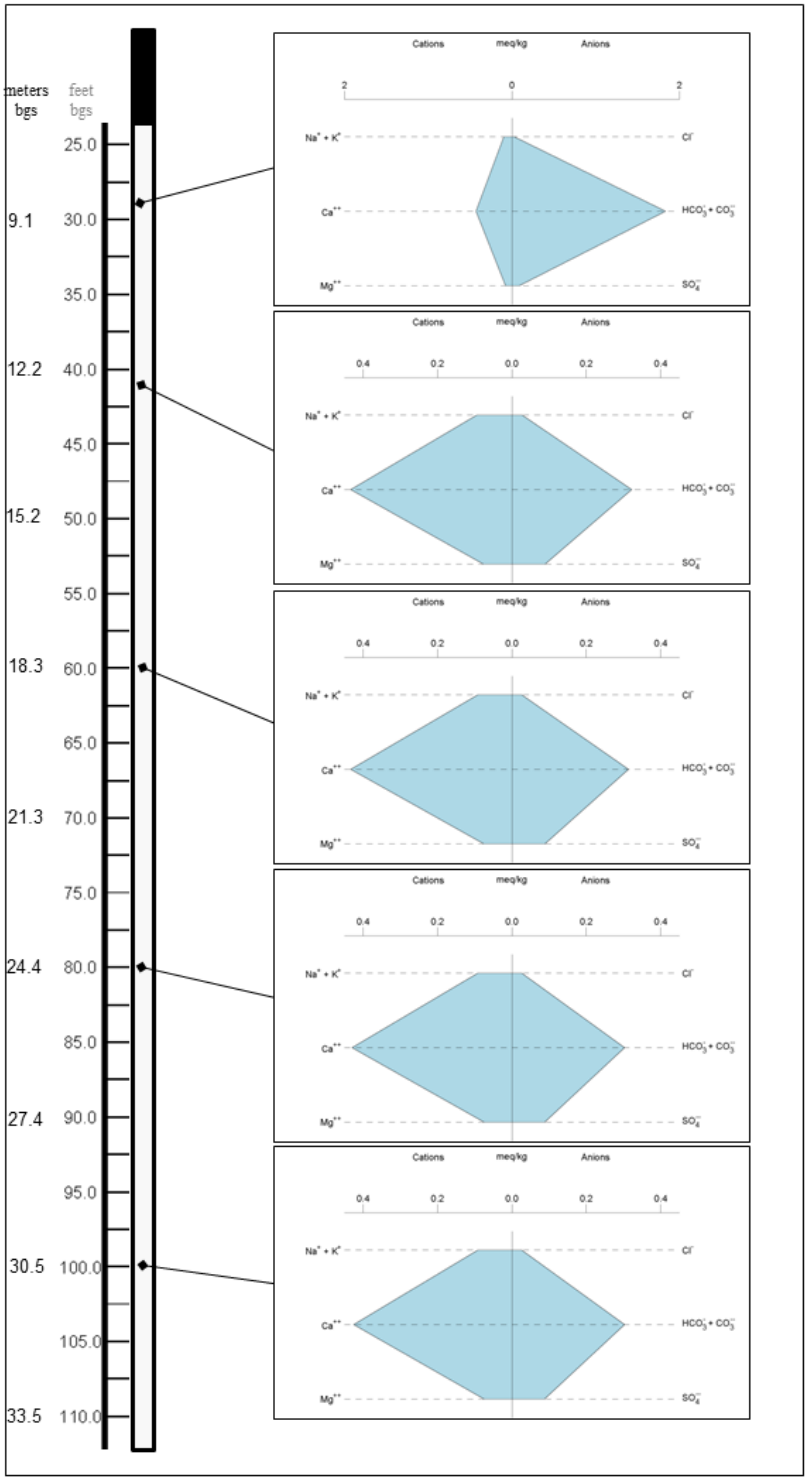

Figure A24: Stiff diagram for July 2015 discrete interval sampling of open borehole well MFS-1, located at the Smith College Ada & Archibald MacLeish Field Station, in Whately, Massachusetts.

APPENDIX B

SUPPLEMENTAL DATA TABLES

Table B1: Well MFS-1 Water Quality Data

Sample ID	Date	pH	Total Alk mg/L	As ug/L	Al mg/L	Ca mg/L	Fe mg/L	K mg/L	Mg mg/L	Mn mg/L	Na mg/L
MFS-1_pre_grab	7/11/2013	6.76	18.68	0.658	NM	8.23	0.0247	1.21	0.928	0.122	1.40
MFS-1_grab	7/11/2013	7.14	39.70	0.934	NM	17.4	0.170	1.63	1.62	0.0135	2.03
	12/11/2013	7.97	28.11		0.0140	8.00	1.15	2.69	0.892	0.0411	1.96
MFS-1_28ft_bgs	7/23/2013			0.512	NM	7.97	0.00	1.23	0.897	0.0904	1.39
	8/20/2013	6.71	105.00	ND	0.00425	8.27	0.111	1.36	0.941	0.128	1.43
	9/17/2013	6.66	33.61	ND	0.00224	13.1	4.20	1.76	1.20	0.197	1.77
	10/15/2013	6.93	116.18	ND	0.00827	13.5	1.63	2.11	1.51	0.188	1.77
	11/13/2013	6.92	214.61	ND	0.0158	15.0	1.64	1.85	1.54	0.178	1.84
	12/11/2013	6.46	201.71		0.0114	9.18	0.234	1.37	1.35	0.0228	1.60
	1/14/2014	6.26	206.83		ND	9.79	1.12	1.44	1.08		1.64
	2/11/2014	6.36	95.19		0.0099	9.90	0.665	1.34	1.00	0.131	1.58
	3/11/2014	6.46	27.80		0.0118	9.60	0.364	1.40	0.970	0.118	1.54
	4/15/2014	6.76	94.87		0.0171	7.90	0.443	1.33	0.900	0.0051	1.61
	5/13/2014	6.62	93.80		0.0091	7.81	0.150	1.33	0.850	0.117	1.40
	6/10/2014	6.43	22.40		0.0140	9.06	0.347	1.42	0.968	0.158	1.51
	7/8/2014	6.74	31.90		0.0064	9.02	0.344	1.38	0.940	0.133	1.44
	8/19/2014	6.94	93.01		0.0142	9.80	0.271	1.38	1.02	0.109	1.52
	9/16/2014	6.73	95.47		0.0116	10.00	1.43	1.36	0.992	0.102	1.50

Sample ID	Date	pH	Total Alk mg/L	As ug/L	Al mg/L	Ca mg/L	Fe mg/L	K mg/L	Mg mg/L	Mn mg/L	Na mg/L
	10/14/2014	6.30	31.17		0.0020	11.00	0.168	1.41	1.05	0.130	1.54
	11/11/2014	6.61	98.60		0.0033	9.84	0.252	1.57	1.02	0.081	1.66
	12/16/2014	6.67	191.54		0.0038	8.82	0.133	1.39	1.03	0.114	1.57
	1/23/2015	6.50	55.19		0.0021	9.09	0.356	1.30	1.05	0.215	1.61
	3/17/2015	6.76	31.54		0.0056	9.49	1.71	1.30	0.994	0.215	1.50
	4/14/2015	7.20	26.90		0.0085	8.49	1.77	1.33	0.952	0.210	1.52
	5/22/2015	6.52	23.24		0.0073	8.39	0.080	1.07	0.905	0.202	1.36
	6/10/2015	6.43	22.40		0.0099	8.75	0.326	1.26	0.921	0.156	1.35
	7/14/2015	6.11	93.06		0.0088	8.70	0.964	1.37	0.933	0.166	1.43
MFS-1_41ft_bgs	7/23/2013	6.97	16.51	0.582		8.28	0.00	1.80	0.958	0.0888	1.85
	8/20/2013	6.52	21.07	ND	0.00728	8.41	0.231	1.37	0.944	0.127	1.41
	9/17/2013	7.19	43.91	0.038	0.00826	19.9	0.374	1.67	1.48	0.0552	2.21
	10/15/2013	7.31	47.70	0.212	0.0266	20.7	1.64	1.36	1.70	0.0266	1.89
	11/13/2013	7.51	50.62	0.28	0.0456	20.5	1.63	1.33	1.65	0.0169	1.82
	12/11/2013	6.63	28.38		0.0156	10.4	0.566	1.60	1.40	0.0332	1.86
	1/14/2014	6.27	24.73		ND	9.56	0.895	1.42	1.03		1.57
	2/11/2014	6.38	25.34		0.0149	9.80	0.892	1.36	0.970	0.117	1.52
	3/11/2014	6.54	25.76		0.0143	9.70	0.351	1.40	0.960	0.124	1.49
	4/15/2014	6.73	21.36		0.0118	7.80	0.539	1.23	0.880	0.0971	1.49
	5/13/2014	6.56	18.12		0.0077	7.54	0.172	1.36	0.830	0.105	1.43
	6/10/2014	6.47	20.09		0.0151	8.96	0.456	1.34	0.966	0.147	1.45

Sample ID	Date	pH	Total Alk mg/L	As ug/L	Al mg/L	Ca mg/L	Fe mg/L	K mg/L	Mg mg/L	Mn mg/L	Na mg/L
	7/8/2014	6.65	23.76		0.0085	8.96	0.593	1.33	0.946	0.114	1.41
	8/19/2014	6.99	25.34		0.0169	10.1	0.526	1.43	1.02	0.104	1.51
	9/16/2014	6.79	26.38		0.0096	10.1	1.60	1.33	0.989	0.109	1.42
	10/14/2014	6.55	28.84		0.0049	11.2	0.545	1.43	1.05	0.157	1.49
	11/11/2014	6.74	27.57		0.0022	10.1	0.495	1.69	0.990	0.113	1.63
	12/16/2014	6.86	25.55		0.0045	9.00	0.246	1.44	1.02	0.178	1.56
	1/23/2015	6.65	25.44		0.0045	9.27	0.215	1.28	1.04	0.221	1.62
	3/17/2015	6.75	20.65		0.0072	9.19	0.620	1.20	0.980	0.194	1.44
	4/14/2015	6.71	21.38		0.0099	8.28	0.733	1.10	0.932	0.177	1.37
	5/22/2015	6.73	22.46		0.0021	8.25	0.105	1.05	0.899	0.168	1.40
	6/10/2015	6.48	20.09		0.0137	8.92	1.38	1.27	0.935	0.117	1.35
	7/14/2015	5.77	16.32		0.0127	8.79	1.22	1.37	0.947	0.113	1.39
MFS-1_60ft_bgs	8/20/2013	6.13	18.41	ND	0.000241	8.36	0.0161	1.37	0.943	0.127	1.41
	9/17/2013	7.32	45.46	0.059	0.00410	20.1	0.430	1.43	1.42	0.0313	1.86
	10/15/2013	7.49	49.83	0.292	0.0194	20.4	1.21	1.30	1.69	0.0235	1.80
	11/13/2013	7.50	49.93	0.557	0.0137	20.2	0.706	1.28	1.64	0.0151	1.77
	12/11/2013	6.86	30.23		0.0125	11.0	0.438	1.52	1.35	0.0502	1.68
	1/14/2014	6.34	24.95		ND	9.65	0.914	1.39	1.03	NM	1.56
	2/11/2014	6.44	25.58		0.0223	9.80	1.09	1.34	0.960	0.117	1.49
	3/11/2014	6.62	25.95		0.0131	9.70	0.369	1.37	0.960	0.123	1.47
	4/15/2014	6.70	22.04		0.0130	7.90	0.661	1.23	0.860	0.0936	1.56

Sample ID	Date	pH	Total Alk mg/L	As ug/L	Al mg/L	Ca mg/L	Fe mg/L	K mg/L	Mg mg/L	Mn mg/L	Na mg/L
	5/13/2014	6.57	18.22		0.0078	7.69	0.197	1.20	0.810	0.0922	1.28
	6/10/2014	6.56	20.61		0.0045	8.30	0.471	1.24	0.850	0.151	1.33
	7/8/2014	6.67	24.01		0.0532	9.16	0.249	1.33	0.965	0.129	1.40
	8/19/2014	6.98	25.42		0.0162	10.14	0.575	1.38	1.01	0.126	1.43
	9/16/2014	6.89	26.53		0.0113	10.10	1.53	1.33	0.981	0.133	1.42
	10/14/2014	6.59	29.22		0.0038	11.10	0.531	1.52	1.05	0.168	1.58
	11/11/2014	6.82	28.47		0.0032	10.40	0.532	1.64	1.01	0.145	1.59
	12/16/2014	6.83	25.73		0.0042	9.12	0.446	1.36	0.015	0.169	1.53
	1/23/2015	6.70	25.55		0.0016	9.29	0.616	1.23	1.03	0.229	1.52
	3/17/2015	6.80	26.57		0.0066	9.46	1.03	1.17	0.970	0.214	1.43
	4/14/2015	6.75	21.28		0.0066	8.54	0.748	1.16	0.925	0.185	1.36
	5/22/2015	6.77	22.63		0.0023	8.29	0.171	1.07	0.888	0.186	1.36
	6/10/2015	6.56	20.61		0.0112	8.86	0.892	1.23	0.909	0.150	1.31
	7/14/2015	5.79	15.89		0.0110	8.79	1.05	1.33	0.932	0.155	1.35
MFS-1_80ft_bgs	7/23/2013	7.12	27.99	0.605		11.5	ND	1.41	1.05	0.0680	1.52
	8/20/2013	6.57	24.48	ND	ND	10.9	0.0548	1.47	1.09	0.117	1.52
	9/17/2013	7.48	51.60	0.232	ND	22.3	0.114	1.30	1.36	0.0108	1.90
	10/15/2013	7.70	52.69	0.874	0.0174	21.4	1.09	1.18	1.63	0.0162	1.80
	11/13/2013	7.72	51.23	1.202	0.0215	21.1	0.764	1.26	1.60	0.0119	1.81
	12/11/2013	6.93	33.32		0.0120	12.3	0.429	1.44	1.33	0.0285	1.54
	1/14/2014	6.42	25.39		ND	9.89	1.08	1.49	1.07		1.60

Sample ID	Date	pH	Total Alk mg/L	As ug/L	Al mg/L	Ca mg/L	Fe mg/L	K mg/L	Mg mg/L	Mn mg/L	Na mg/L
	2/11/2014	6.67	24.88		0.0163	9.30	0.279	1.37	0.960	0.114	1.50
	3/11/2014	6.69	25.51		0.0159	9.50	0.341	1.34	0.940	0.121	1.44
	4/15/2014	6.75	21.77		0.0169	7.80	0.693	1.25	0.870	0.0945	1.56
	5/13/2014	6.56	18.26		0.0091	7.60	0.309	1.24	0.820	0.0962	1.30
	6/10/2014	6.53	20.17		0.0065	8.53	0.780	1.31	0.900	0.143	1.40
	7/8/2014	6.71	23.83		0.0140	9.31	0.490	1.37	0.959	0.133	1.44
	8/19/2014	7.03	26.14		0.0140	10.2	0.394	1.36	1.00	0.123	1.40
	9/16/2014	6.85	26.99		0.0074	9.85	1.00	1.43	0.960	0.113	1.48
	10/14/2014	6.70	29.16		0.0031	11.3	0.640	1.44	1.06	0.146	1.50
	11/11/2014	6.84	27.76		0.0037	10.2	0.549	1.62	1.00	0.129	1.59
	12/16/2014	6.86	26.32		0.0036	9.06	0.384	1.38	1.02	0.191	1.54
	1/23/2015	6.70	24.85		0.0040	9.20	0.434	1.32	1.02	0.239	1.51
	3/17/2015	6.72	25.85		0.0028	9.18	0.691	1.16	0.960	0.213	1.37
	4/14/2015	6.73	21.86		0.0080	8.39	0.564	1.01	0.909	0.185	1.36
	5/22/2015	6.78	22.20		0.0045	8.18	0.135	1.08	0.876	0.185	1.32
	6/10/2015	6.59	20.17		0.0103	8.81	0.751	1.26	0.912	0.151	1.33
	7/14/2015	5.70	15.35		0.0088	8.72	0.554	1.33	0.920	0.147	1.35
MFS-1_100ft_bgs	7/23/2013	7.46	36.34	0.576		15.7	ND	1.36	1.20	0.0482	1.67
	8/20/2013	6.91	43.36	0.033	ND	19.9	0.0959	1.38	1.36	0.0360	1.84
	9/17/2013	7.51	50.41	0.42	ND	22.6	0.210	1.29	1.36	0.0103	1.92
	10/15/2013	7.74	52.45	1.046	0.0196	21.5	1.28	1.22	1.63	0.0220	1.82

Sample ID	Date	pH	Total Alk mg/L	As ug/L	Al mg/L	Ca mg/L	Fe mg/L	K mg/L	Mg mg/L	Mn mg/L	Na mg/L
	11/13/2013			1.308	0.0219	21.2	0.789	1.27	1.61	0.0117	1.82
	12/11/2013	7.21	41.82		0.0273	15.4	0.0827	1.98	1.70	0.0129	2.18
	1/14/2014	6.53	25.72		ND	9.50	0.927	1.45	1.02		1.61
	2/11/2014	6.63	24.70		0.0167	9.30	1.10	1.32	0.950	0.116	1.44
	3/11/2014	6.60	25.86		0.0117	9.50	0.476	1.34	0.940	0.120	1.43
	4/15/2014	6.73	22.05		0.0105	7.90	0.455	1.39	0.870	0.0954	1.52
	5/13/2014	6.53	18.75		0.00805	7.62	0.318	1.27	0.820	0.0934	1.33
	6/10/2014	6.59	18.68		0.00791	8.76	0.541	1.33	0.934	0.147	1.42
	7/8/2014	6.73	24.59		0.0131	9.24	0.657	1.38	0.953	0.133	1.56
	8/19/2014	7.03	26.33		0.0163	10.2	0.909	1.54	1.01	0.131	1.60
	9/16/2014	6.92	27.24		0.0097	9.87	1.060	1.34	0.965	0.133	1.40
	10/14/2014	6.80	32.46		0.0039	13.2	0.666	1.46	1.11	0.127	1.57
	11/11/2014	6.83	27.78		0.0083	10.2	0.744	1.66	1.00	0.142	1.59
	12/16/2014	6.91	25.55		0.0072	9.10	0.425	1.39	1.02	0.180	1.54
	1/23/2015	6.71	25.48		0.0045	9.19	0.580	1.20	1.02	0.223	1.49
	3/17/2015	6.77	24.25		0.0037	9.18	0.789	1.14	0.969	0.211	1.41
	4/14/2015	6.69	22.77		0.0072	8.21	0.516	1.11	0.905	0.171	1.31
	5/22/2015	6.84	22.93		0.0040	8.14	0.233	1.02	0.879	0.188	1.31
	6/10/2015	6.59	18.68		0.0138	8.81	0.794	1.26	0.917	0.146	1.31
	7/14/2015	5.70	15.35		0.0144	8.63	1.18	1.36	0.920	0.146	1.33

Sample ID	Date	Si mg/L	Sr mg/L	Zn mg/L	F mg/L	Cl mg/L	NO_3^- mg/L	SO_4^{-2} mg/L
MFS-1_pre_grab	7/11/2013	4.28	0.0189		ND	0.942	ND	6.42
MFS-1_grab	7/11/2013	6.02	0.0251		0.075	0.932	ND	9.33
	12/11/2013	0.333	0.0470	0.0168	0.112	0.907	ND	3.53
MFS-1_28ft_bgs	7/23/2013	4.17	0.0186		ND	0.942	0.516	6.22
	8/20/2013	4.60	0.0404	ND	0.0237	4.99	0.106	5.86
	9/17/2013	3.96	0.0573	ND	0.0572	1.04	0.147	7.64
	10/15/2013	2.85	0.0672	0.0162	0.0747	0.823	0.0145	6.57
	11/13/2013	3.08	0.0637	0.0172	0.205	0.875	ND	8.99
	12/11/2013	5.53	0.0385	0.0192	ND	1.02	ND	8.12
	1/14/2014	5.00			0.108	1.22	ND	8.06
	2/11/2014	4.27	0.0533	0.0132	0.0513	1.44	ND	8.19
	3/11/2014	4.27	0.0506	0.00855	0.0205	1.21	ND	6.70
	4/15/2014	4.00	0.0426	0.0082	0.0245	1.49	0.305	6.09
	5/13/2014	3.72	0.0404	0.00536	0.0293	1.27	ND	6.40
	6/10/2014	4.06	0.0471	0.00200	0.026	1.07	0.190	6.23
	7/8/2014	4.22	0.0459	0.00247	0.0234	0.985	0.401	6.55
	8/19/2014	4.60	0.0471	0.000791	ND	0.936	0.129	6.58
	9/16/2014	5.04	0.0455	0.00764	0.0199	0.850	0.344	5.89
	10/14/2014	4.67	0.0505	0.00269	0.0217	0.842	0.122	6.67
	11/11/2014	4.90	0.0457	0.00505	0.0192	0.953	0.195	5.97

Sample ID	Date	Si mg/L	Sr mg/L	Zn mg/L	F mg/L	Cl mg/L	NO_3^- mg/L	SO_4^{-2} mg/L
	12/16/2014	5.09	0.0442	0.00387	0.0143	1.114	0.084	5.26
	1/23/2015	4.35	0.0379	0.00540	0.0254	1.213	0.114	5.69
	3/17/2015	4.35	0.0403	0.00748	0.0214	1.343	0.177	5.59
	4/14/2015	4.17	0.0358	0.00709	0.0283	1.578	0.33	5.29
	5/22/2015	3.84	0.0349	0.00474	0.0283	1.032	0.103	4.60
	6/10/2015	4.21	0.0359	0.00519	0.0244	0.992	0.052	4.49
	7/14/2015	4.28	0.0348	0.00513	0.0199	1.010	0.543	4.29
MFS-1_41ft_bgs	7/23/2013	4.23	0.0190	NM	ND	1.86	0.523	6.41
	8/20/2013	4.61	0.0403	ND	0.0209	0.759	0.0408	5.68
	9/17/2013	5.03	0.0586	ND	0.138	0.97	ND	13.4
	10/15/2013	5.27	0.0483	0.0329	0.173	1.03	0.0240	13.0
	11/13/2013	5.16	0.0474	0.0265	0.221	0.897	ND	14.0
	12/11/2013	5.43	0.0427	0.0222	0.0572	1.51	ND	8.45
	1/14/2014	5.02			0.0550	1.11	ND	8.19
	2/11/2014	4.36	0.0499	0.0137	0.0522	1.27	ND	8.24
	3/11/2014	4.17	0.0505	0.00707	0.0194	1.08	ND	6.45
	4/15/2014	4.20	0.0415	0.00589	0.0243	1.33	0.125	6.12
	5/13/2014	3.84	0.0389	0.00369	0.0289	1.48	ND	6.55
	6/10/2014	4.14	0.0461	0.000940	0.027	0.995	ND	6.39
	7/8/2014	4.34	0.0455	0.00146	0.022	0.970	0.116	6.55
	8/19/2014	4.52	0.0482	ND	0.0282	0.920	0.25	6.62

Sample ID	Date	Si mg/L	Sr mg/L	Zn mg/L	F mg/L	Cl mg/L	NO_3^- mg/L	SO_4^{-2} mg/L
	9/16/2014	4.84	0.0464	0.00422	0.0186	0.855	0.048	5.73
	10/14/2014	4.52	0.0519	0.00117	0.0227	0.809	0.013	6.64
	11/11/2014	4.44	0.0468	0.00166	0.0198	0.904	0.019	5.85
	12/16/2014	4.96	0.0444	0.00402	0.0137	1.068	0.101	5.32
	1/23/2015	4.33	0.0381	0.00616	0.0181	1.293	0.048	5.83
	3/17/2015	4.29	0.0379	0.00539	0.0361	1.032	0.071	5.64
	4/14/2015	4.24	0.0346	0.00514	0.0267	1.058	0.093	5.28
	5/22/2015	3.88	0.0339	0.00425	0.0195	1.140	0.062	4.85
	6/10/2015	4.36	0.0362	0.00647	0.0247	0.990	0.071	4.78
	7/14/2015	4.45	0.0351	0.00590	0.0199	0.993	0.206	4.36
MFS-1_60ft_bgs	8/20/2013	4.56	0.0405	ND	0.0205	0.745	ND	5.78
	9/17/2013	5.18	0.0558	ND	0.145	0.948	ND	13.3
	10/15/2013	5.27	0.0476	0.0218	0.175	0.927	0.0047	13.1
	11/13/2013	5.14	0.0468	0.0167	0.234	0.776	ND	14.3
	12/11/2013	5.22	0.0452	0.0204	0.0811	1.12	ND	8.80
	1/14/2014	5.04			0.0751	1.07	ND	8.20
	2/11/2014	4.38	0.0503	0.0183	0.0750	1.25	ND	8.10
	3/11/2014	4.16	0.0503	0.00494	0.0186	1.05	ND	6.52
	4/15/2014	4.15	0.0406	0.00716	0.022	1.47	0.136	6.14
	5/13/2014	3.94	0.0377	0.00408	0.0249	1.10	ND	6.38
	6/10/2014	4.08	0.0399	0.00293	0.0255	1.01	ND	6.33

Sample ID	Date	Si mg/L	Sr mg/L	Zn mg/L	F mg/L	Cl mg/L	NO_3^- mg/L	SO_4^{-2} mg/L
	7/8/2014	4.26	0.0459	0.00192	0.0343	0.953	ND	6.38
	8/19/2014	4.48	0.0479	0.00472	ND	0.879	0.103	6.59
	9/16/2014	4.82	0.0464	0.00430	0.021	0.85	0.029	5.67
	10/14/2014	4.55	0.0512	0.00247	0.0237	0.99	0.016	6.63
	11/11/2014	4.55	0.0490	0.00801	0.0229	0.87	0.026	5.87
	12/16/2014	4.86	0.0449	0.00366	0.017	1.05	0.058	5.26
	1/23/2015	4.32	0.0383	0.00524	0.0247	1.18	0.001	5.78
	3/17/2015	4.23	0.0377	0.00564	0.0151	1.07	ND	5.61
	4/14/2015	4.25	0.0345	0.00582	0.0188	1.02	0.012	5.35
	5/22/2015	3.85	0.0333	0.00494	0.0186	1.14	0.034	4.94
	6/10/2015	4.22	0.03518	0.00528	0.0242	0.95	0.003	4.45
	7/14/2015	4.37	0.034981	0.00594	0.024	0.96	0.051	4.34
MFS-1_80ft_bgs	7/23/2013	4.63	0.0215		0.0480	0.985	0.492	8.79
	8/20/2013	4.84	0.0436	ND	0.0334	0.785	ND	7.98
	9/17/2013	5.21	0.0533	ND	0.183	0.945	0.0021	13.1
	10/15/2013	5.30	0.0461	0.0220	0.192	0.946	0.0245	12.8
	11/13/2013	5.21	0.0456	0.0202	0.243	0.867	ND	14.5
	12/11/2013	5.25	0.0427	0.0200	0.105	0.832	ND	9.64
	1/14/2014	5.13			0.0894	1.08	ND	8.14
	2/11/2014	4.29	0.0494	0.00856	0.2943		ND	8.28
	3/11/2014	4.08	0.0495	0.00507	0.0188	1.05	ND	6.49

Sample ID	Date	Si mg/L	Sr mg/L	Zn mg/L	F mg/L	Cl mg/L	NO_3^- mg/L	SO_4^{-2} mg/L
	4/15/2014	4.18	0.0411	0.00860	0.0238	1.49	0.106	6.21
	5/13/2014	3.94	0.0384	0.00484	0.0264	1.14	ND	6.42
	6/10/2014	3.91	0.0419	0.00299	0.0329	1.05	ND	6.33
	7/8/2014	4.31	0.0437	0.00201	0.0569	0.966	ND	6.33
	8/19/2014	4.42	0.0468	0.000427	0.0257	0.881	0.094	6.80
	9/16/2014	4.65	0.0456	0.00406	0.0197	1.037	0.005	5.59
	10/14/2014	4.61	0.0509	0.00373	0.0223	0.832	0.013	6.70
	11/11/2014	4.49	0.0476	0.00372	0.0188	0.835	0.001	5.68
	12/16/2014	4.85	0.0449	0.00164	0.0138	1.020	0.039	5.09
	1/23/2015	4.26	0.0380	0.00573	0.032	1.170	ND	5.71
	3/17/2015	4.16	0.0375	0.00492	0.0311	0.998	ND	5.60
	4/14/2015	4.18	0.0345	0.00579	0.0235	1.060	0.007	5.44
	5/22/2015	3.82	0.0328	0.00529	0.0279	1.065	0.023	4.91
	6/10/2015	4.21	0.0353	0.00804	0.0237	0.980	0.004	4.52
	7/14/2015	4.30	0.0342	0.00631	0.0195	0.955	0.044	4.30
MFS-1_100ft_bgs	7/23/2013	4.66	0.0249		0.0930	1.00	ND	11.0
	8/20/2013	5.16	0.0536	ND	0.142	0.908	ND	12.1
	9/17/2013	5.25	0.0532	ND	0.180	0.916	ND	13.4
	10/15/2013	5.27	0.0464	0.0200	0.194	0.935	0.00716	13.1
	11/13/2013	5.20	0.0459	0.0173	0.209	0.846	ND	15.1
	12/11/2013	5.10	0.0389	0.0499	0.113	1.03	ND	12.1

Sample ID	Date	Si	Sr	Zn	F	Cl	NO_3^-	SO_4^{-2}
		mg/L	mg/L	mg/L	mg/L	mg/L	mg/L	mg/L
	1/14/2014	5.00			0.0720	1.85	ND	8.24
	2/11/2014	4.29	0.05	0.0123	0.0859	1.13	ND	8.04
	3/11/2014	4.13	0.0499	0.00453	0.0200	1.08	ND	6.64
	4/15/2014	4.20	0.0419	0.00841	0.0263	1.43	0.121	6.12
	5/13/2014	3.94	0.0380	0.00565	0.0243	1.19	ND	6.46
	6/10/2014	4.04	0.0447	0.000159	0.0246	0.993	ND	6.27
	7/8/2014	4.27	0.0462	0.00367	0.0573	1.15	0.09	6.42
	8/19/2014	4.45	0.0488	0.00268	0.0324	1.24	ND	6.56
	9/16/2014	4.70	0.0455	0.00369	0.0191	0.836	0.008	5.42
	10/14/2014	4.72	0.0519	0.00245	0.0487	0.847	0.017	8.03
	11/11/2014	4.51	0.0475	0.00509	0.0205	0.885	0.003	5.72
	12/16/2014	4.88	0.0450	0.00165	0.0164	1.05	0.028	5.24
	1/23/2015	4.25	0.0378	0.00460	0.0232	1.21	ND	5.63
	3/17/2015	4.20	0.0375	0.00433	0.0127	1.00	ND	5.57
	4/14/2015	4.12	0.0341	0.00451	0.0194	1.02	ND	5.20
	5/22/2015	3.80	0.0332	0.00579	0.0333	1.09	0.037	4.84
	6/10/2015	4.23	0.0354	0.00635	0.0228	0.96	ND	4.48
	7/14/2015	4.31	0.0344	0.00541	0.0226	0.95	0.018	4.27

Note:

If no value is provided, no measurement was made

ND = measured concentration in solution is less than the detection limit of the testing

Table B2: Well MFS-2 Water Quality Data

Sample ID	Date	pH	Total Alk mg/L	As ug/L	Al mg/L	Ca mg/L	Fe mg/L	K mg/L	Mg mg/L	Mn mg/L	Na mg/L
MFS-2_grab	7/11/2013	6.52	18.3	0.696		7.89	0.0283	1.07	0.962	0.0131	1.34
MFS-2_15ft_bgs	7/23/2013	7.48	35.4	0.814		15.4	ND	1.73	1.36	0.00254	1.96
	8/20/2013	6.93	40.6	0.273	0.00262	16.4	0.00440	1.98	1.48	0.00892	2.03
	9/17/2013	7.24	43.4	0.249	0.00132	16.1	0.00592	1.99	1.46	0.0386	2.01
	10/15/2013	7.39	44.2	0.308	0.0157	15.8	0.231	1.90	1.74	0.0706	1.96
	11/13/2013	7.35	48.8	0.411	0.0545	15.5	0.449	1.90	1.72	0.0888	1.94
	12/11/2013	7.36	42.9		0.0273	15.4	0.0827	1.98	1.70	0.0129	2.18
	1/14/2014	7.27	42.7		ND	16.7	0.0786	1.95	1.45		2.12
	2/11/2014	7.16	41.0		0.4376	16.7	0.2169	1.65	1.79	0.0103	2.02
	3/11/2014	7.47	45.0		0.0398	17.1	0.0645	1.65	1.42	0.0086	2.06
	4/15/2014	7.64	45.3		0.0253	16.3	0.0569	1.69	1.40	0.0069	2.05
	5/13/2014	7.38	43.85		0.0863	16.6	0.0740	1.82	1.43	0.00590	2.13
	6/10/2014	7.31	41.45		0.06572	18.2	0.0590	2.10	1.61	0.0126	2.35
	7/8/2014	7.43	44.72		0.04372	17.9	0.0476	2.00	1.59	0.0113	2.26
	8/19/2014	7.54	43.56		0.07714	17.3	0.0864	1.77	1.55	0.0102	2.03
	9/16/2014	7.35	41.81		0.03560	15.9	0.0660	1.87	1.38	0.0018	1.97
	10/14/2014	7.02	39.51		0.02250	15.4	0.0460	1.80	1.35	0.0042	1.89
	11/11/2014	7.28	40.71		0.01840	15.8	0.0380	1.90	1.35	0.0008	1.99
	12/16/2014	7.56	40.57		0.01690	15.3	0.0310	1.82	1.33	0.0010	1.90
	1/23/2015	7.55	39.23		0.01082	15.8	0.0182	1.65	1.40	0.0030	1.97

Sample ID	Date	pH	Total Alk mg/L	As ug/L	Al mg/L	Ca mg/L	Fe mg/L	K mg/L	Mg mg/L	Mn mg/L	Na mg/L
	3/17/2015	7.20	39.95		0.00674	17.2	0.0136	1.53	1.54	0.0015	1.99
	4/14/2015	7.67	42.43		0.00980	16.9	0.0229	1.41	1.53	0.0022	1.93
	5/22/2015	7.55	44.64		0.02107	16.9	0.0655	1.44	1.53	0.0033	1.95
	6/10/2015	7.31	41.45		0.0201	17.1	0.0126	1.64	1.53	0.00176	1.96
	7/14/2015	6.49	36.53		0.0240	17.1	0.0227	1.69	1.53	0.00217	1.94
MFS-2_25ft_bgs	8/20/2013	6.95	41.8	0.28	0.00981	16.5	0.00776	1.70	1.48	0.00361	1.94
	9/17/2013	7.20	41.8	0.169	0.00430	16.1	0.00186	1.73	1.46	0.00178	1.93
	10/15/2013	7.48	45.2	0.188	0.0264	15.7	0.0760	1.63	1.75	0.0166	1.82
	11/13/2013	7.32	43.1	0.214	0.0368	15.2	0.133	1.64	1.71	0.0631	1.81
	12/11/2013	7.36	44.9		0.0318	15.3	0.114	1.64	1.71	0.0281	1.87
	1/14/2014	7.32	43.9		ND	16.9	0.0946	1.89	1.49		2.05
	2/11/2014	7.42	41.8		0.1070	15.9	0.1572	1.69	1.39	0.0103	1.93
	3/11/2014	7.52	45.5		0.0467	17.0	0.0757	1.75	1.44	0.0088	2.12
	4/15/2014	7.66	44.8		0.0312	16.5	0.0582	1.67	1.42	0.0075	2.01
	5/13/2014	7.47	43.94		0.107	16.5	0.0940	1.71	1.43	0.00613	2.00
	6/10/2014	7.52	43.66		0.07124	18.3	0.0761	1.91	1.65	0.0138	2.20
	7/8/2014	7.61	46.52		0.04181	18.1	0.0511	1.83	1.62	0.0101	2.14
	8/19/2014	7.70	44.98		0.08184	17.7	0.0936	1.78	1.59	0.00958	2.02
	9/16/2014	7.49	42.11		0.03690	16.1	0.0660	1.72	1.41	0.00200	1.91
	10/14/2014	7.14	39.87		0.01690	15.7	0.0390	1.65	1.37	0.00010	1.86
	11/11/2014	7.38	42.29		0.01170	15.9	0.0260	1.69	1.37	-0.00061	1.89

Sample ID	Date	pH	Total Alk mg/L	As ug/L	Al mg/L	Ca mg/L	Fe mg/L	K mg/L	Mg mg/L	Mn mg/L	Na mg/L
	12/16/2014	7.67	44.27		0.01820	16.3	0.0310	1.71	1.42	-0.00028	1.95
	1/23/2015	7.54	40.06		0.01881	16.9	0.0314	1.59	1.50	0.00277	2.03
	3/17/2015	7.62	44.74		0.01450	15.5	0.0183	1.47	1.39	0.00293	1.86
	4/14/2015	7.68	41.34		0.00755	17.3	0.0188	1.59	1.55	0.00203	1.97
	5/22/2015	7.60	44.74		0.01095	17.0	0.0284	1.49	1.53	0.00275	1.96
	6/10/2015	7.52	43.66		0.0173	17.5	0.0115	1.63	1.56	0.00166	1.95
	7/14/2015	6.76	36.96		0.0204	17.4	0.0205	1.72	1.55	0.00207	1.95
MFS-2_35ft_bgs	7/23/2013			0.810		15.7	ND	1.53	1.39	0.000614	1.89
	8/20/2013	7.19	42.0	0.204	0.00735	16.6	0.00452	1.68	1.50	0.00157	1.95
	9/17/2013	7.43	43.1	0.330	0.00401	16.6	ND	1.63	1.49	0.00119	1.94
	10/15/2013	7.63	44.0	0.306	0.0567	15.8	0.110	1.53	1.78	0.0145	1.82
	11/13/2013	7.62	44.0	0.303	0.0836	15.7	0.147	1.57	1.80	0.0191	1.85
	12/11/2013	7.55	45.0		0.0283	15.5	0.068	1.75	1.77	0.00937	2.16
	1/14/2014	7.47	57.1		ND	16.9	0.0501	1.75	1.51		2.02
	2/11/2014	7.58	44.2		0.0556	16.8	0.0946	1.60	1.44	0.0084	1.94
	3/11/2014	7.51	44.0		0.0550	16.7	0.0665	1.59	1.43	0.008	1.96
	4/15/2014	7.69	43.9		0.0497	16.5	0.0710	1.73	1.43	0.009	2.05
	5/13/2014	7.54	44.26		0.132	17.0	0.111	1.78	1.47	0.00668	2.05
	6/10/2014	7.55	43.48		0.04219	17.8	0.0521	1.73	1.60	0.0111	2.04
	7/8/2014	7.67	47.94		0.03358	18.3	0.0358	1.83	1.68	0.00890	2.13
	8/19/2014	7.77	46.14		0.07211	18.1	0.0775	1.79	1.63	0.0127	2.05

Sample ID	Date	pH	Total Alk mg/L	As ug/L	Al mg/L	Ca mg/L	Fe mg/L	K mg/L	Mg mg/L	Mn mg/L	Na mg/L
	9/16/2014	7.68	45.56		0.03740	16.8	0.0630	1.72	1.47	0.0020	1.96
	10/14/2014	7.38	43.71		0.01550	16.8	0.0350	1.75	1.47	0.0001	1.97
	11/11/2014	7.63	51.45		0.03330	16.9	0.0320	1.75	1.48	0.0002	1.97
	12/16/2014	7.74	44.85		0.01390	16.7	0.0260	1.70	1.47	-0.0007	1.96
	1/23/2015	7.67	54.04		0.00824	17.2	0.0140	1.49	1.55	0.0018	1.99
	3/17/2015	7.66	44.82		0.02606	16.9	0.0378	1.41	1.52	0.0031	1.95
	4/14/2015	7.71	40.55		0.01119	17.2	0.0125	1.56	1.56	0.0023	1.98
	5/22/2015	7.62	45.92		0.00839	17.3	0.0240	1.39	1.55	0.0022	1.95
	6/10/2015	7.55	43.48		0.0199	17.6	0.0157	1.64	1.57	0.00197	1.93
	7/14/2015	6.80	38.71		0.0185	17.8	0.0232	1.76	1.61	0.00225	1.95

Sample ID	Date	Si mg/L	Sr mg/L	Zn mg/L	F mg/L	Cl mg/L	NO_3^- mg/L	SO_4^{-2} mg/L
MFS-2_grab	7/11/2013	5.39	0.01818		ND	0.871	0.494	6.88
MFS-2_15ft_bgs	7/23/2013	5.20	0.0225		0.0547	0.923	0.483	7.89
	8/20/2013	5.53	0.0457	ND	0.0754	0.936	0.0131	7.80
	9/17/2013	5.44	0.0450	ND	0.0685	0.948	0.00406	7.90
	10/15/2013	5.31	0.0400	0.0404	0.0842	1.23	0.0147	7.83
	11/13/2013	5.28	0.0392	0.0263	0.143	1.09	ND	8.47
	12/11/2013	5.10	0.0389	0.0499	0.102	1.80	0.625	9.84
	1/14/2014	5.89			0.116	1.28	0.585	10.7

Sample ID	Date	Si mg/L	Sr mg/L	Zn mg/L	F mg/L	Cl mg/L	NO_3^- mg/L	SO_4^{-2} mg/L
	2/11/2014	5.40	0.0513	0.02366	*14.6*	1.06	0.726	10.9
	3/11/2014	5.79	0.0496	0.02102	0.0706	1.1422	ND	8.86
	4/15/2014	5.70	0.0497	0.0084	0.0716	0.9066	0.491	8.61
	5/13/2014	5.76	0.0484	0.00650	0.081	1.0164	0.417	9.72
	6/10/2014	5.70	0.0548	0.00801	0.0767	0.895	1.12	9.19
	7/8/2014	5.59	0.0546	0.00615	0.0766	0.8417	0.553	8.84
	8/19/2014	5.50	0.0520	0.00374	0.0726	0.7989	0.807	8.83
	9/16/2014	5.42	0.0451	0.00853	0.0691	0.7685	0.901	7.37
	10/14/2014	5.24	0.0444	0.01169	0.0648	0.7594	0.723	7.19
	11/11/2014	5.27	0.0438	0.03010	0.0647	0.7541	1.33	7.06
	12/16/2014	5.19	0.0432	0.00871	0.0544	0.7495	1.15	7.10
	1/23/2015	5.10	0.0370	0.01123	0.0730	0.8249	1.22	8.18
	3/17/2015	5.59	0.0412	0.00506	0.0507	1.0821	0.52	8.80
	4/14/2015	5.63	0.0414	0.00387	0.0666	0.7722	0.20	8.69
	5/22/2015	5.63	0.0412	0.00435	0.0786	0.8023	0.41	8.84
	6/10/2015	5.74	0.0419	0.00653	0.0747	0.7686	0.06	8.27
	7/14/2015	5.69	0.0411	0.00749	0.0721	0.7633	0.27	8.06
MFS-2_25ft_bgs	8/20/2013	5.65	0.0456	ND	0.0735	0.810	0.0933	7.83
	9/17/2013	5.49	0.0450	ND	0.0696	0.831	0.199	7.84
	10/15/2013	5.49	0.0397	0.0323	0.0829	0.937	0.117	7.88
	11/13/2013	5.32	0.0387	0.0246	0.148	0.825	0.157	9.04
	12/11/2013	5.46	0.0390	0.0270	0.111	0.990	0.170	10.3

Sample ID	Date	Si mg/L	Sr mg/L	Zn mg/L	F mg/L	Cl mg/L	NO_3^- mg/L	SO_4^{-2} mg/L
	1/14/2014	6.03			0.123	1.11	0.546	10.9
	2/11/2014	5.44	0.0468	0.0211	0.254	1.09	0.443	10.6
	3/11/2014	5.83	0.05	0.01829	0.0805	1.1937	ND	8.85
	4/15/2014	5.82	0.0496	0.00536	0.0716	0.8942	ND	8.59
	5/13/2014	5.79	0.0482	0.00546	0.0747	0.9155	ND	9.60
	6/10/2014	5.78	0.0559	0.00418	0.074	0.8876	0.318	9.66
	7/8/2014	5.67	0.0549	0.00231	0.0745	0.8027	0.075	9.25
	8/19/2014	5.64	0.0532	0.00137	0.0724	0.7745	0.295	9.52
	9/16/2014	5.54	0.0458	0.00348	0.0707	0.7158	0.172	7.52
	10/14/2014	5.36	0.0447	0.00276	0.0668	0.7479	0.130	7.33
	11/11/2014	5.42	0.0451	0.00459	0.0647	0.7229	0.316	7.23
	12/16/2014	5.67	0.0463	0.00424	0.0668	0.7501	0.213	7.57
	1/23/2015	5.47	0.0421	0.00844	0.0378	0.7702	0.434	7.94
	3/17/2015	5.08	0.0369	0.00928	ND	0.9057	0.175	9.06
	4/14/2015	5.65	0.0412	0.00400	0.0716	0.7948	0.003	8.72
	5/22/2015	5.67	0.0411	0.00386	0.0808	0.7882	0.156	8.69
	6/10/2015	5.85	0.0426	0.00469	0.0767	0.7851	ND	8.52
	7/14/2015	5.80	0.0417	0.00584	0.0708	0.7556	0.137	8.12
MFS-2_35ft_bgs	7/23/2013	5.37	0.0229		0.0618	0.831	0.512	8.16
	8/20/2013	5.76	0.0462	ND	0.0756	0.763	0.0145	8.00
	9/17/2013	5.73	0.0463	ND	0.0744	0.784	0.00548	8.24
	10/15/2013	5.75	0.0404	0.0212	0.0842	0.819	0.0519	8.06

Sample ID	Date	Si mg/L	Sr mg/L	Zn mg/L	F mg/L	Cl mg/L	NO_3^- mg/L	SO_4^{-2} mg/L
	11/13/2013	5.76	0.0404	0.0265	0.162	0.784	ND	9.36
	12/11/2013	5.75	0.0406	0.0181	0.115	1.54	ND	10.5
	1/14/2014	6.29			0.126	0.968	0.233	11.3
	2/11/2014	5.89	0.0496	0.01114	0.160	0.899	ND	11.2
	3/11/2014	5.87	0.0496	0.0056	0.0771	0.8886	ND	8.73
	4/15/2014	5.80	0.0512	0.00739	0.0643	0.997	ND	8.57
	5/13/2014	5.95	0.0492	0.00443	0.0797	0.9841	ND	9.63
	6/10/2014	5.62	0.0538	0.00084	0.0763	0.7922	ND	9.55
	7/8/2014	5.72	0.0554	0.00167	0.0682	0.9712	ND	9.49
	8/19/2014	5.76	0.0542	0.00106	0.0668	0.7723	0.168	9.57
	9/16/2014	5.75	0.0479	0.00304	0.0728	0.735	0.016	7.86
	10/14/2014	5.77	0.0476	0.00235	0.0722	0.8074	0.003	7.85
	11/11/2014	5.81	0.0478	0.01173	0.0689	0.7644	0.058	7.88
	12/16/2014	5.80	0.0480	0.00106	0.0678	0.7667	0.122	7.83
	1/23/2015	5.70	0.0414	0.00485	0.0470	0.8131	0.016	8.94
	3/17/2015	5.56	0.0412	0.00626	ND	0.9339	ND	9.14
	4/14/2015	5.74	0.0415	0.00407	0.0535	0.7956	0.001	8.63
	5/22/2015	5.63	0.0411	0.00415	0.0766	0.788	0.065	8.73
	6/10/2015	5.89	0.0429	0.00333	0.0756	0.7612	ND	8.51
	7/14/2015	5.98	0.0427	0.00387	0.0721	0.7672	0.004	8.40

Note:

If no value is provided, no measurement was made

ND = measured concentration in solution is less than the detection limit of the testing

Table B3: Well MFS-tap Water Quality Data

Sample ID	Date	pH	Total Alk mg/L	As ug/L	Al mg/L	Ca mg/L	Fe mg/L	K mg/L	Mg mg/L	Mn mg/L	Na mg/L
MFS_tap	7/11/2013	7.30	51.6	5.25		22.2	ND	1.31	1.41	0.0000950	3.14
	9/17/2013	6.84	48.7		ND	21.6	ND	1.75	1.37	0.000671	2.83
	10/15/2013	7.44	51.6	2.63	0.0147	20.7	0.0923	1.28	1.66	0.00689	2.98
	11/13/2013	7.31	52.5	4.18	0.00925	21.1	0.141	1.17	1.63	0.00718	3.33
	12/11/2013	7.62	52.7	3.61	0.00602	21.4	0.160	1.21	1.59	0.0106	4.04
	1/14/2014	7.66	51.6		ND	21.8	0.138	1.63	1.39		2.94
	3/11/2014	7.57	51.5		0.0199	22.4	1.343	1.10	1.22	0.0097	3.64
	4/15/2014	7.97	52.0		0.0122	21.7	0.096	1.18	1.24	0.0049	3.21
	5/13/2014	7.85	50.3		0.0090	21.6	0.157	1.56	1.32	0.00435	2.80
	6/10/2014	7.70	50.8		0.0064	23.3	0.035	1.40	1.41	0.00602	3.40
	7/8/2014	7.40	57.0		0.0095	23.9	0.039	1.54	1.47	0.00732	3.32
	8/19/2014	7.54	54.3		0.0111	24.0	0.050	1.41	1.42	0.00574	3.59
	9/16/2014	7.32	52.7		ND	22.5	0.220	1.44	1.34	ND	3.16
	10/14/2014	7.24	51.2		0.00050	22.3	0.021	1.65	1.35	ND	3.00
	11/11/2014	7.60	44.8		ND	22.5	0.018	1.40	1.30	ND	3.32
	12/16/2014	7.68	52.6		ND	22.9	0.055	1.39	1.29	ND	3.73
	1/23/2015	7.86	52.3		ND	22.4	0.061	1.22	1.38	0.00156	3.08
	3/17/2015	7.79	53.0		0.00103	22.8	0.207	1.16	1.33	0.00226	3.50
	4/14/2015	7.80	51.9		0.00347	22.9	0.100	1.08	1.33	0.00172	3.51
	5/22/2015	7.73	51.5		ND	22.0	0.008	1.38	1.39	0.00109	2.78

6/10/2015	7.70	50.8		0.00831	22.7	0.023	1.62	1.44	0.00097	2.82
7/14/2015	7.24	46.2		0.00751	22.6	0.002	1.65	1.45	0.00093	2.80

Sample ID	Date	Si mg/L	Sr mg/L	Zn mg/L	F mg/L	Cl mg/L	NO_3^- mg/L	SO_4^{-2} mg/L
MFS_tap	7/11/2013	4.86	0.0408		0.242	1.23	0.535	15.3
	9/17/2013	4.66	0.0675	ND	0.0929	1.22	0.128	15.0
	10/15/2013	4.77	0.0668	0.0162	0.231	1.21	0.106	13.9
	11/13/2013	4.76	0.0733	0.0291	0.326	1.59	ND	17.6
	12/11/2013	4.79	0.0763	0.0204	0.531	3.69	ND	19.3
	1/14/2014	5.14			0.210	1.31	0.245	19.3
	3/11/2014	4.93	0.0949	0.00585	0.345	1.96	ND	15.9
	4/15/2014	4.74	0.0877	0.00241	0.227	1.18	ND	15.1
	5/13/2014	4.63	0.0722	0.0041	0.236	1.11	ND	15.4
	6/10/2014	4.68	0.0914	0.0112	0.235	1.24	ND	16.0
	7/8/2014	4.76	0.0908	0.0517	0.171	1.15	ND	16.0
	8/19/2014	4.77	0.0955	0.0197	0.299	1.47	0.161	15.9
	9/16/2014	4.89	0.0804	0.0279	0.207	1.12	0.006	14.0
	10/14/2014	4.82	0.0736	0.0223	0.173	1.23	0.023	13.9
	11/11/2014	4.80	0.0818	0.0124	0.244	1.31	ND	14.3
	12/16/2014	4.89	0.0840	0.0176	0.346	2.08	0.117	14.1
	1/23/2015	4.67	0.0670	0.0086	0.1534	1.14	ND	14.9
	3/17/2015	4.70	0.0733	0.0116	0.2769	1.59	ND	15.4

4/14/2015	4.72	0.0738	0.0131	0.2804	1.27	ND	15.2
5/22/2015	4.59	0.0593	0.0094	0.1309	1.11	0.318	14.8
6/10/2015	4.89	0.0628	0.0036	0.1453	1.04	ND	14.2
7/14/2015	4.86	0.0626	0.0052	0.1323	1.03	0.217	14.2

Note:

If no value is provided, no measurement was made

ND = measured concentration in solution is less than the detection limit of the testing

Table B4: Groundwater Isotopic Data

Sample ID	Date	$\delta^{18}O$ VSMOW ‰	δD VSMOW ‰	d-excess ‰
MFS-1_28ft_bgs	8/20/2013	-9.08	-55.7	17.0
	9/17/2013	-9.09	-55.1	17.6
	10/15/2013	-9.11	-54.9	18.0
	11/13/2013	-8.96	-54.4	17.3
	12/11/2013	-8.55	-52.3	16.1
	1/14/2014	-8.58	-51.6	17.1
	2/11/2014	-8.33	-50.3	16.3
	3/11/2014	-8.32	-50.5	16.1
	4/15/2014	-8.55	-50.4	18.0
	5/13/2014	-9.04	-54.8	17.6
	6/10/2014	-9.53	-57.3	18.9
	7/8/2014	-9.32	-58.4	16.2
	8/19/2014	-9.32	-58.2	16.4
	9/16/2014	-9.09	-56.4	16.4
	10/14/2014	-9.00	-56.0	16.0
	11/11/2014	-9.03	-55.4	16.9
	12/16/2014	-8.28	-51.0	15.2
	1/23/2015	-8.25	-50.7	15.3
	3/17/2015	-8.39	-51.9	15.3
	4/14/2015	-8.70	-54.1	15.5
	5/22/2015	-9.47	-56.6	19.2
	6/10/2015	-9.31	-57.5	17.0
	7/14/2015	-9.78	-60.3	18.0
MFS-1_41ft_bgs	10/15/2013	-9.11	-54.8	18.1
	11/13/2013	-8.85	-54.6	16.2
	12/11/2013	-8.72	-52.6	17.2
	1/14/2014	-8.61	-52.0	16.9
	2/11/2014	-8.39	-50.5	16.6
	3/11/2014	-8.40	-50.3	16.8
	4/15/2014	-8.54	-50.6	17.7
	5/13/2014	-9.24	-54.6	19.3

Sample ID	Date	$\delta^{18}O$ VSMOW ‰	δD VSMOW ‰	d-excess ‰
	6/10/2014	-9.48	-57.1	18.7
	7/8/2014	-9.78	-58.3	19.9
	8/19/2014	-9.14	-58.3	14.8
	9/16/2014	-8.88	-56.2	14.9
	10/14/2014	-9.00	-56.1	15.9
	11/11/2014	-9.12	-55.6	17.4
	12/16/2014	-8.36	-51.2	15.7
	1/23/2015	-8.42	-50.8	16.6
	3/17/2015	-8.88	-50.7	20.3
	4/14/2015	-8.80	-55.1	15.3
	5/22/2015	-9.29	-56.7	17.6
	6/10/2015	-9.39	-57.3	17.9
	7/14/2015	-10.16	-59.9	21.4
	8/20/2013	-9.06	-55.5	16.9
	10/15/2013	-9.15	-55.0	18.2
MFS-1_60ft_bgs	11/13/2013	-8.89	-54.4	16.7
	12/11/2013	-8.71	-52.9	16.8
	1/14/2014	-8.65	-52.1	17.1
	2/11/2014	-8.37	-50.4	16.5
	3/11/2014	-8.43	-50.3	17.1
	4/15/2014	-8.53	-49.7	18.6
	5/13/2014	-9.07	-54.3	18.3
	6/10/2014	-9.43	-57.1	18.3
	7/8/2014	-9.33	-58.2	16.4
	8/19/2014	-9.16	-58.4	14.8
	9/16/2014	-8.95	-57.0	14.6
	10/14/2014	-9.05	-56.0	16.4
	11/11/2014	-9.10	-55.7	17.1
	12/16/2014	-8.46	-51.6	16.1
	1/23/2015	-8.32	-50.6	16.0
	3/17/2015	-8.67	-50.7	18.6
	4/14/2015	-9.19	-52.6	20.9
	5/22/2015	-9.23	-56.5	17.3

Sample ID	Date	$\delta^{18}O$ VSMOW ‰	δD VSMOW ‰	d-excess ‰
	6/10/2015	-9.31	-57.0	17.5
	7/14/2015	-10.12	-59.8	21.1
	8/20/2013	-9.10	-54.9	17.8
	9/17/2013	-8.99	-54.8	17.1
MFS-1_80ft_bgs	10/15/2013	-9.15	-54.9	18.3
	11/13/2013	-8.94	-54.7	16.8
	12/11/2013	-8.67	-53.0	16.3
	1/14/2014	-8.54	-52.1	16.3
	2/11/2014	-8.47	-50.5	17.3
	3/11/2014	-8.36	-50.2	16.7
	4/15/2014	-8.55	-50.1	18.3
	5/13/2014	-9.08	-54.4	18.2
	6/10/2014	-9.43	-56.9	18.6
	7/8/2014	-9.44	-58.4	17.1
	8/19/2014	-9.31	-57.7	16.8
	9/16/2014	-9.09	-57.1	15.6
	10/14/2014	-9.00	-56.0	16.0
	11/11/2014	-8.97	-55.6	16.2
	12/16/2014	-8.42	-51.4	16.0
	1/23/2015	-8.19	-50.5	15.0
	3/17/2015	-8.23	-52.2	13.6
	4/14/2015	-8.80	-53.2	17.2
	5/22/2015	-9.71	-55.9	21.8
	6/10/2015	-9.21	-58.3	15.3
	7/14/2015	-9.73	-60.9	16.9
	9/17/2013	-9.17	-55.2	18.1
MFS-1_100ft_bgs	10/15/2013	-9.09	-55.1	17.6
	11/13/2013	-8.94	-54.9	16.6
	12/11/2013	-8.68	-53.0	16.5
	1/14/2014	-8.69	-52.3	17.2
	2/11/2014	-8.52	-50.7	17.5
	3/11/2014	-8.43	-50.4	17.1

Sample ID	Date	$\delta^{18}O$ VSMOW ‰	δD VSMOW ‰	d-excess ‰
	4/15/2014	-8.45	-50.1	17.6
	5/13/2014	-9.07	-54.3	18.3
	6/10/2014	-9.41	-57.0	18.3
	7/8/2014	-9.34	-58.4	16.3
	8/19/2014	-9.42	-57.9	17.4
	9/16/2014	-9.08	-56.9	15.7
	10/14/2014	-9.08	-55.7	17.0
	11/11/2014	-9.05	-55.4	17.0
	12/16/2014	-8.38	-51.6	15.4
	1/23/2015	-8.27	-50.9	15.3
	3/17/2015	-8.69	-50.8	18.7
	4/14/2015	-8.94	-53.1	18.4
	5/22/2015	-9.51	-56.1	20.0
	6/10/2015	-9.20	-57.1	16.5
	7/14/2015	-9.78	-60.0	18.3
	8/20/2013	-8.69	-52.4	17.0
MFS-2_grab	9/17/2013	-8.79	-51.8	18.5
MFS-2_15ft_bgs	10/15/2013	-8.74	-52.4	17.6
	11/13/2013	-8.77	-52.7	17.5
	12/11/2013	-8.52	-51.8	16.4
	1/14/2014	-8.65	-51.4	17.8
	2/11/2014	-8.75	-52.6	17.4
	3/11/2014	-8.67	-51.9	17.5
	4/15/2014	-8.65	-51.2	18.0
	5/13/2014	-8.63	-52.1	16.9
	6/10/2014	-8.69	-52.0	17.5
	7/8/2014	-8.56	-52.2	16.3
	8/19/2014	-8.72	-52.0	17.7
	9/16/2014	-8.56	-51.6	16.9
	10/14/2014	-8.49	-51.1	16.7
	11/11/2014	-8.59	-51.5	17.2
	12/16/2014	-8.68	-51.96	17.5

Sample ID	Date	$\delta^{18}O$ VSMOW ‰	δD VSMOW ‰	d-excess ‰
	1/23/2015	-8.62	-52.13	16.8
	3/17/2015	-8.84	-52.73	18.0
	4/14/2015	-9.09	-52.70	20.0
	5/22/2015	-9.07	-52.91	19.6
	6/10/2015	-9.10	-52.79	20.0
	7/14/2015	-8.76	-54.25	15.8
	8/20/2013	-8.57	-52.0	16.5
	9/17/2013	-8.60	-52.0	16.8
	10/15/2013	-8.73	-52.0	17.8
MFS-2_25ft_bgs	11/13/2013	-8.59	-51.7	17.0
	12/11/2013	-8.55	-51.2	17.2
	1/14/2014	-8.66	-51.7	17.6
	2/11/2014	-8.80	-51.8	18.6
	3/11/2014	-8.59	-51.7	17.0
	4/15/2014	-8.54	-51.2	17.1
	5/13/2014	-8.79	-51.8	18.5
	6/10/2014	-9.12	-51.7	21.3
	7/8/2014	-8.66	-52.5	16.7
	8/19/2014	-8.57	-52.7	15.8
	9/16/2014	-8.65	-51.7	17.5
	10/14/2014	-8.49	-51.5	16.4
	11/11/2014	-8.78	-52.1	18.2
	12/16/2014	-8.71	-52.69	17.0
	1/23/2015	-8.75	-52.18	17.8
	3/17/2015	-9.26	-52.47	21.6
	4/14/2015	-9.26	-52.74	21.4
	5/22/2015	-9.17	-52.42	20.9
	6/10/2015	-8.75	-53.27	16.7
	7/14/2015	-8.73	-54.24	15.6
	8/20/2013	-8.65	-51.7	17.5
	9/17/2013	-8.62	-52.1	16.9
MFS-2_35ft_bgs	10/15/2013	-8.62	-52.1	16.9

Sample ID	Date	$\delta^{18}O$ VSMOW ‰	δD VSMOW ‰	d-excess ‰
	12/11/2013	-8.56	-51.0	17.5
	1/14/2014	-8.69	-51.6	18.0
	2/11/2014	-8.67	-52.0	17.4
	3/11/2014	-8.74	-51.9	18.0
	4/15/2014	-8.65	-51.3	18.0
	5/13/2014	-8.78	-51.9	18.4
	6/10/2014	-8.63	-52.2	16.8
	7/8/2014	-8.79	-52.3	18.0
	8/19/2014	-8.77	-52.7	17.4
	9/16/2014	-8.72	-52.4	17.4
	10/14/2014	-8.59	-52.5	16.2
	11/11/2014	-8.80	-52.8	17.6
	12/16/2014	-8.73	-52.56	17.3
	1/23/2015	-8.82	-52.96	17.6
	3/17/2015	-8.83	-52.99	17.7
	4/14/2015	-9.19	-52.69	20.9
	5/22/2015	-8.76	-53.89	16.2
	6/10/2015	-8.99	-53.05	18.9
	7/14/2015	-8.91	-53.09	18.2
	9/17/2013	-9.01	-54.0	18.1
	10/15/2013	-8.88	-54.0	17.1
MFS_tap	11/13/2013	-8.79	-53.3	17.0
	12/11/2013	-8.85	-53.4	17.4
	1/14/2014	-8.57	-53.1	15.5
	3/11/2014	-9.00	-53.7	18.2
	4/15/2014	-8.93	-53.4	18.1
	5/13/2014	-8.71	-53.7	15.9
	6/10/2014	-8.79	-53.8	16.5
	7/8/2014	-8.80	-53.7	16.7
	8/19/2014	-8.84	-54.1	16.6
	9/16/2014	-8.83	-53.5	17.1
	10/14/2014	-8.77	-53.5	16.7
	11/11/2014	-8.85	-53.7	17.1

Sample ID	Date	$\delta^{18}O$ VSMOW ‰	δD VSMOW ‰	d-excess ‰
	12/16/2014	-8.85	-54.1	16.7
	1/23/2015	-8.84	-53.7	17.1
	3/17/2015	-8.73	-54.1	15.8
	4/14/2015	-8.80	-54.2	16.2
	5/22/2015	-8.60	-54.1	14.7
	6/10/2015	-9.26	-53.0	21.1
	7/14/2015	-8.65	-53.7	15.6

Note:

d-excess (‰) = $\delta D - 8 * \delta^{18}O$

APPENDIX C

MODEL INPUT LOGS

Geochemical modeling to develop expected range of concentrations resulting from the water-rock interactions at the MacLeish Field Station

```
TITLE MacLeish mineralogy in equilibrium with pure water at 12 degrees
C
SOLUTION 1 Pure Water
    temp      12
    pH        7
    pe        4
    redox     pe
    units     mmol/kgw
    density   1
    -water    1 # kg

EQUILIBRIUM_PHASES 1
    Anorthite 0 10
    Calcite   0 10
    Chalcopyrite 0 10
    Muscovite 0 10
    Phlogopite 0 10
    Pyrite    0 10
    Quartz    0 10
    Albite    0 10
SELECTED_OUTPUT 1
    -file                purewater.out
    -totals              K  Mg  Na  Al  Si  Ca  Cu
                         Fe  S  S(6)
END

TITLE MacLeish mineralogy in equilibrium with water and carbonic acid
SOLUTION 2 Pure water in equilibrium with CO2
    temp      12
    pH        7
    pe        4 CO2(g) -3.5
    redox     pe
    units     mmol/kgw
    density   1
    C         1 CO2(g)     -3.5
    O(0)      0 O2(g)      -0.67
    -water    1 # kg
EQUILIBRIUM_PHASES 1
    Anorthite 0 10
    CO2(g)    -3.5 10
    Calcite   0 10
    Chalcopyrite 0 10
    Muscovite 0 10
    Phlogopite 0 10
    Pyrite    0 10
    Quartz    0 10
    Albite    0 10
SELECTED_OUTPUT 1
    -file                purewater_CO2.out
    -totals              K  Mg  Na  Al  Si  Ca  Cu
                         Fe  S  S(6)
END
```

```
TITLE Reaction MacLeish mineralogy with water and carbonic acid at 12 degrees C
SOLUTION 0 Pure Water
    temp      12
    pH        7
    pe        4
    redox     pe
    units     mol/kgs
    density   1
    -water    1 # kg
REACTION 1
    Albite     1
    Anorthite  1
    Calcite    1
    Chalcopyrite 1
    Muscovite  1
    Phlogopite 1
    Pyrite     1
    Quartz     1
    1 millimoles in 1000 steps
SAVE solution 1-1000
TRANSPORT
    -cells                 1000
    -time_step             86400 # seconds
    -lengths               1000*0.001
    -correct_disp          true
EQUILIBRIUM_PHASES 1
    CO2(g)    -3.5 1
SELECTED_OUTPUT 1
    -file                 chapter2_part2.out
    -totals               K  Mg  Na  Al  Si  Ca  Cu
                          Fe  S  S(6)
END
```

Simulation of oxygen diffusion transport through a single fracture in a saturated bedrock formation with low hydraulic conductivity and porosity

Transient Coupled VADOSE/W

Project Settings

Length(L) Units: meters
Time(t) Units: Days
Force(F) Units: kN
Temp(T) Units: C
Energy Units: kJ
Latent Heat of Water: 3.34e+005
Phase Change Temperature: 0
Unit Weight of Water: 9.807 kN/m³
View: 2D

Analysis Settings

Transient Coupled VADOSE/W

Kind: VADOSE/W
Method: Transient Uncoupled
Settings
- Initial PWP: Water Table
- Initial Thermal Conditions Source: Spatial Function
- Temperature Spatial Fn.: New Temperature Function
- Gas Diffusion: Oxygen
- Initial Concentrations from: (none)

Control
- Ground Freezing Latent Heat Effects: No
- Vegetation: No
- Apply Runoff: Yes

Convergence
- Convergence Type: Head Vector Norm
- Maximum Number of Iterations: 25
- Tolerance: 0.001
- Maximum Change in K: 0.1
- Rate of Change in K: 1.02
- Minimum Change in K: 1e-005
- Equation Solver: Parallel Direct
- Potential Seepage Max # of Reviews: 10

Time
- Starting Time: 0 days
- Duration: 1 days
- # of Steps: 24
- Step Generation Method: Linear
- Save Steps Every: 1
- Use Adaptive Time Stepping: No

Materials

Bedrock
Model: Full Thermal
Hydraulic
K-Function: Igneous Bedrock
Vol. WC. Function: Igneous Bedrock
K-Ratio: 1
K-Direction: 0 °
Thermal
Thermal K Fn (K vs VWC): Clay (kJ/day/m/C)
Vol Specific Heat Fn: Clay (kJ/m3)
Gas
Gas Decay (Yrs.): 0
Eff. Reaction Rate Coef.: 0 /days

Open Fracture
Model: Full Thermal
Hydraulic
K-Function: Uniform Fine Sand #2, Ksat = 0.0976 m/day
Vol. WC. Function: Uniform Fine Sand #1
K-Ratio: 1
K-Direction: 0 °
Thermal
Thermal K Fn (K vs VWC): Sand (kJ/day/m/C)
Vol Specific Heat Fn: Sand (kJ/m3)
Gas
Gas Decay (Yrs.): 0
Eff. Reaction Rate Coef.: 0 /days

Boundary Conditions

Head - left
Type: Head (H) 150

Oxygen
Type: Unit Mass Flux (qm) 1

Average GW Temp
Type: Temperature (T) 12

Head - right
Type: Head (H) 149

Initial Water Tables

Initial Water Table 1
Max. negative head: 5
Coordinates
Coordinate: (0, 150) m

Coordinate: (1000, 149) m
Coordinate: (,) m

K Functions

Uniform Fine Sand #2, Ksat = 0.0976 m/day

Model: Data Point Function
Function: X-Conductivity vs. Pore-Water Pressure
Curve Fit to Data: 100 %
Segment Curvature: 36 %
K-Saturation: 0.0976
Data Points: Matric Suction (kPa), X-Conductivity (m/days)
Data Point: (0.05, 0.0976)
Data Point: (0.1, 0.0976)
Data Point: (0.59948, 0.0976)
Data Point: (3.5938, 0.018951)
Data Point: (21.544, 7.8554e-006)
Data Point: (129.15, 3.756e-008)
Data Point: (774.26, 5.0705e-010)
Data Point: (1111.1, 2.3587e-010)
Data Point: (4641.6, 1.2634e-011)
Data Point: (27826, 2.7279e-013)
Data Point: (105930, 1.3346e-014)
Data Point: (166810, 4.5985e-015)
Data Point: (210740, 2.6153e-015)
Data Point: (315560, 9.4601e-016)
Data Point: (420370, 4.3325e-016)
Data Point: (525190, 2.2192e-016)
Data Point: (630000, 1.1888e-016)
Data Point: (734810, 6.2644e-017)
Data Point: (839630, 3.2207e-017)
Data Point: (944440, 2.673e-017)
Data Point: (1000000, 2.673e-017)
Estimation Properties
Hydraulic K Sat: 0 m/days
Hyd. K-Function Estimation Method: Van Genuchten Function
Maximum: 1000
Minimum: 0.01
Num. Points: 20
Residual Water Content: 0 m^3/m^3

Igneous Bedrock

Model: Data Point Function
Function: X-Conductivity vs. Pore-Water Pressure
Curve Fit to Data: 100 %
Segment Curvature: 100 %
K-Saturation: 2.6e-009
Data Points: Matric Suction (kPa), X-Conductivity (m/days)
Data Point: (0.01, 2.6e-009)
Data Point: (0.023357215, 2.5999995e-009)

Data Point: (0.054555948, 2.5999954e-009)
Data Point: (0.1274275, 2.5999652e-009)
Data Point: (0.29763514, 2.5997407e-009)
Data Point: (0.6951928, 2.598071e-009)
Data Point: (1.6237767, 2.5856035e-009)
Data Point: (3.7926902, 2.4926082e-009)
Data Point: (8.8586679, 1.8648983e-009)
Data Point: (20.691381, 2.4364244e-010)
Data Point: (48.329302, 9.7968339e-013)
Data Point: (112.88379, 1.3148869e-015)

Estimation Properties
Volume Water Content Function: Uniform Fine Sand #1
Hydraulic K Sat: 9.34e-005 m/days
Hyd. K-Function Estimation Method: Van Genuchten Function
Maximum: 1e+005
Minimum: 0.01
Num. Points: 20
Residual Water Content: 0.0025 m³/m³

Vol. Water Content Functions

Uniform Fine Sand #1

Model: Fredlund-Xing Function
Function: Vol. Water Content vs. Pore-Water Pressure
A: 2.9893 kPa
N: 3.8329
M: 0.50764
Saturated Water Content: 0.3 m³/m³
Suction Limit: 1e+006
Mv: 1e-007 /kPa
Porosity: 0.29999998

Igneous Bedrock

Model: Data Point Function
Function: Vol. Water Content vs. Pore-Water Pressure
Curve Fit to Data: 100 %
Segment Curvature: 70 %
Mv: 0 /kPa
Porosity: 0.015018307
Data Points: Matric Suction (kPa), Vol. Water Content (m³/m³)
Data Point: (0.20461148, 0.015)
Data Point: (0.40922295, 0.015)
Data Point: (1.0230574, 0.015)
Data Point: (2.0461148, 0.015)
Data Point: (4.0922295, 0.015)
Data Point: (10.230574, 0.0144)
Data Point: (20.461148, 0.0099)
Data Point: (40.922295, 0.004)
Data Point: (102.30574, 0.0026)
Data Point: (204.61148, 0.0025)

Data Point: (409.22295, 0.0025)
Data Point: (1023.0574, 0.0025)
Data Point: (2046.1148, 0.0025)

Estimation Properties

Vol. WC Estimation Method: Sample functions
Sample Material: Clay
Saturated Water Content: 0 m^3/m^3
Liquid Limit: 0 %
Diameter at 10% passing: 0
Diameter at 60% passing: 0
Maximum: 1000
Minimum: 0.01
Num. Points: 20

Thermal K vs Vol WC Functions

Clay (kJ/day/m/C)

Model: Spline Data Point Function
Function: Thermal Conductivity vs. Vol. Water Content
Curve Fit to Data: 100 %
Segment Curvature: 41 %
Y-Intercept: 39.455
Data Points: Vol. Water Content (m^3/m^3), Thermal Conductivity (kJ/days/m/°C)
Data Point: (0, 39.455)
Data Point: (0.021579, 46.507)
Data Point: (0.043158, 53.558)
Data Point: (0.064737, 57.683)
Data Point: (0.086316, 60.61)
Data Point: (0.10789, 62.88)
Data Point: (0.12947, 64.735)
Data Point: (0.15105, 66.303)
Data Point: (0.17263, 67.662)
Data Point: (0.19421, 68.86)
Data Point: (0.21579, 69.932)
Data Point: (0.23737, 70.902)
Data Point: (0.25895, 71.787)
Data Point: (0.28053, 72.601)
Data Point: (0.30211, 73.355)
Data Point: (0.32368, 74.057)
Data Point: (0.34526, 74.713)
Data Point: (0.36684, 75.33)
Data Point: (0.38842, 75.912)
Data Point: (0.41, 76.462)

Estimation Properties

MineralThermalK: 0 kJ/days/m/°C
Maximum: 1
Minimum: 0
Num. Points: 20

Sand (kJ/day/m/C)

Model: Spline Data Point Function
Function: Thermal Conductivity vs. Vol. Water Content
Curve Fit to Data: 100 %
Segment Curvature: 41 %
Y-Intercept: 98.33
Data Points: Vol. Water Content (m^3/m^3), Thermal Conductivity (kJ/days/m/°C)
Data Point: (0, 98.33)
Data Point: (0.015789, 116.29)
Data Point: (0.031579, 134.25)
Data Point: (0.047368, 144.75)
Data Point: (0.063158, 152.21)
Data Point: (0.078947, 157.99)
Data Point: (0.094737, 162.71)
Data Point: (0.11053, 166.71)
Data Point: (0.12632, 170.17)
Data Point: (0.14211, 173.22)
Data Point: (0.15789, 175.95)
Data Point: (0.17368, 178.42)
Data Point: (0.18947, 180.67)
Data Point: (0.20526, 182.75)
Data Point: (0.22105, 184.67)
Data Point: (0.23684, 186.45)
Data Point: (0.25263, 188.13)
Data Point: (0.26842, 189.7)
Data Point: (0.28421, 191.18)
Data Point: (0.3, 192.58)
Estimation Properties
MineralThermalK: 0 kJ/days/m/°C
Maximum: 1
Minimum: 0
Num. Points: 20

Vol. Specific Heat Functions

Clay (kJ/m3)

Model: Spline Data Point Function
Function: Volumetric Specific Heat Capacity vs. Vol. Water Content
Curve Fit to Data: 100 %
Segment Curvature: 43 %
Y-Intercept: 1354.1
Data Points: Vol. Water Content (m^3/m^3), Volumetric Specific Heat Capacity ($kJ/m^3/°C$)
Data Point: (0, 1354.1)
Data Point: (0.045556, 1544.7)
Data Point: (0.091111, 1735.3)
Data Point: (0.13667, 1925.9)
Data Point: (0.18222, 2116.5)
Data Point: (0.22778, 2307.1)
Data Point: (0.27333, 2497.7)
Data Point: (0.31889, 2688.3)

Data Point: (0.36444, 2878.9)
Data Point: (0.41, 3069.5)
Estimation Properties
MassSpecHeat: 0 kJ/g/°C
Maximum: 1
Minimum: 0
Num. Points: 20

Sand (kJ/m3)
Model: Spline Data Point Function
Function: Volumetric Specific Heat Capacity vs. Vol. Water Content
Curve Fit to Data: 100 %
Segment Curvature: 43 %
Y-Intercept: 1323
Data Points: Vol. Water Content (m³/m³), Volumetric Specific Heat Capacity (kJ/m³/°C)
Data Point: (0, 1323)
Data Point: (0.015789, 1389.1)
Data Point: (0.031579, 1455.1)
Data Point: (0.047368, 1521.2)
Data Point: (0.063158, 1587.3)
Data Point: (0.078947, 1653.3)
Data Point: (0.094737, 1719.4)
Data Point: (0.11053, 1785.4)
Data Point: (0.12632, 1851.5)
Data Point: (0.14211, 1917.6)
Data Point: (0.15789, 1983.6)
Data Point: (0.17368, 2049.7)
Data Point: (0.18947, 2115.8)
Data Point: (0.20526, 2181.8)
Data Point: (0.22105, 2247.9)
Data Point: (0.23684, 2313.9)
Data Point: (0.25263, 2380)
Data Point: (0.26842, 2446.1)
Data Point: (0.28421, 2512.1)
Data Point: (0.3, 2578.2)
Estimation Properties
MassSpecHeat: 0 kJ/g/°C
Maximum: 1
Minimum: 0
Num. Points: 20

Spatial Functions

New Temperature Function
Model: Linear Interpolation
Limit Range By: Data Values
Data Points: X (m), Y (m), Temperature (°C)
Data Point: (0, 150, 15)
Data Point: (1000, 150, 15)
Data Point: (1000, 0, 15)

Data Point: (0, 0, 15)

Regions

	Material	Points	Area (m²)
Region 1	Bedrock	1,10,2,3,4	99500
Region 2	Open Fracture	1,5,9,6,2,10	100
Region 3	Bedrock	5,7,8,6,9	50400

Lines

	Start Point	End Point	Gas Boundary	Thermal Boundary
Line 1	2	3		
Line 2	3	4		
Line 3	4	1		
Line 4	1	5	Oxygen	
Line 5	6	2		
Line 6	5	7		
Line 7	7	8		Average GW Temp
Line 8	8	6		
Line 9	5	9	Oxygen	
Line 10	9	6		
Line 11	1	10	Oxygen	
Line 12	10	2		

Points

	X (m)	Y (m)	Hydraulic Boundary
Point 1	0	100	
Point 2	1000	99	
Point 3	1000	0	Head - right
Point 4	0	0	Head - left
Point 5	0	100.1	
Point 6	1000	99.1	
Point 7	0	150	
Point 8	1000	150	
Point 9	10	100.09	
Point 10	10	99.99	

Simulation of oxygen diffusion transport through a single fracture in a saturated bedrock formation with low hydraulic conductivity and porosity

Advection-Dispersion

Project Settings

Length(L) Units: Meters
Time(t) Units: Days
Mass(M) Units: Grams
Concentration(C) Units: g/m³
Density Units: g/m³
Mass Flux Units: g/days
View: 2D
Element Thickness: 1

Analysis Settings

Advection-Dispersion

Kind: CTRAN/W
Parent: Oxygen transport along fracture_1 day
Method: Advection-Dispersion
Settings
- Set Velocities to zero: No
- Seep Results Source: Parent Analysis
- Initial Concentrations from: (none)
- Exclude cumulative values: No

Control
- Time: Backward Difference

Convergence
- Maximum Number of Iterations: 25
- Minimum Concentration Difference: 1e-005
- Significant Digits: 2
- Equation Solver: Parallel Direct

Time
- Starting Time: 0 days
- Duration: 1 days
- # of Steps: 24
- Step Generation Method: Linear
- Save Steps Every: 2

Materials

Bedrock

Contaminant
- Diffusion Function: Constant Diffusion
- Longitudinal Dispersivity: 0.01 m
- Transverse Dispersivity: 0.01 m
- Decay Half-Life: 0 days

Dry Density: 0 g/m³

Open Fracture

Contaminant

Diffusion Function: Constant Diffusion
Longitudinal Dispersivity: 100 m
Transverse Dispersivity: 100 m
Decay Half-Life: 0 days
Dry Density: 0 g/m³

Boundary Conditions

Unit Concentration

Type: Unit Mass Flux (qm) 1

Contaminant Diffusion Functions

Constant Diffusion

Model: Spline Data Point Function
Function: Diffusion Coefficient vs. Vol. Water Content
Curve Fit to Data: 100 %
Segment Curvature: 100 %
Y-Intercept: 1e-006
Data Points: Vol. Water Content (m³/m³), Diffusion Coefficient (m²/days)
Data Point: (0, 1e-006)
Data Point: (1, 1e-006)

Points

	X (m)	Y (m)
Point 1	0	100
Point 2	1,000	99
Point 3	1,000	0
Point 4	0	0
Point 5	0	100.1
Point 6	1,000	99.1
Point 7	0	150
Point 8	1,000	150
Point 9	10	100.09

Point 10	10	99.99

Lines

	Start Point	End Point	Length (m)	Angle (°)	Contam Boundary
Line 1	2	3	99	90	
Line 2	3	4	1,000	0	
Line 3	4	1	100	90	
Line 4	1	5	0.1	90	Unit Concentration
Line 5	6	2	0.1	90	
Line 6	5	7	49.9	90	
Line 7	7	8	1,000	0	
Line 8	8	6	50.9	90	
Line 9	5	9	10	-0.0573	Unit Concentration
Line 10	9	6	990	-0.0573	
Line 11	1	10	10	-0.0573	Unit Concentration
Line 12	10	2	990	-0.0573	

Regions

	Material	Points	Area (m^2)
Region 1	Bedrock	1,10,2,3,4	99,500
Region 2	Open Fracture	1,5,9,6,2,10	100
Region 3	Bedrock	5,7,8,6,9	50,400

Inverse geochemical modeling to determine mineral weathering reactions controlling the water chemistry at the MacLeish Field Station

```
TITLE Inverse modeling using water from MFS-1 and MFS-tap  -  PHREEQC Database

SOLUTION 1 MFS-1
    temp      12
    pH        6.61
    pe        4
    redox     pe
    units     mg/l
    density   1
    Al        0.0056
    Ca        9.69
    Cl        1.259
    F         0.0412
    Fe        0.78
    K         1.42
    Mg        1.048
    Mn        0.1376
    N(5)      0.215
    Na        1.55
    S(6)      6.33
    Si        4.3
    Sr        0.0443
    Zn        0.0074
    Alkalinity 39.12
    -water    1 # kg


SOLUTION 2 MFS-tap
    temp      12
    pH        7.55
    pe        4
    redox     pe
    units     mg/l
    density   1
    Al        0.008
    Ca        22.328
    Cl        1.422
    F         0.238
    Fe        0.148
    K         1.388
    Mg        1.398
    Mn        0.004
    N(5)      0.186
    Na        3.224
    S(6)      15.446
    Si        4.787
    Sr        0.075
    Zn        0.015
    Alkalinity 51.4
    -water    1 # kg
```

```
INVERSE_MODELING 1
    -solutions      1        2
    -uncertainty    0.25     0.25
    -phases
        Albite
        Anorthite
        Calcite
        Dolomite
        Chlorite(14A)
        Kaolinite
        Pyrite
        Siderite
        Quartz
        Gibbsite
        Goethite
        CO2(g)
    -range             1000
    -tolerance         1e-10
    -mineral_water     true
SELECTED_OUTPUT 1
    -file                 inverse model.sel
    -inverse_modeling     true
END
```

TITLE Inverse modeling using water from MFS-1 and MFS-tap - LLNL Database

```
SOLUTION 1 MFS-1
    temp      12
    pH        6.61
    pe        4
    redox     pe
    units     mg/l
    density   1
    Al        0.0056
    Ca        9.69
    Cl        1.259
    F         0.0412
    Fe        0.78
    K         1.42
    Mg        1.048
    Mn        0.1376
    N(5)      0.215
    Na        1.55
    S(6)      6.33
    Si        4.3
    Sr        0.0443
    Zn        0.0074
    Alkalinity 39.12
    -water    1 # kg


SOLUTION 2 MFS-tap
    temp      12
    pH        7.55
    pe        4
    redox     pe
```

```
    units     mg/l
    density   1
    Al        0.008
    Ca        22.328
    Cl        1.422
    F         0.238
    Fe        0.148
    K         1.388
    Mg        1.398
    Mn        0.004
    N(5)      0.186
    Na        3.224
    S(6)      15.446
    Si        4.787
    Sr        0.075
    Zn        0.015
    Alkalinity 51.4
    -water    1 # kg
INVERSE_MODELING 1
    -solutions      1        2
    -uncertainty    0.25     0.25
    -phases
        Albite
        Anorthite
        Calcite
        Dolomite
        Kaolinite
        Pyrite
        Siderite
        Quartz
        Gibbsite
        Goethite
        Chalcopyrite
        Muscovite
        Phlogopite
        CO2(g)
    -range             1000
    -tolerance         1e-10
    -mineral_water     true
SELECTED_OUTPUT 1
    -file                 inverse model_v2.sel
    -inverse_modeling     true
END
```

REFERENCES

Acero, P., L.F. Auque, J.P. Galve, D. Carbonel, M.J. Gimeno, Y. Yechiele, M.P. Asta, and J.B. Gomez, 2015, Evaluation of geochemical and hydrogeological processes by geochemical modeling in an area affected by evaporite karstification. Journal of Hydrology, v. 529, p. 1874-1889.

Appelo, C.A.J. and D. Postma, 2005, Geochemistry, groundwater and pollution, Second Edition. A.A. Balkema Publishers: Amsterdam, the Netherlands.

Barranco, F.T., Jr., W.L. Balsam, and B.C. Deaton, 1989, Quantitative reassessment of brick red lutites: Evidence from reflectance spectrophotometry. Marine Geology, v. 89, p. 299-314.

Barton, C., 1996, Characterizing bed rock fractures in outcrop for ground-water hydrology studies – an example from Mirror Lake, Grafton County, New Hampshire. In Morganwalp, D. and D. Aronson, eds., U.S. Geological Survey Toxic Substances Hydrology Program – Proceedings of the technical meeting, Colorado Springs, CO. U.S. Geological Survey Water Resources Investigations Report 94-4015.

Berkley, L., 1999, Water and soil chemistry of the Smith Experimental Forest, West Whately, Massachusetts. Mill River Watershed Project Assessment Report.

Berner, R.A., 1978, Rate control of mineral dissolution under the Earth surface conditions. American Journal of Science v. 278, p. 1235-1252.

Bethke, C.M., 1996, Geochemical Reaction Modeling: Concepts and Applications. Oxford University Press, Inc.: New York, New York.

Bigham, J.M., D.C. Golden, S.W. Buol, S.B. Weed, and L.H. Bowen, 1978, Iron oxide mineralogy of well-drained ultiols and oxisols: II. Influence on Color, Surface Area, and phosphate retention. Soil Science Society of America Journal, v. 42, p. 816-825.

Binning, P.J., D. Postma, T.F. Russell, J.A. Wesselingh, and P.F. Boulin, 2007, Advective and diffusive contributions to reactive gas transport during pyrite oxidation in the unsaturated zone. Water Resources Research, v. 43.

Blum, P., 1997, Physical properties handbook: a guide to the shipboard measurement of physical properties of deep-sea cores. Oceanic Drilling Program Technical Note, 26 pp.

Boutt, D.F., P. Diggin, S. Mabee, 2010, A field study (Massachusetts, USA) of the factors controlling the depth of groundwater flow systems in crystalline fractured-rock terrain. Hydrogeology Journal, v. 18, p. 1839-1854.

Brantley, S.L., M.E. Holleran, L.Jin, and E. Bazilevskaya, 2013, Probing deep weathering in the Shale Hills Critical Zone Observatory, Pennsylvania (USA): the hypothesis of nested chemical reaction fronts in the subsurface. Earth Surface Processes and Landforms, v. 38, p. 1280-1298.

Bustos Medina, D.A., G.S. van den Berrg, B.M. van Breukelen, M. Juhasz-Holterman, and P.J. Stuyfzand, 2013, Iron-hydroxide clogging of public supply wells receiving artificial recharge: near-well and in-well hydrological and hydrochemical observations. Hydrogeology Journal, v. 21, p. 1393-1412.

Caine, J.S., and S.R.A. Tomusiak, 2003, Brittle structures and their role in controlling porosity and permeability in a complex Precambrian crystalline-rock aquifer system in the Colorado Rocky Mountain Front Range. Geological Society of America Bulletin v. 115, p. 1410-1424.

Clark, R.N., 1999, Chapter 1: Spectroscopy of Rocks and Minerals, and Principles of Spectroscopy, in Manual of Remote Sensing, Volume 3, Remote Sensing for the Earth Sciences, A.N. Rencz, ed. John Wiley and Sons, New York, p 3- 58.

Dai, Z., J. Samper, and R. Ritzi, Jr., 2006, Identifying geochemical processes by inverse modeling of multicomponent reactive transport in the Aquia aquifer. Geoshpere, v. 2, n. 4, p. 210-219.

Davis, S.N., and L.J. Turk, 1964, Optimum depth of wells in crystalline rocks. Ground Water v. 2, p. 6-11.

Deaton, B.C. and W.L. Balsam, 1991, Visible spectroscopy – A rapid method for determining hematite and goethite concentration in geologic materials. Journal of Sedimentary Petrology v. 61, n. 4, p. 628-632.

Demers, I., B. Bussiere, M. Mbonimpa, and M. Benzaazoua, 2009, Oxygen diffusion and consumption in low-sulphide tailings covers. Canadian Geotechnical Jounral, v. 46, p. 454-469.

Deutsch, W.J., 1997, Groundwater Geochemistry: Fundamentals and Applications to Contamination. Lewis Publishers: Boca Raton, Florida.

DeWalle, D.R., P.J. Edwards, B.R. Swistock, R. Aravena, and R.J. Drimmie, 1997, Seasonal isotope hydrology of three Appalachian forest catchments. Hydrological Processes v. 11, p. 1895-1906.

Domenico, P.A. and F.W. Schwartz, 1990, Physical and Chemical Hydrogeology. John Wiley & Sons: New York, New York.

Drake, H. and E.-L. Tullborg, 2006, Hydrothermal red-staining adjacent to fractures in granodioritic to dioritic rock, Simpevarp, south-east Sweden. Bulletin of Geological Society of Finland Special Issue 1, p. 26.

Drake, H., E.-L Tullborg, and H. Annersten, 2008, Red-staining of the wall rock and its influence on the reducing capacity around water conducting fractures. Applied Geochemistry v. 23, p. 1898-1920.

Drever, J.I., 2002, The Geochemistry of Natural Waters: Surface and Groundwater Environments, 3rd Edition. Prentice-Hall Inc.: Upper Saddle River, New Jersey.

Ehlen, J., 2002, Some effects of weathering on joints in granitic rocks. Cantena, v. 49, p. 91-109.

Ennis, D.J., N.W. Dunbar, A.R. Campbell, and C.E. Chapin, 2000, The effects of K-metasomatism on the mineralogy and geochemistry of silicic ignimbrites near Socorro, New Mexico. Chemical Geology, v. 167, p. 285-312.

Flanagan, S.M., J.D. Ayotte, and G.R. Robinson, 2011, Quality of Water from Crystalline Rock Aquifers in New England, New Jersey, and New York, 1995-2007. U.S. Geological Survey Scientific Investigations Report 2011-5220.

Fletcher, L.S., 1999, The geochemistry of the Avery Brook subcatchment in the Mill River watershed, Conway, MA. Mill River Watershed Project Assessment Report.

Ganor, J., E. Roueff, Y. Erel, and J.D. Blum, 2005, The dissolution kinetics of a granite and its minerals – Implications for comparison between laboratory and field dissolution rates. Geochimica et Cosmochimica Acta v. 69, n. 3, p. 607-621.

Gauthier, G., A.L. Burke, and M. Leclerc, 2012, Assessing XRF for the geochemical characterization of radiolarian chert artifacts from northeastern North America. Journal of Archaeological Science, v. 39, p. 2436-2451.

Geo-Slope, 2014, Vadose Zone Modeling with VADOSE/W An Engineering Methodology, 2014 Edition. Geo-Slope International Ltd. Calgary, Alberta, Canada.

Geo-Slope, 2012. Contaminant Modeling with CTRAN/W An Engineering Methodology, February 2012 Edition. Geo-Slope International Ltd.: Calgary, Alberta, Canada

Geotek, 2014, Multi-Sensor Core Logger Manual. Geotek Ltd., Northamptonshire, United Kingdom.

Grisak, G.E., and J.F. Pickens, 1980, Solute transport through fractured media: 1, The effect of matrix diffusion. Water Resources Research v. 16, p. 719-730.

Guimaraes, J.T.F., M.C.L. Cohen, M.C. Franca, A.K.T da Silva, and S.F.S. Rodrigues, 2013, Mineralogical and geochemical influences on sediment color of Amazon wetlands analyzed by visible spectrophotometry. Acta Amazonica, v. 43, n. 3, p. 331-342.

Gustafson, G. and J. Krasny, 1994, Crystalline rock aquifers: Their occurrence, use and importance. Applied Hydrogeology v. 2, p. 64-75.

Haberer, C.M., O.A. Cirpka, M. Rolle, and P. Grathwohl, 2014, Experimental sensitivity analysis of oxygen transfer in the capillary fringe. Groundwater v. 52, n. 1, p. 37-49.

Halihan, T., A. Love, and J.M.J. Sharp, 2005, Identifying connections in a fractured rock aquifer using ADFTs. Ground Water v. 43, p. 327-335.

Harte, P.T., 2013, Hydraulically controlled discrete sampling from open boreholes. Ground Water v. 51, p. 822-827.

Harte, P.T., 2015, Ambient flow in open boreholes in crystalline-rock aquifers: observations from SBDT and Borehole Logging. 2015 National Groundwater Association Conference on Groundwater in Fractured Rock, Burlington, VT.

Harte, P.T., G.R. Robinson, J.D. Ayotte, and S.M. Flanagan, 2008, Framework for Evaluating Water Quality of the New England Crystalline Rock Aquifers. U.S. Geological Survey Open-File Report 2008-1282.

Harte, P.T., J.A. Anderson, J.H. Williams, and A. Fuller, 2014, Observations from borehole dilution logging experiments in fractured crystalline rock under ambient and pump test conditions. Environmental and Engineering Geophysical Society (SAGEEP) Annual Meeting, March 16-20, 2014. Boston, Massachusetts. 14 p.

Hatch, N.L., Jr., D. Robinson, and R.S. Stanley, 1988, Stratigraphy of the Connecticut Valley Belt, Chapter B. IN Hatch, N.L., Jr. Bedrock geology of Massachusetts. U.S. Geological Survey Professional Paper 1366 A-D, p. B1-B34.

Helgeson, H.C., R.M. Garrels, and F.T. Mackenzie, 1969, Evaluation of irreversible reactions in geochemical processes involving minerals and aqueous solutions – II. Applications. Geochimica et Cosmochimica Acta v. 33, p. 455-481.

Hem, J.D., 1985, Study and Interpretation of the Chemical Characteristics of Natural Water. U.S. Geological Survey Professional Paper 2254.

Hsieh, P., 1996, An overview of field investigations of fluid flow in fractured crystalline rocks on the scale of hundreds of meters. In Stevens, P. and T. Nicholson, eds,. Joint U.S. Geological Survey, Nuclear Regulatory Commission Workshop on Research Related to Low-Level Radioactive Waste Disposal, May 4-6, 1993. U.S. Geological Survey Water Resources Investigation Report 95-4015.

Hsieh, P. and A. Shapiro, 1996, Hydraulic characteristics of fractured bedrock underlying the fse well field at the Mirror Lake site, Grafton County, New Hampshire. In Morganwalp, D. and D. Aronson, eds., U.S. Geological Survey Toxic Substances Hydrology Program – Proceedings of the technical meeting, Colorado Springs, CO: U.S. Geological Survey Water Resources Investigations Report 94-4015, Reston, VA.

Hunt, G.R., J.W. Salisbury, and C.J. Lenhoff, 1971, Visible and near-infrared spectra of minerals and rocks: III Oxides and hydroxides. Modern Geology v. 2, p. 195-205.

Interstate Technology & Regulatory Council, 2006, Technology Overview of Passive Sampler Technologies, DSP-4. 115 pp.

Interstate Technology & Regulatory Council, 2007, Protocol for use of five passive samplers to sample for a variety of contaminants in groundwater, DSP-5. 122 pp.

Isaacson, M., in progress, The influence of threshold soil dynamics on stream and groundwater temperature distribution. University of Massachusetts Amherst Master of Science Thesis.

Jin, L. R. Ravella, B. Ketchum, P.R. Bierman, P. Heaney, T. White, and S.L. Brantley, 2010, Mineral weathering and elemental transport during hillslope evolution at the Susquehanna/Shale Hills Critical Zone Observatory. Geochimica et Cosmochimica Acta v. 74, p. 3669-3691.

Jin, L., D.M. Andrews, G.H. Holmes, H. Lin, and S.L. Brantley, 2011, Opening the "Black Box": water chemistry reveals hydrological controls on weathering in the Susquehanna Shale Hills Critical Zone Observatory. Vadose Zone Journal v. 10, p. 928-942.

Johnson, C. and A. Dunstan, 1998, Lithology and fracture characterization from drilling investigations in the Mirror Lake area – from 1979 through 1995 in Grafton County, New Hampshire. U.S. Geological Survey Water Resources Investigations Report 98-4183.

Kendall, C. and J.J. McDonnell, 1998, Isotope Tracers in Catchment Hydrology. Elsevier: Amsterdam, the Netherlands.

Keys, W.S., 1990, Borehole geophysics applied to ground-water investigations. U.S. Geological Society Techniques of Water-Resources Investigations, Book 2, Chapter E2, 150 pp.

Kim, H. and C.H. Benson, 2004, Contributions of advective and diffusive oxygen transport through multilayer composite caps over mine waste. Journal of Contaminant Hydrology v. 71, p. 193-218.

Klein, C. and C.S. Hurlburt, Jr., 1993, Manual of Mineralogy, 21st Edition. John Wiley & Sons: New York, New York.

Krauskopf, K.B., 1967, Introduction to geochemistry. McGraw-Hill International Series in the Earth and Planetary Sciences: New York, New York.

Lapham, W.W., 1990, A plan for the study of the hydrogeology of bedrock New England. U.S. Geological Survey Open-File Report 90-374.

Ledesma-Ruiz, R., E. Pasten-Zapata, R. Parra, T. Harter, and J. Mahlknecht, 2015, Investigation of the geochemical evolution of groundwater under agricultural land: A case study in northeastern Mexico. Journal of Hydrology v. 521, p. 410-423.

Li, L., C.I. Steefel, and L. Yang, 2008, Scale dependence of mineral dissolution rates within single pores and fractures. Geochimica et Cosmochimica Acta v. 72, p. 360-377.

Lipson, D.S., J.E. McCray, and G.D. Thyne, 2007, Using PHREEQC to Simulate Solute Transport in Fractured Bedrock. Groundwater v. 45, n. 4, p. 468-472.

Maher, K., 2010, The dependence of chemical weathering rates on fluid residence time. Earth and Planetary Science Letters v. 294, p. 101-110.

Malmstrom, M. and S. Banwart, 1997, Biotite dissolution at 25°C: The pH dependence of dissolution rate and stoichiometry. Geochimica et Cosmochimica Acta v. 61, n. 14, p. 2779-2799.

Malmstrom, M.E., G. Destouni, S.A. Banwart, and B.H.E. Stromberg, 2000, Resolving the scale dependence of mineral weathering rates. Environmental Science & Technology v. 34, n. 7, p. 1375-1378.

Malmstrom, M.E., G. Destouni, and P. Martinet, 2004, Modeling expected solute concentration in randomly heterogeneous flow systems with multicomponent reactions. Environmental Science & Technology v. 38, n. 9, p. 2673-2679.

Manda, A.K., S.B. Mabee, D.U. Wise, 2008, Influence of rock fabric on fracture attribute distribution and implications for groundwater flow in the Nashoba Terrane, eastern Massachusetts. Journal of Structural Geology v. 30, p. 464-477.

Manning, A.H., P.L. Verplanck, J.S. Caine, and A.S. Todd, 2013, Links between climate change, water-table depth, and water chemistry in a mineralized mountain watershed. Applied Geochemistry v. 37, p. 64-78.

Mathurin, F.A., H. Drake, E.-L. Tullborg, T. Berger, P. Peltola, B.E. Kalinowski, and M.E. Astrom, 2014, High cesium concentrations in groundwater in the upper 1.2 km of fractured crystalline rock – Influence of groundwater origin and secondary minerals. Geochimica et Cosmochimica Acta v. 132, p. 187-213.

Mbonimpa, A., M. Aubertin, M. Aachib, and B. Bussiere, 2003, Diffusion and consumption of oxygen in unsaturated cover materials. Canadian Geotechnical Journal, v. 40, n. 5, p. 916-932.

McGuire, K.J., D.R. DeWalle, and W.J. Gburek, 2002, Evaluation of mean residence time in subsurface waters using oxugen-18 fluctuations during drought conditions in the mid-Appalachians. Journal of Hydrology v. 261, p. 132-149.

Meinzer, O.E., 1923, The occurrence of ground water in the United States, with a discussion of principles. U. S. Geological Survey: Reston, VA, United States.

Mills, C., 1995. *An Introduction to Acid Rock Drainage.* Infomine website: http://technology.infomine.com/enviromine/ard/home.htm. information verified January 9, 2015.

Mix, A.C., W. Rugh, N.G. Pisias, S. Vier, T. Hagelberg, S. Hovan, A. Kemp, M. Leinen, M. Levitan, C. Ravelo, and Leg 138 Scientific Party, 1992, 4. Color Reflectance Spectroscopy: A tool for rapid characterization of deep-sea sediments. Proceedings of the Ocean Drilling Program, Initial Reports, v. 138.

Navarre-Sitchler, A., C.I. Steefel, P.B. Sak, and S.L. Brantley, 2011. A reactive-transport model for weathering rind formation on basalt. Geochimica et Cosmochimica Acta v. 75, p. 7644-7667.

Pacheco, F.A.L. and A.M.P. Alencoao, 2006, Role of fractures in weathering of solid rocks: narrowing the gap between laboratory and field weathering rates. Journal of Hydrology v. 316, p. 248-265.

Paillet, F., 1985, Geophysical well log data for study of water flow in fractures near Mirror Lake, new Hampshire. U.S. Geological Survey Open-File Report 85-340.

Paillet, F. and K. Kapucu, 1989, Fracture characterization and fracture-permeability estimates from geophysical logs in the Mirror Lake watershed, New Hampshire. U.S. Geological Survey Water Resources Investigations Report 89-4058.

Parkhurst, D.L. and C.A.J. Appelo, 2013, Description of input and examples for PHREEQC version 3 – A computer program for speciation, batch-reaction, one-dimensional transport, and inverse geochemical calculations. U.S. Geological Survey Techniques and Methods, Book 6, Chapter A43, 497 pp.

Parkhurst, D.L., L.N. Plummer, and D.C. Thorstenson, 1982, BALANCE – A computer program for calculating mass transfer for geochemical reactions in ground water. U.S. Geological Survey Water-Resources Investigation Report 82-14, 29pp.

Penna, D., B. Stenni, M. Šanda, S. Wrede, T.A. Bogaard, M. Michelini, B.M.C. Fischer, A. Gobbi, N. Mantese, G. Zuecco, M. Borga, M. Bonazza, M. Sobotková, B. Čejková, and L.I. Wassenaar, 2012, Technical Note: Evaluation of between-sample memory effects in the analysis of δ^2H and $\delta^{18}O$ of water samples measured by laser spectroscopes. Hydrologic Earth System Science, v. 16, p. 3925-3933.

Plummer, L.N. and W.W. Back, 1980, The mass balance approach – Application to interpreting the chemical evolution of hydrologic systems. American Journal of Science, v. 280, p. 130-142.

Plummer, L.N., E.C. Prestemon, and D.L. Parkhurst, 1991, An interactive code (NETPATH) for modeling net geochemical reactions along a flow path. U.S. Geological Survey Water-Resources Investigations Report 91-4087, 227 pp.

Plummer, L.N., E.C. Prestemon, and D.L. Parkhurst, 1994, An interactive code (NETPATH) for modeling net geochemical reactions along a flow path, version 2.0. U.S. Geological Survey Water-Resources Investigations Report 94-4169, 130 pp.

Pohlmann, K.F. and A.J. Alduino, 1992, Potential sources of error in groundwater sampling at hazardous waste sites. U.S. Environmental Protection Agency Groundwater Issue. EPA/540/S-92/019.

Rajeev, P., D. Chan, and J. Kodikara, 2012, Ground-atmosphere interaction modelling for long-term prediction of soil moisture and temperature. Canadian Geotechnical Journal, v. 49, p. 1059-1073.

Reddy, M.M., P. Schuster, C. Kendall, and M.B. Reddy, 2006, Characterization of surface and ground water $\delta^{18}O$ seasonal variation and its use for estimating groundwater residence time. Hydrologic Processes v. 20, p. 1753-1772.

Reeves, J.B. III and D.B. Smith, 2009, The potential of mid- and near-infrared diffuse reflectance spectroscopy for determining major- and trace-element concentrations in soils from a geochemical survey of North America. Applied Geochemistry, v. 24, p. 1472-1481.

Samuel, E.A., 1968, Convective flow and its effects on temperature logging in small-diameter wells. Geophysics, v. 33, n. 6, p. 1004-1012.

Saravana, K., K. Srinivasamoorthy, R. Prakash, S. Gopinath, and C.S. Suma, 2015, An Evaluation of hydrogeochemistry of groundwater in Upper Vellar Sub-basin using mineral stability and solute transport modelling. International Conference on Water Resources, Coastal and Ocean Engineering (ICWRCOE 2015), Aquatic Procedia v. 4, p 1119-1125.

Seaton, W.J. and T.J. Burbey, 2005, Inflence of ancient thrust faults on the hydrogeology of the Blue Ridge Province. Groundwater, v. 43, n. 3, p. 301-313.

Segerstrom, K., 1955, Geologic Map of the Williamsburg Quadrangle, Massachusetts Surficial Geology. U.S. Geological Survey Geologic Quadrangle Map GQ-80.

Sellwood, S.M., D.J. Hart, and J.M. Bahr, 2015, Evaluating the use of in-well heat tracer tests to measure borehole flow rates. Groundwater Monitoring & Remediation, v. 35, n. 4, p. 85-94.

Shapiro, A., P. Hsieh, W. Burton, and G. Walsh, 2007, Integrated multi-scale characterization of groundwater flow and chemical transport in fractured crystalline rock at the Mirror Lake site, New Hampshire. In Hyndman, F., D.W. Day-Lewis, and K. Singha, eds., Subsurface Hydrology-Data Integrations for Properties and Processes – Geophysical Monograph Series. American Geophysical Union, p. 201-225.

Sharif, M.U., R.K. Davis, K.F. Steele, B. Kim, T.M. Kresse, and J.A. Fazio, 2008, Inverse geochemical modeling of groundwater evolution with emphasis on arsenic in the Mississippi River Valley alluvial aquifer, Arkansas (USA). Journal of Hydrology v. 350, p. 41-50.

Shelly, D., 1993, Igneous and Metamorphic Rocks Under the Microscope: Classification, textures, microstructures, and mineral preferred orientations. Chapman & Hall: London, England.

Sidborn, M., B. Sandstrom, E.L. Tullborg, J. Salas, F. Maia, A. Delos, J. Molinero, L. Hallbeck, and K. Pedersen, 2010, SR-Site: Oxygen ingress in the rock at Forsmark during a glacial cycle. Swedish Nuclear Fuel and Waste Management Project Technical Report 10-57.

Siva Soumya, B., M. Sekhar, J Riotte, S. Audry, C. Lagane, and J.J. Braun, 2011, Inverse modeling to analyze the spatiotemporal variations of chemical weathering fluxes in a granite-gneissic watershed: Mule Hole, South India. Geoderma v. 165, p. 12-24.

Smith, M. and A.N. Roychoudhury, 2013, Mobilisation of Iron from rocks in a fractured aquifer: Lithological and geochemical controls. Applied Geochemistry v. 31, p. 171-186.

Song, Q. and E.K. Yanful, 2001, Oxygen influx and geochemistry of percolate water from reactive mine waste rock underlying a sloping channeled soil cover. Applied Geochemistry, v. 26, p. 655-665.

Steefel C.I. and P.C. Lichtner, 1998, Multicomponent reactive transport in discrete fractures: I. Controls on reaction front geometry. Journal of Hydrology v. 209, p. 186-199.

Steefel C.I., D.J. DePaolo, and P.C. Lichtner, 2005, Reactive transport modeling: An essential tool and a new research approach for the Earth sciences. Earth and Planetary Science Letters v. 240, p. 539-558.

Stone, J.R. and M.L. DiGiacomo-Cohen, 2010, Surficial Geologic Map of the Heath-Northfield-Southwick-Hampden 24-Quadrangle Are in the Connecticut Valley Region, West-Central Massachusetts. U.S. Geological Survey Open File Report 2006-1260-G.

Steinmann, P., P.C. Lichtner, and W. Shotyk, 1994, Reaction path approach to mineral weathering reactions. Clays and Clay Minerals, v. 42, n. 2, p. 197-206.

Surrette, M.J., and Allen, D.M., 2008, Quantifying heterogeneity in variably fractured sedimentary rock using a hydrostructural domain. Geological Society of America Bulletin v. 120, p. 225-237.

Tallini, M., V. Carucci, and B. Parisse, 2014, Isotope hydrology and geochemical modeling: new insights into the recharge processes and water-rock interactions of a fissured carbonate aquifer (Gra Sasso, central Italy). Environmental Earth Science v. 72, p. 4957-4971.

Tiedeman, C.R., and Hsieh, P.A., 2001, Assessing an open-well aquifer test in fractured crystalline rock. Ground Water v. 39, p. 68-78.

Tsoflias, G.P., T. Halihan, and M.A. Muldoon, 2004, Fracture fluid flow properties investigations using gpr and hydraulic testing methods. Tenth International Conference on Ground Penetrating Radar, p. 521-524.

Tullborg, E.L., H. Drake, and B. Sandstrom, 2008, Paleohydrogeology: A methodology based on fracture mineral studies. Applied Geochemistry, v. 23, p. 1881-1897.

Turekian, K.K. and K.H. Wedepohl, 1961, Distribution of the elements in some major units of the Earth's crust. Geologic Society of America Bulletin, v. 72, p. 175-192.

Velbel, M.A., 1985, Geochemical mass balance and weathering rates in forested watersheds of the Southern Blue Ridge. American Journal of Science v. 285, pp. 904-930.

Velbel, M.A., 1993, Constancy of silicate-mineral weathering-rate ratios between natural and experimental weathering: implications for hydrologic control of differences in absolute rates. Chemical Geology, v. 105, p. 89-99.

Vroblesky, D.A. and J.E. Peterson, 2004. Flow-meter and passive diffusion bag tests and potential influences on the distribution of contaminants in wells at Galena Airport, Galena, Alaska, August to October 2002. U.S. Geological Survey Open-File Report 2004-1241.

Wellman, T., A. Shaprio, and M. Hill, 2009, Effects of simplifying fracture network representation on inert chemical migration in fracture-controlled aquifers. Water Resources Research v. 45.

White, A.F., 2002, Determining mineral weathering rates based on solid and solute weathering gradients and velocities: application to biotite weathering in saprolites. Chemical Geology v. 190, p. 69-89.

Willard, M.E., 1956, Geologic Map of the Williamsburg Quadrangle, Massachusetts Bedrock Geology. U.S. Geologic Survey Geologic Quadrangle Map GQ-85.

Wright, E., 1992, The hydrogeology of crystalline basement aquifers in Africa. In Wright, E. and W. Burgess, eds., *Hydrogeology of crystalline basement aquifers in Africa*. Geological Society Special Publication v. 66, p. 1-27.

X-Rite, 2007, A Guide to Understanding Color Communication. Grand Rapids, Michigan.

Zhou, Q., H. Liu, F. Molz, Y. Zhang, and G. Bodvarsson, 2007, Field-scale effective diffusion coefficient for fractured rock: Results from literature survey. Journal of Contaminant Hydrology v. 93, p. 161-187.

Zhu, C. and G. Anderson, 2002, Environmental Applications of Geochemical Modeling. Cambridge University Press: Cambridge, United Kingdom.